Repair of Conductive Layer on Carbon Fibre Reinforced Polymer Composite with Cold Gas Dynamic Spray

By

Daniel Cormier

Thesis submitted to the Department of Mechanical Engineering
in conformity with the requirements for the degree of
Masters of Science (Engineering)

University of Ottawa
Ottawa, Ontario, Canada
May 2015

Abstract

Carbon fibre reinforced composites are known for their high specific strength-to-weight ratio and are of great interest to the aerospace industry. Incorporating these materials into the fuselage, like in Boeing's 787 "Dreamliner", offers considerable weight reduction which increases flying efficiency, and reduces the cost of flying.

In flight, aircraft are often subject to lightning strikes which, in the case of composites, can result in localized melting given the high resistive nature of the material. Aerospace carbon fibre composites often incorporate a metallic mesh or foil within the composite layers to dissipate the electrical charge through the large aircraft. The damage to the aircraft is minimized but not always eliminated. This research aims to elaborate a practical technique to deposit thin layers of conductive material on the surface of aerospace grade composites. Using Cold Gas Dynamic Spray (CGDS), such coatings could be used to repair damaged components.

An experimental research approach was used to develop metallic coated composites. Using the CGDS equipment of Centerline (SST-P), specific parameters (such as gas temperature and stagnation pressure) were determined for each type of metallic coating (tin-based & copper-based). The use of bond coats was explored in order to attain the desired coatings. Once optimized, these coatings were evaluated with respect to their corrosive, adhesive, and electrical properties following industry standards.

Acknowledgement

I would like to start by thanking my thesis supervisor, Professor Bertrand Jodoin. I greatly appreciate the opportunity he provided me with. I would not have pursued this great endeavor if not for his initial interest in my abilities during my undergraduate studies. He has been nothing short of a great mentor and I am eternally grateful.

I am thankful to have had the opportunity to work with many industrial partners throughout my graduate studies. This research would not have been as successful without the collaboration of the Boeing Company, Centerline, and Mitacs. I would like to give a special thanks to Stephen Gaydos for his continued enthusiasm towards our research for the Boeing Company.

I would like to thank my colleagues for their enduring support. It is safe to say that without their prior work, my research would have not taken place. They have greatly contributed to my personal growth and turned what could have been hard long hours into great fun. Guillaume Archambault, Daniel MacDonald, Ruben Fernandez, Deliange (Leon) Goudl, Yannick Cormier, Phillippe Dupuis, Antoine Bacciochini, Patrick Trahan, Tyler Samson, thank you for your help.

I give great thanks to the group of technicians at the machine shop of the engineering department at the University of Ottawa. Their knowledge and skill were helpful in the execution of this research. I would also like to thank Dr. Mohammed Yandouzi for his earlier work on the subject matter. His work and guidance were time-saving.

Last but not least, I wish to thank my family for their immense support. Lou-Anne et Guy, votre soutien m'a permis de persister peu importe les circonstances. Tia & Spawn, you have been a great source of comfort throughout the years. Je ne serais pas ici sans ma famille.

Table of Contents

Abstract ii

Acknowledgement iii

List of Tables vii

List of Figures ix

List of Symbols xx

1 Introduction 1

1.1 Subject Background 1

1.2 Motivation and Research Objectives 5

1.3 Thesis Outline 5

2 Literature Review 7

2.1 Lightning Strike Protection on Aircraft 7

2.1.1 Background 7

2.1.2 Lightning Strike Protection Systems 11

2.2 Composites 13

2.2.1 Composite Classification 13

2.2.2 History of OMCs 14

2.2.3 Properties & Applications of OMCs 16

2.2.4 Manufacturing 20

2.2.5 Selection Factors 22

2.2.6 BMS 8-276 22

2.2.7 Metallization of PMC 24

2.3 Cold Gas Dynamic Spray (CGDS) 51

2.3.1 Classification 51

2.3.2 Historical Development 53

2.3.3 Process Overview 55

2.3.4 Gas Dynamics Principles in CGDS 56

2.3.5 Effects of CGDS Parameters 60

2.3.6 Bonding Mechanism 61

2.3.7 Critical Velocity Concept 63

2.3.8 Advantages of CGDS 65

2.4 Taguchi Method 65

2.4.1 Taguchi Experimental Design 65

2.4.2 Taguchi Analysis 66

3 Research Objectives 69

3.1 Feasibility and Coating Development 69

3.2 Coating Evaluation 69
3.2.1 Electrical Resistivity 70
3.2.2 Corrosion 70
3.2.3 Adhesion Strength 70
3.2.4 Additional Tests 71

4 Experimental Research Approach 72

4.1 Feedstock Powder Characterization 72
4.1.1 Centerline Pure Tin (SST-S6001) 72
4.1.2 Praxair Surface Technologies Pure Copper (Cu-159) 73
4.1.3 Centerline Pure Copper (SST-C5003) 74
4.1.4 Victrex PolyEtherEtherKetone (PEEK 150PF) 75

4.2 Powder Preparation 76
4.2.1 Sieving 76
4.2.2 Milling 77

4.3 Substrate 78
4.3.1 Toray Composites (America) Inc. BMS8-276 78
4.3.2 Composite Manufacturing 78

4.4 Surface Preparation 82
4.4.1 Grinding 83
4.4.2 Grit Blasting 83

4.5 CGDS Equipment 88
4.5.1 Heater 88
4.5.2 Controls 89
4.5.3 Orifice and Nozzle 90
4.5.4 Spray Gun Traverse System 91
4.5.5 Powder Feeding Equipment 91
4.5.6 Spray Chamber 94
4.5.7 Gas Delivery System 94

4.6 Taguchi Method Setup 95

4.7 Analysis Equipment 96
4.7.1 Processing and Polishing 96
4.7.2 Optical/Digital Imaging 100
4.7.3 Scanning Electron Microscope (SEM) 101

4.8 Testing Equipment and Procedures 102
4.8.1 Indentation Hardness 102
4.8.2 Surface Roughness 103
4.8.3 Electrical Resistivity 103
4.8.4 Adhesion Strength 104
4.8.5 Salt Fog Corrosion Spray Test 105

5 Coating Development and Adhesion Optimization 107

5.1 Tin Coating Development 107
5.1.1 Pressure & Temperature 107

5.1.2 Substrate Preparation 111
5.1.3 Traverse Velocity (TV) 115
5.1.4 Deposition 118
5.1.5 Build-up 122
5.1.6 Coating Thickness 124
5.1.7 Mechanical Interlocking 126
5.1.8 Wipe Tests 136
5.1.9 Summary 142
5.2 Copper Coating Development 143
5.2.1 Pure Copper Deposition 143
5.2.2 Bond Coat Powder Selection 145
5.2.3 Deposition 157
5.2.4 Composite Bond Coat on WGFP 160
5.2.5 Taguchi Optimization 163
5.2.6 Bond Coat Composition 183
5.2.7 PEEK Particles Size Distribution 185
5.2.8 Copper on Tin Bond Coat 192
6 Coating Evaluation (Characterization) 195
6.1 Surface Electrical Resistivity 195
6.2 Salt Fog Corrosion Behavior 201
6.3 Adhesion Strength 209
6.4 Allotropic Transformation Test 211
6.5 Curved Surface 214
7 Conclusion and Future Work 216
References 219
Appendix I: Dr. Mohammed Yandouzi's Work on Bond Coat Development 224
Appendix II: Attempts to Expose a Single LCFP 225
Appendix III: Effect of Surface Finish on Resistivity Measurements 234
Appendix IV: Attempts to Increase Adhesion of Tin Coating to BMS 8-276 235
Appendix V: Bond Coat Theoretical Volume Composition Calculation 239
Appendix VI: Attempts to Increase Adhesion of Composite Bond Coat to BMS 8-276 240

List of Tables

Table 1: Airplane Lightning Zones as Defined by SAE ARP 5414 [2] 10

Table 2: Typical Fibre Reinforcement Characteristics and Properties Used in OMCs [15] 17

Table 3: Important Materials Used in OMC Matrices and Their Characteristics [15] 18

Table 4: Chemical Vapor Deposition (CVD) Methods and Characteristics [7]. 26

Table 5: Results of Chemical Analysis of Two Different Sn-0.5Cu Samples (Conc. represents the absolute concentration and CI represents the confidence interval) [48] 49

Table 6: The Effect of Alloy Addition on Retarding the Transformation from β-Tin Into α-Tin [48] ... 50

Table 7: Thermal Spray Process Comparison - Adapted from [7] 53

Table 8: Chemical Composition Analysis of SST-S6001 Ingot 72

Table 9: Properties and Purchasing Information of Abrasives Used for Grit Blasting..... 85

Table 10: Material Composition of the "Ebonygrit" Abrasive (20 grit) according to the manufacturer (Opta Minerals Inc.) 86

Table 11: Material Composition of the Aluminum Oxide Abrasive (80 grit) according to the manufacturer (Opta Minerals Inc.) 87

Table 12: Levels of Each Parameter of the Taguchi Optimization for the Composite Bond Coat..... 96

Table 13: CGDS Parameters Held Constant for the Tin Coating Development Test for Pressure and Temperature..... 108

Table 14: CGDS Parameters Held Constant for the Surface Preparation Development Test 113

Table 15: CGDS Parameters Held Constant for the Tin Coating Traverse Velocity Development Test. 116

Table 16: CGDS Parameters Held Constant for Both First Layer and Build-up Layer 128

Table 17: Tin Coating Build-Up Layer Number of Passes Along With Foreseen Thickness (Note: all other parameters can be viewed in Table 16)..... 128

Table 18: CGDS Parameters Held Constant for the Pure Copper Deposition Test..... 144

Table 19: Three Different Powder Combinations Used for the 97.5wt% Copper and 2.5wt% PEEK Bond Coat Trials..... 145

Table 20: CGDS Parameters Held Constant for the 97.5wt% Copper and 2.5wt% PEEK Bond Coat Trials..... 146

Table 21: CGDS Parameters Held Constant for the 97.5wt% Copper and 2.5wt% PEEK Bond Coat Selection..... 147

Table 22: CGDS Parameters Held Constant for the Pure Copper Top Coats Trials 149

Table 23: Comparison of Different Copper Top Coats and Bond Coats 153

Table 24: CGDS Parameters Held Constant for the 97.5wt% SST-C5003 and 2.5wt% PEEK Bond Coat on WGFP BMS 8-276..... 160

Table 25: Parameters Used for 97.5wt% SST-C5003 and 2.5wt% PEEK Bond Coats When Varying the Traverse Velocity 167

Table 26: Parameters Used for 97.5wt% SST-C5003 and 2.5wt% PEEK Bond Coats When Varying the Standoff Distance 169

Table 27: Taguchi Experiment Parameter in Orthogonal Array 171

Table 28: Constant Parameters Used for the Bond Coat in the Taguchi Experiments 172

Table 29: Parameters Used for Composite Bond Coat Optimization 183

Table 30: Bond Coat Composition Different PEEK Particle Size Distribution Ranges 188

Table 31: Parameters Used for Pure PEEK Deposition on LCFP of BMS 8-276 190

Table 32: Constant Parameters Used for the Top Coat Trials on Tin Coated WGFP BMS 8-276 193

Table 33: Combinations of Top Coats and Bond Coats on BMS 8-276 with Comparative Copper Sheeting Used for Resistivity Measurements 196

Table 34: Tin Coating Parameters Used (Top Coat and Bond Coat) 196

Table 35: 98wt% SST-C5003 and 2.0wt% Sieved (0-45µm) PEEK Coating Parameters Used (Top Coat and Bond Coat) 197

Table 36: Pure Copper Top Coat Parameters Used 198

Table 37: List of Coatings Placed in Salt Spray Corrosion Chamber 201

Table 38: Tin Coating Parameters Used for Convexe and Concave CFRP 214

Table 39 Feedstock Powder Composition (metalwt% - polymerwt%) (Green indicates successful deposition and red indicates no deposition) 224

Table 40: Parameters Used for the Heat Test on the BMS8-276 Substrate 225

Table 41: Before and After Images of BMS8-276 Substrate Surface Grit Blasting Process at Different Pressures 229

Table 42: Constant Parameters Used for the Hot Grit Blasting Process on the BMS8-276 Substrate 230

Table 43: Sheet Resistance of As-Sprayed and Polished Surface Finish 234

Table 44: Traverse Velocity of Samples T40 and T42 235

Table 45: Constant Spray Parameters Used to Produce Tin Coatings on LCFP BMS 8-276 Substrates 235

Table 46: Constant Spray Parameters Used to Produce Tin Coatings of Different Thicknesses on LCFP BMS 8-276 Substrates 240

Table 47: Spray Parameters Used for Milled Composite Powder on LCFP BMS 8-276 Substrate 245

List of Figures

Figure 1: Damage caused by lightning moving along an airplane causing many exit locations [2]. 2

Figure 2: Worldwide Lightning Observations (flashes/kilometers^2/year) for April 1995 through February 2003 from the Combined Observations of the National Aeronautics and Space Administration (NASA) Optical Transient Detector and Land Information Systems Instruments [2]. 8

Figure 3: The distribution of lightning strikes by altitude from a survey of the United States commercial jets [2]. 9

Figure 4: Lightning strike prone areas of an airplane indicated by zone [2]. 11

Figure 5: Common forms of fibre reinforcement. In general, the reinforcements can be straight continuous fibres, discontinuous or chopped fibres, particles or flakes, or continuous fibres that are woven, braided, or knitted [15]. 14

Figure 6: The Boeing Company's 787 "Dreamliner" material distribution. "Carbon Laminate" represent carbon fibres impregnated with polymer built up in layers. "Carbon Sandwich" are two thin carbon laminate skins attached to a thick and lightweight core providing the composite with high bending stiffness and extremely low overall density. "Other Composites" represent a variety of other materials integrated together (i.e. fibreglass and glass/carbon hybrid) [1]. 15

Figure 7: "Ashby plot" of normalized stiffness Vs normalized strength of various materials. Dark areas represent continuous fibre reinforced OMCs. Specific fibre materials such as carbon fibres (graphite), polyacrylonitrile fibres (P), and aramid fibres (A) are located within this area. MMCs such as discontinuously reinforced aluminum (DRA), discontinuously reinforced titanium (DRTi), and continuous fibre reinforced (f) aluminum (Al) and Titanium (Ti) fall between the extremes of axial (0°) and transverse (90°) graphite OMCs. The "Metals" area represents structural metals such as β–titanium alloys and ultrahigh-strength steels. Q/I represent quasi-isotropic fibre orientation [15]. 19

Figure 8: Unidirectional versus quasi-isotropic lay-ups [15]. 20

Figure 9: Complex structure wound on six-axis winding machine [15]. 21

Figure 10: Optical micrograph of the BMS 8-276 toughened matrix system [14]. 23

Figure 11: Trade-off between compression strength after impact and hot-wet compression for the Boeing Company CFRP [14]. 24

Figure 12: (a) Resistance heat evaporation process and (b) typical sputter coating process [7]. 25

Figure 13: Typical electroplating process [7]. 26

Figure 14: Schematic of thermal spray coating microstructure showing common features [7]. 27

Figure 15: Microstructure of Al_2O_3 coating on polyimide composite substrate with plasma-sprayed Al bond coat [17]. 28

Figure 16: Schematic diagrams of erosion process in unidirectional fibre reinforced composites under (a) parallel and (b) perpendicular impact conditions [30]. 29

Figure 17: Schematic representations of brittle and ductile type of erosive wear [30]. 30

Figure 18: Influence of impingement angle, fibre orientations on the erosive wear of (a) carbon fibre reinforced epoxy and (b) glass fibre reinforced epoxy composites (v=45±5 m/s, steel balls diameter=300–500 µm, exposure time=180 s] [30]. 30

Figure 19: Peel strength as a function of roughness depth R_z for electroless/electroplated copper onto carbon fibre reinforced polymer [8]. 31

Figure 20: Average surface roughness (R_a) and accompanying adhesion strength of three different materials (composite A, composite B, and resin) coated with aluminum on their surfaces. Standard deviation for adhesion strength was less than 0.2MPa [16]. 32

Figure 21: Adhesion strength of copper coating on CFRE with respect to different surface treatment for two different coating thickness ranges [20]. 32

Figure 22: Enhancement of adhesion strength of an aluminum coating for composites A, B, and resin with surface activation as compared to untreated materials. Standard deviation for adhesion strength was less than 0.2 MPa [16]. 34

Figure 23: Fracture surface types between aluminum coating and composite surface without (left) and with (right) plasma activation [16]. 34

Figure 24: Effect of co-cured metallic bond coat finish on copper deposition (polished, unaltered rough, and resin rich) [29]. 35

Figure 25: Cross-sections of columnar copper deposition on spherical copper particles of co-cured layer using CGDS [29]. 35

Figure 26: Cross-sectional micrograph of copper coating deposited onto (a) polycarbonate-acrylonitrile butadiene styrene (PC/ABS Polymer), (b) Glass Fibre Composite, and (c) high density polyethylene using cold spray [19], [21]. 36

Figure 27: Tin coating on a variety of polymer substrates [21]. 37

Figure 28: Micrographs of tin coating cross-sections on a variety of polymer substrates. Please note that the coating was chemically etched for (d) [21]. 37

Figure 29: Copper coating on the PVC substrate (a) with tin interlayer, (b) with spherical copper particle interlayer, and (c), (d) interface of the two respectively [23]..... 38

Figure 30: Copper coating on the polymer substrate: (a) dendritic copper coating on the PVC substrate using spherical copper interlayer, (b) dendritic copper coating on the epoxy substrate using tin interlayer, (c, d) high magnifications images of (a, b) show the coating interface [24]. 39

Figure 31: Schematic representation of spherical copper particle interaction with (a) PVC and (b) epoxy with accompanying (c) FIB bisection of spherical copper particle embedded in the PVC substrate and (d) SEM image of spherical copper particle trapped inside the crater on the epoxy substrate [24]. 40

Figure 32: Schematic representation of cold sprayed (a) dendritic copper and (b) tin particle interaction with polymer substrate with accompanying SEM images of the interaction of cold sprayed (c) dendritic copper particle and (d) tin particle on epoxy substrate [24]. 41

Figure 33: Schematic representation of interaction of dendritic with different interlayers: (a) spherical copper interlayer, (b) tin interlayer [24]. 41

Figure 34: Normalized deposition efficiency (DE) and deposition rate (DR) at different powder feeding rates [28]. 42

Figure 35: (a) Cross-sectional SEM morphology of pure Al coating and (b) zoom the interface between the coating and the substrate [9]. 43

Figure 36: (a) Cross-sectional SEM morphology of Al/Cu coating and (b) zoom the interface between the Al coating and the Cu coating [9]. 43

Figure 37: Electrical conductivity of as sprayed, annealed at 300°C, and annealed at 600°C copper coatings produced by cold spray (CS), HVOF, and arc spray (AS) compared to a bulk copper sample (reference material) [35]. 45

Figure 38: Electrical resistivity of in plane and through thickness of cold sprayed Al coatings – Adapted from [38]. 45

Figure 39: CS Process Characterization Chart for Polymer Substrates [21]. 46

Figure 40: Allotropic transformation of tin from its β phase to its α phase [41]. 47

Figure 41: The transformation of β-tin (white tin) into α-tin (gray tin) occurring in Sn-0.5 wt.% Cu solder alloy, after prolonged exposure at -18°C [43]. 48

Figure 42: Influence of the cold work on the transformation rate in a tin 0.8wt% copper alloy at -30°C [42]. 51

Figure 43: Thermal spray processes and subsets - Adapted from [7]. 52

Figure 44: Temperature and velocity regimes for several thermal spray processes [7]. 52

Figure 45: Cross-section of Ni-Al Coatings Manufactured Using Different Spray Techniques – Adapted from [51]. 53

Figure 46: Timeline of significant developments during the growth of the thermal spray industry [7]. 55

Figure 47: Schematic diagram of a cold gas dynamic spray process outline. Equipment is labelled in normal font, and variables are labelled in italic font. 56

Figure 48: Image of impinging gas jet showing bow shock and oblique shock waves [58]. 61

Figure 49: Computational model of 25 µm Cu particle impacts on a Cu substrate at 500 m/s with an initial temperature of 20°C (left). (a, b) Strain field and (c, d) temperature field at specific times after impact [61]. Titanium particle impact on titanium substrate showing ejected material from impact (right) [63]. 62

Figure 50: Schematic correlation between particle velocity, deposition efficiency (DE) and impact effects for a constant impact temperature. 64

Figure 51: Window of sprayability of particle velocity vs. particle impacting temperature [71]. 65

Figure 52: Orthogonal array indicating the variation level (1, 2, 3) of each parameter (P1, P2, P3, P4) to be used for a given experiment [78]. 66

Figure 53: Orthogonal array highlighting the SN ratios that correspond to the same level for parameter 3 (P3) [78]. 67

Figure 54: Tabulated SN ratio for each level and parameter with accompanying R values (modified from [78]). 68

Figure 55: SEM image of tin powder (SST-S6001). 73
Figure 56: SEM image of copper powder from Praxair (Cu-159). 74
Figure 57: SEM image of copper powder from Centerline (SST-C5003). 75
Figure 58: SEM Image of PEEK powder from Victrex (PEEK 150PF). 76
Figure 59: RX-29 sieve for W. S. Tyler. 77
Figure 60: (a) Pulverisette 7 planetary mill from Fritsch and (b) 80 mL grinding bowls with balls. 77
Figure 61: (a) Overview of the BMS 8-276 composite structure with (b) zoom on toughening heterogeneous system. 78
Figure 62: (a) Wire EDM automated machine with (b) close-up of wire cutting process. 79
Figure 63: Concave and convex curved moulds. 79
Figure 64: Stacking process for CFRP depicting prepreg stacking plies mid plane symmetry and compacted prepreg stack. 80
Figure 65: Vacuum bagging method for manufacturing CFRP - Adapted from [29]. 81
Figure 66: Gast DAA-V715A-EB diaphragm vacuum pump. 81
Figure 67: Carbolite PF120 curing oven. 82
Figure 68: Curved CFRP substrates produced (a) with excess epoxy and (b) trimmed. 82
Figure 69: BMS 8-276 substrate with (a) a WGFP exposed and (b) a single LCFP exposed. 83
Figure 70: Grit blasting unit. 84
Figure 71: (a) Image of "Ebonygrit" abrasive (20 grit) with (b) high magnification zoom. 85
Figure 72: (a) Image of aluminum oxide abrasive (80 grit) with (b) high magnification zoom. 86
Figure 73: (a) Image of "Garnet Grit" abrasive (36 grit) with (b) high magnification zoom. 87
Figure 74: (a) Image of "Steel Grit" abrasive (25 grit) with (b) high magnification zoom. 88
Figure 75:Gas heater from Centerline (Windsor) Ltd. 89
Figure 76: Control cabinet from Centerline (Windsor) Ltd. 90
Figure 77: Disassembled and Assembled De Laval nozzle showing (from left to right): heater nut, brass orifice, collet, tightening nut, and stainless steel nozzle. 90
Figure 78: Automated X-Y traverse system from IAI America Incorporated. 91
Figure 79:Praxair powder feeder (Model 1264). 92
Figure 80: Assembled view of feeding wheel in canister with hammer. 93
Figure 81: (a) Medium hole (240) and (b) small hole (320) powder feeder wheel. 93
Figure 82: Centerline (Windsor) Ltd custom built spray chamber. 94
Figure 83: Nitrogen bottle reservoir (bottle pack). 95
Figure 84: (a) Struers Secotom-10 cutting apparatus and (b) diamond coated metal cut-off wheel. 97
Figure 85: Accelerated cured resin. 97

Figure 86: Resin filled moulds in glass bell vacuum chamber. 98
Figure 87: (a) Struers TegraPol-31 polishing machine and (b) mounted sample underwent polishing steps. 98
Figure 88: Elma TS 540 transsonic bath (ultrasonic cleaning bath). 99
Figure 89: Parker Denton Vacuum Desk IV gold sputter machine. 100
Figure 90: (a) Kingdak NMM-800TRF optical microscope and (b) Keyence VHX digital microscope. 101
Figure 91: Zeiss EVO MA10 SEM. 102
Figure 92: (a) Struers Duramin-1 micro-hardness tester with (b) close-up of indenter. 103
Figure 93: (a) Four point probe resistivity sensor and (b) Keithley Model 2010 digital multimeter. 104
Figure 94: DeFelsko PosiTest AT-A adhesion testing apparatus. 104
Figure 95: Example of pull-stub with excess cured glue (a) before and (b) after removal. 105
Figure 96: Salt spray apparatus. 106
Figure 97: Pressure and temperature combinations for tin coating development test. 109
Figure 98: Cross-section of eroded BMS 8-276 after tin deposition (T14). 109
Figure 99: Cross-section of tin coated BMS 8-276. 110
Figure 100: Micro-indentation of tin coating (T6) depicting crack propagation along particle perimeters. 111
Figure 101: Roughness (R_a) measurements for an array of surface preparations including grit and blasting pressure combinations on laminar carbon-fibre ply (LCFP) and woven glass fibre ply (WGFP) of BMS 8-276. 112
Figure 102: Seeped glue on tin coated BMS 8-276 (a) post PATTI pull and (b) cross-section. 113
Figure 103: PATTI adhesion strength of tin coatings on LCFP and on WGFP BMS 8-276 for a variety of roughness. The relation between the roughness and the adhesion strength are emphasized using a linear trendline. 114
Figure 104: Tin coated BMS 8-276 with porous wave-like pattern. 116
Figure 105: Traverse velocity development test with accompanying tin coating thickness on laminar carbon-fibre ply (LCFP) of BMS 8-276. 117
Figure 106: Tin coating thickness plotted with respect to the traverse velocity for two different powder feeder wheels: a 240 medium hole and a 320 small hole. 118
Figure 107: Cross-section of dense tin coating on LCFP BMS 8-276 (sample T22). 118
Figure 108: (a) textured surface of tin coating deposited at high traverse velocity (100 mm/s) on WGFP BMS 8-276 with (b) zoom of surface. 119
Figure 109: Cross-section of (a) tin coating deposited at high traverse velocity (100 mm/s) on WGFP BMS 8-276 with (b) close-up of deposition interruption. 120
Figure 110: Representation of the usual preparation method exposing a single LCFP and the inclined preparation method exposing multiple LCFPs. 120
Figure 111: Tin coatings on multiple LCFPs of BMS 8-276 sprayed at 100 mm/s and 50 mm/s. 121

Figure 112: Discontinuous tin coating on BMS 8-276 with multiple LCFPs exposed the toughening heterogeneous system. 122

Figure 113: Tin coating thickness variation through receding multiple passes. 123

Figure 114: WGFP BMS 8-276 coated with tin deposited at high TV (200 mm/s) at (a) 1 pass, (b) 2 passes, (c) 3 passes, (d) 4 passes, (e) 5 passes, (f) 6 passes, (g) 7 passes, (h) 8 passes. 123

Figure 115: Thick tin coating deposited on WGFP BMS 8-276 at high TV using multiple passes. 124

Figure 116: Surface preparation with blasting pressure for the coating thickness development test. 125

Figure 117: PATTI adhesion strength of tin coatings (sprayed with different passes) on “As Received” BMS 8-276, 80 grit blasted at 200 psi (1.38 MPa) and 80 grit blasted at 100 psi (0.69 MPa). 126

Figure 118: Tin Coating Traverse Velocity and Feed Rate Used for the First Pass Along With Estimated Thickness. 127

Figure 119: Cross-sections of samples T31, T32, T33, and T34. Discontinuities are present in samples T31 & T34. 129

Figure 120: Adhesion values of varying heat multi-pass samples (T31, T32, T33, and T34). Three pulls were performed on each sample. The results of sample T31 is presented in red because tests were unreliable. Sample T34 only has two data points since one was deemed unreliable. 130

Figure 121: Cross-sections of samples T31, T32 T33, and T34 at 200X. The tin and glass fibre interlocking is highlighted by red ovals. Note that the tin coating of sample T31 is partially debonded from the BMS 8-276 substrate. 131

Figure 122: Cross-sections of samples T31, T32, T33, and T34 at 500X. Note that sample T32 has deeper fibre embedment in the tin coating than samples T31 & T34 and note that sample T33 has even deeper fibre embedment. 132

Figure 123: SEM images of the BMS 8-276 surface of samples T31, T32, T33, and T34 post PATTI pull depicting exposed glass fibres. 133

Figure 124: Backscattered images of the BMS 8-276 surface of samples T31, T32, T33, and T34 post PATTI pull depicting tin residue near glass fibres. 134

Figure 125: (a) Secondary electron (SE) image and (b) backscattered detection (BSD) image at a 1000 magnification of sample T33. 135

Figure 126: Etched cross-section of sample T32 at (a) low and (b) high magnification. 136

Figure 127: Coating traverse velocity and feed rate used for the wipe tests. 137

Figure 128: Wipe tests W1, W2, W3, and W4. 137

Figure 129: Low magnification SEM images of wipe test W1, W2, W3, and W4. 138

Figure 130: (a) SEM image of tin particles primarily deposited on areas where glass fibres are close to the surface, (b) showing an increase in the number of indentation marks near these areas and (c) tin particles directly adhering to locations above which reinforcement fibres are close to the surface (d) with high magnification of single tin particle deformed above epoxy covered glass fibre. 139

Figure 131: SEM images of fractured BMS 8-276 of (a) sample W4 with (b) close-up of fracture zone, (c) sample W1, and (d) micro-crack of sample W4. 140

Figure 132: SEM images of wipe test W3 showing (a) tin platter with (b) magnified view of wave-like formation and (c) damaged substrate with (d) magnified view. 141

Figure 133: SEM images of (a) wipe test W2 with (b) angled magnification. 142

Figure 134: Pure copper deposition temperature and pressure. 143

Figure 135: CGDS traces of pure copper deposition test. 144

Figure 136: Traverse velocities for the bond coat powder selection test. 147

Figure 137: (a) 97.5wt% SST-C5003 and 2.5wt% PEEK bond coat on grit blasted BMS 8-276, (b) 97.5wt% Cu-159 and 2.5wt% PEEK bond coat on grit blasted BMS 8-276, and (c) 48.75wt% SST-C5003, 48.75wt% Cu-159 and 2.5wt% PEEK bond coat on grit blasted BMS 8-276. 148

Figure 138: Pressure/temperature combinations used for the top coat trials (trial numbers are indicated beside each data point). 150

Figure 139: (a) Top coat trials on 97.5wt% SST-C5003 and 2.5wt% PEEK bond coat, (b) top coat trials on 97.5wt% Cu-159 and 2.5wt% PEEK bond coat, (c) top coat trials on 48.75wt% SST-C5003, 48.75wt% Cu-159 and 2.5wt% PEEK bond coat. 151

Figure 140: Bond coat composition percentages. 156

Figure 141: Discontinuities in 97.5wt% SST-C5003 and 2.5wt% PEEK bond coat on (a) a smooth BMS 8-276 substrate and (b) a BMS 8-276 substrate grit blasted with a 20 grit size at 150 psi (1.03 MPa). Both substrates have multiple LCFPs exposed. 158

Figure 142: Analyzed sections of (a) 97.5wt% SST-C5003 and 2.5wt% PEEK Bond Coat on (a) a smooth BMS 8-276 substrate and (b) a BMS 8-276 substrate grit blasted with a 20 grit size at 150 psi (1.03 MPa) (see Figure 141). Both substrates have multiple LCFPs exposed. 158

Figure 143: (a) Overall cut of a 97.5wt% SST-C5003 and 2.5wt% PEEK bond coat on a BMS 8-276 substrate (see Figure 142a), (b) Zoom of the location where the thermoplastic layer starts, (c) Zoom of the location where the carbon fibre reinforced epoxy layer starts, and (d) another 97.5wt% SST-C5003 and 2.5wt% PEEK bond coat on an island of CFRE surrounded by the toughening heterogeneous system (see Figure 142b). 159

Figure 144: Traverse velocities, step sizes, and number of passes for the 97.5wt% SST-C5003 and 2.5wt% PEEK bond coats on WGFP BMS 8-276. 161

Figure 145: 97.5wt% SST-C5003 and 2.5wt% PEEK bond coat trial number 148, 149, and 150 on WGFP BMS 8-276. 162

Figure 146: Variation between the thickest (1) and thinnest (2) (excluding the discontinuities) points of the composite coating on WGFP BMS 8-276. 162

Figure 147: (a) 97.5wt% SST-C5003 and 2.5wt% PEEK bond coat trial number 149 on WGFP BMS 8-276 with (b & c) zoom on discontinuities. 163

Figure 148: The arithmetic average of absolute roughness values (R_a) are shown with respect to the grit blasting pressure for both 20 and 80 grit. Note that some error bars are not visible due to their small size. 165

Figure 149: 97.5wt% SST-C5003 + 2.5wt% PEEK bond coat sprayed at different traverse velocities (15, 20, 25, and 30 mm/s) on a BMS 8-276 substrate. 168

Figure 150: 97.5wt% SST-C5003 + 2.5wt% PEEK bond coat sprayed at different standoff distances (5, 10, 15, and 20mm). 170

Figure 151: Single carbon fibre reinforced epoxy layer substrates used for the nine Taguchi experiment sets. The nine different sets of experiments are outlined in Table 27. 172

Figure 152: (a) All Taguchi bond coats deposited onto BMS 8-276 substrates and (b) delaminated bond coats. 173

Figure 153: Thickness of the bond coats deposited on the nine sets of substrates with standard deviation. Please note that the blue, red and green bars represent the first, second and third test plates for each Taguchi experiment set respectively. Some sets contain two test plates whereas others have three. 174

Figure 154: Signal-to-noise ratio of the thickness for each parameter according to the corresponding level. 175

Figure 155: (a) Resistivity of the bond coats deposited on the nine sets of substrates with standard deviation. (b) Zoom of the smaller values. Please note that the blue, red and green bars represent the first, second and third test plates for each Taguchi experiment set respectively. Some sets contain two test plates whereas others have three. 176

Figure 156: Signal-to-noise ratio of the resistivity for each parameter according to the corresponding level. 177

Figure 157: Number of adhesion measurements made with the PATTI for the Taguchi experiment. 178

Figure 158: Adhesion of the bond coats deposited on the nine sets of substrates with standard deviation. Adhesion values of zero were assigned to the experiment sets 3, 6, and 9 because the bond coat delaminated. Please note that the blue, red and green bars represent the first, second and third test plates for each Taguchi experiment set respectively. Some sets contain two test plates whereas others have three. 179

Figure 159: Signal-to-noise ratio of the adhesion for each parameter according to the corresponding level. 180

Figure 160: Porosity of the bond coats deposited on the nine sets of substrates with standard deviation. Please note that the blue, red and green bars represent the first, second and third test plates for each Taguchi experiment set respectively. Some sets contain two test plates whereas others have three. 181

Figure 161: Signal-to-noise ratio of the porosity for each parameter according to the corresponding level. 182

Figure 162: Composite Bond Coat Composition Optimization Test. 184

Figure 163: Deposited bond coats with varying feedstock composition. 184

Figure 164: PATTI results of samples 153 (3 results), 154 (4 results) and 155 (3 results). The red coloured results indicate unreliable results caused by glue seeping between the coating and the substrate. 185

Figure 165: PEEK size distribution optimization test. 186

Figure 166: Deposited bond coats with 97.5wt% SST-C5003 + 2.5wt% PEEK with PEEK particle size distribution ranges of 75-150µm, 45-75 µm, and 0-45 µm. 186

Figure 167: Adhesion strength of Composite bond coat made from 97.5wt% SST-C5003 + 2.5wt% PEEK feedstock powder with 0-45 µm and 45-75 µm PEEK particle size distribution ranges. 187

Figure 168: Cross-section of composite bond coat produced with 97.5wt% SST-C5003 and 2.5wt% PEEK with (a) 0-45 µm, (b) 45-75 µm, and (c) 75-150 µm PEEK particle distribution. 188

Figure 169:Pure PEEK deposition test. 189

Figure 170: Pure PEEK coating on BMS 8-276 substrate. 190

Figure 171: Cross-section of pure PEEK coating on BMS 8-276 substrate. 191

Figure 172: Pure copper top coat trials on tin coated WGFP BMS 8-276. 192

Figure 173: Pure copper (SST-C5003) top coat trials on tin (SST-S6001) coated WGFP BMS 8-276 composite. 193

Figure 174: Cross-section of trial number 9. 194

Figure 175: Example of thickest and thinnest points of the coating used to calculate the average thickness for each sample. 198

Figure 176: (a) Sheet resistance with respect to thickness of a variety of samples (see Table 33) plotted against BAC5056 classifications. (b) Zoom of samples fit to protect the BMS 8-276 against a lightning strike (highlighted in green). 199

Figure 177: Agglomerated tin particles on a coated BMS 8-276. 200

Figure 178: Example of a taped 1.5" X 2" (5.1 cm X 3.8 cm) sample before salt spray corrosion test. 202

Figure 179: Salt spray corrosion test cases 1 and 2. The time spent in the salt spray chamber is indicated under each sample. 203

Figure 180: Salt spray corrosion test cases 3 and 4. The time spent in the salt spray chamber is indicated under each sample. 203

Figure 181: Salt spray corrosion test cases 5, 6, 7, and 8. The time spent in the salt spray chamber is indicated under each sample. 204

Figure 182: Salt spray corrosion test case 9. The time spent in the salt spray chamber is indicated under each sample. 205

Figure 183: The sheet resistance with respect to the time spent in the corrosion chamber. 206

Figure 184: Cross-sectional image of non-scribed area of (a) Test Case 1, (b) Test Case 3, (c) Test Case 5, (d) Test Case 7, and (e) Test Case 9. 207

Figure 185: Cross-sectional image of scribe of (a) Test Case 2, (b) Test Case 4, (c) Test Case 6, and (d) Test Case 8. 208

Figure 186: The adhesion strength with respect to the time spent in the corrosion chamber. 210

Figure 187: Allotropic transformation test where samples from section 5.1.6 and section 5.1.7 were placed in three different refrigerators held at -18°C, -80°C, and 6°C respectively for a period of 3000 hours. 212

Figure 188: An example of the tin coated WGFP BMS 8-276 samples prior to the 3000h allotropic transformation test. 212

Figure 189: Allotropic transformation test samples after 3000 hours in a (a)- 80°C, (b) -18°C, and (c) 6°C temperature environment. 213

Figure 190: (a) Convex and concave pre-impregnated carbon fibre reinforced epoxy composites (b) coated with tin. 215

Figure 191: (a) 500X and (b) 200X cross-sections of the heat tested BMS8-276 depicting voids formed by the high temperatures. 226

Figure 192: Twenty-four hour acid test using (a) hydrochloric acid (HCl), (b) methylene chloride (CH_2Cl_2), (c) hydrofluoric acid (HF), and (d) nitric acid (HNO_3). 226

Figure 193: (a) A section view of the nitric acid tested BMS8-276 substrate and (b) a 500X zoom of the upper right corner. 227

Figure 194:Twenty-four hour solvent test using (a) isopropyl alcohol (C_3H_7OH), (b) ethyl acetate ($CH_3COOCH_2CH_3$), and (c) ethanol (CH_3CH_2OH). 227

Figure 195: Hot grit blasting test at 100°C, 200°C, 300°C, 400°C and 500°C, passing only once above the same area at the parameters specified in Table 42. There is an increase in the exposure of the toughening heterogeneous system (in white) regardless of the temperature. 231

Figure 196: Hot grit blasting test at 100°C, 200°C, 300°C, 400°C and 500°C, passing 5 times above the same area at the parameters specified in Table 42. Severe wear is apparent and the blasting process seems to target and erode the LCFP more efficiently than the toughening heterogeneous system. 231

Figure 197: Milled BMS 8-276 substrate with two LCFP exposed. 232

Figure 198: Grinded BMS 8-276 substrate with a single LCFP exposed. 233

Figure 199: Tin coated BMS 8-276 as-sprayed (left) and polished (right). 234

Figure 200: Glass beaded tin coatings (T40 & T42) on BMS 8-276 substrates. 236

Figure 201: Adhesion of glass beaded tin coatings deposited at two different spray parameters. Note that the high adhesion of the T40 spray parameters that were glass beaded at 60 psi (green) emanates from a single high adhesion value of 513 psi while the rest of the adhesion were recorded near 265 psi. 237

Figure 202: Tin coating deformation on top (a) and at the interface (b) of the BMS 8-276 substrate. 238

Figure 203: Bond coat thickness variation with respect to traverse velocity for different feedstock powder compositions (three sets). There is no column for the 1.5wt% PEEK + 98.5wt% SST-C5003 bond coat sprayed at 30 mm/s because no coating was deposited at this parameter. It is important to note that some of the thinner coatings were discontinuous in nature. .. 241

Figure 204: Adhesion values for the bond coats composed of 2.5wt% PEEK feedstock powder deposited at traverse velocities of 15 mm/s, 20 mm/s, and 25 mm/s. Note that there is no

standard deviation for the bond coat deposited at 25 mm/s because only one value was successfully recorded. 242

Figure 205: PEEK content in the bond coat deposited at traverse velocities of 15 mm/s, 20 mm/s, 25 mm/s, and 30 mm/s for feedstock powder compositions of 9.5vol% (1.5wt%), 12.3vol% (2.0wt%), and 15.0vol% (2.5wt%). 243

Figure 206: Effect of heat treatment process on the adhesion strength of the composite bond coat to the BMS 8-276. 244

Figure 207: (a) SEM image of 97.5 wt% SST-C5003 + 2.5 wt% PEEK (0-45µm) powder milled for 16 minutes in a planetary mill and (b) not milled. 245

Figure 208: (a) Deposited milled powder on BMS 8-276 substrate with (b) cross-sectional. 246

List of Symbols

Abbreviations

ABS: Acrylonitrile Butadiene Styrene

APS: Air Plasma Spray

ARP: Aerospace Recommended Practices

AS: Arc Spray

BSE: Back-Scattered Electron

CFRE: Carbon Fibre Reinforced Epoxy

CGDS: Cold Gas Dynamic Spray

CMC: Ceramic-Matrix Composite

CS: Cold Spray

CT: Compute Tomography

CVD: Chemical Vapor Deposition

DE: Deposition Efficiency

DR: Deposition Rate

DRA: Discontinuously Reinforced Aluminum

DRTi: Discontinuously Reinforced Titanium

EBSD: Electron Back-Scatter Diffraction

EDM: Electric Discharge Machining

EDS: Energy Dispersive Spectroscopy

PFR: Powder Feed Rate

HPCS: High Pressure Cold Spray

HVOF: High Velocity Oxygen Fuel

IWWF: Interwoven Wire Fabric

LCFP: Laminar Carbon-Fibre Ply

LPCS: Low Pressure Cold Spray

LTE: Local Thermodynamic Equilibrium

MMC: Metal-Matrix Composite

OEM: Original Equipment Manufacturer

OMC: Organic-Matrix Composite

PATTI: Portable Adhesion Tensile Testing Instrument

PEEK: PolyEtherEtherKetone

PC: Polycarbonate

PGDS: Pulsed Gas Dynamic Spray

PMC: Polymer Matrix Composite

Prepreg: Pre-impregnated (refers to composites where the fibres are pre-impregnated with resin)

PVC: Polyvinyl Chloride

PVD: Physical Vapor Deposition

R: Range

RTM: Resin Transfer Molding

SAE: Society of Automotive Engineers

SE: Secondary Electron

SEM: Scanning Electron Microscopy

SN: Signal-to-Noise (Ratio)

SOD: Standoff Distance

TV: Traverse Velocity

WGFP: Woven Glass Fibre Ply

Nomenclature

a: Acceleration

A: Cross-section Area

c: Speed of Sound

C: Coefficient

F: Force

H_2O_2: Hydrogen Peroxide

HF: Hydrofluoric Acid

HNO_3: Nitric Acid

HV: Vickers Micro-hardness

k: Heat Capacity Ratio

L: Length

M: Mach Number

m: Mass

$\dot{m}$: Mass Flow Rate of Gas

P: Gas Pressure

R: Molar Gas Constant or Electrical Resistance or Range

R_a: Roughness (Arithmetic average of absolute values)

R_z: Mean Peak-to-Valley Height

T: Temperature

V: Velocity of Fluid

α: Temperature Coefficient of Resistance

μ: Micro (10^{-6})

ρ: Density (Specific Weight)

θ: Electrical Resistivity

Subscripts and Superscripts

d: Drag (for Force and Coefficient)

g: Glass Transition (for Temperature)

o: Stagnation (for Pressure, Temperature, and Density)

p: Particle (for Velocity, Area)

*: Throat (for Area)

1 Introduction

1.1 Subject Background

In the innovative driven market of today, companies are constantly searching for new technologies in order to gain an advantage over their competitors. The implications of these new advancements allow companies to provide a safe, effective, and economical product and/or service to the public. In the aerospace industry, minimizing the overall weight of the aircraft leads to fuel cost savings which can benefit not only the airline, but also the passengers and the environment. In order to achieve large weight reductions, large primary structures such as the wings and fuselages of airplanes, which were mainly composed of aluminum alloys, are now being replaced by polymer matrix composites (PMCs). Notably, in the Boeing Company's 787 Dreamliner, fifty percent by weight of the airplane is composed of composites. Composites used include predominately carbon fibre reinforced epoxies (CFRE) in the form of carbon sandwiches and carbon laminates along with minor combinations of various fibreglasses and glass/carbon hybrids [1]. The high strength to weight ratio of these materials permits weight reductions in the Dreamliner lowering fuel consumption by 20% [1]. Besides the primary benefit of reducing the weight and fuel consumption of the aircraft, other advantages include better corrosion and fatigue properties lowering maintenance costs, greater impact resistance, and minimizing waste products during manufacturing [1]. However, the relatively high electrical resistivity of PMCs raises an important issue for in-flight airplanes.

Lightning strikes on airplanes are relatively common and cause costly delays and interruptions [2]. It is estimated that an aircraft is struck by lightning on average every 1,000 flight hours which translates to one air strike per commercial aircraft per year [3]. Several factors, including geographic location, altitude, cloud coverage, and rain affect the frequency at which airplanes are struck by lightning [2], [3]. Thunderstorms tend to occur near hot continental regions due to increased convection activity [2]. Travelling to such regions increases the likelihood of an airplane being struck by lightning. Furthermore, over 90% of airplane lightning strikes occur when the aircraft is flying in clouds and 70% occur in the presence of rain [2], [3]. A survey of the U.S. commercial jets shows that lighting strikes occur between altitudes of 1,500 meters (5,000 feet) and 4,600 meters (15,000 feet) [2]. Commercial airplanes are therefore more likely to be struck during climb or descent phases of flight for these are altitudes at which lighting activity is greater. When lightning strikes an

airplane, it enters from one end and exits from another, using the plane as a temporary conduit. As a strike may pulse, many entry and exit locations can be present as depicted in Figure 1. A single lightning bolt can contain up to 1 million volts and 30,000 amps [2]. The extent of damage experienced by an airplane when struck by lightning varies depending on the energy level of the strike, the attachment and exit locations, and the duration of the strike [2]. The low conductive nature of composite structures requires higher voltages in order for a current to pass through them. In addition, the low conductivity makes the electrical discharge slower. This inevitably leads to large quantities of heat being produced, which ultimately damages the composite through melting or burning [2], [3].

Figure 1: Damage caused by lightning moving along an airplane causing many exit locations [2].

Modern lightning strike protection systems are devised to not only protect the structural airframe of the aircraft but also the fuel, electrical, and electronic (avionics) systems onboard [3]. The airframe protection's main goal is to control the lightning entry and exit points. Delicate components such as the wing tips, stabilizers, and fins are fastened with static dischargers to protect them from the lightning's damaging entry and/or exit [3]. Other techniques include providing an adequate pathway to guide the electrical charge from the entry points to the protected exit points. Typically, strike locations occur at the radome, forward fuselage, nacelle, empennage, or wing tip [2]. Therefore, in order to protect all of these areas, the entire airframe usually acts as a common conductive outer later. This lightning protection technique, where the

airframe acts like a Faraday cage protecting the content within, is often referred to as shielding [3]. A secondary shielding is sometimes used to protect cables and other electronics from unwanted electromagnetic interference using a similar technique [3]. However, the use of PMCs in most of the primary structures, notably the fuselage, eliminates the shielding properties of the plane. By incorporating a metallic mesh, foil or expandable foil as an outside ply or embedded within the layered composite during the manufacturing process, the electrical shielding is restored [2]–[4]. Unfortunately, this shielding system is not perfect for a lightning strike can cause any hull material to increase in temperature, melt, and burn [3]. For obvious reasons, locating the conductive layer as close to the surface as possible optimizes its effectiveness when dealing with PMCs. It has been said that even the thickness of the finishing paint can have an effect on the level of damage produced by the lightning [4]. Even though aerospace companies, such as the Boeing Company, incorporate extensive lightning strike protection in their airplanes, costly repairs and service interruptions are unavoidable [2]. If damaged, the electrical path must be restored. Repaired areas may not perform as well as in their pristine manufactured state. Current techniques involve overlapping part of the repair metallic mesh, foil or expandable foil with the parent metallic layer in order to surround the repair area [5]. Besides bolted, riveted or bonded repairs, no specific technique has been brought forth to repair the damaged metallic meshing to its manufactured state [1]. In addition, these methods can be labor intensive and costly [6].

There exists a wide variety of processes that can be used to deposit thin layers of material on a variety of substrates. Chemical vapor deposition (CVD) is a process that produces dense, uniform, and well-adhered coatings with controlled microstructures [7]. However, the high operating temperatures limit the choice of substrate material [7]. Unlike CVD, Physical vapor deposition (PVD) processes can deposit virtually any solid material, with the exception of certain polymers, onto any other solid surface [7]. Still, PVD is unfit to produce large scaled components for it is a vacuum-coating process operating at pressures ranging from 13.33 Pa to 1.33×10^{-6} Pa with a low deposition rate (DR) [7], [8]. In addition, both CVD and PVD have high equipment and processing costs [9]. Electroplating and electroless deposition have also been successfully utilized to deposit a metallic coating on CFRE composites [8]. However, electroplating, electroless deposition and other processes alike are notorious for producing low adhesive coatings and generate a great deal of pollution [9]. Furthermore, these processes are not suitable for on-site repair because they require the coating material to be in an ionic state which often involve submersion in an ionic bath [7].

On the other hand, there exist various types of thermal spray processes that can deposit layers of material on a variety of substrates. Conventional thermal spray processes such as plasma, electric arc, and combustion spray often rely on high heat to produce coatings [7]. Projected particles are brought to a molten or semi-molten state which causes various defects, such as oxidation inclusions, voids, impurities, and un-melted particles, to be imbedded in the coating [7], [10]. More importantly, the high temperatures used in these processes are detrimental to epoxies used in CFRE materials rendering these thermal spray processes unfit for this task [7].

Unlike previously mentioned thermal spray, kinetic sprays such as Cold Gas Dynamic Spray (CGDS), also simply known as Cold Spray (CS), and Pulsed Gas Dynamic Spray (PGDS) are a subdivision of the thermal spray processes that rely on the dynamic energy imparted to the sprayed particles to deposit coatings rather than high operating temperatures [7]. As a result of this low operating temperature, both CGDS and PGDS sparsely encounter oxidation, recrystallization, and debonding of their deposited coatings [7]. In CGDS, the feedstock powder is fed into an inert gas stream flowing through a converging-diverging nozzle and accelerated to a critical velocity [7], [11]. As the particles reach the substrate, they deform plastically and can adhere to it by various bonding mechanisms including mechanical anchoring, metallurgical bonding, and Van der Waals electrostatic forces [7]. These bonding mechanisms depend on the properties of the powder, the properties of the substrate, and the spray parameters and ultimately determine the adhesion strength of the coating [11].

The metallization of PMCs using CGDS is a fairly recent research domain. Work done by X.L. Zhou et al. has established that aluminum can be successfully deposited on a carbon fibre reinforced PolyEtherEtherKetone (PEEK) matrix composite using CGDS [9]. However, history shows that using aluminum with carbon fibre will result in galvanic corrosion [4]. According to Ed Rupke, senior engineer for Lightning Technologies Inc. (LTI, Pittsfield, Mass.), aluminum wire was one of the first lightning strike protection materials interwoven with carbon fibre as part of the laminate. Copper wires, on the other hand, relieve the threat of galvanic corrosion [4]. In order to increase the overall conductivity, a copper coating can be subsequently deposited on top of the intermediate aluminum coating produced by X.L. Zhou et al. using CGDS [9]. However, this additional coating only aggravates the galvanic corrosion situation. As such, a copper coating must be directly deposited onto a CFRE or onto a bond coat of similar nature to eliminate corrosion.

1.2 Motivation and Research Objectives

Toray Composites America Inc. (Tacoma, Wash.) produces an interwoven wire fabric (IWWF) known as BMS 8-276 which was selected by the Boeing Company for the Fuselage of the 787 [12]–[14].

The present research was motivated by the potential use of CGDS process for on-site repair of the damaged conductive layer on carbon fibre reinforced polymer composite aerospace parts. Further motivation for this study was brought about for the potential use of CGDS process as a standalone method to apply conductive coatings on aerospace grade carbon fibre reinforced polymer composites. The primary research objective was to successfully deposit a conductive coating on an aerospace grade composite produced by Toray Composites (America) Inc., as selected by the Boeing Company for the fuselage of the 787 [12], using commercially available feedstock powders deposited with commercially available CGDS equipment. In order to be considered conductive, the coating must meet BAC5056 electrical resistivity specifications. The following procedures were undertaken to achieve the desired research goals set out in this study:

1) Explore relevant potential powders to be deposited using the CGDS process.
2) Investigate the coatings produced to optimize CGDS parameters as well as appropriate substrate preparation procedures.
3) Evaluate the electrical, mechanical, and chemical properties of the conductive coatings produced.

1.3 Thesis Outline

The content of this thesis is organized into seven chapters. Chapter 1 introduces the study topic by providing information regarding the subject background. In addition, this chapter presents the motivation behind the research as well as the general research objectives that will be addressed.

Chapter 2 provides a summary of pertinent literature. This includes information regarding current lightning strike protection in airplanes, composites fabrication, relevant coating techniques (notably CGDS), and a summary of current PMC metallization research.

A detailed description of the specific objectives of this study is outlined in Chapter 3. These objectives are established so as to answer to the motivation of this research and to justify the procedural steps taken later on.

Chapter 4 presents, in detail, the experimental research approach used to achieve the objectives outlined in this study. This includes information with respect to experimental material, experimental and analytical equipment, procedural methods, and established standards.

Chapter 5 presents the experimental design, outlining specific steps and tests required to establish optimal CGDS parameters and proper material preparation. This chapter also provides certain results accompanied with proper explanations and discussions to emphasise the importance and effect of each parameter.

Experimental results will be presented in Chapter 6. This chapter includes, the evaluation of the coatings produced with respect to electrical, chemical, and mechanical performance. The obtained results are accompanied with a scientific analysis and detailed discussion.

Chapter 7 summarizes the findings presented in this thesis and provides concluding remarks. This chapter also suggests future work that should be undertaken to further substantiate the overall objective of this study. A complete list of references and appendices follow this chapter.

2 Literature Review

This chapter serves as a review of important information pertinent to the research subject matter. Current industry lightning strike protection practices are presented along with PMC manufacturing and metallization research as well as the theory behind CGDS. The purpose of this literature review is to acquire the necessary background information in order to complete the objectives of this research.

2.1 Lightning Strike Protection on Aircraft

2.1.1 Background

Clarence E. Rash explains that lightning is produced by friction between particles suspended in air. Super-cooled liquid and ice particles collide to form separate positive and negative charges. Once a sufficient quantity of these charges resides in the cloud, discharges occur in the form of lighting. Lightning can occur between two different clouds, within sections of the same cloud, between cloud and air, or between a cloud and the ground. Ninety percent of all lightning strikes occur between cloud and ground in a "negative lightning" while only five percent occur in a "positive lightning". "Negative lightning" takes place when a negatively charged cloud discharges onto a positively charged ground [3]. Negative charges from the cloud descend towards the ground along a path of ionized air particles called the leader stroke while positive charges move up from the ground along a similar path called the streamer [2], [3]. Upon contact between the leader and the streamer, electrical discharge travels up the streamer into the cloud creating visible light lasting less than a tenth of a second. In "positive lightning" the leader carries a positive charge while the streamer carries a negative charge. Unlike its more common counterpart, "positive lightning" can travel greater distances, lasts longer, and is more powerful [3].

The earliest lightning-caused aviation accident dates back to September 3rd 1915 when a German Zeppelin LZ40 (L10), venting hydrogen gas, was destroyed in Germany off Neuwerk Island. In 1929, the first heavier-than-air aircraft was destroyed by a lightning strike ultimately causing the death of all eight passengers aboard. Since then, scientists have recognized the importance of lightning strikes protection and have studied the mechanisms and consequences of lightning strikes on aircraft for decades. It is important to note, however, that in more recent reports involving

confirmed lightning strikes, the majority of the aircraft landed safely. Nevertheless, all aircraft subjugated to lightning sustain some sort of damage [3].

2.1.1.1 Strike Occurrence and Trends

Lightning strikes are naturally occurring events that are notoriously difficult to predict. Only in the last decade have airplane lightning strikes been effectively documented. With this data, it has been found that airplane strikes are relatively common because of their travel conditions [2]. A variety of factors affect the frequency at which airplanes are struck by lightning.

Geographically, warm regions have more lightning than cooler regions [2]. Heat from the ground creates convection which increases friction in the air resulting in a higher potential for lightning. Airplanes travelling across warm continental areas are therefore much more likely to fly through a thunderstorm than when travelling over oceans and polar areas [2]. Figure 2 shows the geographical distribution of lightning across the world. Areas in yellow, orange, red, and black represent locations with a high degree of lightning occurrences whereas areas in white, gray, purple, and blue are locations with low lightning activity.

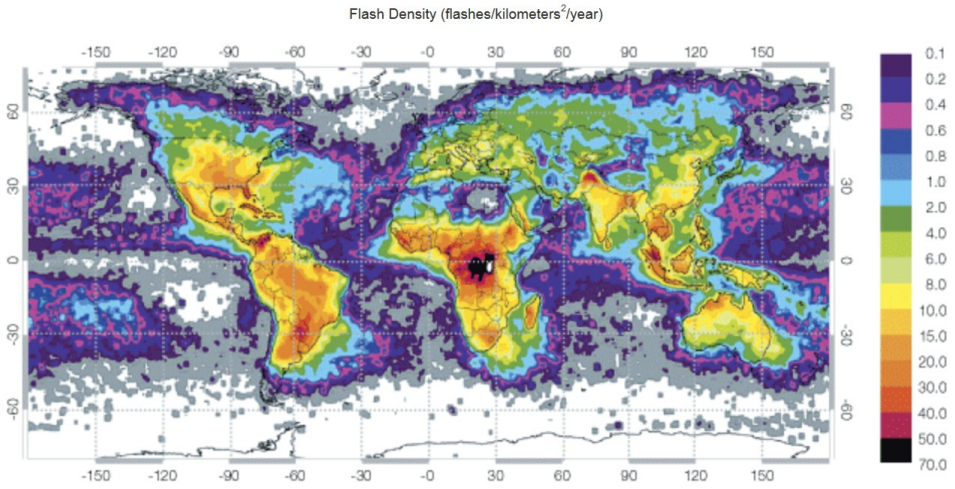

Figure 2: Worldwide Lightning Observations (flashes/kilometers^2/year) for April 1995 through February 2003 from the Combined Observations of the National Aeronautics and Space Administration (NASA) Optical Transient Detector and Land Information Systems Instruments [2].

The altitude at which an aircraft travels is also of considerable importance. Lightning activity is considerably greater between 5,000 and 15,000 feet (1,572 to 4,572 meters) in altitude [2]. The

reason behind this heighten activity is because clouds are more prevalent at these altitudes [2]. With typical cruising altitudes of 30,000 to 40,000 feet, commercial airplanes are most often struck by lightning during the climb and decent phases of flight as seen in Figure 3 [2]. It is therefore more probable for an airplane flying multiple short routes to be struck by lightning than an airplane travelling a long route a single time. However, a dominant factor is the presence of clouds. Nine out of ten airplane lightning strikes occur when the aircraft if flying in clouds and seven out of ten occur in the presence of rain [2], [3]. Of course, sometimes, these situations are unavoidable.

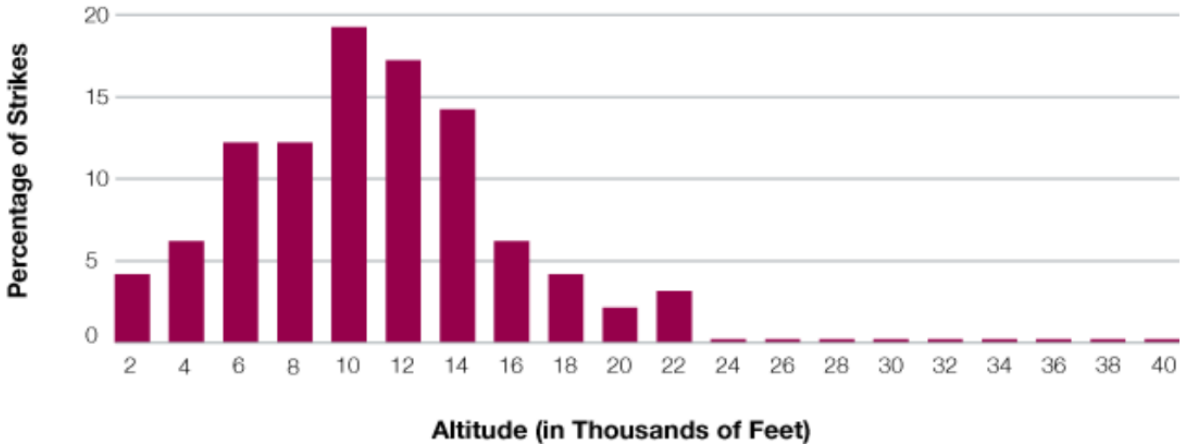

Figure 3: The distribution of lightning strikes by altitude from a survey of the United States commercial jets [2].

2.1.1.2 Lightning Interaction with Aircraft

When lightning strikes an airplane, it uses the plane as a temporary conduit, entering from one end and exiting from another. At the initial stage, an increased electromagnetic field density is generated by the leading edges and sharp points of the airplane interacting violently with the air causing ionization [2]. This ionization can be distinguished by a glow surrounding the nose and wing tips of the plane [2]. This stage is followed by the extension of leaders from the ionized area of the airplane as well as from surrounding clouds [2]. Once leaders meet, a lightning strike initiates. It has been reported by the Boeing Company that an airplane, in flight, can travel farther than its own length in the time that it takes a lightning strike to begin and end [12]. As the airplane flies through a charged atmosphere, the leader may reattach itself at other locations, causing the strike to pulse [2], [12]. A pulsing strike can often be detected by the presence of many entry and exit location marks along the plane. Up to 1 million volts and 30,000 amps can be discharged by a single lightning

bolt [2]. The energy level of the strike, the attachment and exit locations, and the duration of the strike all factor in the extent of damage experienced by an airplane when struck by lightning [2].

It is estimated that an aircraft is struck by lightning on average every 1,000 flight hours which translates to one air strike per commercial aircraft per year [3]. However, not all components of an airplane have equal risks of being struck by lightning. As defined by the Society of Automotive Engineers (SAE) Aerospace Recommended Practices (ARP) 5414, a typical airplane is divided into three different strike zones: Zone 1, Zone 2, and Zone 3 (as seen in Table 1) [2].

Table 1: Airplane Lightning Zones as Defined by SAE ARP 5414 [2]

Zone Designation	Description	Definition
1A	First return stroke zone	All areas of the airplane surfaces where a first return is likely during lightning channel attachment with a low expectation of flash hang on.
1B	First return stroke zone with a long hang on	All areas of the airplane surfaces where a first return is likely during lightning channel attachment with a low expectation of flash hang on.
1C	Transition zone for first return stroke	All areas of the airplane surfaces where a first return stroke of reduced amplitude is likely during lightning channel attachment with a low expectation of flash hang on.
2A	Swept stroke zone	All areas of the airplane surfaces where a first return of reduced amplitude is likely during lightning channel attachment with a low expectation of flash hang on.
2B	Swept stroke zone with long hang on	All areas of the airplane surfaces into which a lightning channel carry subsequent return stroke is likely to be swept with a high expectation of flash hang on.
3	Strike locations other than Zone 1 and Zone 2	Those surfaces not in Zone 1A, 1B, 1C, 2A, or 2B, where any attachment of the lightning channel is unlikely, and those portions of the airplane that lie beneath or between the other zones and/or conduct a substantial amount of electrical current between direct or swept stroke attachment points.

Zone 1 contains components that are most likely to be struck by lightning [2]. This includes: radome, nacelles, wing tips, horizontal stabilizer tips, elevators, vertical fin tips, ends of the leading edge flaps, trailing edge flap track fairings, landing gear, water waste masts, and air data sensors (pitot probes, static ports, angle of attack [AOA] vane, total air temperature probe). Components from Zone 2 are rarely the entry or exit points for lightning strikes; however, they are known to be

involved in sweeping or moving lightning attachments, pushed back by the motion of the plane. Zone 3 comprises the rest of the components, not included in the two other zones, very rarely involved in lightning strikes attachments. Components in Zone 3 however, may experience substantial amounts of conductive current. Some zones can be further divided into known strike hang on time. Figure 4 presents a diagram illustrating the strike zones on a typical airplane [2].

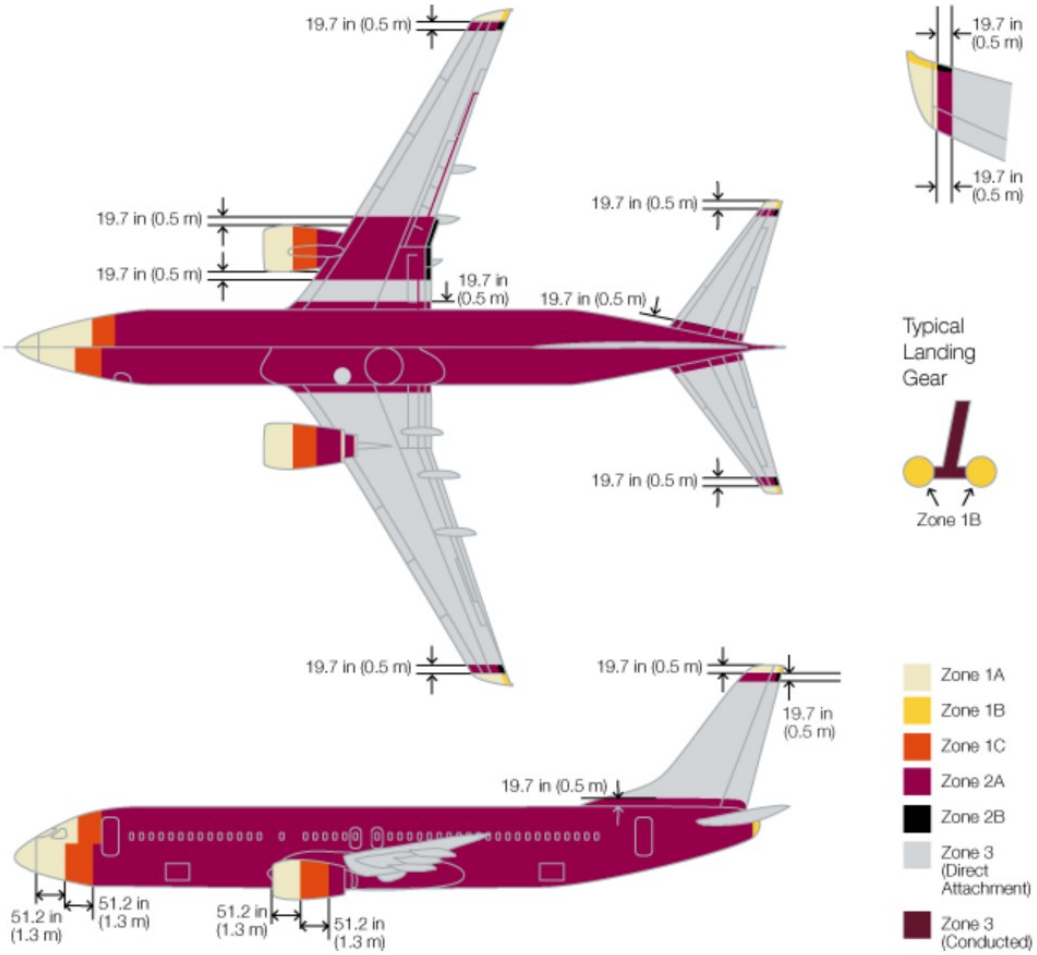

Figure 4: Lightning strike prone areas of an airplane indicated by zone [2].

2.1.2 Lightning Strike Protection Systems

Lightning strike protection systems have been developed to allow an aircraft that has been struck by lightning to continue flying and land safely at a suitable airport [3]. Aviation regulating agencies worldwide have established certification standards for lightning strike protection on aircraft [3]. Aerospace companies, such as the Boeing Company, incorporate extensive lightning strike

protection in their airplanes [2]. Typically, lightning strike protection systems provide preferred conductive pathways for electric currents to enter and exit from the aircraft to prevent damage to the aircraft and injury to the occupants [3]. Modern lightning strike protection systems can be divided into three main categories: fuel system protection, avionics (electronic) system protection, and structural airframe protection [3].

2.1.2.1 Fuel

Fuel protection systems have been developed to prevent fuel ignition where unwanted. Components such as joints, hinges, and fasteners located near fuel tanks are designed to prevent sparks [3]. In addition, aircraft skin of a certain proximity to fuel tanks is fabricated to prevent burn-through from a lightning strike. Other steps can also be taken with respect to the fuel itself. Additives and advance fuels have been developed to produce lower fuel vapors, minimizing ignition potential [3].

2.1.2.2 Avionics

Modern aircraft rely heavily on electronic systems for flight control and communication. An example of this is fly-by-wire control systems [1]. Avionics systems can be jeopardized by both direct and indirect effects of lightning strikes. Common protection techniques include: shielding, grounding, and surge protection. Shielding refers to common conductive layer surrounding an isolated wire or a group of wires. The shield acts as a Faraday cage and prevents current from directly entering the protected wires. As a current travels through an airplane, it can induce temporary current oscillations into adjacent wires and electronic equipment. Therefore, a secondary inner shield is usually added to aircraft wiring to eliminate electromagnetic interference. Surge protection is used alongside grounding to prevent circuit melting. High voltage increases are limited by surge protection equipment and the excess power is diverted to a grounding line [3].

2.1.2.3 Structural

The primary goal of the airframe protection is to control the lightning entry and exit points for these locations are statistically more likely to be damaged (see Figure 4) [3]. Static dischargers, commonly known as wicks or rods, are usually positioned at the wing tips, stabilizers, and fins to steer an exit

point of an electrical discharge away from these delicate components [3]. Another common practice is to provide an adequate pathway to guide the electrical charge from the entry points to the exit points fastened with wicks or rods. Since lightning travels through an aircraft, establishing conductive pathways across the plane minimizes the possibility of arcing and localized heating [3]. However, burning and melting can still occur during lightning strikes, regardless of hull material [3]. Even minute details such as the thickness of the finishing paint can have an effect on the level of damage produced by the lightning [4].

2.2 Composites

Out of the limitless combinations of composites possible, PMCs are the predominant type of composite used in today's aircraft. As such, the following section will focus on the technical aspects particular to PMCs.

2.2.1 Composite Classification

Composites represent a broad category of materials that combine two or more distinctly different materials on a macroscopic scale [15]. As a result, the composite produced has a balance of structural properties that are superior to its constituents independently. Typically, composites combine a reinforcement phase, composed of stiff and strong fibres or particles, within a continuous matrix phase. Exceptions exist making this category of materials difficult to accurately describe. Rubber-modified polymers are a distinct class of exceptions where the ductile and compliant rubber phase is incorporated to improve the overall toughness of the composite [15].

Composites can be classified on two distinct levels: matrix and reinforcement [15]. The first level of classification specifies the constituent of the matrix. Composites can be categorized into three distinct classes: organic-matrix composites (OMCs), metal-matrix composites (MMCs), and ceramic-matrix composites (CMCs). OMCs include both PMCs and carbon-matrix composites (commonly referred to as carbon-carbon composites). The second level of classification specifies the type reinforcement present in the composite. Reinforcements can be categorized into continuous laminated fibres, discontinuous fibres (whiskers), particles (spheres, flakes, and all other roughly equally dimensioned shapes), and fabrics (including woven, braided, and knitted arrangements) as

depicted in Figure 5. The distinction between the continuous and the discontinuous fibres classes can be defined by the influence that the fibres length have on the composite's properties. For example, when further increasing the length of the fibres does not further increase the elastic modulus or strength of the composite, the composite is considered to be continuous fibre reinforced. Discontinuous fibres differ from particulate reinforcement in the sense that they have aspect ratios ranging between 20 and 100. Fabric fibre architecture distinguishes itself from continuous laminate fibre reinforcement by means of interlocking fibres and out-of-plane dimensions and properties (orthogonal to the primary structural plane). Usually, a substantial volume fraction of the composite must be allocated to the reinforcement in order to produce a useful increase in the properties regardless of reinforcement type. However, certain polymer composites incorporate low cost filler particles to extend the material rather than increase performance. These exceptions are generally not considered particulate composites regardless of unexpected secondary non-structural benefits (e.g. Shrinkage control, increased thermal or electrical conductivity, fire resistance) [15].

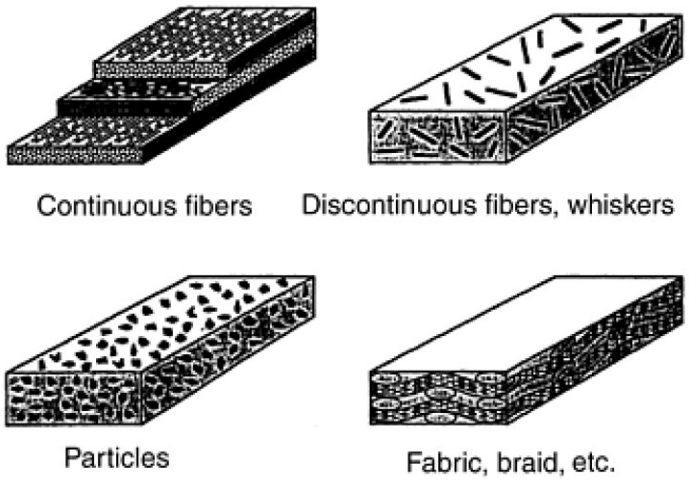

Figure 5: Common forms of fibre reinforcement. In general, the reinforcements can be straight continuous fibres, discontinuous or chopped fibres, particles or flakes, or continuous fibres that are woven, braided, or knitted [15].

2.2.2 History of OMCs

Unlike MMCs and CMCs, OMCs were originally created for the aerospace community during World War II [15]. Materials with high strength, high stiffness, and low density were pursued to boost aircraft performance. By the end of the war, glass fibre reinforced plastics were successfully used in

rocket motors and in certain structural prototype applications [15]. During the 1950s, OMCs were implemented in a broader range of applications [15]. In the 1960s, OMCs became available in consumer sporting equipment. This commercialization of OMCs lowered manufacturing costs and increased production to satisfy the larger market need [15]. During the Cold War, resources were put forth to develop high-performance OMCs for new military aircraft [15]. In the 1970s, energy and fuel costs increased drastically. As a result, OMCs were introduced in commercial aircraft to mitigate the cost of flight travel [14], [15]. From that point on, OMCs have undergone many design, manufacturing, material improvements notably in upper-use temperature of PMCs. This progress has allowed OMCs to gain an increase in mass fraction of aircraft and spacecrafts alike [15]. For example, 2% of the F-15 E/F was made of OMCs whereas 24% of the F-22 structure are OMCs [15]. This weight percentage continued to increase to 41% for the tilt-rotor V-22 Osprey and more recently to over 50% for the 787 Dreamliner [1], [15], [16]. Figure 6 provides a visual representation of the material distribution of the Boeing Company's 787.

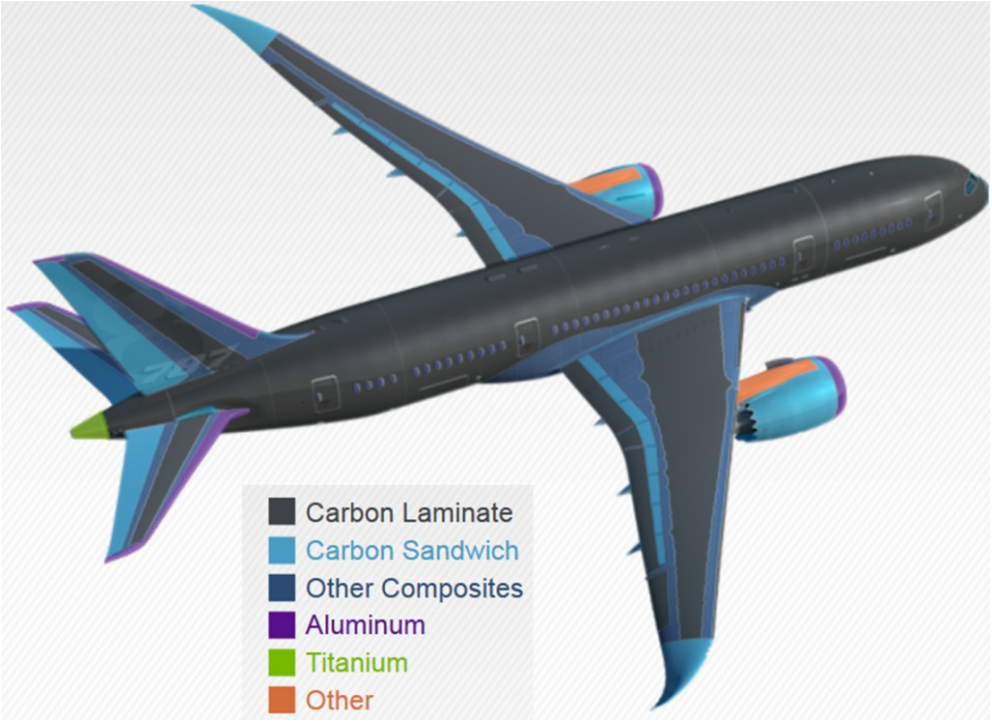

Figure 6: The Boeing Company's 787 "Dreamliner" material distribution. "Carbon Laminate" represent carbon fibres impregnated with polymer built up in layers. "Carbon Sandwich" are two thin carbon laminate skins attached to a thick and lightweight core providing the composite with high bending stiffness and extremely low overall density. "Other Composites" represent a variety of other materials integrated together (i.e. fibreglass and glass/carbon hybrid) [1].

2.2.3 Properties & Applications of OMCs

Historically, the primal reason for the development of OMCs is to produce a material with high specific stiffness and specific strength; that is to say, OMCs have a high stiffness and strength per material density [14], [15]. In addition to these prevalent properties, OMCs offer considerably high corrosion resistance, long fatigue life, good impact resistance, tailorable thermal expansion coefficients, and the ability to be manufactured in large and complex shapes [1], [15]. Over time, developments have increased the operating temperature that PMCs can sustain. Early epoxies were considered useable at 121°C (250°F) whereas current generation polymers, such as polyimide-matrix composites have extended the range to 288°C (550°F) [15]. The high stiffness and high strength of OMCs come from the embedded reinforcements [14], [15]. Table 2 presents a list of fibre reinforcements typically used in OMC applications.

Table 2: Typical Fibre Reinforcement Characteristics and Properties Used in OMCs [15]

Material	Characteristics	Properties
Glass Fibres	• Competitive price • Availability • Good Handleability • Ease of processing • Good matrix adhesion	Tensile Strength: 3450 to 4830 MPa Young's Modulus: 75.8 to 96.5 GPa Diameter: ≥ 100 µm
Boron Fibres	• Expensive • Monofilament (single fibre) • Good thermal stability • Low matrix reactivity (compared to carbon fibres)	Tensile Strength: 3450 MPa Young's Modulus: 400 GPa Diameter: 100 to 200 µm
Polyacrylonitrile (PAN) Fibres	• Type of carbon fibre with high yield • Economical (no need for "graphitization" step) • High strain capacity	Tensile Strength: 3515 to 6380 MPa Young's Modulus: 240 to 310 GPa Diameter: 8 to 10 µm Elongation: 2.2%
Carbo Fibres (Pitch Based)	• Type of carbon fibre with high stiffness • High thermal conductivity • Low electrical resistivity	Tensile Strength: 1900 to 2750 MPa Young's Modulus: 400 to 950 GPa Diameter: 10 µm Elongation: 0.5%
Aramid Fibres	• Includes a broad range of aromatic polyamide fibres (ex: Kevlar) • Complex manufacturing process • High damage tolerance • Low compression strength • Poor resin matrix adhesion	Tensile Strength: 3450 to 3620 MPa Young's Modulus: 131 to 180 GPa
Ultrahigh-Molecular-Weight Polyethylene Fibres	• High chemical resistance • High impact resistance • High moisture resistance • Low density • Good vibration damping • Low dielectric constant	Tensile Strength: 3250 MPa Young's Modulus: 113 GPa

These reinforcements are protected from environmental corrosion and impact by the highly inert organic matrix. In addition, the matrix provides a solid form for the composite along with a cohesive medium that transfers loads between fibres ensuring optimal distribution. Furthermore, the matrix renders a vital inelastic response to crack propagation, blunting stress concentration [15]. Table 3 provides a list of important matrix material used in OMCs with certain key characteristics. The high fatigue life of OMCs derive from the fact that fibre materials are inherently stronger than the bulk

form [15]. For bulk materials, flaws within them propagate when stressed and cause catastrophic failure of the entire material. When dealing with fibres, the flaw is limited to a single fibre diameter [15].

Table 3: Important Materials Used in OMC Matrices and Their Characteristics [15]

Matrix Material	Characteristics
Polyester and Vinyl Ester Resins	• Used predominantly in low performance applications (ex: piping, appliances, doors, bathtubs, and automobile hoods) • Binds very well to glass fibres due to silane coupling agents • Large shrinkage during curing
Epoxy Resins	• Used in high performance applications (ex: tennis rackets, fishing rods, piping for chemical processing plants, and airplane fuselages) • Moisture sensitivity (decreases the glass transition temperature (T_g)) • Can be toughened through thermoplastics or rubber additives • Maximum service temperature: 120°C • Maximum service temperature: 80°C to 105°C for toughened epoxies
Bismaleimide Resins	• Comparable to epoxies in most characteristics (handleability, relative ease of processing, and excellent properties) • Quite brittle (very low elongation) • Maximum service temperature: 177°C to 230°C
Polyimide Resins	• Cure by condensation (voids are produced in resulting composite) • Brittle • Maximum service temperature: 232°C to 370°C
Phenolic Resins	• Very high heat resistance (thermal stability) • Excellent char and ablative performance • Cure by condensation (voids are produced in resulting composite) • Used in aircraft interior panels
Cyanate Ester	• Low moisture absorption • Superior electrical properties • Used in satellite structures, radomes, antennas, and electronic components
High-Temperature Thermoplastic Resins	• Superior temperature resistance • High Toughness and High strain-to-failure • Good moisture resistance • Susceptible to organic solvents • Ex: polyether etherketone, polyphenylene sulfide, polyetherimide, and polyamideimide

In general, composites' properties such as specific stiffness and specific strength depend on the type of reinforcements and the volume fraction of reinforcements [15]. In fibre reinforced composites, the orientation of the fibres also heavily impacts the properties of the composite (see Figure 7). The highest specific stiffness and strength is achieved when the fibres are oriented in the

primary loading direction (0°) [15]. The opposite can be said when the fibres are oriented perpendicular to the primary loading direction (90°) [15].

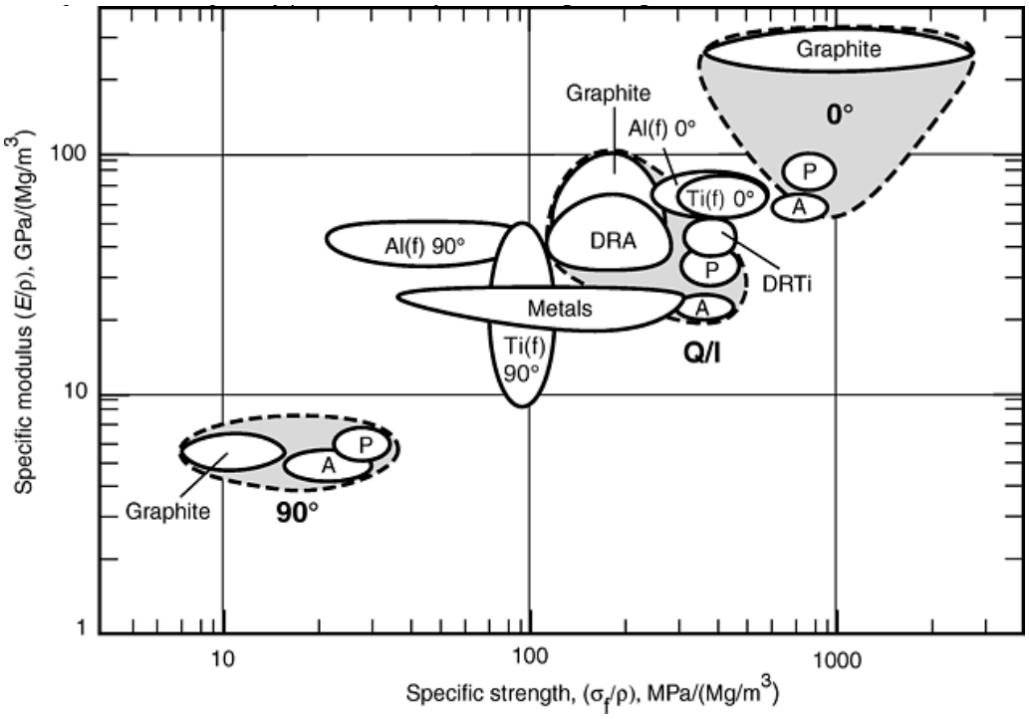

Figure 7: "Ashby plot" of normalized stiffness Vs normalized strength of various materials. Dark areas represent continuous fibre reinforced OMCs. Specific fibre materials such as carbon fibres (graphite), polyacrylonitrile fibres (P), and aramid fibres (A) are located within this area. MMCs such as discontinuously reinforced aluminum (DRA), discontinuously reinforced titanium (DRTi), and continuous fibre reinforced (f) aluminum (Al) and Titanium (Ti) fall between the extremes of axial (0°) and transverse (90°) graphite OMCs. The "Metals" area represents structural metals such as β–titanium alloys and ultrahigh-strength steels. Q/I represent quasi-isotropic fibre orientation [15].

In situations where loading is not primarily axial, laminate architectures can be developed and tailored in proportion to the load that must be supported. A quasi-isotropic (Q/I) laminate can be produced by laminating plies sequentially in different orientations in equal proportions (e.g. 0°, 90°, 45°, and -45°) (see Figure 8). Compared to OMCs, the technology for fibre- reinforced MMCs is much less evolved [15]. However, MMCs are beginning to substitute OMCs in applications where metal properties such as high bearing strength, good wear resistance, high electrical conductivity, and elevated temperature operation are important. Discontinuously reinforced aluminum (DRA) is by far the most popular MMC. On the other hand, discontinuously reinforced titanium (DRTi) is much less mature making the material quite expensive. Discontinuous fibre reinforcement and particle reinforcement are also available for OMCs despite their infrequent use. These types of

materials severely underperform when compared to conventional structural metals and are thus not the focus of this research [15].

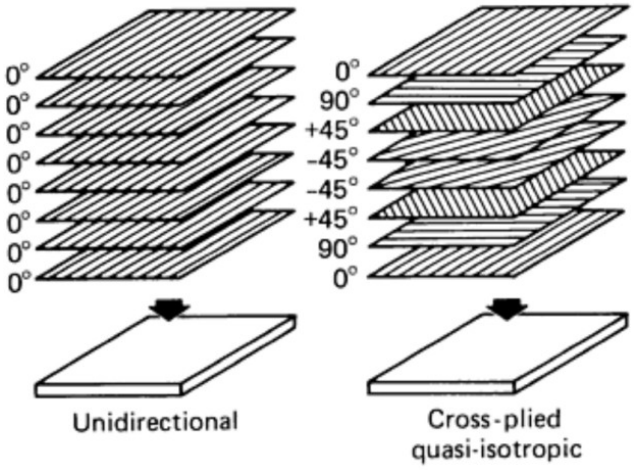

Figure 8: Unidirectional versus quasi-isotropic lay-ups [15].

2.2.4 Manufacturing

A large quantity of processes exists for the fabrication of OMCs. Again, we will focus on the production of OMCs with continuous fibre reinforcement. The production of typical OMCs can be divided into three major steps: fibre placement, resin infusion, and curing [15]. Certain procedures require the resin to be applied on the fibres before placement.

A variety of fibre placement processes can be utilized to achieve a desired arrangement. The two most common ones are filament winding placement (see Figure 9) and lay-up placement [15]. In filament winding placement, a fibre bundle or ribbon is initially impregnated with resin and subsequently wound around a simple geometry. The resin may be in liquid form or prepreg (the fibres are pre-impregnated with resin). In lay-up placement, the fibres are cut and laid in the desired arrangement by hand or by machines. During this step, the fibres can either be in dry (without resin) or in prepreg form. If the fibres are in prepreg form, the resin infusion step can be skipped. Fibre placement is a labor intensive procedure which is often automated for most major composite fabricators in order to minimize cost [15].

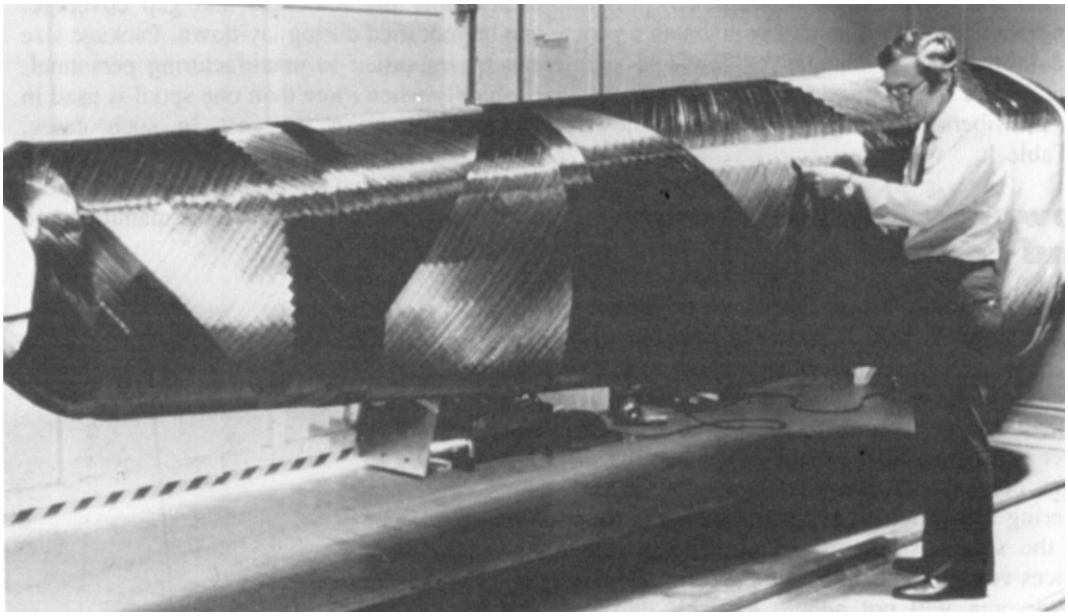

Figure 9: Complex structure wound on six-axis winding machine [15].

Resin infusion is the following step if the fibre placement involved dry fibres. A common method to perform this step is called resin transfer molding (RTM) [15]. RTM is a process where fibres are placed in an open mold that can be closed afterwards. Once closed, liquid resin is injected through ports and air is forced out through exhaust ports. Variations to RTM can be added to improve the process. For example, the mold can be vacuumed before the resin infusion to minimize trapped air in the final product. Compression can also be added to RTM to minimize voids. Other RTM procedures incorporate a high permeability layer to allow sufficient resin flow and maximize even resin distribution. A cost efficient alternative is to use an open mold in combination with a sealed bag which can be vacuumed thereafter. Older techniques involve placing the resin infused fibres on a single-sided mold [15].

Once the fibres are placed and infused with resin, the polymer must be hardened through some type of curing [15]. During this stage, polymer molecules cross link creating a well bonded and uniform polymer matrix. Curing is often done by increasing the temperature at a specific degree for a certain time span. This can be accomplished by placing the mold in an oven or by heating the mold through other means. However, some curing processes occur at room temperature through low-cure-temperature resins or two-part mix thermoset polymers [15]. Either way, once cured, the composite can be removed from the mold and the part remains in its final solid shape.

OMCs can also be produced using a continuous "line" process called pultrusion [15]. In this process, fibres are mechanically pulled from spools, through a resin bath, followed by a heated die of desired shape. This process combines all three steps in one continuous process. Fibre orientation of the final product is predominantly in one direction. Pultrusion is a low-cost and high-volume method used to produce long components with nearly constant cross-sections [15].

2.2.5 Selection Factors

Cost savings go hand in hand with proper material selection. In order to minimize cost, the following three trends regarding fibre, resin, and prepreg should be kept in mind [15]. First and foremost, the greater the number of fibre filaments per tow, the lower the cost. A tow refers to the untwisted continuous filament of fibres in a bundle. In the case of carbon fibre, demand for smaller tows (1000, 3000, and 6000 filaments per tow) to produce complex shapes was present. As carbon fibres became popular in commercial and industrial applications, big tows (48,000 to over 200,000 filaments per tow) became available lowering cost. In addition, the cost drops when resin with lower performance temperature and prepreg with wider dimensions are selected. As a general rule, adding performance almost always adds cost and mass production almost always lowers cost. It is therefore important to select the proper material for a given task. Also, it is important to keep in mind that composite manufacturing is highly flexible and that it is demand that shapes what becomes commercially available [15].

2.2.6 BMS 8-276

The Boeing Company's experimental project, specification XBMS 8-276, was formally initiated on January 6th, 1982. However, the development of the material, now known as BMS 8-276, began in the 1970s and is a direct result of a joint effort by Toray Industries, the University of Washington, and the Boeing Company. This material was originally intended for laminate constructions to replace heavy aluminum used in large primary structures of commercial aircraft and was first implemented in the Boeing 777. Certain components, such as horizontal stabilizers, vertical fins, and floor beams, of the Boeing 777 were entirely made of BMS 8-276 [14].

BMS 8-276 is a toughened epoxy-based CFRP from Toray Industries (T800 fibres in a 3900-2 epoxy-based resin system). During the initial development stage, efforts were focussed on choosing the optimal matrix material. The option between thermoset and thermoplastic polymers was not so clear cut as each has its own drawback. Composite systems available at that time were noted to have less than optimal toughness which often resulted in delamination and premature wear during incidental handling and maintenance damage [14]. "Thermo-plastic resin systems provided toughness values that were almost an order of magnitude larger than conventional thermosetting toughness values. However, the lack of thermoplastic prepreg tack and drape capabilities presented severe disadvantages in terms of manufacturing issues" [14]. As a result, a toughened thermosetting matrix composite was specifically engineered to contain resin interlayers between plies of the composite using a heterogeneous layering concept in order to prevent ply delaminations during impact. The heterogeneous system utilized rigid particles, 10 to 60 µm in diameter, to create the resin rich interlayers between each ply (see Figure 10) [14].

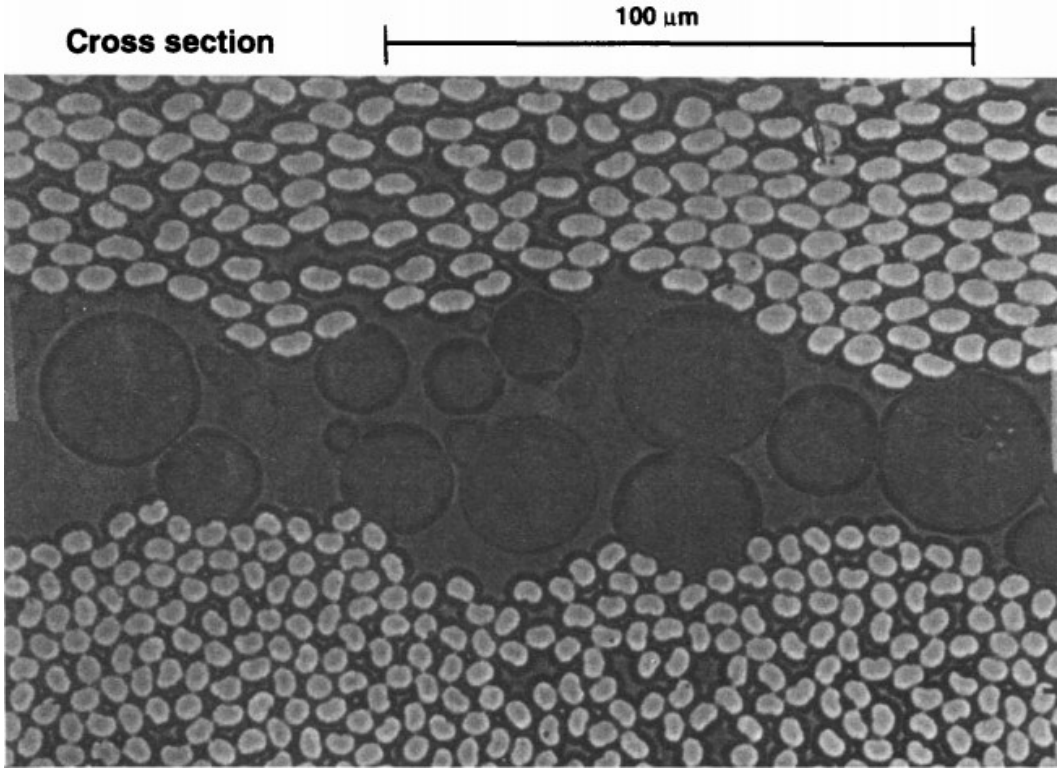

Figure 10: Optical micrograph of the BMS 8-276 toughened matrix system [14].

Much like previous generations (BMS 8-212), the BMS 8-276 is cured at 177°C (350°F). The improvement in the fibre properties of the BMS 8-276 results in increased strength and stiffness. However, the most important improvements are the resistance to impact damage as well as the durability of the BMS 8-276. The Boeing Company measures these properties via residual compression strength after impact (1500 in-lb/in) and hot-wet compression (180°F (82°C) test). Figure 11 depicts the trade-off traditionally observed between resistance to impact and durability of resins utilized in the Boeing Company CFRP. BMS 8-212 is located along the 1970s technology region [14].

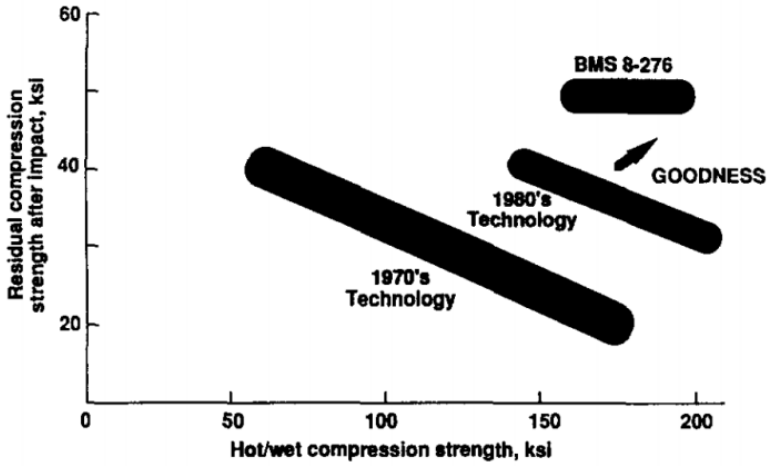

Figure 11: Trade-off between compression strength after impact and hot-wet compression for the Boeing Company CFRP [14].

With the enhanced properties of BMS 8-276, weight savings for improved fuel efficiency as well as increased range and payload are a possibility. Simpler construction implies greater manufacturing flexibility, simpler interfacing, and lower fabrication and assembly costs. The Boeing Company continues to work to improve product quality by reducing variations through statistical process control [14].

2.2.7 Metallization of PMC

The metallization of PMCs can be achieved by a wide variety of processes. Unfortunately, these processes contain limitations that restrict their application to aerospace components. Here are a few of some well-established processes that can currently be used to metalize a post manufacturing

PMC. PVD is a process that can deposit virtually any solid material, with the exception of certain polymers, onto any other solid surface in line-of-sight [7]. PVD includes techniques such as evaporation, ion plating, and sputtering (see Figure 12). Depending on the specific technique, material is vaporized through heat or energetic particle bombardment [7]. The evaporated particles then condense on the surface of the component producing mechanical and/or chemical bonding [7]. However, PVD is limited in the size of the components that it produces for it is a vacuum-coating, line-of-sight process operating at pressures ranging from 13.33 Pa to 1.33×10^{-6} Pa with a low DR [7], [8]. In addition, PVD is often associated with high equipment and processing costs [9].

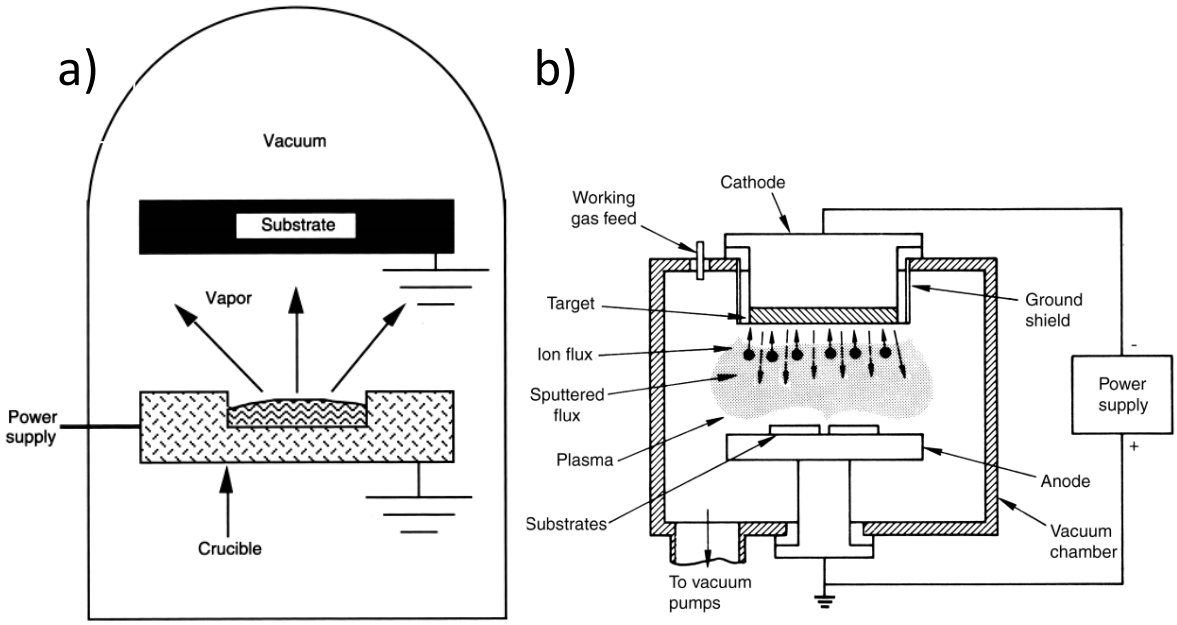

Figure 12: (a) Resistance heat evaporation process and (b) typical sputter coating process [7].

Similarly to PVD, CVD is a process that uses thermal decomposition of fluorides, chlorides, bromides, iodides, organometallics, hydrocarbons, phosphorus trifluorides, and ammonia complexes to deposit coatings onto surfaces (see Table 4) [7]. However, CVD is an omnidirectional process that relies on chemical and/or diffusion bonding to produce adherent coatings [7]. Although CVD is an operation that produces dense, uniform, and well-adhered coatings with controlled microstructures, the majority of these processes operate at high temperatures which eliminates the possibility to use polymer based substrates (see Table 4) [7].

Table 4: Chemical Vapor Deposition (CVD) Methods and Characteristics [7].

CVD method	Most distinguishing characteristic	Range of typical substrate temperatures	
		°C	°F
Conventional CVD	Omnidirectional coating of a wide variety of shapes and sizes	350–1600	660–2910
Metal-organic CVD	Lowered deposition temperatures using metal-organic precursor	200–800	390–1470
Plasma-assisted CVD	Reduced substrate temperature	200–800	390–1470
Laser CVD	Coat localized areas on a surface without bulk heating	200–1000	390–1830
Packed-bed CVD	Alloy/conversion coatings in powder packed-bed environment	500–1200	930–2190
Fluidized-bed CVD	Coat powders and small components	350–1600	660–2910
Continuous fiber coating	Deposit coatings on mono-filament and multifilament tows	350–1600	660–2910
Chemical vapor infiltration	Coat internal surfaces of porous media	350–1600	660–2910

Electroplating and electroless deposition have been proven to successfully deposit a metallic coating on CFRE composites, as demonstrated in E. Njuhovic et al.'s work [8]. These low cost processes utilize currents to dissolve ions from an anode and deposit them onto a cathode through a solution (see Figure 13) [7]. Variations exist where the plating ions are already dissolved in the plating solution and the anode is simply used to complete the electrical circuit. Adherence of electroplated and electroless deposition coatings are generally provided by mechanical and/or chemical bonding. Yet, these omnidirectional processes are notorious to produce low adhesive coatings with poor stability and generate a great deal of pollution [7], [9]. Disposal of the by-products produced are of major economical concern [7]. Furthermore, these processes are not suitable for on-site repair because they require submersion in an ionic bath.

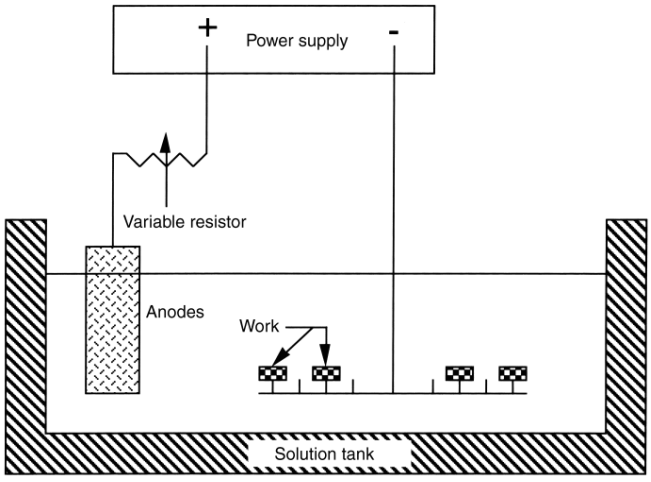

Figure 13: Typical electroplating process [7].

Thermal spray encloses a vast and diverse group of line-of-sight processes that are used to create coatings. Thermal spray differs from PVD, CVD, and plating processes in that it does not deposit individual ions, atoms, or molecules of material but rather large particulates [7]. These particulates can be liquid droplets or semi-molten or solid particles and are produced from powder, wire, or rod feedstock material. Once atomized, the material is propelled onto a substrate [7]. Adherence for thermal spray coatings is generally provided by mechanical bonding. Thermal spray is characterized by a high DR which is useful for mass production and large components. In addition, thermal spray processes are capable of operating over a broad range of temperature, velocity, and atmospheric conditions which allows them to coat a wide variety of material [7]. Although the majority of these techniques operate at high temperatures which can result in distortion or degradation of common polymer base substrates, CGDS may be suitable for the metallization of a variety of PMCs. Common coating features among thermal spray processes include pores and oxide inclusions as depicted in Figure 14.

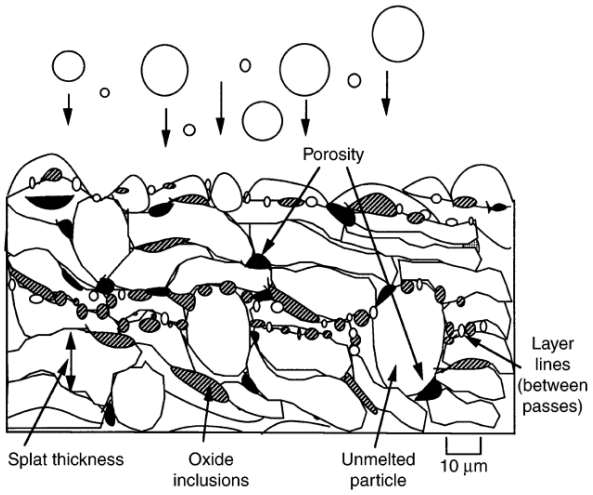

Figure 14: Schematic of thermal spray coating microstructure showing common features [7].

Figure 15 presents the microstructure of a Al_2O_3 coating on polyimide composite substrate with plasma-sprayed Al bond coat [17]. One of the major challenges with thermal spray coatings is its specification and standardization [7]. Historically, the majority of the coatings produced relied on internal company development and over time became acceptable practice with the outgrowth of reliable documentation [7].

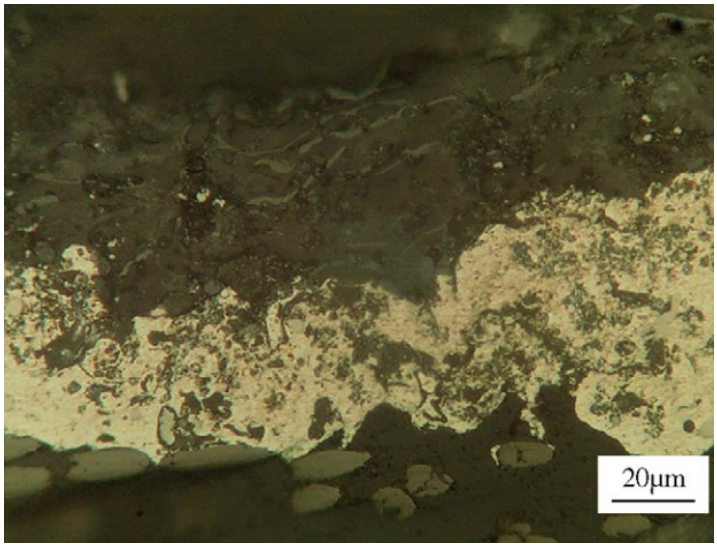

Figure 15: Microstructure of Al_2O_3 coating on polyimide composite substrate with plasma-sprayed Al bond coat [17].

2.2.7.1 Industry Practice

PMCs that are designated for aerospace applications are manufactured with metallic components. The metallization of PMCs during the manufacturing stage can be accomplished by incorporating a metallic mesh, foil, or expandable foil either as an outside ply or embedded within the layered composite prior to the liquid resin infusion [2], [4], [18]. Unfortunately, this conductive layer does not always protect the PMC. As previously mentioned, a lightning strike may cause burning, melting, and increased temperature to any hull material [3]. Once damaged, special care must be taken during repairs to assure that the electrical path is restored. Current techniques involve overlapping part of the repair with metallic mesh or foil with the parent metallic layer in order to surround the repair area [5]. However, a study by H. Kawakami and P. Feraboli shows that depending on the quality of the repair, the CFRE may perform worse than a fully unprotected specimen (without copper mesh) when subjected to a simulated lightning strike [5]. In the situation where extensive care is taken to overlap the repair mesh with the parent metallic layer, lightning strike protection may be fully restored and comparable to pristine protected specimen (without damage) [5]. Other techniques currently utilized by aerospace companies include bolted, riveted, or bonded repairs [1]. However, all of these methods are labor intensive and costly [6].

2.2.7.2 Relevant Research

The metallization of PMCs and simple polymers has become increasingly popular over the past years with the rise in the potential composite applications. More and more research is becoming available with varying degrees of success [5], [8], [9], [16], [17], [19]–[29]. The prevailing reasons behind coating these polymer based materials with metallic layers include permeation barrier [8], increase thermal and electrical conductivity [29], erosion resistance [5], [17], [20], [23]–[25], [27], [28], thermal resistance [22], aesthetic appearance [21], [26], amongst other functionalities [16], [19]. Even though various combinations of powders and substrates have been investigated to date, the deposition behavior of the metal particles on polymeric substrate remains poorly understood [28]. In addition, the heterogeneity of matrix-fibre systems makes the behavior inconsistent at times [8], [25], [29].

2.2.7.2.1 Substrate Erosion

Erosion of the substrate is a genuine issue when attempting to deposit metallic particles onto polymers and PMCs with CGDS [21], [30]. A study on wear revealed that parameters such as impingement angle and orientation affect the wear properties of both carbon fibre reinforced epoxy and glass fibre reinforced epoxy composites (see Figure 16) [30].

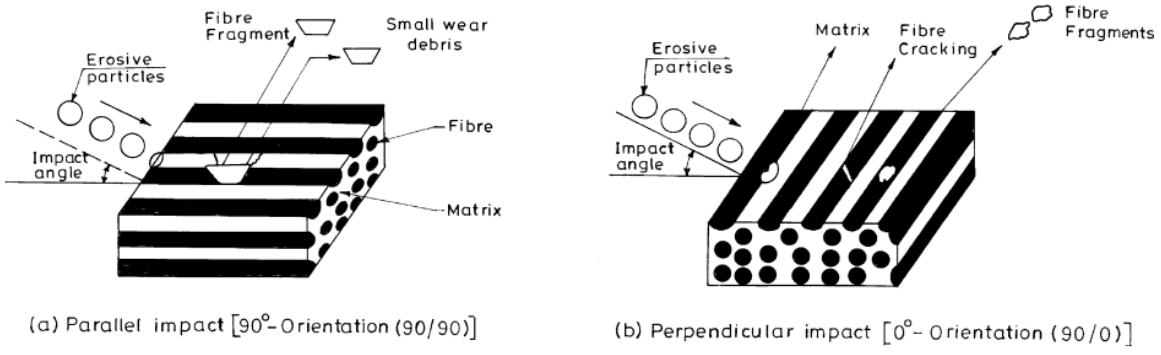

Figure 16: Schematic diagrams of erosion process in unidirectional fibre reinforced composites under (a) parallel and (b) perpendicular impact conditions [30].

Past studies have described the erosion of any material as a combination of brittle and ductile behavior [7], [30]. Brittle erosive wear is maximized at near normal impingement angle whereas ductile erosive wear is usually maximized at a 30 degree impingement angle and exhibits an incubation period prior to weight loss (see Figure 17).

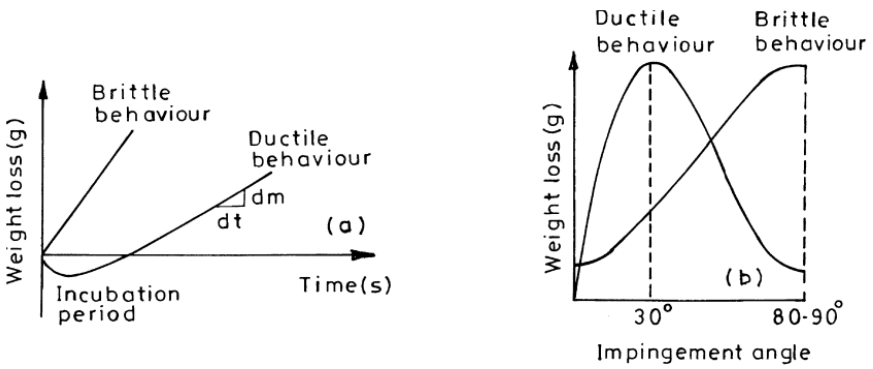

Figure 17: Schematic representations of brittle and ductile type of erosive wear [30].

Tewari et al. divulged that the maximum wear for both glass fibre and carbon fibre reinforced epoxy occurred at a 60 degree impingement angle (see Figure 18) [30]. In this study steel balls of 300 to 500µm were used as erodent. This research further revealed that the fibre orientation has a significant influence on the erosive wear of composites. The erosion is higher when the steel balls impact on fibres normally than when they impact the composite in a direction parallel to the fibres. In addition, fibre orientation seems to have an effect on the degree of fibre breakage. "In [the] case of perpendicular impact, the resistance to the lateral component of bending moment is lower and bundles of fibres get bent and broken more easily. This results in an increase in erosive wear" [30]. Erosion of composites is also characterized by matrix microcracking and debonding between the fibres and matrix [30].

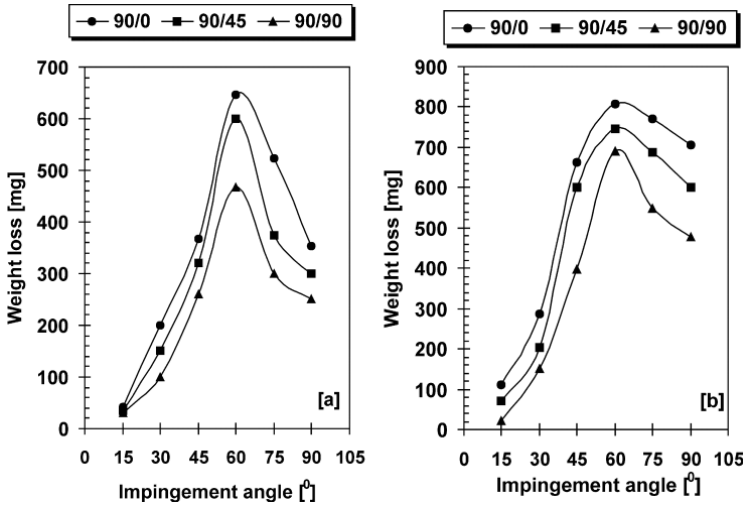

Figure 18: Influence of impingement angle, fibre orientations on the erosive wear of (a) carbon fibre reinforced epoxy and (b) glass fibre reinforced epoxy composites (v=45±5 m/s, steel balls diameter=300–500 µm, exposure time=180 s] [30].

2.2.7.2.2 Adhesion

Besides erosion, a major difficulty encountered during the metallization of PMCs is the low adhesion between the coating and the substrate [8], [16], [20], [22]–[24], [27], [31]. A coating's adhesion strength is believed to come from a combination of mechanical interlocking, chemical bonding (often referred to as metallurgical bonding), and hydrostatic forces [8], [9], [16], [19], [23], [24], [27]. General consensus dictated that the low adhesion between a metallic coating and the polymer based substrate comes from the low surface free energy (45 mJ/m^2) of polymer materials [8], [16]. A variety of techniques has been elaborated over time to increase the adhesion strength of these metallic coatings. Surface treatments, consisting of increasing the surface roughness to promote mechanical interlocking, are among the most popular to significantly influence the coating adhesion strength (see Figure 19 and Figure 20) [8], [20], [25], [31]. Several methods are available to describe the surface roughness of a substrate among which the most popular are the mean peak-to-valley height (R_z) and the average roughness (R_a) [8], [16], [25], [31]. Yet, the information provided by these values is insufficient to render a complete description of the topography of the surface in question [25], [31].

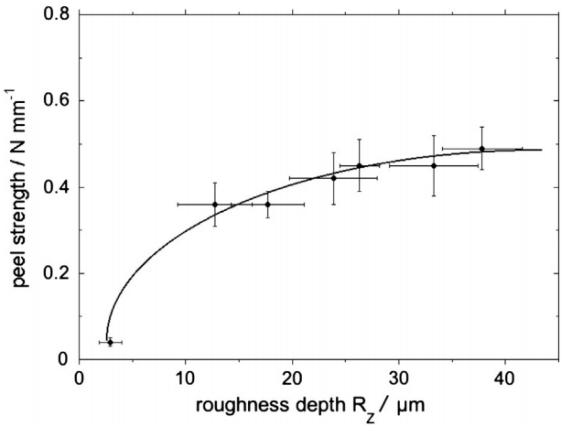

Figure 19: Peel strength as a function of roughness depth R_z for electroless/electroplated copper onto carbon fibre reinforced polymer [8].

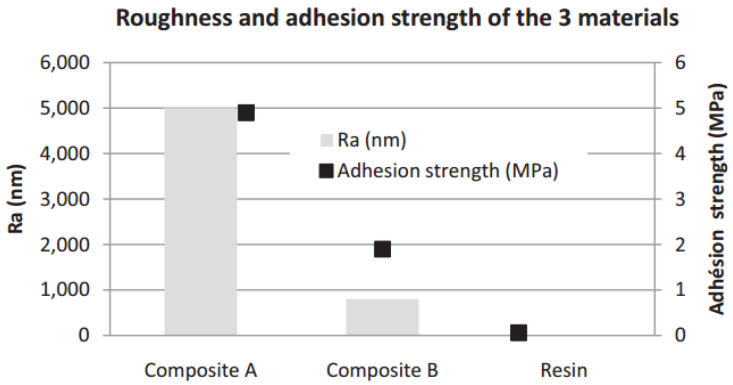

Figure 20: Average surface roughness (R_a) and accompanying adhesion strength of three different materials (composite A, composite B, and resin) coated with aluminum on their surfaces. Standard deviation for adhesion strength was less than 0.2MPa [16].

Chemical, mechanical (sandblasting), and thermal treatments have been investigated to increase coating adhesion [8], [16], [17], [20], [25]–[27]. However, thermal treatments have proven to be less effective than chemical and mechanical treatments (see Figure 21) [20]. It is important to note that the surface roughness of the polymer based substrate prior to coating deposition may change after metallization especially in the case of CS as seen in Ye and Wang's research [28]. The low glass transition temperature of polymers makes them susceptible to deformation under low loads. In addition, once the mechanical anchoring eliminated, adhesion is suppressed. During polishing, it was found that high load can cause metallic particles embedded in polymers to be exposed, detach, and fall out" [19]. Other factors such as coating thickness have also proven to have an effect on the adhesion strength. Thicker coatings are known to have lower adhesion (see Figure 21) [20].

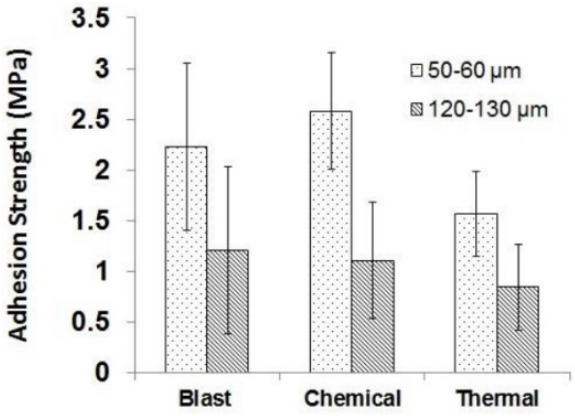

Figure 21: Adhesion strength of copper coating on CFRE with respect to different surface treatment for two different coating thickness ranges [20].

In a paper published by Coulon et al., adhesion strength of aluminum coatings on carbon fibre reinforced epoxy (CFRE) composites was enhanced through chemical bonding [16]. Coulon et al. describe that the key mechanism involved in plasma activation is the formation of C–O–metal bonds [16]. Through plasma activation, the formation and influence of chemical bonds are researched instead of mechanical interlocking.

> *An atmospheric plasma treatment was applied using the Ultra Light System arc plasma torch from AcXysTM . The discharge was obtained by introducing filtered air into two cylindrical concentric electrodes and applying a high voltage (1.5 kV) and low frequency power (100 kHz). The air inlet pressure was 4 bar. An outlet in the outer electrode creates an afterglow region, which is used for treatments, at a nozzle exit. This discharge is under non-local thermodynamic equilibrium (non-LTE) and hence produces a cold plasma, which can be applied on heat-sensitive substrates such as polymers. The afterglow contains activated neutral and metastable species but is devoid of ions, which ensures that the effects on the surface are mainly chemical in nature. The temperature at the nozzle exit does not exceed 200°C. The atmospheric plasma surface activation process was optimised to maximize the effect of the treatment on the sample surface and prevent thermal degradation. The experiments were performed on model resin surfaces prepared in the laboratory. To optimise the process, a single strip of the surface was exposed to plasma to compare the untreated and activated surfaces using the same sample. [16]*

Figure 22 presents the increase in adhesion strength of the aluminum coating on a variety of composites treated with plasma activation.

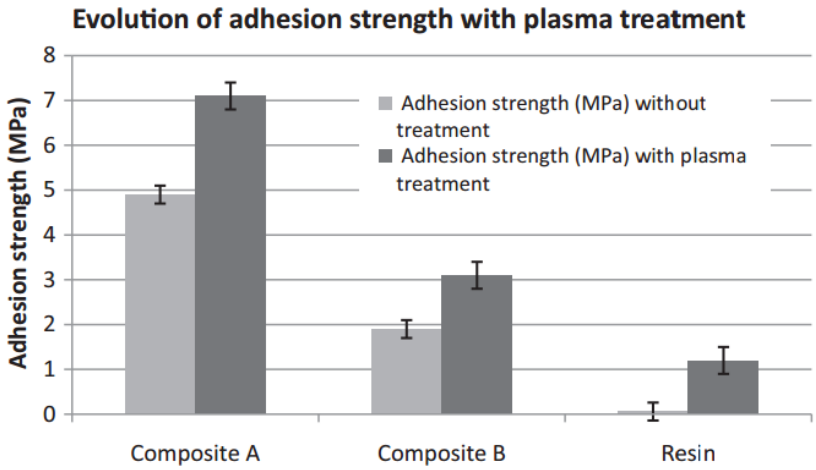

Figure 22: Enhancement of adhesion strength of an aluminum coating for composites A, B, and resin with surface activation as compared to untreated materials. Standard deviation for adhesion strength was less than 0.2 MPa [16].

Figure 23 depicts the 1 µm thick aluminum coating, deposited using an Alcatel thermal evaporator, after having performed the adhesion test [16].

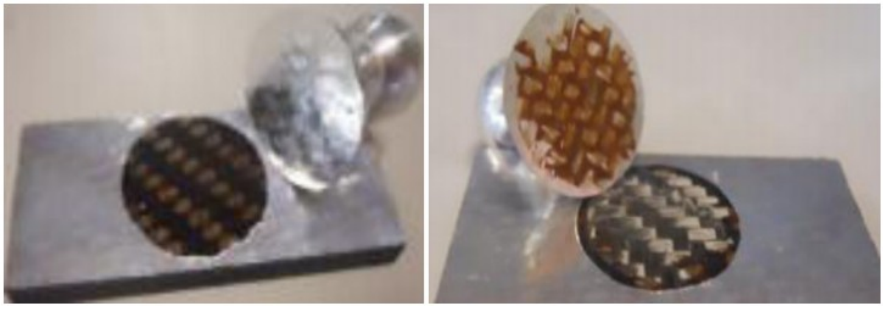

Figure 23: Fracture surface types between aluminum coating and composite surface without (left) and with (right) plasma activation [16].

Other researchers have looked towards the use of bond coats in order to successfully metalize a composite [17], [20], [22]–[24], [29], [32]. In addition to increasing the inter-laminar strength, bond coats can act as a transition layer to mitigate the thermal expansion coefficient mismatch [22]. Furthermore, bond coats can be used to prevent erosion during deposition. Empirical research demonstrated that even slight variations to a bond coat can alter its susceptibility to erosion. For instance, an experiment conducted by Simon Baril-Gosselin at the university of Ottawa shows that simply polishing the surface or modifying the ratio of resin to metal content of a bond coat can drastically change the deposition behavior (see Figure 24) [29].

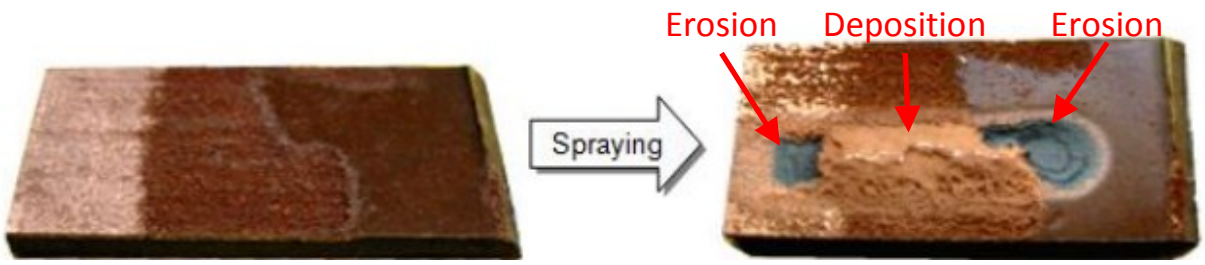

Figure 24: Effect of co-cured metallic bond coat finish on copper deposition (polished, unaltered rough, and resin rich) [29].

In his work with kinetic thermal spray, Simon Baril-Gosselin successfully coated carbon fibre/epoxy PMCs with copper coatings using bond coats composed of copper particles and epoxy which were co-cured with the composite substrates [29]. It was concluded that coatings produced from dendritic copper particles created denser coatings with better cohesion and resistance to failure than coatings produced with spherical copper particles. However, coatings produced with spherical copper particles exhibited greater adhesion to the bond coat. When tested, all coatings produced by kinetic thermal spray displayed a brittle failure thought to be caused by the high level of strain during deposition. Findings indicated that one of the weakest region of the metalized PMC was at the interface of the bond coat and the copper coating which delaminated at times. However, the high adhesion of the bond coat to the substrate is not surprising given that the bond coat was co-cured with the substrate. Simon also found that the CGDS spayed copper particles had a tendency to adhere to the exposed copper particles of the co-cured layer rather than the epoxy. In the case of dendritic copper, this caused columnar coating deposition which was severely dependant on the surface of the substrate (see Figure 25) [29].

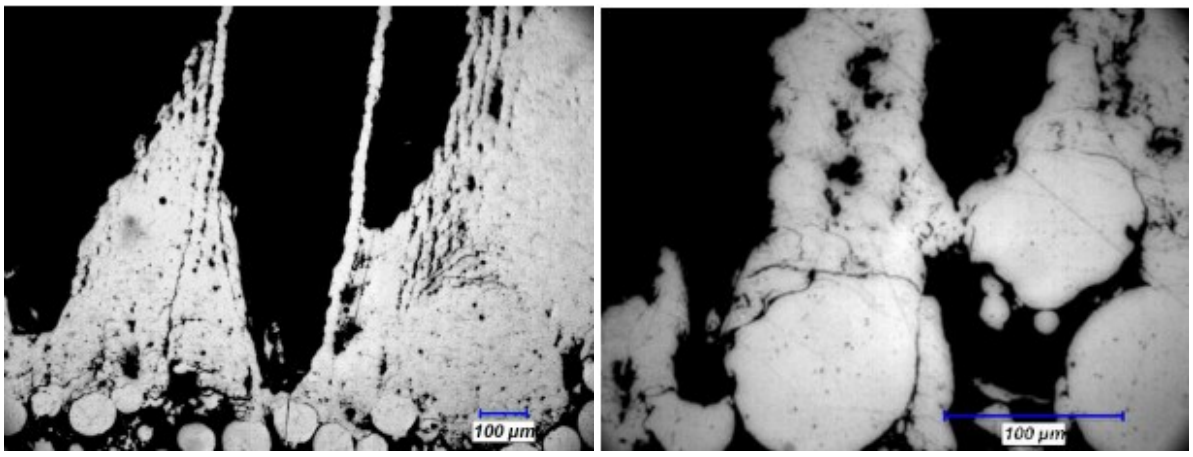

Figure 25: Cross-sections of columnar copper deposition on spherical copper particles of co-cured layer using CGDS [29].

A variety of materials can be used to produce bond coats including non-metallic materials. For example, polyolefin powders have been deposited by CS onto polyethylene substrates at substantially lower velocities (up to about 135 m/s) than those used in the CGDS process for metals [32]. These essentially fully-dense coatings were deposited using 700 kPa pressure (7 bar gauge pressure) air exiting the nozzle near room temperature (20 ± 2°C) [32]. [20]. However, when it comes to depositing metallic coatings on a polymer using CGDS, thick and dense coatings are difficult to produce. Many researchers have attempted to deposit copper directly onto polymers [19], [21]. These coatings often result in the embedment of individual particles without continuity (see Figure 26). Increasing the temperature increases the embedment distance as well as the amount of particles that can be embedded [19].

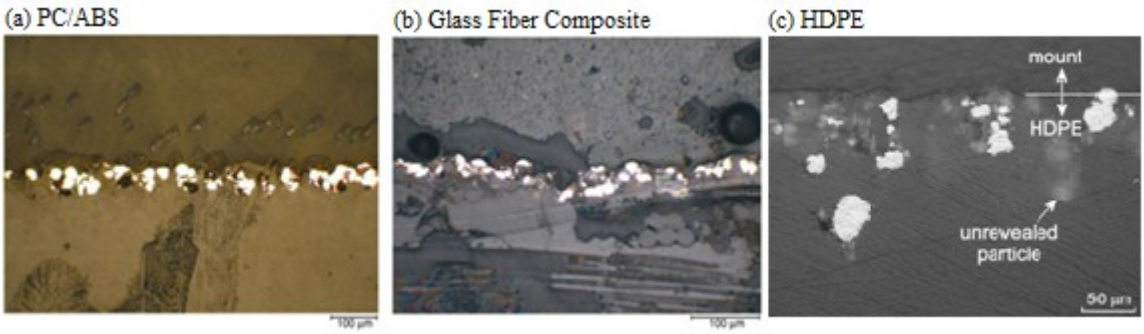

Figure 26: Cross-sectional micrograph of copper coating deposited onto (a) polycarbonate-acrylonitrile butadiene styrene (PC/ABS Polymer), (b) Glass Fibre Composite, and (c) high density polyethylene using cold spray [19], [21].

In a specific research, it was concluded that materials with high melting points, like Ni or Cu, were not suitable as bond coats for CS deposition on carbon fibre reinforced polyimide [17]. On the other hand, soft metals such as aluminum or tin with low melting temperatures are more suitable candidates for bond coat material [17]. Using CGDS, a thick tin coating was successfully deposited onto a variety of polymer substrates (see Figure 27 and Figure 28).

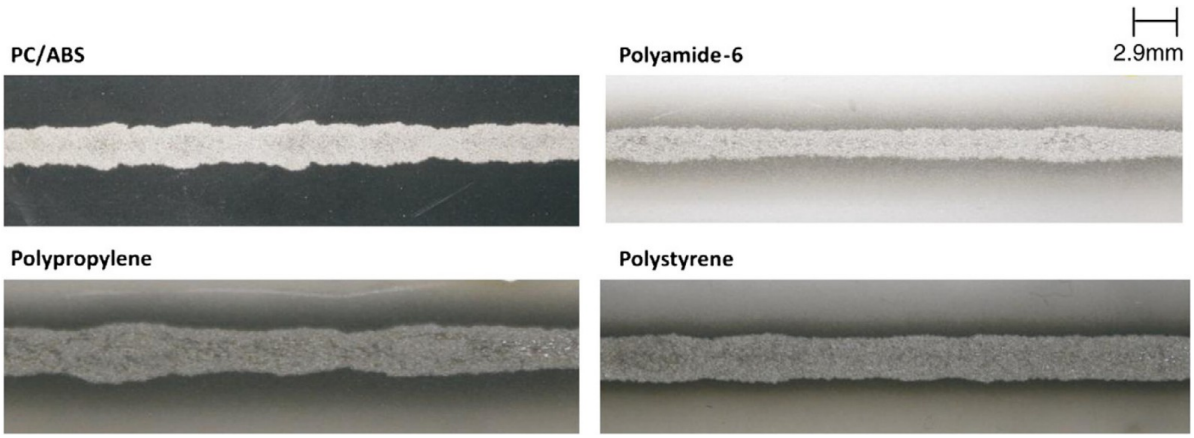

Figure 27: Tin coating on a variety of polymer substrates [21].

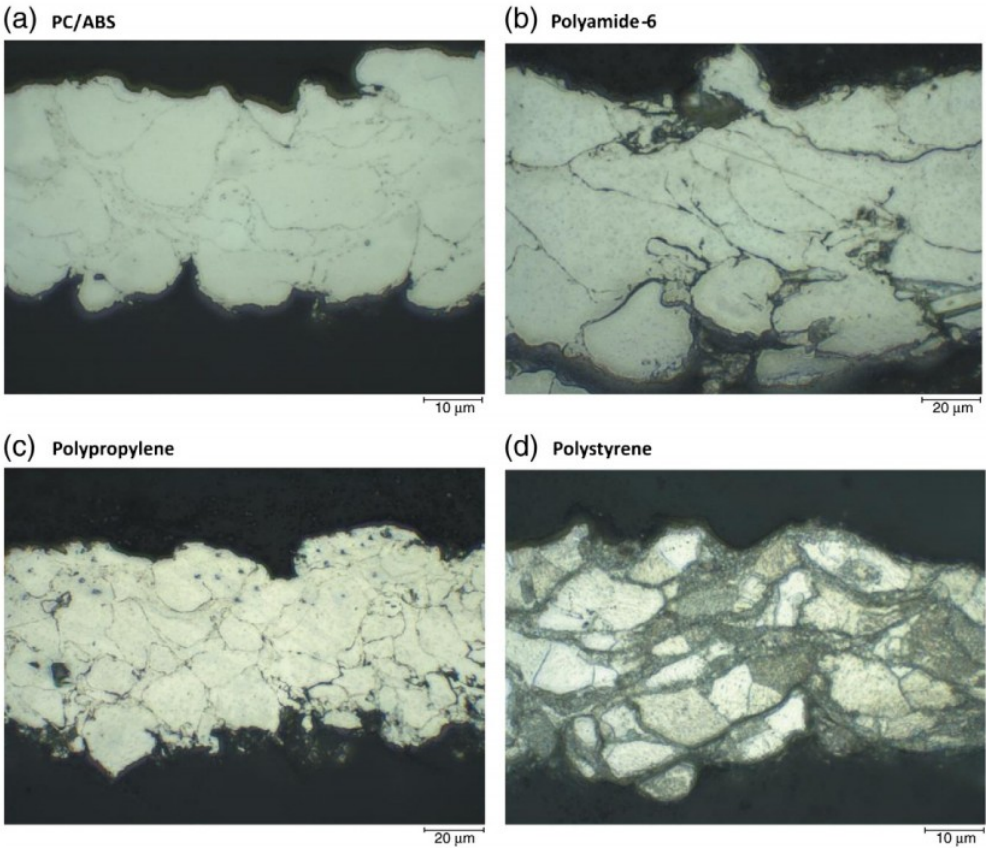

Figure 28: Micrographs of tin coating cross-sections on a variety of polymer substrates. Please note that the coating was chemically etched for (d) [21].

A great example of metallic bond coats is apparent in the work of Ganesan et al. [23]. In this study, dendritic copper particles were coated with CGDS onto polyvinyl chloride (PVC) utilizing a tin bond coat (see Figure 29a & Figure 29c). However, Genesan et al. also were capable of depositing a

copper coating on PVC with the use of a spherical copper particle interlayer (Figure 29b & Figure 29d). It was noted that the deposition efficiency (DE) of the tin powder was much higher than the spherical and dendritic copper powder. The low yield strength of tin was thought to be the primal reason behind this. Ganesan et al. also noted that the spray temperature had a much more important influence on the deposition than the gas pressure when depositing on a PVC substrate. The addition of these metallic coatings successfully lowered the electrical resistivity of the final product (11.39±1.6 μΩ cm for the spherical copper bond coat and 9.43±1 μΩ cm for the tin bond coat). However, the reported electrical resistivity of the pure oxygen free copper is 1.7 μΩ cm. The lack of plastic deformation and material mixing at the substrate interface resulted in a low shear adhesion strength (1.93±0.7 MPa for the spherical copper bond coat and 5.4±0.9 MPa for the tin bond coat). These values are much lower than those of cold sprayed copper coating on the aluminum substrate [23].

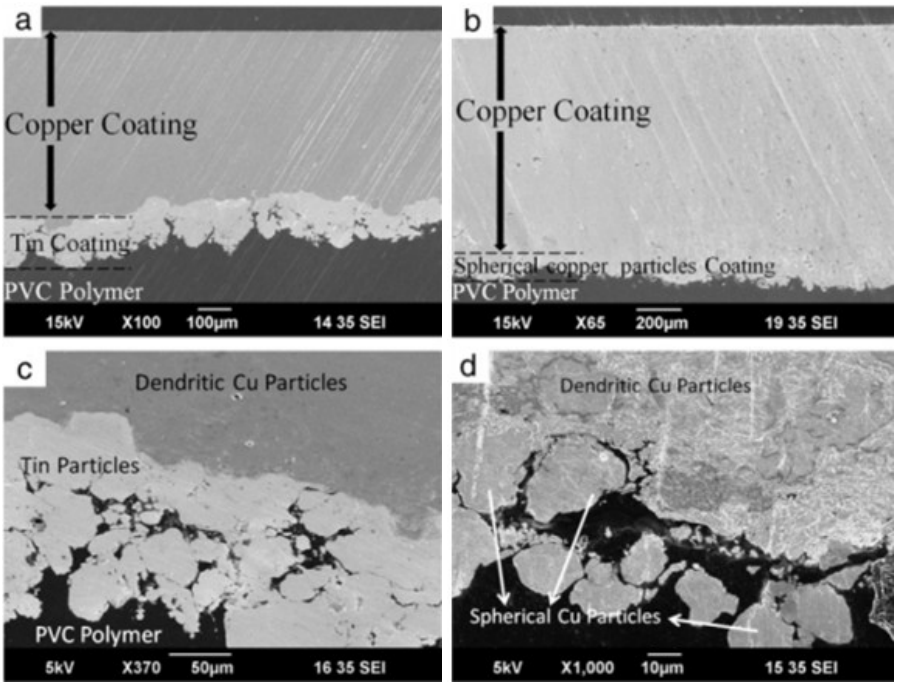

Figure 29: Copper coating on the PVC substrate (a) with tin interlayer, (b) with spherical copper particle interlayer, and (c), (d) interface of the two respectively [23].

In a later study, Genesan et al. re-deposited past copper coatings achieving shear adhesion strength of 1.93±0.7 MPa and 5.3±1.4 MPa on PVC with spherical copper powder and tin powder interfaces, respectively (see Figure 30a & Figure 30c) [24]. In addition, a dendritic copper coating was

deposited onto an epoxy substrate using a tin interlayer with an adhesion strength of 4.93 ±1.2 MPa (see Figure 30b & Figure 30d) [24].

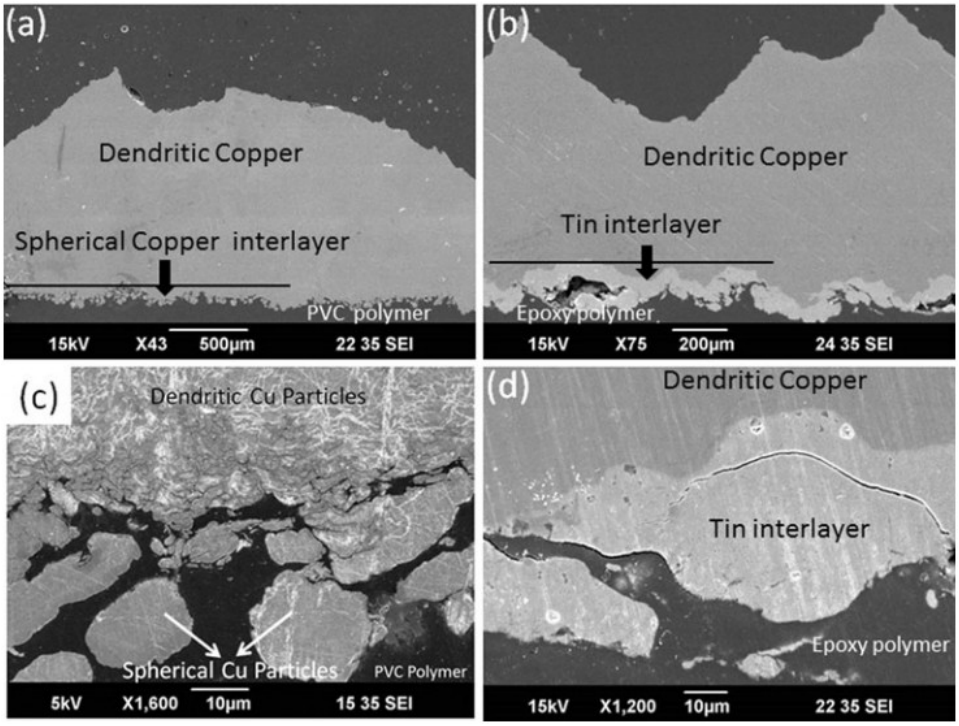

Figure 30: Copper coating on the polymer substrate: (a) dendritic copper coating on the PVC substrate using spherical copper interlayer, (b) dendritic copper coating on the epoxy substrate using tin interlayer, (c, d) high magnifications images of (a, b) show the coating interface [24].

Spherical copper particles were not able to deposit on epoxy. Figure 31a & Figure 31b shows a schematic of the interaction between the spherical copper particle and the substrate. When impacting PVC, hard particles penetrate the polymer and are subsequently locked by the laterally covering polymer (see Figure 31c) [24]. On the other hand, when the copper particle impacts the hard epoxy substrate, the polymer is broken creating a crater (see Figure 31d). The copper particle can merely attach at the bottom of the crater, however, continuous coating build-up is not possible. If sufficient heat is produced, PVC, a thermoplastic polymer, can deform plastically upon high stress whereas an epoxy, a thermosetting polymer, will break in a brittle nature [24].

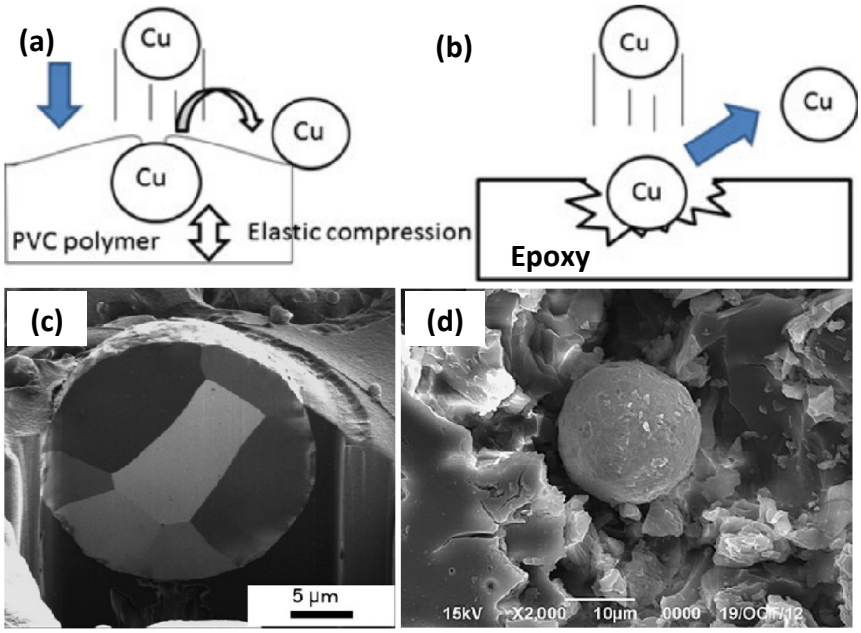

Figure 31: Schematic representation of spherical copper particle interaction with (a) PVC and (b) epoxy with accompanying (c) FIB bisection of spherical copper particle embedded in the PVC substrate and (d) SEM image of spherical copper particle trapped inside the crater on the epoxy substrate [24].

When comparing the deposition of tin and copper, it is apparent that the tin primarily deforms itself whereas copper deforms the polymer substrate [24]. A dendritic copper particle forms many contact points with the polymer substrate as seen in Figure 32a & Figure 32c. However, these weak interactions cannot sustain subsequent impacting particles, hindering particle-to-particle cohesion bonding and coating build-up. On the other hand, tin deforms itself, undergoing large plastic deformation and creating mechanical anchoring when possible. As a result, tin forms large contact areas between itself and the polymer substrate ultimately increasing its shear adhesion strength compared to copper (see Figure 32b & Figure 32d) [24].

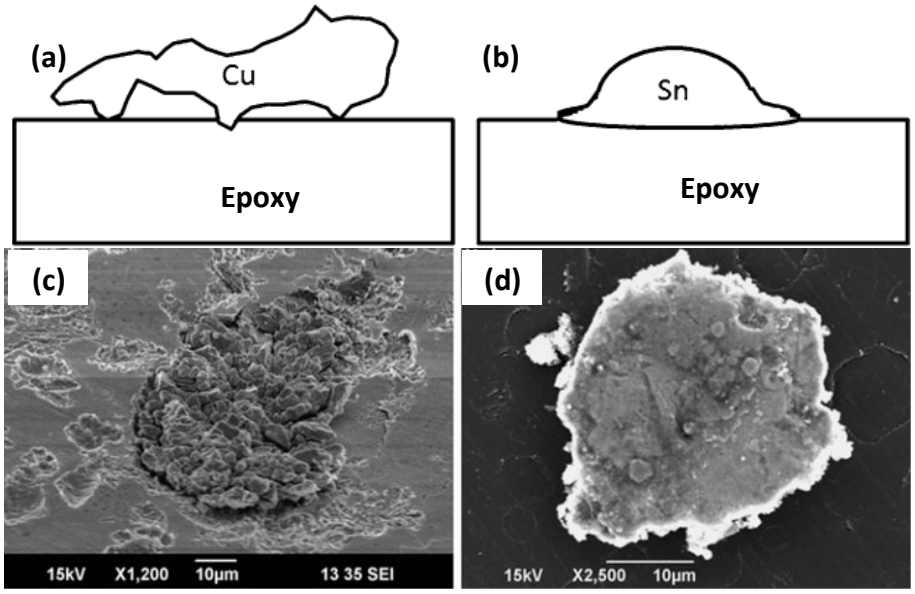

Figure 32: Schematic representation of cold sprayed (a) dendritic copper and (b) tin particle interaction with polymer substrate with accompanying SEM images of the interaction of cold sprayed (c) dendritic copper particle and (d) tin particle on epoxy substrate [24].

Furthermore, it is believed that the high impact energy spherical copper particles create polymer debris which are subsequently trapped between the interface of the spherical copper and dendritic copper which deteriorate the good bonding formation ultimately lowering the adhesion of the coating [24]. In the case of tin, the lack of damage to the substrate eliminates this issue. Once the interlayer is deposited, dendritic copper particles can easily adhere to the other metals creating several points of contact (see Figure 33) [24].

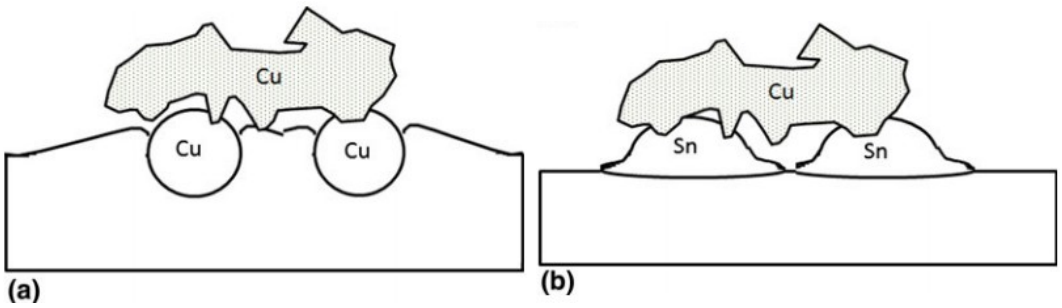

Figure 33: Schematic representation of interaction of dendritic with different interlayers: (a) spherical copper interlayer, (b) tin interlayer [24].

Other researchers have tried using aluminum as bond coat. Ye and Wang have used CGDS to deposit aluminum on Lexan [28]. They discovered that the powder feed rate (PFR) has a great importance on the DE and the DR (see Figure 34) [28].

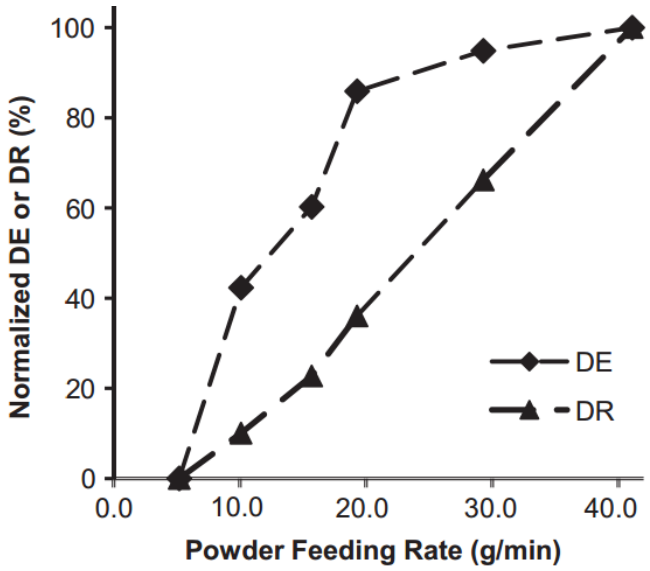

Figure 34: Normalized deposition efficiency (DE) and deposition rate (DR) at different powder feeding rates [28].

Similarly, Zhou et al. metalized a PMCs via a CS process with aluminum [9]. Metallic coatings deposited include aluminum and aluminum/copper directly on top of a 30wt% carbon fibre reinforced PEEK. PEEK is a semi-crystalline thermoplastic with excellent wear resistance and high temperature resistance. The aluminum coating had a uniform porosity of 2.9% as seen in Figure 35a. The once smooth surface of the PMC became uneven at the interface due to the heat and impacting particles during deposition (see Figure 35b). This mechanical interlocking is thought to be the root of the adhesion strength of the coating [9].

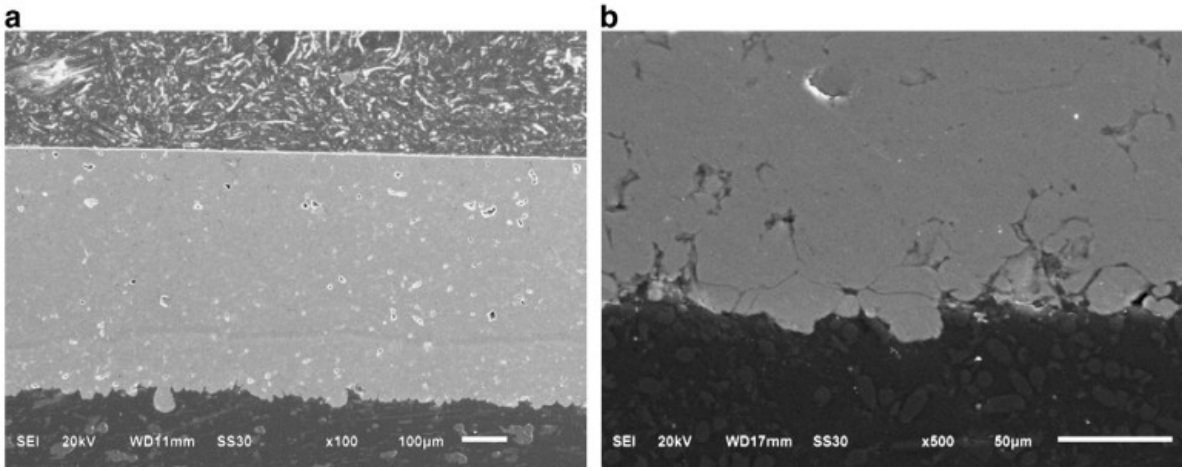

Figure 35: (a) Cross-sectional SEM morphology of pure Al coating and (b) zoom the interface between the coating and the substrate [9].

The subsequent deposition of a pure copper coating on top of the aluminum coating resulted in reduced porosity of the aluminum coating (1.1%) and increased microhardness (see Figure 36a) [9]. Figure 36b presents the jet mixing between the aluminum and copper indicating strong mechanical bonding. All deposited coatings retained the original microstructure of the powders and no oxides were produced during spray [9]. However, the adhesion strength of the coating is 2.26 MPa which is about half the tin coating adhesion strength reached by of Genesan et al. [9], [24].

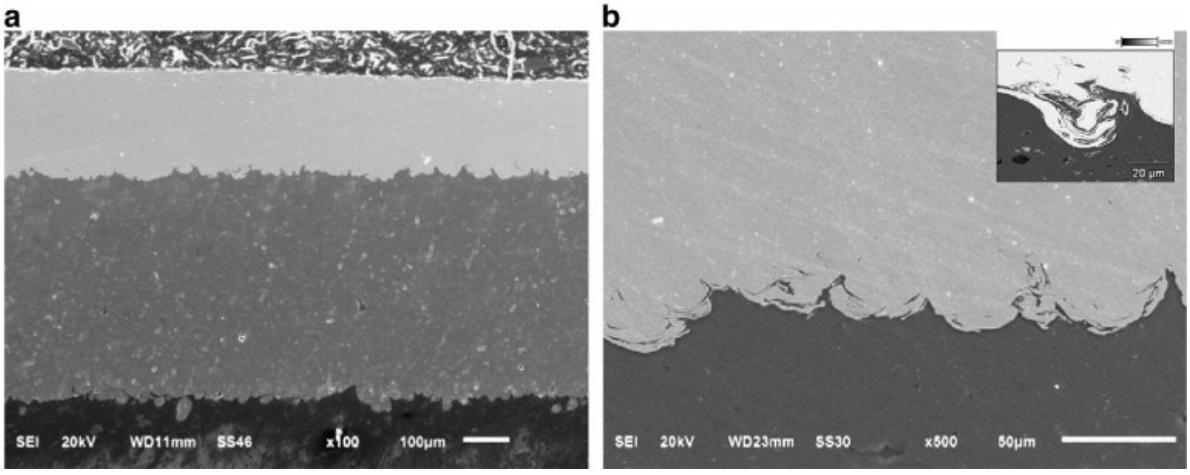

Figure 36: (a) Cross-sectional SEM morphology of Al/Cu coating and (b) zoom the interface between the Al coating and the Cu coating [9].

2.2.7.2.3 Electrical Resistivity

The electrical resistivity, or specific resistance, is the resistance of a sample of the material having both a length and cross-section of unity. Its reciprocal measurement is the conductivity. The resistance is a measurement of how a material's composition impedes the flow of electron. The resistivity θ (Ωm) can be calculated by the following equation,

$$\theta = R\frac{A}{L}$$

where R (Ω) is the resistance, A (m2) is the uniform cross-sectional area, and L (m) is the length of the test specimen [33]. It is well established that the resistance of a material varies with temperature. The resistance of the pure metals increases with temperature (T) and can be approximated with the temperature coefficient of resistance (α) through the following equation [33].

$$R_2 = R_1[1 + \alpha(T_2 - T_1)]$$

The electrical resistivity of bulk copper (1.724 μΩ cm at 20°C) is lower than aluminum (2.828 μΩ cm at 20°C) which are both lower than tin (11.63 μΩ cm at 20°C) [33]. However, the quality of the coating may affect this value. As previously mentioned, Genesan et al reported lower resistivity for the tin coated PVC polymer (9.43±1 μΩ cm) than the copper coated one (11.39±1.6 μΩ cm) [23]. Many studies have been done to explain why coating resistivity often stray from bulk material. Researchers concluded that the presence of interfacial defects, oxidation, dislocations, and higher porosity levels in the sprayed coatings are the primary reasons behind increased resistivity [19], [23], [34]–[36]. A study from Seo et al. concluded that annealing a coating under vacuum will minimize resistivity. Annealing increases the surface area contact between the particles by minimizing micro voids, residual stresses, and dislocations through a diffusive process which ultimately promotes electron flow. Selecting the appropriate thermal spray process can greatly affect the resistivity of a coating. An experiment done by Stoltenhoff et al. revealed that copper coating produced by CS had higher conductivity than copper coating produced by HVOF and arc spray (AS). We can see in Figure 37 the electrical conductivity comparison of as sprayed, annealed at 300°C for 1 hour, and annealed at 600°C for 1 hour copper coatings produced by CGDS, HVOF,

and AC as compared to a bulk copper sample [35]. CS has higher conductivity (or lower resistivity) because it produces dense coating with low oxide content [35]–[37].

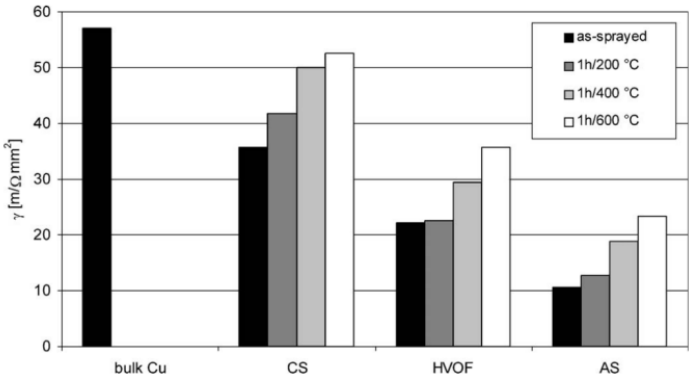

Figure 37: Electrical conductivity of as sprayed, annealed at 300°C, and annealed at 600°C copper coatings produced by cold spray (CS), HVOF, and arc spray (AS) compared to a bulk copper sample (reference material) [35].

Choi et al. conducted a study demonstrating the anisotropic behavior of cold sprayed coatings [38]. The high porosity and dislocation density through the coating thickness restrict the electron path resulting in higher resistivity than when measured in plane with the coating. As a result, the coating thickness influences the resistivity of the coating which is more significant in thicker coatings. Figure 38 shows the resistivity of as sprayed and annealed aluminum coatings taken along (in plane) and through the coating thickness [38].

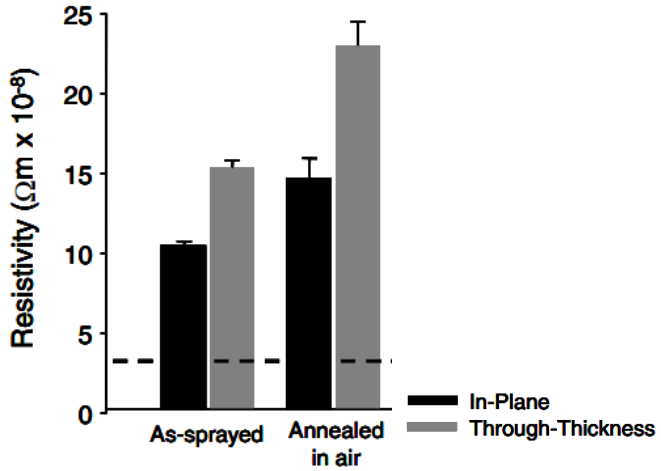

Figure 38: Electrical resistivity of in plane and through thickness of cold sprayed Al coatings – Adapted from [38].

2.2.7.2.4 Material Limitations

As seen above, a variety of metals have been deposited on diverse substrates with varying degrees of success. However, it is apparent that copper, aluminum, and tin are amongst the most widely used metals to coat PMCs using CGDS systems. The selection of commercially available powders is limited by their demand. Copper, aluminum, and tin powders have been extensively used in commercial applications thereby establishing their commercial availability [39].

Historically speaking, aluminum was one of the first lightning strike protection materials with carbon fibre laminate according to Ed Rupke [4]. However, the threat of galvanic corrosion pushed the migration to copper [4]. Copper also has higher electrical conductivity than aluminum which makes it ideal choice for lightning strike protection.

In order to be used as a conductive coating, the material in question must be capable of deposition on PMCs through CGDS. Figure 39 provides the estimated impact energy required to deposit a variety of metals with respect to the amount of energy that will erode a common polymer substrate [21]. From this, tin and lead are the only metals that can be deposited onto polymers with more or less certainty. As mentioned above, the DE of tin powder is much higher than copper powder [23]. The high DE of tin is most likely due to its low yield strength (1.6 to 2.1ksi) when compared to other metals (aluminum: 5 to 21ksi, copper: 5 to 60ksi) [23], [33]. Although some researchers have claimed to deposit copper coatings directly onto polymers, these coatings are discontinuous which can negate their conductivity [19], [21].

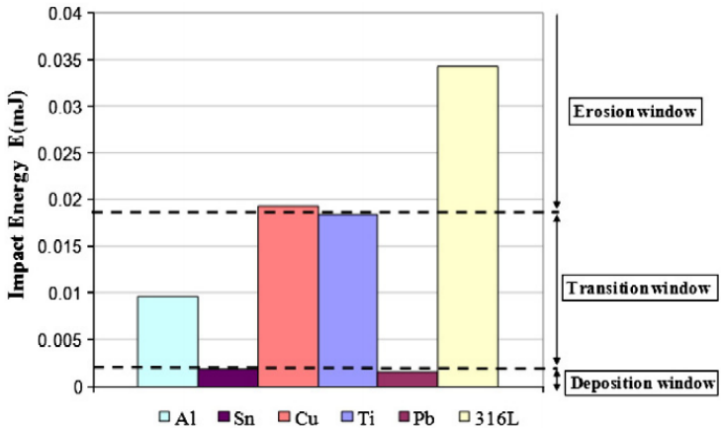

Figure 39: CS Process Characterization Chart for Polymer Substrates [21].

Although tin may be the most well suited metal to be deposited on PMCs, it may not be suitable for this particular application. Tin undergoes an allotropic transformation from its β phase, a body centered tetragonal (bct) crystal structure, to an α phase, a diamond cubic crystal structure, below 13.2°C (55.8°F) (see Figure 40) [40]–[48]. Tin can also transform into a γ phase, a rhombic crystal structure of similar density with β-tin, between 161°C and its melting point [49]. However, the focus remains on the α phase since this transformation could occur in ambient weather.

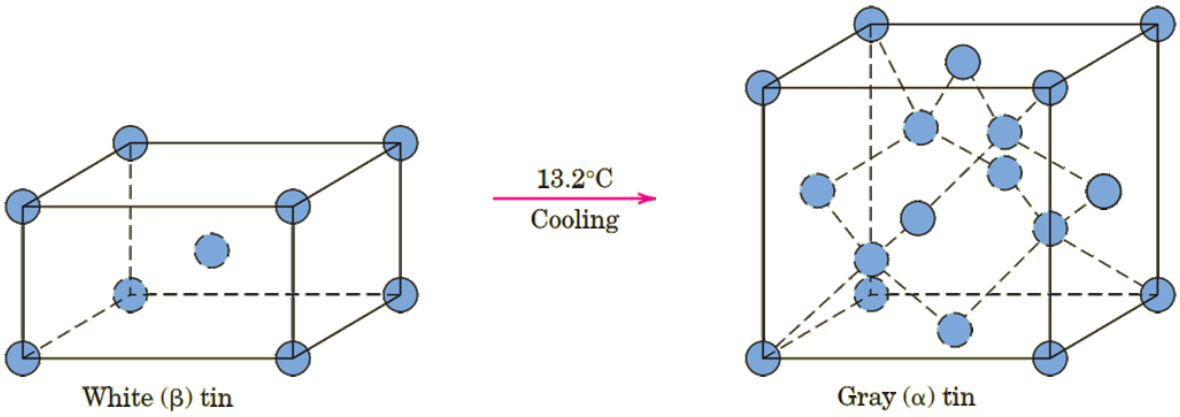

Figure 40: Allotropic transformation of tin from its β phase to its α phase [41].

This phase transformation from white tin (β) to gray tin (α) induces an increase in volume of 27% and a decrease in density from 7.30 g/cm^3 to 5.77 g/cm^3 [40]–[42], [46]. Gray tin is a semiconducting material with unique electrical and optical properties [42]. During this transformation, cracking and wart growth can be observed at the surface. With extended aging periods, the brittle α phase tin crumbles, resulting in a coarse powder like product (see Figure 41) [40], [42], [46].

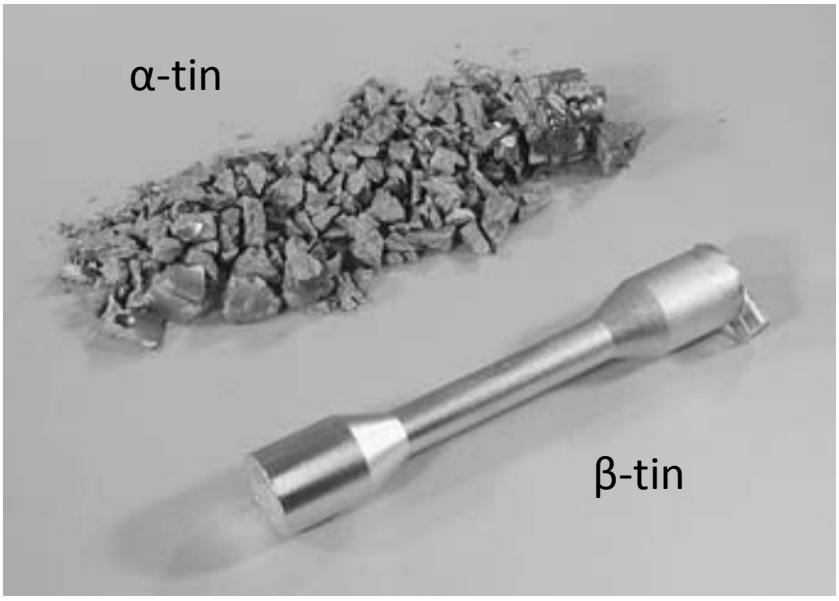

Figure 41: The transformation of β-tin (white tin) into α-tin (gray tin) occurring in Sn-0.5 wt.% Cu solder alloy, after prolonged exposure at -18°C [43].

Although the allotropic transformation temperature is 13.2°C, the rate at which this reaction takes place is extremely slow and only takes place after a large degree of undercooling and after a considerable incubation time [41], [42]. It is understood that the temperature is the driving force behind this reaction. In other words, the lower the temperature (below 13.2°C) the faster the rate of transformation [41]. However, it is important to note that any reaction can be kinetically hindered at low temperatures [50].

This phenomenon was discovered in the mid 1800s but only extensively studied in the mid 1900s [40]. The transformation was not of serious concern for it only takes place in high purity tin (over 90%) [47]. In addition, the transformation of β-Sn to α-Sn is difficult to study since the sluggish nature of the transformation requires a very long time (sometimes years) to produce reliable and reproducible laboratory experiments [40], [46], [47]. In some studies, experimental results remain very contradictory [44].

The allotropic transformation of tin can be divided into two steps. First there is the incubation period where the time to nucleate an α tin structure is considered. This is followed by a growth period where the α phase propagates through the remaining sample [46], [47]. Researchers agree that the surface of a tin sample is the favourable region for the nucleation of the α-phase tin. The

surface poses no barriers to the volume expansion and the surface free energy eases the phase transformation [46].

Many researchers have tried to quantify the effect of certain factors in the tin pest formation. These factors include: composition, manufacturing condition, and exposure (time and temperature). The composition of tin remains one of the most influential factors in the allotropic transformation. Alloying elements with an appreciable solid solubility, such as lead (Pb), bismuth (Bi), cadmium (Cd), and antimony (Sb), suppress the β-to-α transition. It is thought that the matrix is strengthened by the solute concentration. In some instances, minor impurities (parts per million range) of such elements have completely inhibited the allotropic transformation (see Table 5) [42], [44], [46].

Table 5: Results of Chemical Analysis of Two Different Sn-0.5Cu Samples (Conc. represents the absolute concentration and CI represents the confidence interval) [48]

	Sample Without Tin Pest		Fully Transformed Sample	
Elements	**Conc. (μg/g)**	**CI (μg/g)[a]**	**Conc. (μg/g)**	**CI (μg/g)[a]**
Ag	9.1	1.1	1.27	0.13
Al	2.8	1.9	2.01	0.48
As	<		<	
Au	<		<	
Bi	156	6.4	28	3
Cd	2.07	0.16	0.90	0.13
Co	7.26	0.51	1.34	0.28
Cr	0.37	0.21	0.16	0.03
Cu	4.77×10^3	0.36×10^3	4.63×10^3	0.23×10^3
Fe	35.7	2.65	29.7	2.24
Ga	<		<	
Ge	23.7	2.5	<10	
In	96.5	8.8	14.2	0.8
Mn	0.31	0.03	0.26	0.01
Mo	<		<	
Ni	23.0	1.7	5.8	1.6
Pb	430	20	280	10
Sb	340	20	140	10
Ta	<		<	
Te	<		<	
Tl	10.0	0.9	7.5	1.4
W	<		<	
Zn	<		<	

[a]Confidence interval: α = 0.02; "<" = below detection limit; "–" = not determined se

Elements that are more or less insoluble, such as zinc (Zn), aluminum (Al), magnesium (Mg), and manganese (Mn), are known to accelerate tin pest formation [42], [44], [46]. These elements, along with SnO and ice, are thought to accelerate the nucleation phase by creating disruptions in the matrix [46]. Other substances such as CdTe, InSb, and α-Sn itself have been characterised as "seeds". Seeds are substances with the same crystal structure and close lattice parameters to those

of α-Sn. The insertion of seeds enables bypassing the incubation period and quantifying the growth rate of the α phase tin (see Table 6) [47].

Table 6: The Effect of Alloy Addition on Retarding the Transformation from β-Tin Into α-Tin [48]

Material (Inoculated with 0.1mg α-Sn)	Time for the Formation of a Visible Wart
99.998% pure Sn	2 hours
Sn+0.024mass%Pb	12 days
Sn+0.48mass%Pb	29 days
Sn+50mass%Pb	190 days
Sn+0.1mass%Sb	14 hours
Sn+0.5mass%Sb	No wart visible after 5 years
Sn+0.3mass%Bi	330 days
Sn+0.1mass%Cu	4 hours
Sn+0.5mass%Cu	7 hours

Materials' properties and geometry mostly affect the α-tin growth whereas composition can also affect the nucleation time. Mechanical treatment of the samples before aging at low temperatures also appears to play a significant role in the allotropic transformation. Manufacturing conditions such as the cooling rate when casting, the cold working percentage, as well as the annealing time and temperature have been known to influence the transformation of tin [40], [42]–[46]. Matvienko and Sidelnikov proposed that the penetration of tin pest into the body of the sample is controlled by the relaxation of stress ahead of the expanding α-Sn [45]. In other words, factors that lead to higher strength of the tin matrix would help resist propagation of tin pest. Other researchers defend that the stress generated by cold work or the energy stored in the deformed structure increased the driving force for the transformation (see Figure 42) [40], [42].

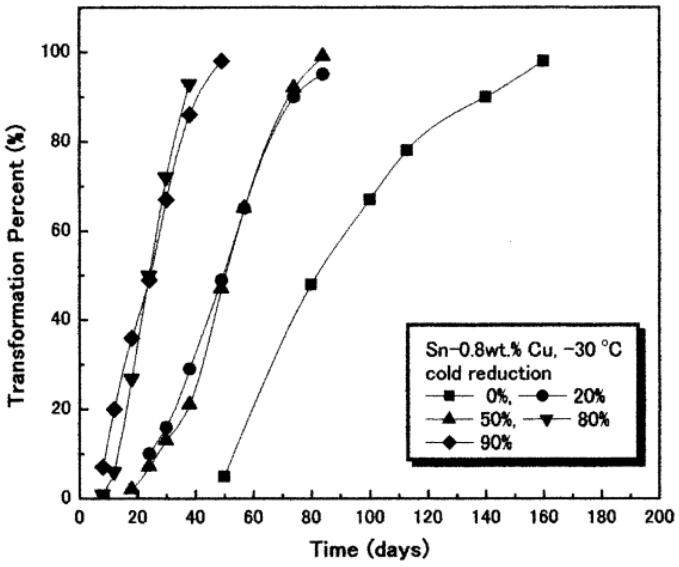

Figure 42: Influence of the cold work on the transformation rate in a tin 0.8wt% copper alloy at -30°C [42].

2.3 Cold Gas Dynamic Spray (CGDS)

Cold gas dynamic spray is a successful and promising coating technique for many engineering applications due to its high-rate and high-dense coating development abilities. Its practical use on polymer substrates however, is still in the fledgling phase [24].

2.3.1 Classification

In order to properly classify CGDS, one must look at the ramifications of all thermal spray processes. As previously mentioned, thermal spray processes differ from most other coating processes because they are characterized by the deposition of large particulates instead of single atoms of material onto particular substrates [7]. Thermal spray can be effectively divided into four branches: plasma, electric arc, combustion, and kinetic spraying (see Figure 43) [7]. Each of these processes possesses many subsets, each of which has specific characteristic temperatures, enthalpies, and velocities [7]. CGDS, also known as "Cold Spray", is part of the kinetic spray branch as seen in Figure 43. There are two variants within CGDS that will be explained in the process overview section of this chapter.

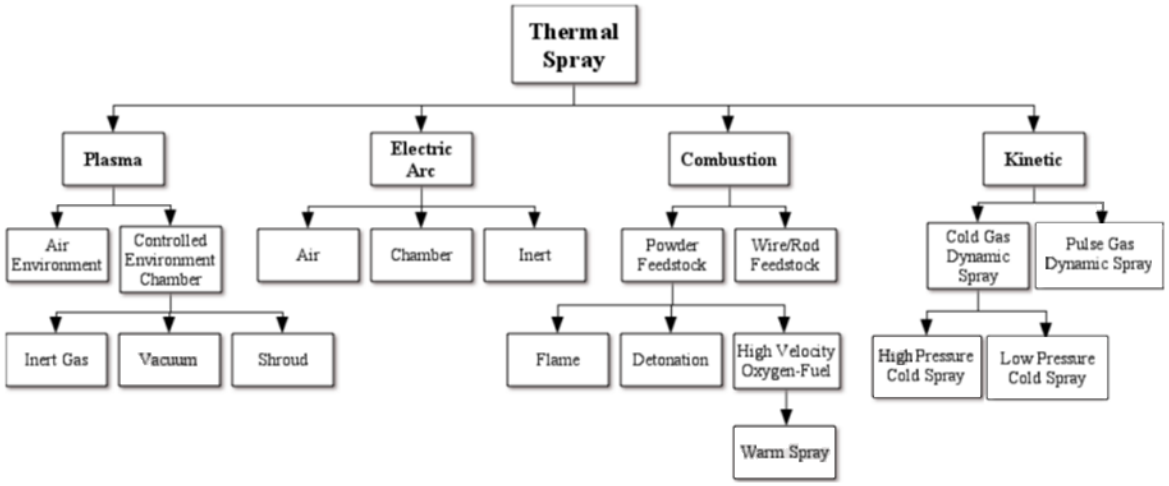

Figure 43: Thermal spray processes and subsets - Adapted from [7].

Kinetic spray differs from the other three large classes of thermal spray in the way that it mainly utilizes kinetic energy rather than thermal energy to deposit material. Figure 44 presents a graph of the approximate operating regimes of a variety of thermal spray processes.

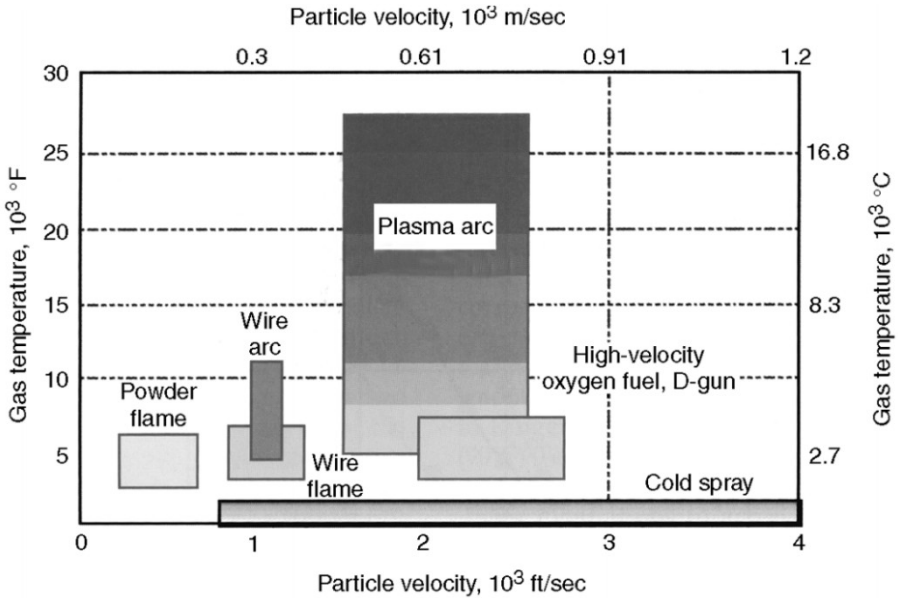

Figure 44: Temperature and velocity regimes for several thermal spray processes [7].

Table 7 compares CS to various thermal spray processes regarding their power consumption as well as coating residual oxides, density, and bond strength.

Table 7: Thermal Spray Process Comparison - Adapted from [7]

Attribute	Cold Spray	Air Plasma Spray	High Velocity Oxygen Fuel Spray	Flame Spray	Wire Arc Spray
Gas Types	Air, He, N_2	Ar, He, H_2, N_2	CH_4, C_3H_6, H_2, O_2	O_2, acetylene	Air, N_2, Ar
Power Consumption, (kW)	5 - 25	40 - 200	150 - 300	20	2 - 5
Coating Oxides	None	Moderate to high	Moderate	High	Moderate to high
Coating Density Range, (%)	>95	90 - 95	>95	85 - 90	80 - 95
Bond Strength, MPa (ksi)	70 (10) [39]	<68 (<10)	68 (10)	7 - 18 (1 - 3)	10 - 40 (1.5 - 6)

S. Sampath et al. investigated the microstructure change in Ni-5 wt.% Al coatings produced by diverse methods (see Figure 45). It was concluded that coatings produced by CGDS have lower porosity in comparison to air plasma spray (APS) and high velocity oxygen fuel (HVOF) [51].

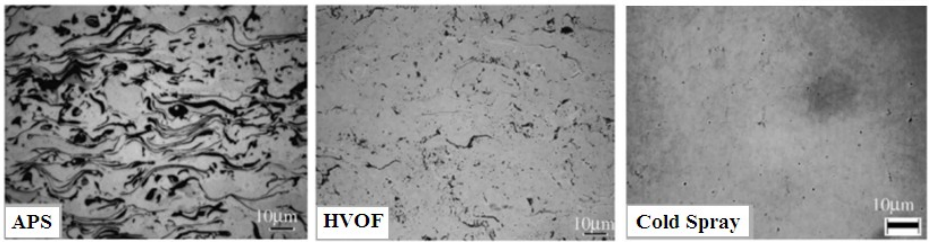

Figure 45: Cross-section of Ni-Al Coatings Manufactured Using Different Spray Techniques – Adapted from [51].

2.3.2 Historical Development

As one of the latest advances in kinetic spray, CGDS's historical background heavily relies on the development of its thermal spray predecessors [7].

The earliest records of thermal spray originate in the patents of M.U. Schoop (Zurich, Switzerland), dating from 1882 to 1889. These patents describe a process that fed lead and tin wires into a modified oxyacetylene welding torch. Later torches were modified to accept powdered materials. The powders were caught up in the hot expanding jet flow where the particles were heated while being accelerated toward the surface to impact, spread (if molten), and solidify. The results were coatings that were incrementally formed from impacting droplets. Electric arc spray was also patented by Schoop around 1908, which enabled more metals to be sprayed. Steel, stainless steel, and zinc by wire-arc metalizing advanced through improvements in equipment and process control as well as through promotion of process applications for applying zinc as a protective coating, primarily to prevent corrosion on structures. [7]

The first plasma spray coating process was introduced by Reinecke in 1939 [7]. Plasma spray offered a higher level of material flexibility including non-carbide, carbide, and ceramics, ideal for thermal protection. Significant expansion of the thermal spray industry, however, did not occur until after World War II, as shown in Figure 46. Between 1960 and the late 1990s unprecedented growth occurred with the commercial introduction of plasma, electric arc, and HVOF processes. During this period, new materials were introduced with improved process control equipment through original equipment manufacturer (OEM) applications however, the basic operating principles remain unchanged since Schoop [7]. A noteworthy milestone is the introduction of aircraft engine applications which was a major contributor to the early expansion of the technology (see Figure 46) [7]. Applications of the gas turbine in the early 1960s included components such as compressor blades, compressor stator vanes, bearing housings, and labyrinth seals [7]. As such, plasma spray emerged in the early 1970s as the most widely used high-tech thermal spray coating technology [7]. Subsequent increases in particle speeds have increased coating densities and bond strengths to the point where today thermal spray is widely used in aircraft and even in biomedical coating applications. Although spray device developments have slowed, many thermal spray advances now

focus on developing better feedstock materials (consumables) as well as improving process control (computer-controlled consoles, robotics, real-time sensors, automated handling systems, etc.) [7].

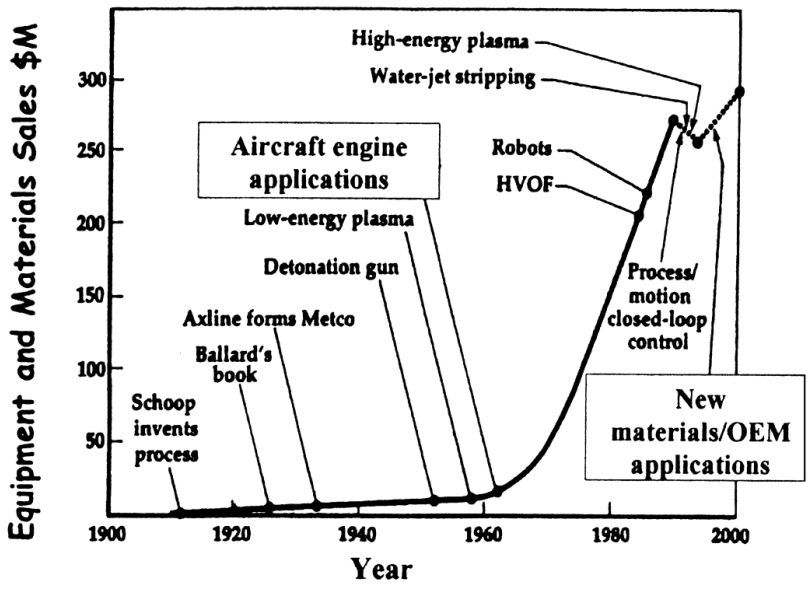

Figure 46: Timeline of significant developments during the growth of the thermal spray industry [7].

CGDS was originally conceptualized in the 1980s by A. Papyrin while studying supersonic two-phase flow (gas & solid particles) in a wind tunnel at the Institute of Theoretical and Applied Mechanics of the Russian Academy of Science in Novosibirsk [7], [52]. After Papyrin's work, a U.S. patent was issued in 1994 and the European patent in 1995 [7]. Nowadays, research regarding cold spray is being lead by institutions in the United States, Russia, Germany, Canada, and Japan [7]. Research topics include gas dynamics, physics of high-speed particle impact, powder materials, novel application methods, and the development of specific applications [7].

2.3.3 Process Overview

In CGDS, high pressure gas is heated and accelerated through a converging-diverging (De Laval-type) nozzle where particles are injected into the inert gas stream (see Figure 47) [7], [52]. The gas accelerates in the converging section of the nozzle until it reaches sonic velocity at the throat region [7]. The flow then becomes supersonic (Mach numbers ranging from 2 to 4) as it further expands in the diverging section of the nozzle [7]. Heating the gas does little to heat and/or soften spray particles [7]. The primary goal is to achieve higher sonic flow velocities, thus gas velocities, which

ultimately results in higher particle impact velocities [7]. In fact, the gas exiting the spray gun is often below ambient temperatures as it undergoes large expansion in the spray nozzle cooling it down substantially [7]. Nitrogen is a favored process gas for CGDS (see Table 7) because it can be used to spray some materials without promoting oxidation and because it is much less expensive than helium, also used [7]. The powder can be introduced into the flow either before the throat (high-pressure/upstream injection) or after the throat (low-pressure/downstream injection) of the nozzle, thus differentiating high pressure cold spray (HPCS) and low pressure cold spray (LPCS) [7]. This ultimately influences the time and temperature interaction between the particles and the gas. In HPCS, the particles interact with the high pressured gas which can increase their temperature and DE. However, HPCS requires high feeding gas pressure and is more likely to result in throat clogging [53].

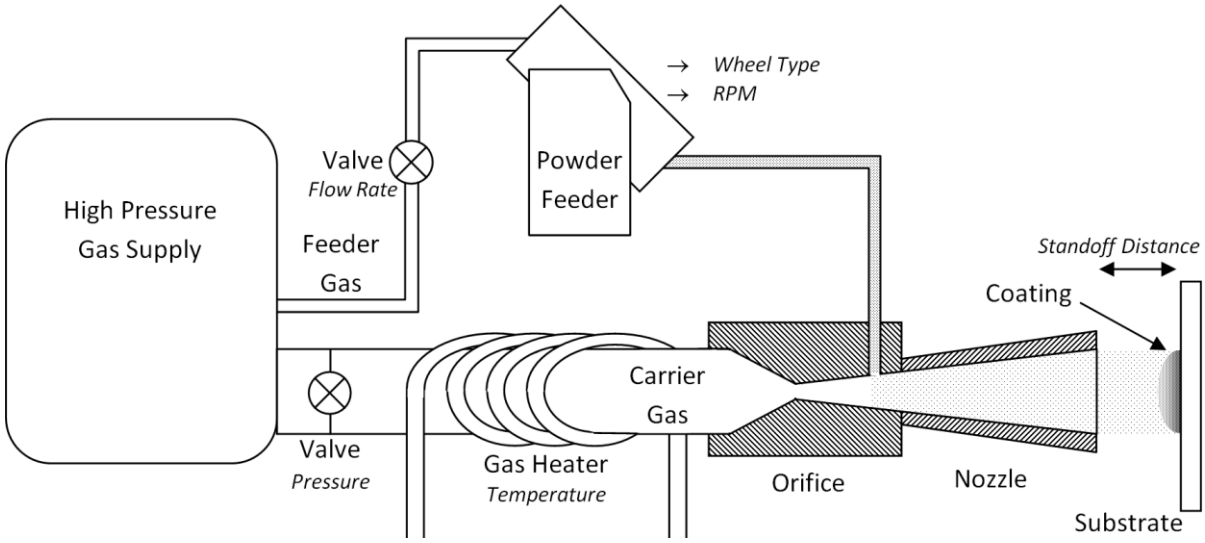

Figure 47: Schematic diagram of a cold gas dynamic spray process outline. Equipment is labelled in normal font, and variables are labelled in italic font.

2.3.4 Gas Dynamics Principles in CGDS

The deposition capabilities of CGDS reside in the high kinetic energy imparted onto the particles through the De Laval nozzle. This section briefly lists the major gas dynamics principles present in CGDS in order to explain the effect of specific parameters on the travelling particle within the converging/diverging nozzle. The equations of this subsection are not meant to be solved but rather show the effect of different parameters on the final velocity of the particle. All equations in this

section are directly from (or derived from) known fluid and gas dynamics equations, as can be found in Fox and McDonald's Introduction to Fluid Mechanics [54].

In order to successfully accelerate a particle through a De Laval nozzle, a force must be imparted onto such said particle following the relation:

$$F = ma$$

where F is the force applied on the particle, m is the mass of the particle, and a is the acceleration of the particle. In the case of CGDS, the force acting on the particle results from the drag force, which can be described by:

$$F_d = \frac{1}{2}\rho\left(V - V_p\right)^2 C_d A_p$$

where F_d is the drag force, ρ is the density of the fluid, V is the velocity of the fluid, V_p is the velocity of the particle, C_d is the drag coefficient, and A_p is the cross-sectional area of the particle. The drag force is thus dependent on all of the above mentioned parameters which change along the length of the nozzle with the possible exception of the cross-sectional area of the particle. This drag force must then be calculated over time to accurately quantify the velocity of the particle.

When dealing with supersonic flows, the Mach number is often used to describe the velocity of the flow. The Mach number is defined by:

$$M = \frac{V}{c}$$

where M is the local Mach number of the fluid and c is the local speed of sound in the fluid. Through this equation, we see that the drag force is directly dependent on the Mach number of the fluid. The speed of sound, travelling in a fluid which undergoes an isentropic evolution, depends on the fluid properties and temperature through the following equation:

$$c = \sqrt{kRT}$$

where R is the specific gas constant, T is the temperature of the fluid, and k is the heat capacity ratio of the fluid. As a result, the drag force equation becomes linked with the temperature of the fluid along with other fluid properties.

Both the local density of the fluid and the local temperature of the fluid can be characterized by the local Mach number of the fluid and their relative stagnation values through the following equations:

$$\frac{\rho_o}{\rho} = \left(1 + \frac{(k-1)}{2} M^2\right)^{\frac{1}{k-1}}$$

$$\frac{T_o}{T} = 1 + \frac{(k-1)}{2} M^2$$

where ρ_o is the stagnation density and T_o is the stagnation temperature. Through these equations, the local density and temperature of the fluid can be defined from the stagnation values, local Mach number, and heat capacity ratio. The first equation indicates that an increasing the stagnation density will result in an increase in the local density which will increase drag force. The second equation shows that an increase in the stagnation temperature will increase the speed of sound and therefore increase drag force.

The density of fluids is most often altered by changing the pressure. If the fluid acts as an ideal gas at stagnation conditions, the stagnation density can be related to the stagnation pressure through the perfect gas law:

$$P_o = \rho_o R T_o$$

where P_o is the stagnation pressure. As such, increasing the stagnation pressure increases the gas density, which increases the drag force. However, this equation highlights a trade-off where an increase of stagnation temperature may decrease drag force by decreasing the density of the fluid. By combining all of these equations and with some light algebraic manipulation, an equation for drag force can be shown as,

$$F_d = \frac{1}{2}\frac{P_o}{RT_o\left(1+\frac{(k-1)}{2}M^2\right)^{\frac{1}{k-1}}}\left(\sqrt{kR\frac{T_o}{1+\frac{(k-1)}{2}M^2}}-V_p\right)^2 C_d A_p$$

This equation clearly highlights major parameters and their relationship to the drag force of a flow from a fluid dynamics standpoint [55]. Many parameters from this equation represent fluid or particle properties that remain more or less constant. However, the stagnation pressure and the stagnation temperature represent two of the most important variable parameters with respect to CGDS. The local Mach number of the flow is predetermined by the local nozzle geometry. The most important nozzle geometric factor is the area ratio of the nozzle which is characterized as the local area of a nozzle at any point within the nozzle with respect to the area of the throat of the nozzle. The area ratio determines the local Mach number regardless of other parameters through the following equation,

$$\frac{A}{A^*} = \frac{1}{M}\left[\left(\frac{2}{k+1}\right)\left(1+\frac{(k-1)}{2}M\right)\right]^{\frac{k+1}{2(k-1)}}$$

where A is the nozzle area and A^* is the throat area. Although the nozzle length has no effect on the local Mach number, it dictates the length of time the particles are exposed to the flow.

Besides describing the acceleration of the particle, gas dynamics can also oversee the trends in gas consumption with respect to the stagnation pressure and the stagnation temperature with the equation,

$$\dot{m} = \frac{A^* P_o}{\sqrt{T_o}}\sqrt{\frac{k}{R}}\left(\frac{k+1}{2}\right)^{-\frac{k+1}{2(k-1)}}$$

where $\dot{m}$ is the mass flow rate of gas. In light of this equation, increasing stagnation pressure and decreasing stagnation temperature will increase mass flow rate, which may influence operational cost in CGDS.

2.3.5 Effects of CGDS Parameters

In addition to stagnation pressure and stagnation temperature, there are a number of other CGDS parameters that can affect deposition results. Past literature has quantified, for the most part, the effects of each parameter. To start, the traverse velocity (TV) of the nozzle with respect to the substrate is known to have an effect on the substrate temperature. Lowering the TV increases the local heat concentration during deposition. Both substrate and coating temperature can affect the DE and the coating quality during the deformation process for both particle and substrate take part in the deformation process [56]. The powder feed rate (PFR) is another important CGDS parameter which must be set. A positive correlation exists between the PFR and the DR [57]. However, the DE does not display a clear correlation with the PFR. The deposition efficiency (DE) represents the percentage (usually by mass) of particles that deposit on the substrate over the total number of particles sprayed. This differs from the deposition rate (DR) where the mass change is calculated over time. It was also reported that increasing the PFR beyond a certain limit can result in poor coating quality [57]. The powder feeder gas flow is a CGDS parameter that has not seen much experimental tinkering. As a result, the effects of this gas on the flow are not well known, but are assumed to be minimal. However, it is recognized that only a minor quantity of carrier gas is required in order to fluidize the powder and carry it to the nozzle further ascertaining its minimalistic impact. The standoff distance (SOD) is a CGDS parameter that must remain within a certain range to effectively deposit particles on a substrate. Once the particles exit the nozzle, they tend to decelerate before reaching the substrate [58]. This is especially important when dealing with light materials that quickly change momentum with little force. This deceleration is predominantly caused by a high pressure region formed directly above the substrate. This region, known as the bow shock, forms when the gas jet impinges on the substrate. The bow shock effect can be reduced by increasing the SOD [58]. However, this also increases the distance and time that the particles must travel to reach the substrate which can effectively slow them down. Figure 48 presents an image of a bow shock produced by an impinging gas jet. Figure 48 also depicts oblique shock waves at the nozzle exit. These shock waves are produced in over-expanded gas flows to equalize the pressure of the gas and the ambient atmosphere. These shock waves may also affect the particles velocities.

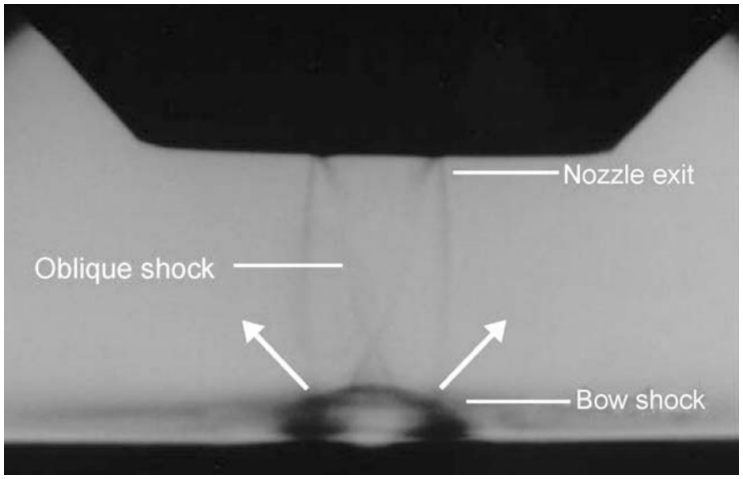

Figure 48: Image of impinging gas jet showing bow shock and oblique shock waves [58].

2.3.6 Bonding Mechanism

The bonding mechanism between the particles and the substrate as well as themselves in kinetic spray was not well understood in early development stages [7]. However, a large quantity of research has been performed to better understand the bonding mechanisms present in CGDS. Currently, a complete understanding of the bonding mechanism in CS is still under investigation. The bonding mechanism between metals and polymers remains even more ambiguous. However, for the time being, it is assumed that adhesion emanates from a combination of mechanical and metallurgical bonding [7]–[9], [11], [16], [19], [23], [24], [27], [59].

In CGDS, particles are given large quantities of kinetic energy when accelerated in the supersonic flow. Upon impact, this energy must be converted into other forms to maintain energy conservation. As such, the majority of the energy (approximately 90%) is transferred into thermal energy. Given that the impact occurs in a very short period of time (10^5 s^{-1} to 10^8 s^{-1}), thermal energy remains localized to the largely strained areas. Typically, the locally heated areas undergo varying degrees of deformation. This phenomenon is known as adiabatic shear instability [11], [59]–[62]. Figure 49 shows a computational model highlighting this high shear area. Figure 49 also provides an SEM image of a titanium particle impact where material has been ejected from the shear instability zone.

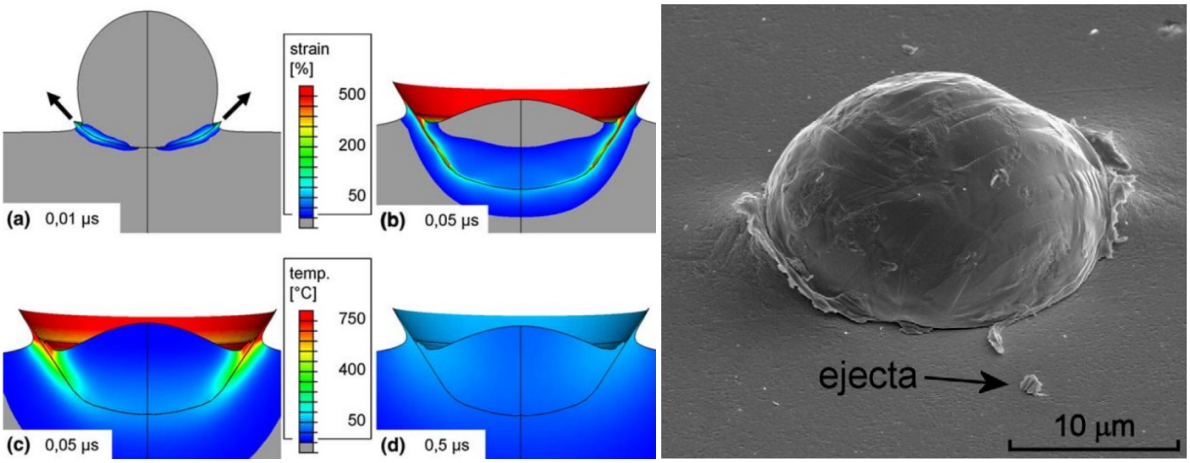

Figure 49: Computational model of 25 µm Cu particle impacts on a Cu substrate at 500 m/s with an initial temperature of 20°C (left). (a, b) Strain field and (c, d) temperature field at specific times after impact [61]. Titanium particle impact on titanium substrate showing ejected material from impact (right) [63].

In metal to metal impact, metallurgical bonding can arise depending on the materials, temperature, time, and force of impact [59], [64]. During the adiabatic shear instability, the protective oxide layer is thought to break or dissolve due to the flow of material caused by the high impact and heat. The cleaned interface allows metallic atomic structures to press into intimate contact with one another under momentarily high interfacial pressures and temperatures which results in metallurgical bonding (in a similar way than cold welding) [7].

Mechanical bonding is mostly due to intertwining deformations creating anchoring points throughout the coating. Appreciable intertwining requires both substrate and impacting particles to deform [64], [65]. The fact that attempts to deposit brittle or hard materials, such as ceramics, have not been successful unless they are co-deposited with a ductile matrix material further substantiates the importance of this type of bonding. Grit blasting is the process most often used to increase mechanical bonding in CS [66], [67]. However, other novel surface preparation techniques such as pulsed waterjet have also proven to be affective [67]. These processes are thought to increase the adhesion strength by increasing the surface roughness of the substrate which creates favorable anchoring features [66], [67].

2.3.6.1 Residual Stress

Unlike most other thermal spray processes, CGDS has a relatively low cooling rate mainly due to its low operating temperature. High cooling rates found in other thermal spray processes induce tensile stresses which are detrimental for fatigue behavior [68]. Coatings created through CGDS result in a residual compressive state which results from the impinging high velocity particles at low temperatures. Compressive residual stresses are beneficial for bonding and prevents crack propagation [67], [69]. However, it is important to note that as the coating thickness increases, the substrate progressively compensates in a tensile manner. This makes the resulting compressive residual stress at the interface, near the substrate, gradually decrease which lower adhesion of the coating [68].

2.3.7 Critical Velocity Concept

In order to achieve deposition and bonding during CGDS, a certain velocity threshold must be reached. This is often referred to as the critical velocity and has been the subject of many studies [11], [59], [70]–[74]. Equations are often developed through semi-empirical and numerical models; however they usually only focus on the powder properties and neglect the substrate entirely. Research has shown that below the critical velocity, only abrasion of the substrate will occur. Above this critical velocity, initial particles will deposit on the substrate. In order for subsequent particles to adhere to previously deposited particles, a different velocity may be required. In other words, since the deposition occurs on the coated material instead of the substrate, a different critical velocity will be put into effect. Increasing the particle velocity beyond a certain limit may remove previously deposited particles and cause erosion of the substrate. This is known as the erosion velocity [52], [58], [71]. The particle velocity impacts a variety of factors including the DE [64], [75]–[77]. Figure 50 illustrates how the DE changes with respect to the particle velocity.

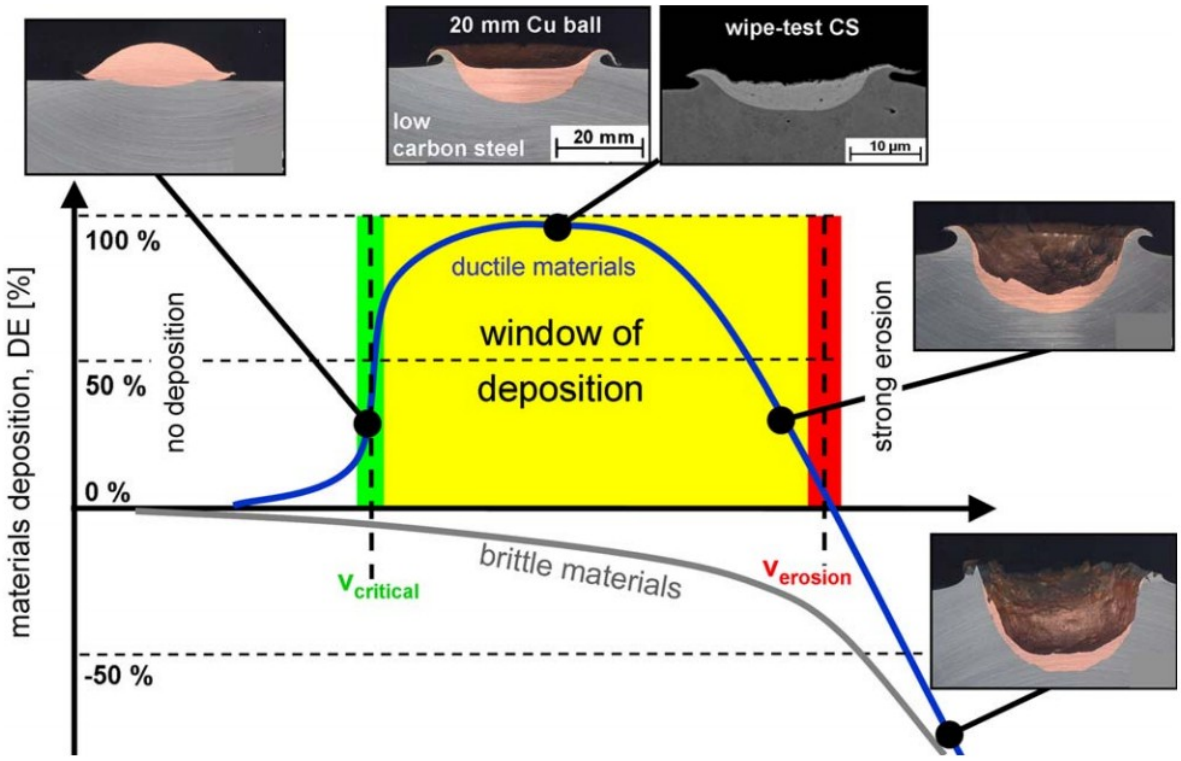

Figure 50: Schematic correlation between particle velocity, deposition efficiency (DE) and impact effects for a constant impact temperature.

Both the critical velocity and the erosion velocity decrease when the particle impact temperature is increased (see Figure 51). At high temperatures, the particles require less energy to deform which explains the drop in critical velocity. Figure 51 demonstrates that a no deposition zone forms above the erosion velocity as the particle impact temperature is increased. It is believed that this no deposition zone forms when soft particles hit a hard substrate. Further increasing the particle impact velocity will result in erosion of the substrate. The area between the critical velocity and the erosion velocity represents the window of sprayability. It is within this window that the particle impact conditions favor particle deposition and a coating can be formed.

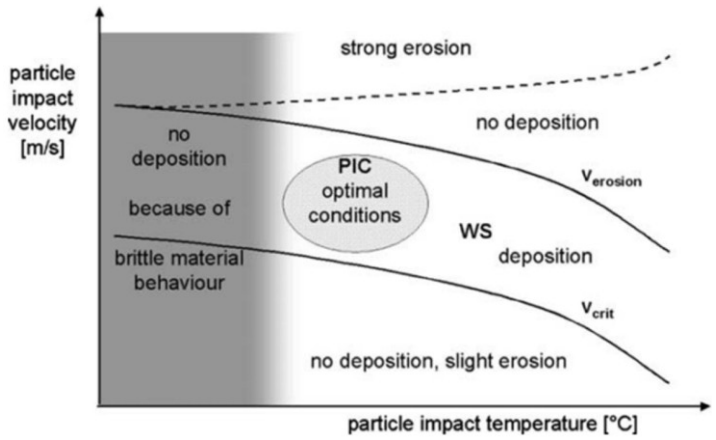

Figure 51: Window of sprayability of particle velocity vs. particle impacting temperature [71].

2.3.8 Advantages of CGDS

The main advantage of using CGDS to metalize PMCs is its large scale manufacturing potential. CGDS can deposit large quantities of material in an on-site type location making it ideal for repairs. When compared to other types of thermal spray, CGDS's low operating temperatures can avoid substrate degradation and oxidation. Furthermore, low variations in temperatures will minimize stresses induced by shrinkage and/or expansion [7].

2.4 Taguchi Method

The Taguchi method is a statistical method developed by Genichi Taguchi that aims to improve the quality of products with minimal experimentation [78]. The Taguchi method does this by testing pairs of combinations instead of testing them individually which saves time and resources. The following subsections describe the specific steps involved in the application of the Taguchi method.

2.4.1 Taguchi Experimental Design

The first step to design the Taguchi experiment is to select the objectives (output variables) to be optimized. Each objective either has a specific target value or is simply maximized or minimized. This is known as the performance characteristics [78], [79]. The next step is to determine the parameters (input variables) affecting output variables and to choose the levels of these parameters. The levels refers to the number of set values each parameter may be varied. The

subsequent step is to select a proper orthogonal array [79]. The selection process is based on the number of parameters as well as the levels of variation for each parameter. The array indicates the number of experiments and specified the conditions (level) of all parameters for each experiment. Orthogonal arrays can either be found in literature or mathematically using an algorithm developed by Taguchi [78], [79]. Figure 52 presents an example of an orthogonal array with four parameters each containing three levels. During the execution of the experiments, it is important to randomize the trials in order to minimize the systematic error [79].

Experiment	P1	P2	P3	P4
1	1	1	1	1
2	1	2	2	2
3	1	3	3	3
4	2	1	2	3
5	2	2	3	1
6	2	3	1	2
7	3	1	3	2
8	3	2	1	3
9	3	3	2	1

Figure 52: Orthogonal array indicating the variation level (1, 2, 3) of each parameter (P1, P2, P3, P4) to be used for a given experiment [78].

2.4.2 Taguchi Analysis

Once the necessary observations are made, the analysis of the results is done using a signal-to-noise ratio (SN). The SN ratio is a logarithmic function that represents the inverse of variance [78]. By selecting the largest SN ratio, the variability of the process is minimized. In other words, uncontrollable factors (noise) are reduced. The calculation of the SN ratio varies depending on the performance characteristic. When minimizing the performance characteristic the following equation is used [78].

$$SN_i = -10 \log \left(\sum_{u=1}^{N_i} \frac{y_u^2}{N_i} \right)$$

Where y_u is the value of the performance characteristic for a specific trial number (u), N_i is the total number of trials for a given experiment (i). When maximizing the performance characteristic the following equation is used [78].

$$SN_i = -10 \log\left(\frac{1}{N_i}\sum_{u=1}^{N_i}\frac{1}{y_u^2}\right)$$

When the performance characteristic has a specific target value, the following equation is used [78].

$$SN_i = 10 \log\left(\frac{\left(\frac{1}{N_i}\sum_{u=1}^{N_i} y_u\right)^2}{\left(\frac{1}{N_i - 1}\sum_{u=1}^{N_i} y_u - \bar{y}_i\right)^2}\right)$$

Where $\bar{y}_i$ is the mean value of the performance characteristic for a given experiment. The number of trials can vary depending on the objective. Once the SN ratio is calculated for each experiment, the average SN ratio is calculated for each level of a specific parameter. For example, the SN ratio of experiment 1, 6, and 8 would be used to calculate the average SN ratio for level 1 of the third parameter (P3) according to the following equation (see Figure 53) [78].

$$SN_{P3,level1} = \frac{(SN_1 + SN_6 + SN_8)}{3}$$

Experiment Number	P1	P2	P3	P4	SN
1	1	1	1	1	SN1
2	1	2	2	2	SN2
3	1	3	3	3	SN3
4	2	1	2	3	SN4
5	2	2	3	1	SN5
6	2	3	1	2	SN6
7	3	1	3	2	SN7
8	3	2	1	3	SN8
9	3	3	2	1	SN9

Figure 53: Orthogonal array highlighting the SN ratios that correspond to the same level for parameter 3 (P3) [78].

High SN ratios indicate superior performance characteristics for all parameters. By applying the proper performance characteristic equation (target value, minimizing, or maximizing) the data will be manipulated in such a way that high SN ratios will always indicate the optimal process parameters. After tabulating the SN ratio of each parameter and level, the range (R) is calculated for

each parameter (see Figure 54). The range is the difference between the highest and lowest SN ratio. The R values represent the effectiveness of each parameter. Parameters with larger R values have a larger impact on the process outcome.

Level	P1	P2	P3	P4
1	$SN_{P1,level1}$	$SN_{P2,level1}$	$SN_{P3,level1}$	$SN_{P4,level1}$
2	$SN_{P1,level2}$	$SN_{P2,level2}$	$SN_{P3,level2}$	$SN_{P4,level2}$
3	$SN_{P1,level3}$	$SN_{P2,level3}$	$SN_{P3,level3}$	$SN_{P4,level3}$
Range	R_{P1}	R_{P2}	R_{P3}	R_{P4}

Figure 54: Tabulated SN ratio for each level and parameter with accompanying R values (modified from [78]).

3 Research Objectives

The goal of this thesis is to produce a conductive coating on a BMS 8-276 composite produced by Toray Composites (America) Inc., as selected by the Boeing Company for the fuselage of the 787 [12], using commercially available CGDS technology and feedstock powders. The conductive coating should not exceed 254µm (10thou) in thickness and meet various other requirements set by industry. Metallization of BMS 8-276 divided into two phases. The first is a feasibility and coating development phase where commercial powder is selected, spray parameters are optimized, and the best substrate surface preparation is determined. The second phase entails characterising the metalized BMS 8-276 on an electrical, corrosion, and adhesion standpoint.

3.1 Feasibility and Coating Development

Given the relatively small quantity of published research, CGDS parameters to successfully deposit any metallic coating onto BMS 8-276 were not yet established. Two different conductive materials were considered for this research: tin and copper. Tin is a very soft material and was expected to easily deform and deposit on BMS 8-276, as covered in the literature review. Copper may be more difficult to deposit but is highly conductive and already used for metallization purposes in aerospace applications. If for any reason, the copper cannot deposit onto the BMS 8-276 substrate, a bond coat will be incorporated to assure copper deposition. In addition, the BMS 8-276 is manufactured with two different types of fibre layers, a carbon-fibre laminate and a woven glass fibre layer. Both of these fibre layers are explored in this research.

3.2 Coating Evaluation

All of the coatings produced were evaluated according to the same industry standards. The metalized BMS 8-276 must first meet electrical resistivity requirements set by industry, as this is the primary objective of this research. Chemical inertness was then evaluated through a corrosion test, simulating possible aircraft weathering conditions. Testing also took place to determine the adhesion strength of the coating to the BMS 8-276 and the cause of failure was evaluated. Lastly, tests were performed specifically on the tin coated BMS 8-276 to evaluate if an allotropic transformation would take place and to demonstrate the versatility of the CGDS procedure used.

3.2.1 Electrical Resistivity

One of the most important parameter to consider is the conductivity of the metalized BMS 8-276. The electrical resistivity were measured with a four point probe resistivity sensor (identical to industry) connected to a digital multimeter. The electrical resistivity must comply with BAC5056 (a Boeing Company process specification). This industry standard for metalized structural plastic parts was one of the most well suited standard for this type of application. According to BAC5056, the electrical resistance must not exceed 1.3 milliohm for a 175 µm thick coating (Type I), 0.8 milliohm for a 267 µm thick coating (Type II), and 0.5 milliohm for a 305 µm thick coating (Type III).

3.2.2 Corrosion

The metalized BMS 8-276 samples must also tolerate similar environmental conditions typically seen by aircraft. If applied to aircraft, the conductive coating could be possibly covered by a protective finishing layer such as a primer, paint, and/or epoxy; however, this was not a guarantee. As discussed in section 1.1, even the thickness of the finishing paint can affect the performance of the lightning protection system. In addition, wear and accidental scuffs could expose the conductive coating and/or underlying BMS 8-276. A neutral salt fog test (ASTM B117) was used to test the samples similarly as in industry [80]. Salt fog testing is a popular method often utilized to test corrosion resistance of surface coatings. In this test, samples were placed in a corrosive spray chamber for a certain period of time. A piece of bulk copper was also placed along with the metalized BMS 8-276 samples and visual inspection provided a comparative evaluation. The metalized BMS 8-276 samples were considered acceptable if they perform in a similar manner than the bulk copper.

3.2.3 Adhesion Strength

The adhesion strength is another vital factor in this research. Without proper adhesion, the conductive coating could delaminate and disrupt the conductive pathway. Given the originality of this research, the minimal adhesion value came from the Boeing Company standard D6-51343 which is intended for other thermal spray processes. The testing process was done using a Pneumatic Adhesion Tensile Testing Instrument (PATTI) further described in Chapter 4.

3.2.4 Additional Tests

As a coating possibly applied to an aircraft, the material needed to endure long periods of varying temperatures. At high altitudes, the atmospheric temperature can drop to -50°C. As a result, the deposited tin coated BMS8-276 was specifically tested with respect to the possibility of an allotropic transformation. Samples were places in refrigerators at a variety of temperatures for a total of 3000 hours. A tin coating was also applied to a curved CFRP to demonstrate the versatility of the CGDS process.

4 Experimental Research Approach

4.1 Feedstock Powder Characterization

A variety of powders were selected to deposit or to help deposit a conductive coating on the BMS 8-276. This included a tin powder (SST-S6001) from Centerline (Windsor) Ltd., two copper powders: one from Praxair (IN, USA) (Cu-159) and one from Centerline (Windsor) Ltd. (SST-C5003), and a PEEK powder from Victrex (UK) (PEEK 150PF).

4.1.1 Centerline Pure Tin (SST-S6001)

The tin powder for this project was SST-S6001 from Centerline (Windsor) Ltd. This powder was specifically produced for CS applications and primarily used for corrosion protection and electrical conduction. Tin has a very low melting point of 231.9°C and a thermal expansion coefficient of 22.0µm/m K^{-1}. This spherically shaped powder had a particle size distribution of 5 µm to 45 µm and a purity of at least 99.7wt% according to the supplier. A chemical composition analysis of the ingot used for this powder was completed by the manufacturer (See Table 8).

Table 8: Chemical Composition Analysis of SST-S6001 Ingot

Chemical	Percentage in Weight (wt%)
As	0.01-0.02
Pb	0.042
Bi	0.03
Cu	0.023-0.033
Sb	0.009-0.015
Ni	0.002-0.004
Co	0.002
Fe	0.006
Ag	<0.001
Sn	Bal (>99.85)

From Figure 55 we see that there were a considerable number of small (<5 µm) particles (known as satellites) and some particles were irregularly shaped. These manufacturing discrepancies could have caused inconsistencies during deposition.

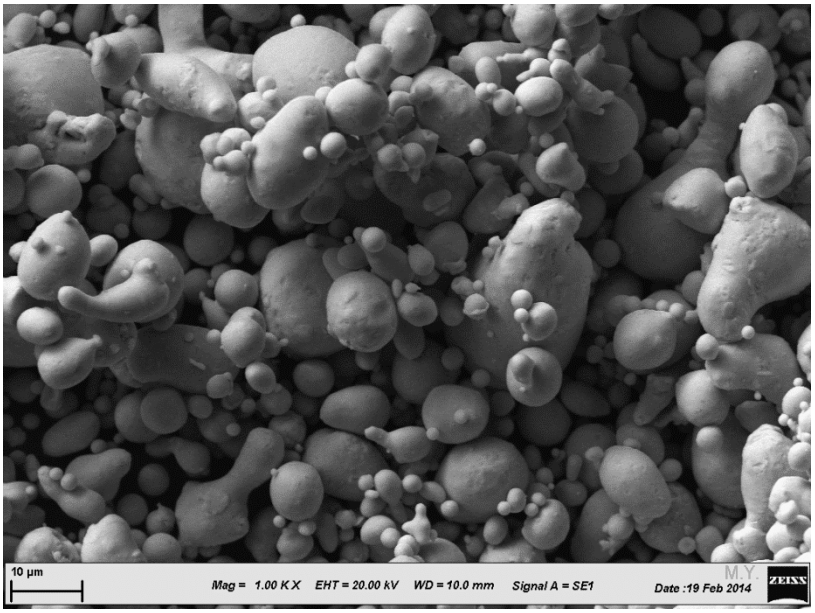

Figure 55: SEM image of tin powder (SST-S6001).

4.1.2 Praxair Surface Technologies Pure Copper (Cu-159)

One of the copper powders selected for this project was Cu-159 from Praxair (IN, USA). This powder had a more or less spherical shape which is a characteristic typically seen in gas atomization production process (see Figure 56). According to a Microtrac analysis, the powder had an average particle diameter (d90) of 20 µm and a particle size distribution where 1% of the total particles were smaller than 5.5 µm and 1% were above 31.1 µm. Cu-159 had a composition of at least 99.0wt% copper and a maximum of 0.10wt% of oxygen. High oxygen content indicates the degree of oxides which is known to increase hardness and lower DE [81].

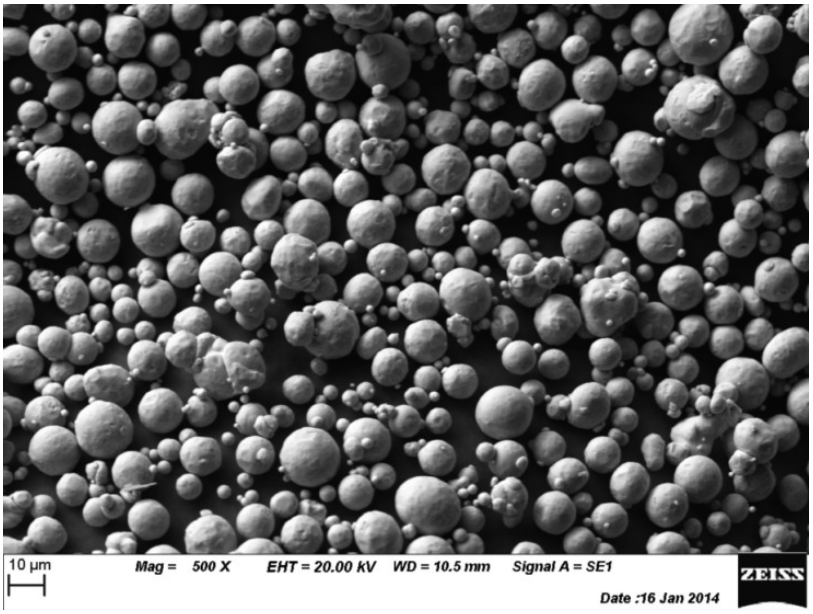

Figure 56: SEM image of copper powder from Praxair (Cu-159).

4.1.3 Centerline Pure Copper (SST-C5003)

The other copper powder selected for this project was SST-C5003 from Centerline (Windsor) Ltd. This commercially pure copper powder is known for its use in CS applications that require high electrical conductivity, antimicrobial surface, or thermal management. The melting temperature of copper is 1085°C and its thermal expansion coefficient is 16.6 µm/m K^{-1}. This powder was irregularly shaped by a manufacturing process called electrolytic forming which according to the manufacturer, maximized spray velocity and increased the density of the coating produced (see Figure 57). This powder had a particle size distribution of 5 µm to 45 µm and a purity of at least 99.7wt%. The distributor stated that the density of the powder was 2.07g/cm^3 whereas bulk copper has a density of 8.94g/cm^3 [41].

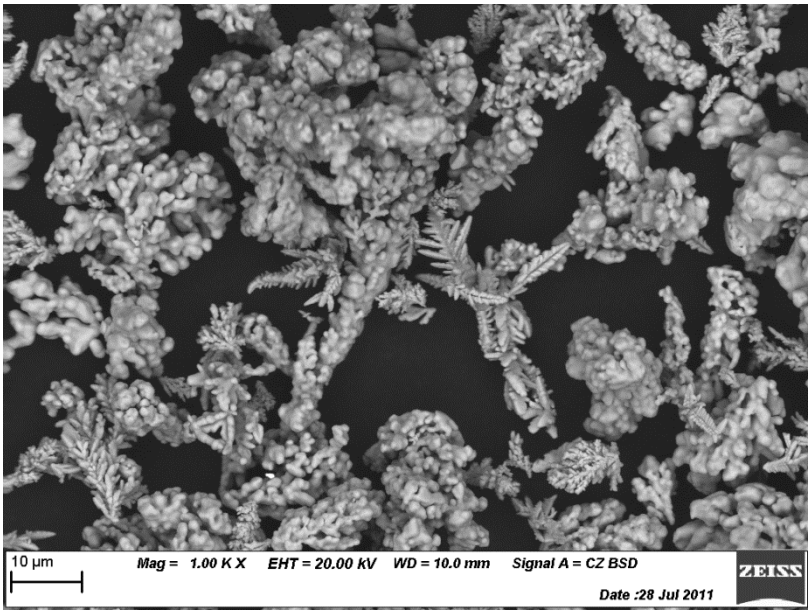

Figure 57: SEM image of copper powder from Centerline (SST-C5003).

4.1.4 Victrex PolyEtherEtherKetone (PEEK 150PF)

This PEEK powder was selected as bond coat material. PEEK 150PF is a semi-crystalline thermoplastic fine powder material produced by Victrex (UK). The average particle size was 50 µm with a maximum of 150 µm (see Figure 58). According to the manufacturer, its melting and glass transition (T_g) temperatures are 343°C and 143°C respectively and the material density is 1.30g/cm^3. The thermal expansion coefficient of PEEK is roughly 65 µm/m K^{-1} above T_g and 25 µm/m K^{-1} below T_g. PEEK is also known to have excellent wear resistance and is commonly used in thermal spray processes because of its high temperature resistance [9], [82]. Experiments conducted by Dr. Mohammed Yandouzi, a fellow colleague at the University of Ottawa, prior to this study indicated enticing results regarding the use of this material as a bonding agent (see Appendix I: Dr. Mohammed Yandouzi's Work on Bond Coat Development). PEEK has excellent mechanical and chemical resistance properties that are retained to high temperatures. Thermoplastics were much more appealing for this type of application since they only required heat to be reshaped as desired. Deformation is of utmost importance for CS. In addition, PEEK is already utilized in certain aerospace applications [83].

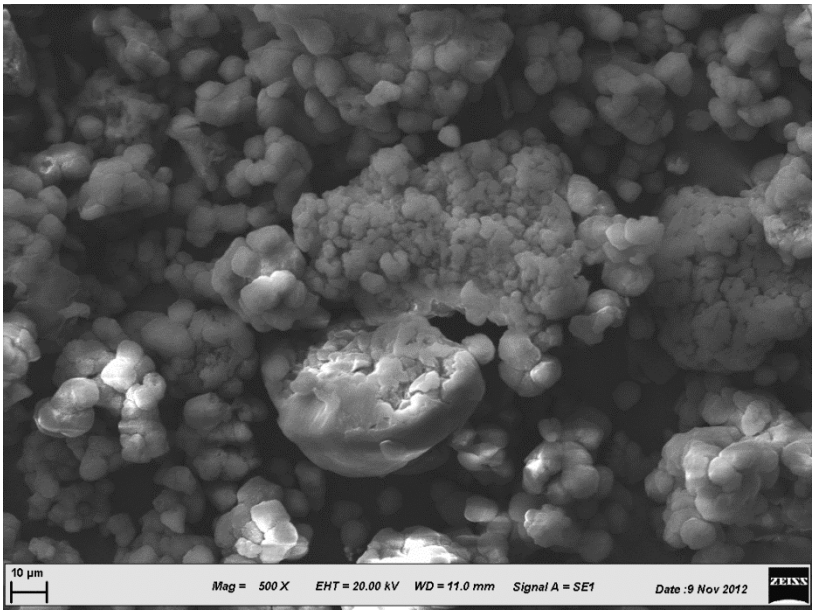

Figure 58: SEM Image of PEEK powder from Victrex (PEEK 150PF).

4.2 Powder Preparation

For some particular experiments, certain powders were modified or manipulated using specific equipment.

4.2.1 Sieving

A sieve from W. S. Tyler (model RX-29) was used to separate PEEK powder from Victrex (PEEK 150PF) into three distinct size ranges of 0-45 µm, 45-75 µm, and 75-150 µm. The sieve itself is contained within a sound enclosure (R-30050) also produced by W. S. Tyler as shown in Figure 59.

Figure 59: RX-29 sieve for W. S. Tyler.

4.2.2 Milling

Copper and PEEK powder were milled together using a Pulverisette 7 planetary mill from Fritsch (see Figure 60a). Powder was placed into two separate 80 mL grinding bowls containing 20 balls each (see Figure 60b). A weight ratio of 20:1 was maintained between the powder and the balls. The milling was done for 16 minutes under argon to prevent unwanted reactions from happening. A rotational speed of 500 rpm (52 rad/s) was set with a direction reversal every 2 minutes.

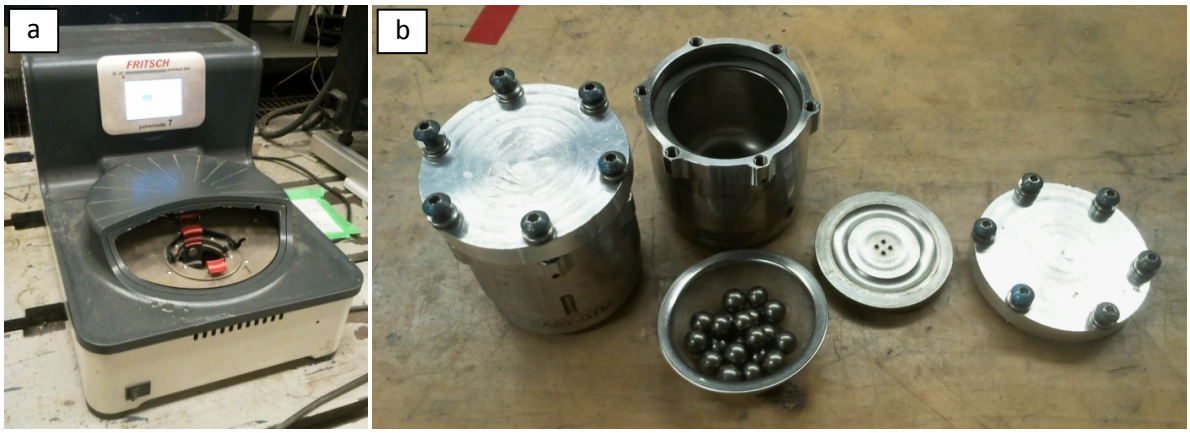

Figure 60: (a) Pulverisette 7 planetary mill from Fritsch and (b) 80 mL grinding bowls with balls.

4.3 Substrate

4.3.1 Toray Composites (America) Inc. BMS8-276

Toray Composites America Inc. (Tacoma, Wash.) produce BMS8-276, a composite used by the Boeing Company for the 787 [1], [12], [14]. This material was received in 4" X 6" (10.16 cm X 15.24 cm) plates roughly 1/4" (6.35 mm) in thickness. These plates were cut into more manageable sizes of 2" X 1.5" (5.1cm X 3.8 cm) using a band saw. The BMS 8-276 plates were composed of continuous laminated carbon fibres plies (LCFP) within an epoxy matrix. The fibre orientation alternated between plies and a heterogeneous system of particles separated each ply. BMS 8-276 also possessed a woven glass fibre ply (WGFP) on the very top of the CFRE. The carbon fibres were 7 µm in diameter while the glass fibres were slightly smaller (see Figure 61). The thermal expansion coefficient of the BMS 8-276 was said to be 1.4 µm/m K^{-1}. A heat experiment outlined in Appendix II places the degradation temperature of the BMS 8-276 below 500°C.

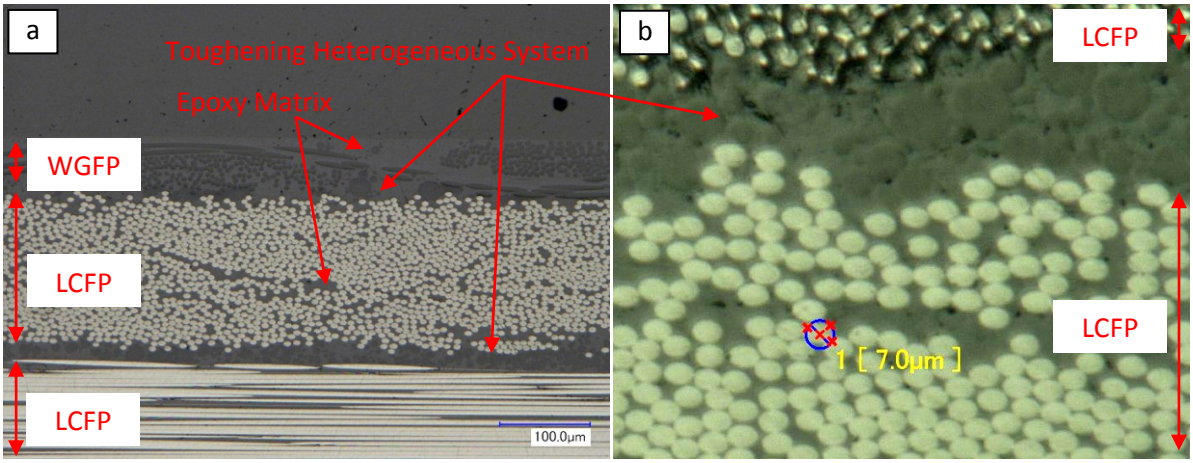

Figure 61: (a) Overview of the BMS 8-276 composite structure with (b) zoom on toughening heterogeneous system.

4.3.2 Composite Manufacturing

The BMS 8-276 was only provided in flat plates. In order to demonstrate the application potential of the CS process, an attempt to deposit conductive coatings was done on curved CFRP. Unfortunately, the composites produced were not a perfect match to the BMS 8-276 material but served as a comparable material. Simon's research places the degradation temperature of this composite near

400°C [29]. Both a convex and a concave composite surface were manufactured using the following steps.

4.3.2.1 Mould Production

An appropriate mould was made to produce curved CFRP. A steel block measuring 100 mm X 38 mm X 30 mm was used as a mould. Wire electric discharge machining (EDM) was used to cut the rectangular block. The EDM machine used an electric current fed through a wire to locally heat material in order to cut it (see Figure 62).

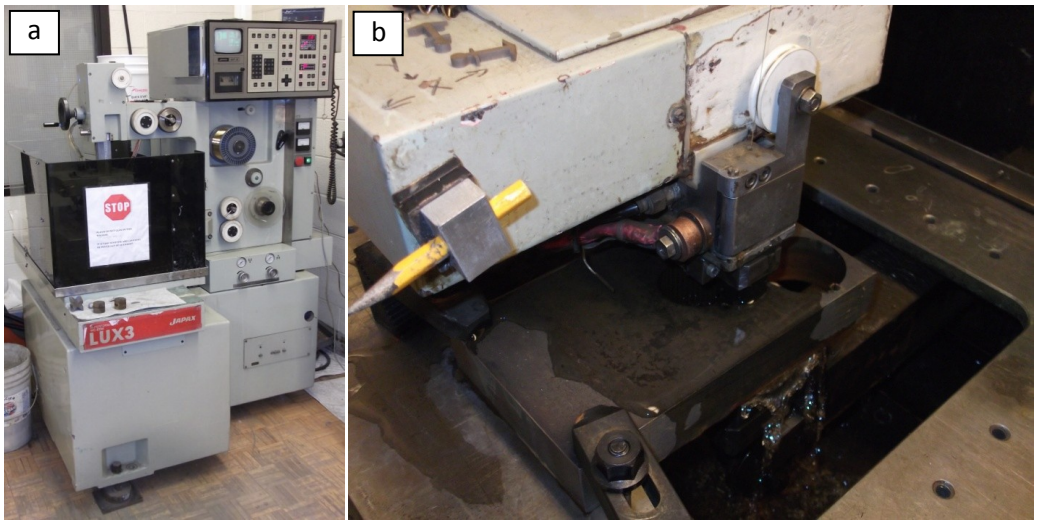

Figure 62: (a) Wire EDM automated machine with (b) close-up of wire cutting process.

The narrow cut generated by the automated EDM was programmed to produce a shape with varying curvatures. The two curved moulds produced from the single rectangular block are depicted in Figure 63.

Figure 63: Concave and convex curved moulds.

4.3.2.2 CFRP Production and Vacuum Bagging

To produce the CFRP, low cure temperature and high toughness carbon/epoxy prepreg (SE-70 from Gurit Ltd.) layers were used. The prepreg layers were cut to an appropriate size to fit the curved mould. Each ply was composed of unidirectional carbon fibres embedded in an epoxy matrix. To produce the desired composite thickness, twelve plies were stacked as illustrated in Figure 64. Six plies with perpendicular fibre directions were pressed to one another in an alternating manner. Manual compaction was done with a roller to ensure that air bubbles were not entrapped between the plies and ensured a good adhesion. Two stacks of six plies were then pressed together with the middle plies in the same fibre orientation (in a mirror like fashion). The symmetry within the stack prevented bending and warping of the composite during the curing phase.

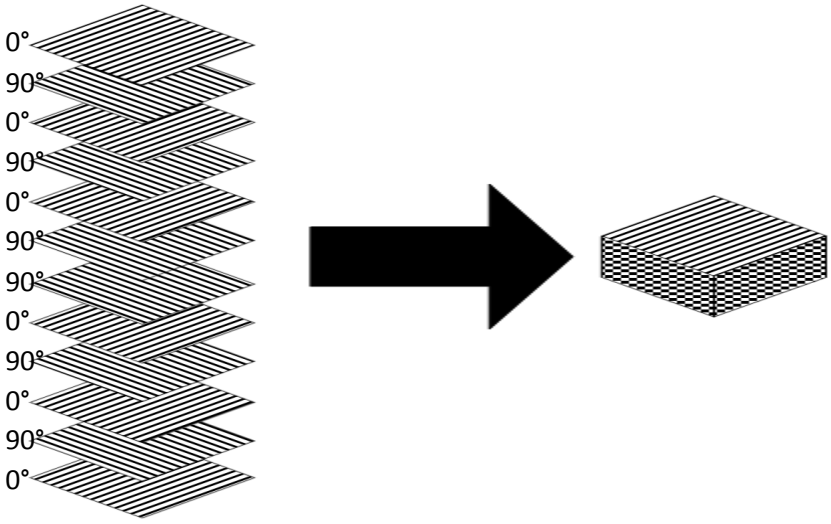

Figure 64: Stacking process for CFRP depicting prepreg stacking plies mid plane symmetry and compacted prepreg stack.

The next step was to cure the prepreg stack using the curved moulds and an aluminum plate. Both moulds were covered with a protective release film (polymer lining sheet) which prevented the stack of twelve plies from adhering to them. The aluminum plate was also lined with this protective release film in the event that excess epoxy would drip to the plate. In addition, the composite was covered with a perforated film and bleeder material. Both layers combined permitted air to flow out of the bag (Dahlar release bag 125 from Airtech International) and prevented the flow of impurities that could damage the diaphragm vacuum pump (DAA-V715A-EB from Gast). As seen in Figure 65, the whole configuration was covered by a film held by high temperature sealant tape (SM 5126 Tacky Tape from Schnee-Morehead Inc.).

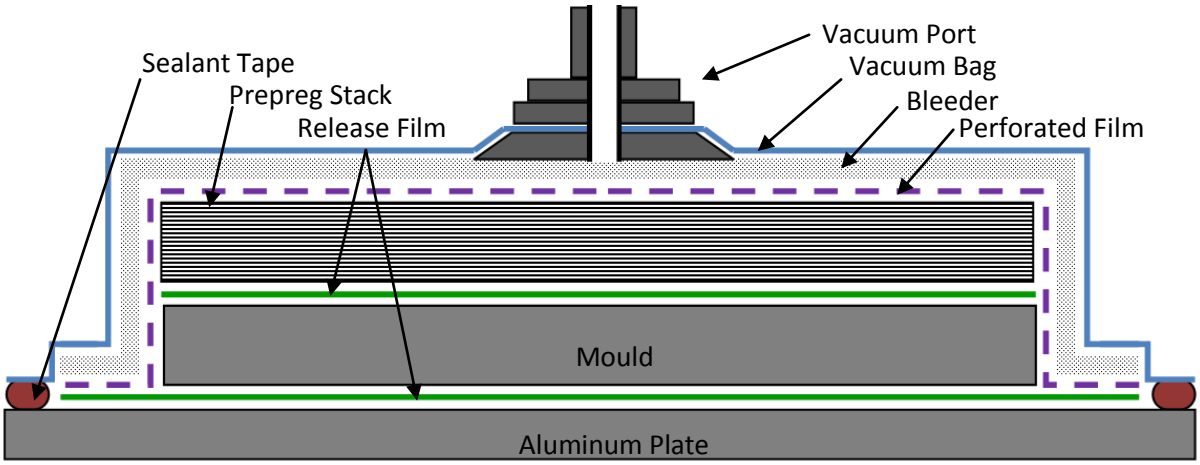

Figure 65: Vacuum bagging method for manufacturing CFRP - Adapted from [29].

A valve connected the vacuum pump (see Figure 66) to the bag in order to remove all excess air within the setup.

Figure 66: Gast DAA-V715A-EB diaphragm vacuum pump.

4.3.2.3 Curing

An oven (PF120 from Carbolite Inc.) was used to reach the CFRP curing temperature (see Figure 67). The prepreg stack with moulds were heated at a rate of 2°C per minute until a dwell temperature of 120°C was reached. The temperature was then kept constant for 1 hour and finally ramped down at a rate of 5°C per minute until room temperature was reached.

Figure 67: Carbolite PF120 curing oven.

Once cured, the curved CFRP were removed from the moulds. Excess epoxy that had flowed to the edges of the curved CFRP was trimmed (see Figure 68).

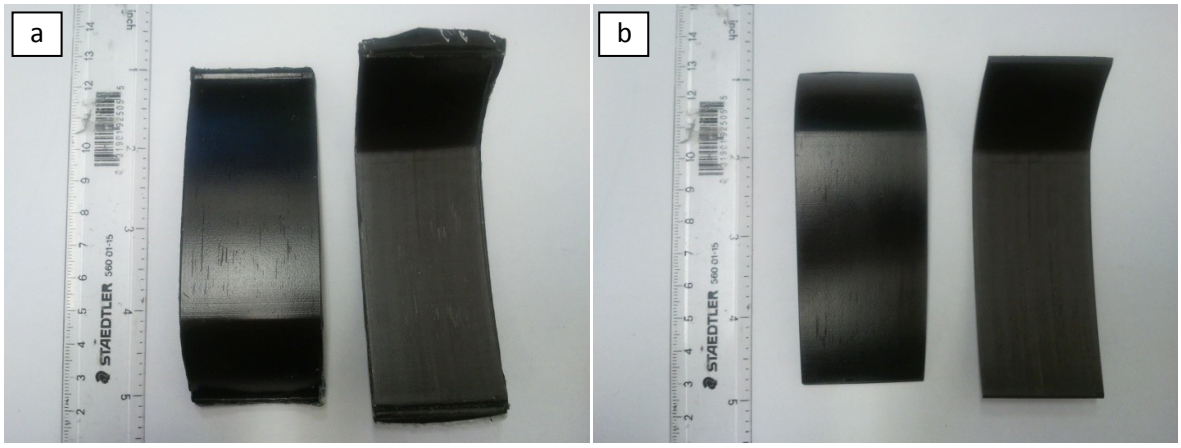

Figure 68: Curved CFRP substrates produced (a) with excess epoxy and (b) trimmed.

4.4 Surface Preparation

The BMS 8-276 substrates were always received with a single WGFP as the top layer. In order to expose other plies (including LCFP) or create a desired surface roughness, a variety of preparation techniques were developed.

4.4.1 Grinding

A grinding technique was utilized to erode a given ply of the BMS 8-276 in order to expose the subjacent ply. Given that the BMS 8-276 was composed of flat laminar plies, a planar abrasive medium had to be used to only expose a single ply (<200 µm). A 220 grit sand paper was mounted to the rotating base of a polishing machine (TegraPol-31, TegraForce-5, and TegraDoser-5 from Struers). This machine is further described in section 4.7.1. The substrate was manually held in place while the sand paper rotated at a constant angular velocity of 250 rpm (26.2 rad/s). The end result was very smooth surface finish. Using mechanical restraints (such as a vise) caused the substrate to bend which complicated the matter of exposing a single ply. Water was introduced into the process to prevent the BMS 8-276 from over-heating (which lead to peeling) and to prevent dust from becoming airborne. Substrates were visually inspected regularly throughout the process to verify that the grinding process remained roughly perpendicular to the ply orientation. If a second ply was accidentally exposed, adjustments were made and grinding process continued into subjacent plies. Figure 69 presents both a BMS 8-276 sample with a WGFP exposed and a single LCFP exposed. (see Appendix II for other attempts to expose a single LCFP)

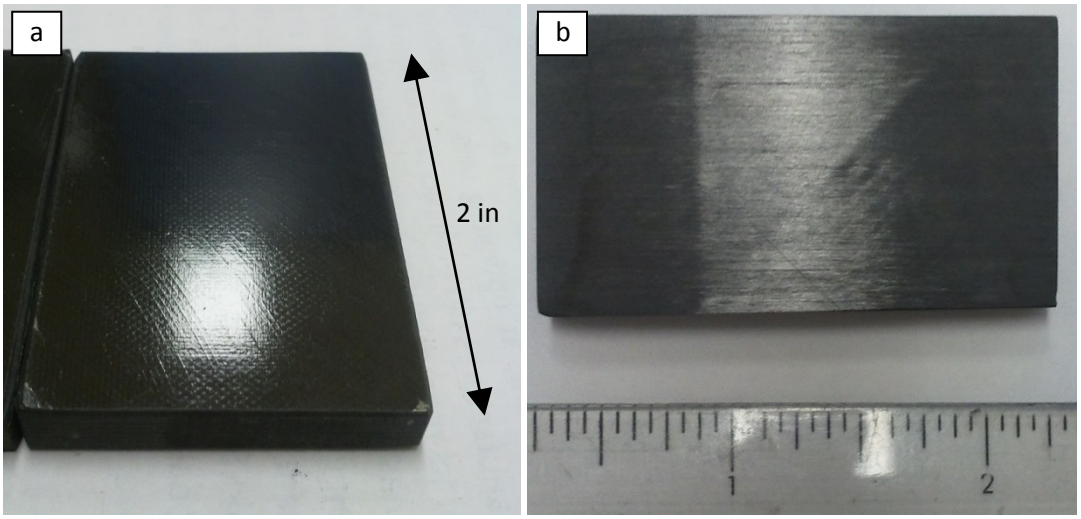

Figure 69: BMS 8-276 substrate with (a) a WGFP exposed and (b) a single LCFP exposed.

4.4.2 Grit Blasting

If required, a grit blasting procedure was performed on the BMS 8-276 substrates to create a desired surface roughness. The grit blasting unit (by Power Fist) was comprised of a hand held,

gravity fed gun with a 13/64” (5.2 mm) I.D. steel nozzle within a confined cabinet (Princess Auto SKU: 8140709) (see Figure 70). The grit blasting unit used nitrogen as the process gas. A bottle of compressed nitrogen was connected to the unit. The blasting pressure was controlled using a pressure regulator fitted with the necessary gauges. For this study, all blasting was done at an angle of approximately 45° with a SOD of roughly 2" (5 cm). On average, 250 mL of grit was required to grit blast a 2" X 1.5" (5.1 cm X 3.8 cm) BMS 8-276 sample. Over grit blasting caused severe erosion of the BMS 8-276 sample and was able to easily erode through an entire ply. Once grit blasted, the samples were cleaned with water and blown with compressed air.

Figure 70: Grit blasting unit.

Four different types of abrasives were used in this study. The largest abrasive was a 20 grit (1.000 mm) ferrosilicate called "Ebonygrit" from Opta Minerals Inc. The smallest abrasive was an 80 grit (0.180 mm) aluminum oxide also from Opta Minerals Inc. A 36 grit (0.500 mm) and a 25 grit (0.710 mm) abrasives respectively called "Garnet Grit" and "Steel Grit" were also used in this study. A short comparative summary of the abrasives used in this study is presented in Table 9.

Table 9: Properties and Purchasing Information of Abrasives Used for Grit Blasting

Abrasive Type	*Ferrosilicate*	*Aluminum Oxide*	*Garnet*	*Steel*
Size (grit / mm)	20 / 1.000	80 / 0.180	36 / 0.500	25 / 0.710
Hardness (Mohs)	7	9	8 to 9	8 to 9
Manufacturer	Opta Minerals Inc.	Opta Minerals Inc.		
Distributer	Princess Auto	Princess Auto	McMaster-Carr	McMaster-Carr
SKU	8200594	8200578	8072T41	3165K51

4.4.2.1 "Ebonygrit" Abrasive (20 Grit)

The "Ebonygrit" abrasive was an insoluble grit commonly used for the removal of light rust, paint, and mill scale according to the manufacturer (Opta Minerals Inc.). Figure 71 presents images of the morphology of the abrasive medium.

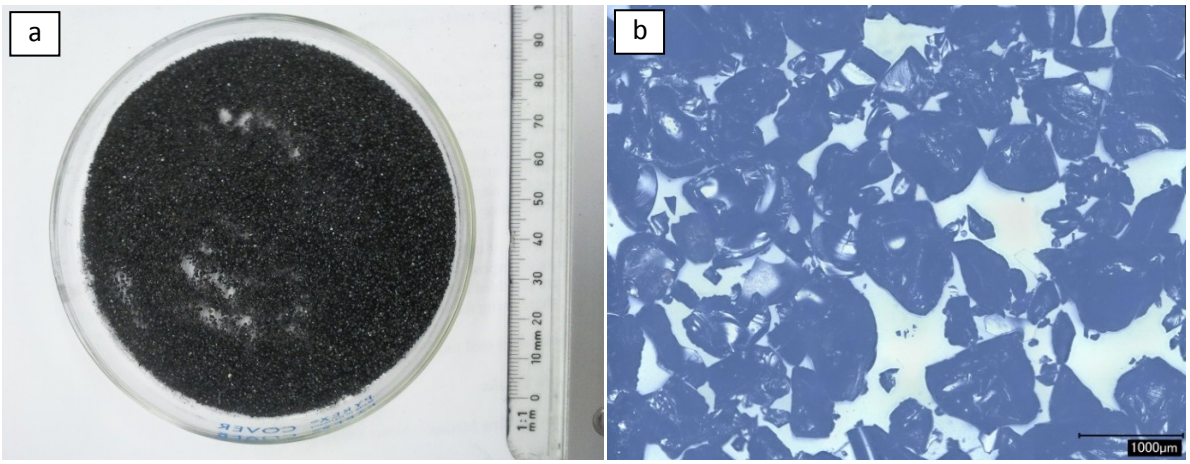

Figure 71: (a) Image of "Ebonygrit" abrasive (20 grit) with (b) high magnification zoom.

The black abrasive was mainly composed of iron oxide and silicon dioxide, formed when molten slag was quenched in cold water (see Table 10).

Table 10: Material Composition of the "Ebonygrit" Abrasive (20 grit) according to the manufacturer (Opta Minerals Inc.)

Components	Percentage (wt%)
Fe_2O_3	53 to 60
SiO_2	32 to 37
Al_2O_3	3 to 6
CaO	1 to 3
MgO	1 to 2
Zn	<1

4.4.2.2 Aluminum Oxide Abrasive (80 Grit)

The aluminum abrasive was an insoluble grit commonly used for cleaning, deburring, etching, and finishing applications according to the manufacturer (Opta Minerals Inc.). Figure 72 presents images of the morphology of the abrasive medium.

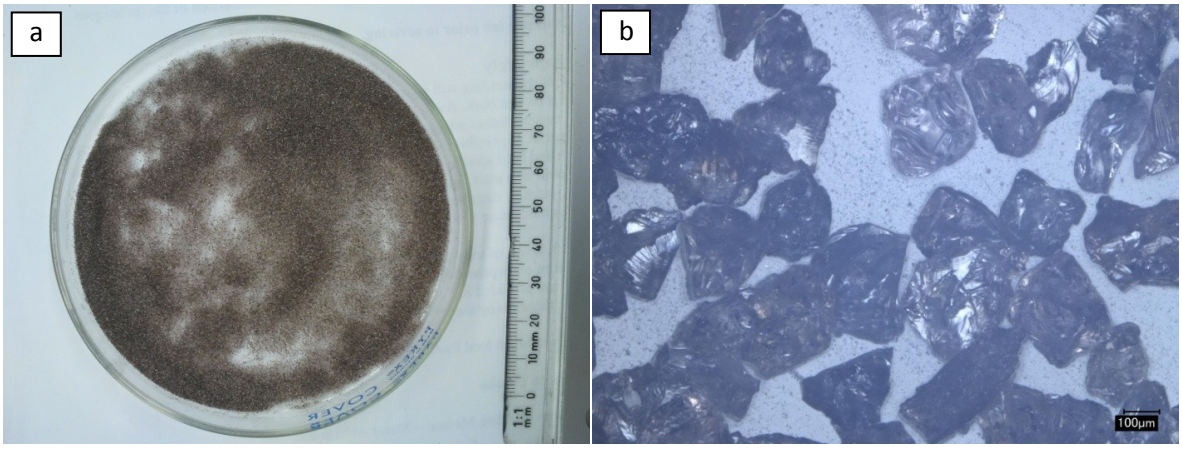

Figure 72: (a) Image of aluminum oxide abrasive (80 grit) with (b) high magnification zoom.

The brown abrasive was produced by fusing bauxite and anthracite in an electric arc furnace at high temperature. The composition of this abrasive material is specified in Table 11.

Table 11: Material Composition of the Aluminum Oxide Abrasive (80 grit) according to the manufacturer (Opta Minerals Inc.)

Components	Percentage (wt%)
Al_2O_3	92.0 to 96.5
TiO_2	1.0 to 4.0
Fe_2O_3	0.1 to 1.5
SiO_2	0.15
Other	<1.0

4.4.2.3 "Garnet Grit" Abrasive (36 Grit)

The "Garnet" abrasive was a semi-precious stone derived from mined Almandite and Andradite mineral deposits. Its natural physical properties made it a safe and effective abrasive for a variety of applications. Figure 73 presents images of the morphology of the abrasive medium.

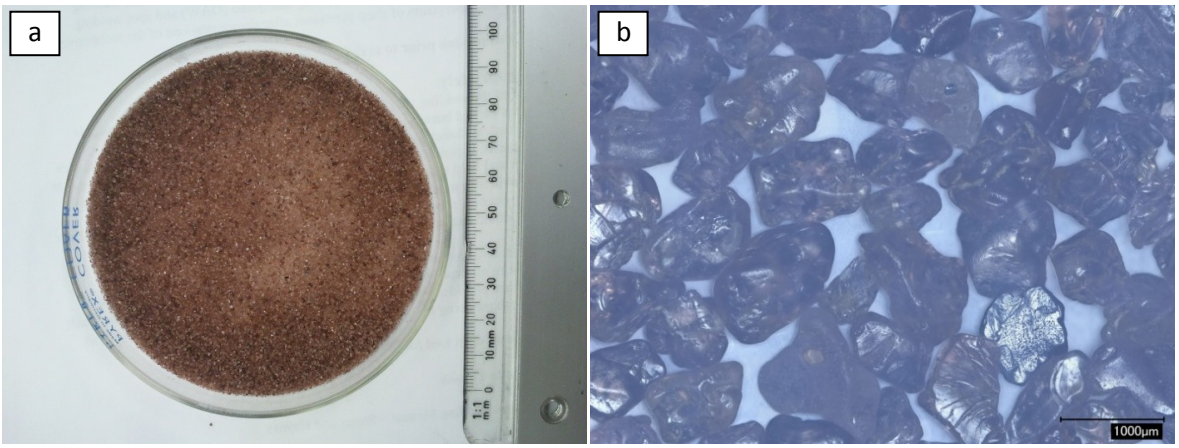

Figure 73: (a) Image of "Garnet Grit" abrasive (36 grit) with (b) high magnification zoom.

4.4.2.4 "Steel Grit" Abrasive (25 Grit)

The steel abrasive was specifically tailored to leave a textured surface to enhance the bonding ability of paint and other coatings. Figure 74 presents images of the morphology of the abrasive medium.

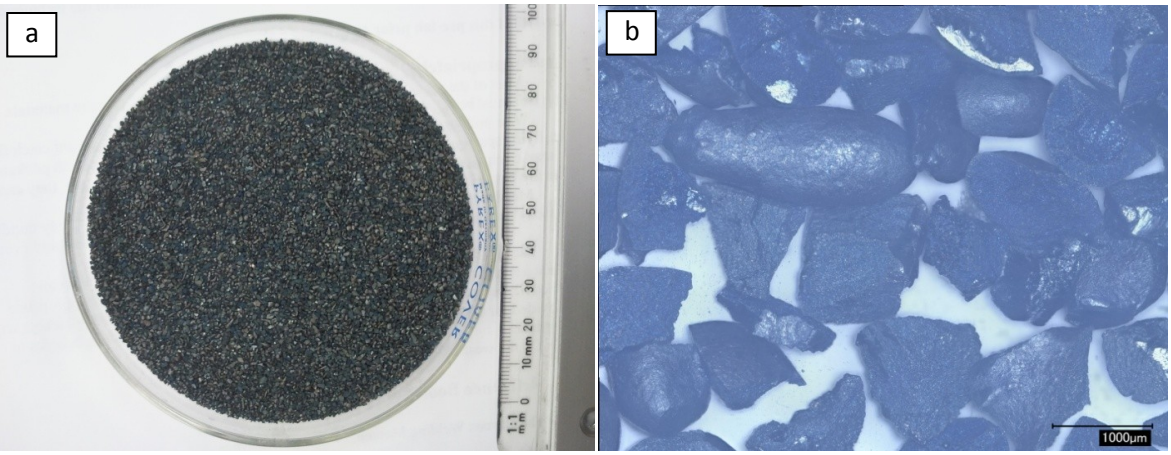

Figure 74: (a) Image of "Steel Grit" abrasive (25 grit) with (b) high magnification zoom.

4.5 CGDS Equipment

A commercially available CGDS system from Centerline (Windsor) Ltd. was used to produce all the conductive coatings on the CFRP substrates, as requested by The Boeing Company. The Centerline SST LPCS system (SST-P) included a gas heater, a control cabinet, an orifice and accompanying nozzle, an automated spray gun traverse system, powder feeder, a spray chamber, and a gas delivery system.

4.5.1 Heater

The commercial SST-P system included a 4.3 kW heater which was used to quickly increase the temperature of the gas flow to the desired value. The gas heater, shown in Figure 75, was designed to achieve a maximal gas temperature of 500°C for a gas flow with a maximum gas pressure of 250 psi (1.72 MPa).

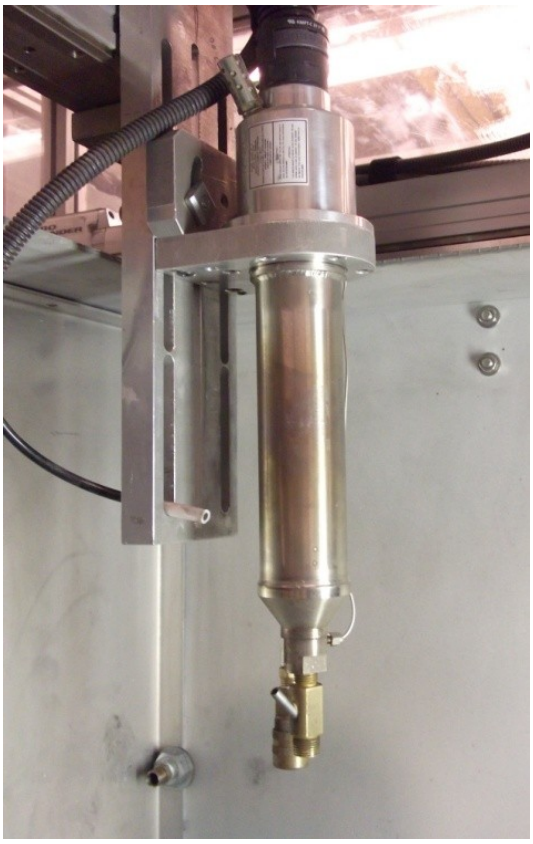

Figure 75:Gas heater from Centerline (Windsor) Ltd.

4.5.2 Controls

The SST-P system from Centerline (Windsor) Ltd. also consisted of a cabinet which controlled certain spray parameters of the spray gun (see Figure 76). The control cabinet contained a touch screen panel which was used to regulate the gas temperature amongst other functions. A valve on the side of the cabinet controlled the gas pressure. Both pressure and temperature were regularly calibrated using Centerline (Windsor) Ltd. approved equipment.

Figure 76: Control cabinet from Centerline (Windsor) Ltd.

4.5.3 Orifice and Nozzle

The nozzle was connected to the heater by the orifice. The supersonic flow created by the throat is contained within the orifice. The divergent stainless steel nozzle is held in place on the brass orifice by a tightening nut and a tungsten carbide throat insert (known as a collet). Another nut is used at the opposite end of the orifice to fix the assembly directly to the heater (see Figure 77).

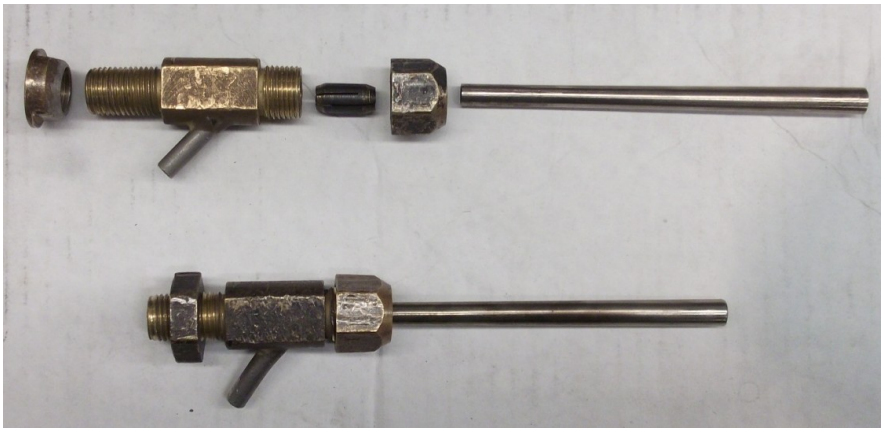

Figure 77: Disassembled and Assembled De Laval nozzle showing (from left to right): heater nut, brass orifice, collet, tightening nut, and stainless steel nozzle.

The throat size of the orifice used in this study was 2 mm in diameter. Centerline (Windsor) Ltd also offered 2.5 mm throat size orifices in addition to the 2 mm throat size orifices. The smaller diameter was chosen over the larger one in order to reach full temperature and pressure without exceeding the 4.3 kW limit of the heater. The orifice also had a 45° inlet to allow fluidized powder to enter the gas flow. This inlet was located after the throat making the process LPCS.

4.5.4 Spray Gun Traverse System

The spray gun (heater with nozzle assembly) was mounted on an automated X-Y traverse system from IAI America Incorporated (see Figure 78). The X-Y plane spatial displacement was enabled by slider type actuators. This system was capable of velocities between 1 mm/s and 500 mm/s, with step sizes as little as 1 mm between passes. This unit was controlled through commercial software provided by IAI.

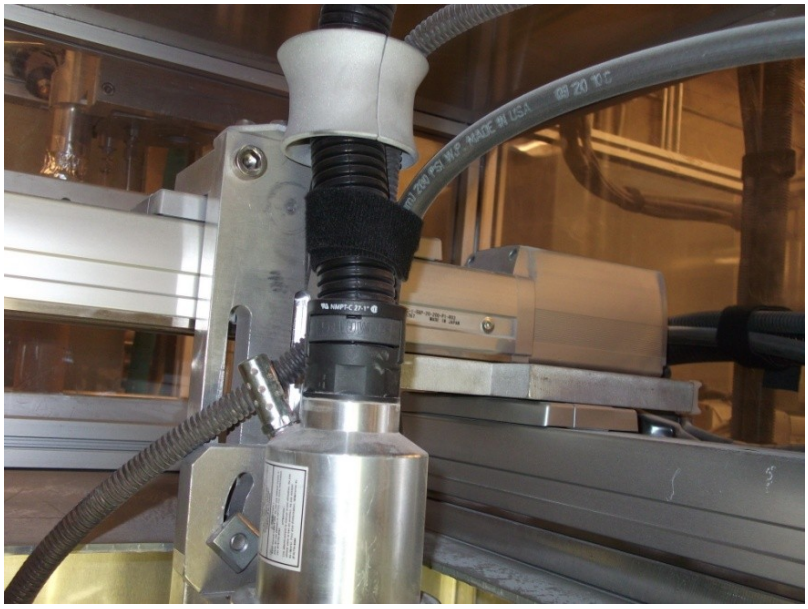

Figure 78: Automated X-Y traverse system from IAI America Incorporated.

4.5.5 Powder Feeding Equipment

Powder was fluidized and fed into the high velocity gas flow through the orifice with the help of a powder feeder. The powder feeder used in this research was the commercially available Model 1264 powder feeder from Praxair Surface Technologies (Concord, NH, USA) presented in Figure 79.

Figure 79:Praxair powder feeder (Model 1264).

A specific quantity of powder was loaded into the canister. The lid was then closed and sealed from the external atmosphere. The canister was then pressurised with inert nitrogen gas which creates a flow in a feed line that connected the powder feeder to the orifice. A rotating disk within the canister delivered the powder to the pressurized flow. Small holes in the wheel trapped a set quantity of powder when travelling through the canister. The powder filled holes were subsequently aligned with the carrier gas stream which fluidized the powder and emptied the holes of the wheel in a perpetual manner.

The flow rate of the powder was determined by the rotational velocity of the wheel and the size/frequency of the holes. The powder morphology also affected the flowability through the holes. The powder feeder was equipped with a hammer which assisted in the completion of filling and unloading powder in the wheel holes. The hammer tapped the wheel as the disk rotated which helped the fluidity of particles that may have tendency to clog (see Figure 80).

Figure 80: Assembled view of feeding wheel in canister with hammer.

Two different wheels were used in this research: a 240 medium hole (1.75mm) and a 320 small hole (1.4mm) wheel (see Figure 81).

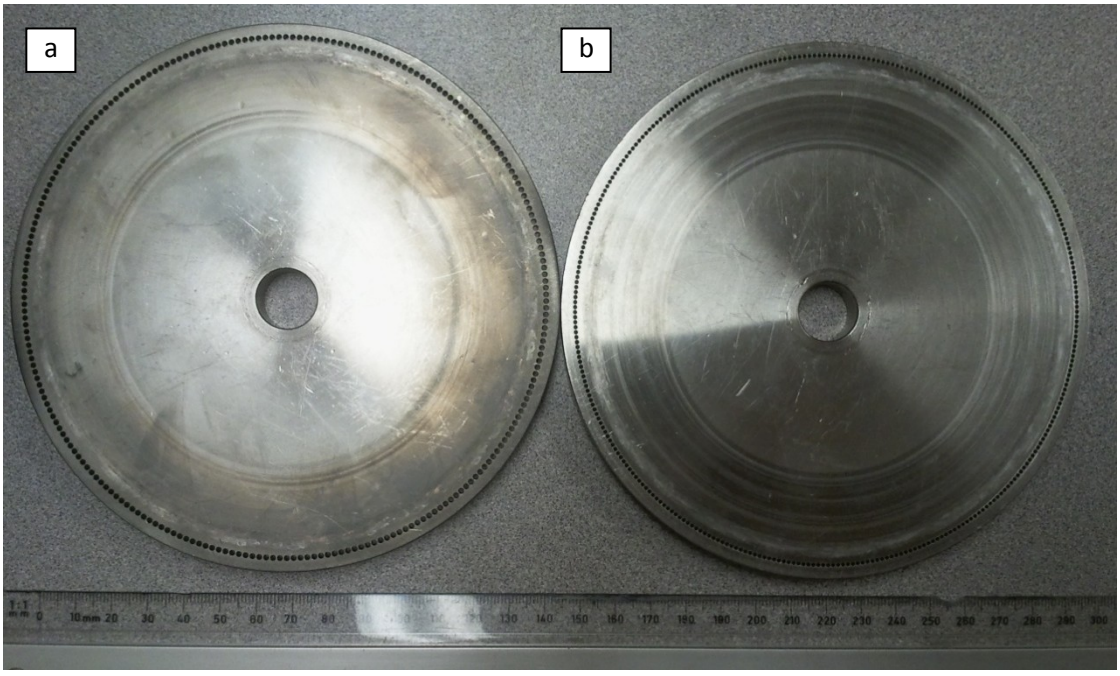

Figure 81: (a) Medium hole (240) and (b) small hole (320) powder feeder wheel.

4.5.6 Spray Chamber

The CGDS gun and deposition zone was contained within a chamber. A ventilation system pulled the air and non-deposited powders through a water filtration system followed by a HEPA filtration step. The water filter safely trapped all remaining powders that did not adhere to the substrate. This spray chamber was custom built by Centerline (Windsor) Ltd (see Figure 82).

Figure 82: Centerline (Windsor) Ltd custom built spray chamber.

4.5.7 Gas Delivery System

The nitrogen reservoir consisted of a bottle pack of 11 cylinders connected to an inlet in the control cabinet (see Figure 83). Each cylinder was filled with commercially pure nitrogen gas pressurized at approximately 18MPa. Gas from the supply line was also routed in the powder feeding system where a flow meter was used to adjust the volumetric flow of nitrogen through the powder feeder.

Figure 83: Nitrogen bottle reservoir (bottle pack).

4.6 Taguchi Method Setup

This technique was used to efficiently optimize secondary spray parameters of the composite bond coat in section 5.2.5. Specific values and parameters were applied to this technique in order to observe their effect on objectives of interest. The output variables selected were the thickness, resistivity, adhesion, and porosity of the bond coat. The performance characteristics of the thickness, resistivity, and porosity were minimized while performance characteristic of the adhesion was maximized. The proper SN ratio equations (specified in section 2.4.2) were applied for each output. The four parameters selected to optimize the composite bond coat were the surface finish, the bond coat composition, the TV coupled with the PFR, and the SOD. Three levels were chosen for each parameter of the bond coat optimization (see Table 12). The orthogonal array presented in Figure 52 was followed resulting in 9 experiments. By following this array, each parameter level is pre-established for each experiment.

Table 12: Levels of Each Parameter of the Taguchi Optimization for the Composite Bond Coat

Level	*Parameter*			
	Surface Finish	PEEK% (wt%)	Traverse Velocity (mm/s) – Powder Feed Rate (rpm)	Standoff Distance (mm)
1	Polished	2.5	10 – 2	5
2	80 grit	5	15 – 3	10
3	20 grit	10	20 – 4	15

4.7 Analysis Equipment

Coatings produced were analyzed by observing a representative cross-section of the sample. The following subsections present the equipment and procedures used to fulfill this analysis.

4.7.1 Processing and Polishing

The sprayed samples were cut using the Secotom-10 from Struers (see Figure 84a). This automated cutting apparatus was mounted with a diamond cut-off wheel from Struers (#40000072) (see Figure 84b). A rotational speed of 2200 rpm (230 rad/s) was given to the cutting wheel and a coupon feed rate of 0.050mm/s was used to cut the metal coated BMS 8-276 samples.

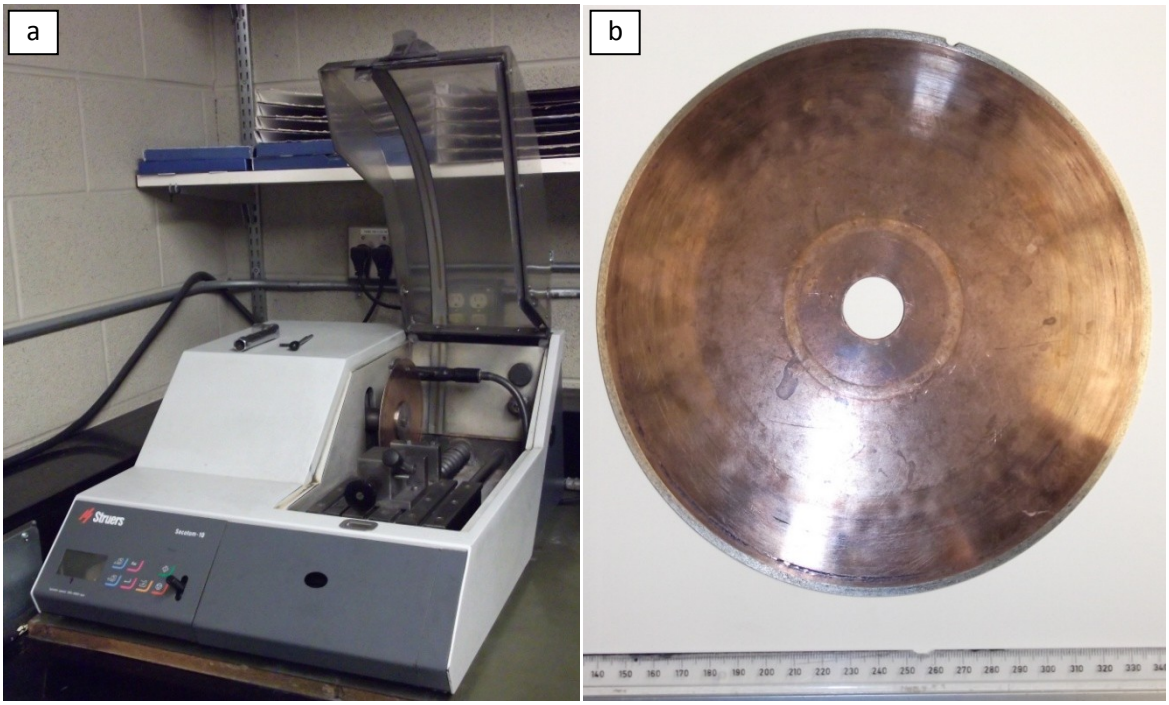

Figure 84: (a) Struers Secotom-10 cutting apparatus and (b) diamond coated metal cut-off wheel.

The appropriately cut samples were mounted in a transparent epoxy solution through a process known as cold mounting. A silicone spray (#230-19 from Anamet) was applied to the HDPE moulds to prevent the mounting material from adhering to them. An epoxy resin (#233-R from Anamet) was combined with an epoxy hardener (#233-H from Anamet) in a 9 to 1 mass ratio. Although it was specified on the containers to use a 7 to 1 ratio, this mixture resulted in accelerated curing rates which caused the mounting material to boil and turn yellow (see Figure 85). By reducing the proportion of the hardener, the resin cured in a more gradual manner and resulted in a better product.

Figure 85: Accelerated cured resin.

The cut samples were placed in the moulds and the mounting material was poured over top. The mounting samples were then placed in a glass bell vacuum chamber for 10 to 15 minutes to extract trapped air bubbles in the mounting solution (see Figure 86). The mounting samples were then placed in a well ventilated area where they cured overnight.

Figure 86: Resin filled moulds in glass bell vacuum chamber.

Mounted samples were polished using a setup including a TegraPol-31, a TegraForce-5, and a TegraDoser-5 from Struers (see Figure 87a). Up to 6 samples were polished at the same time using this setup. The sample rotational speed and direction, polishing wheel rotational speed, applied pressure, solution volumetric flow, and polishing time were all automated and set according to recommended procedures from Struers. Progressively finer polishing wheels and solutions were used to obtain a mirror finish (see Figure 87b).

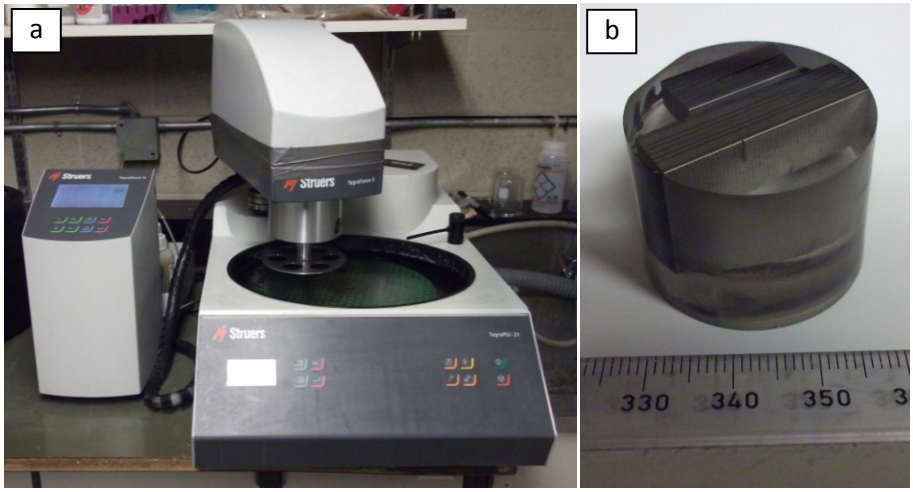

Figure 87: (a) Struers TegraPol-31 polishing machine and (b) mounted sample underwent polishing steps.

In some instances, the cold mounting procedure left bubbles within the epoxy. This often caused scratch marks to appear on the sample after being polished. Solution containing coarser particles sometimes remained within the cavities of the epoxy and re-emerged during a finer polishing step causing scratches. In such cases, an extra cleaning procedure was required between polishing steps to guarantee a mirror finish free of scratches. The samples were placed in a beaker filled with water, which was then placed in an ultrasonic vibratory bath (TS 540 transsonic bath from Elma) for 5 minutes which dislodged the polishing solution within the cavities (see Figure 88).

Figure 88: Elma TS 540 transsonic bath (ultrasonic cleaning bath).

When the samples were investigated through electron microscopy, a gold sputtering step was required. Using a Denton Vacuum Desk IV from Parker (see Figure 89), a thin layer of gold was applied to the polished sample's surface which ensured proper dissipation of any accumulated electrical charges during electron microscopy.

Figure 89: Parker Denton Vacuum Desk IV gold sputter machine.

4.7.2 Optical/Digital Imaging

Visual analysis was done using either an optical microscope (NMM-800TRF from Kingdak) or a digital microscope (VHX-2000 from Keyence) (see Figure 90). The optical microscope was equipped with a user interface software (Vision Lite105 from Clemex) which was specifically used for the composition analysis of deposited copper/PEEK bond coat images. The use of the software allowed determining area ratios through contrast differentiation. The digital microscope produced colour images of higher magnification. The digital microscope was also equipped with hardware and software (from Keyence) which allowed for three dimensional imaging. The automated vertical and horizontal moving stage combined with the automatically focusing lense created a depth perception which could then be reconstructed into a three dimensionnal image of the surface. This technique is known as "depth from defocus image reconstruction".

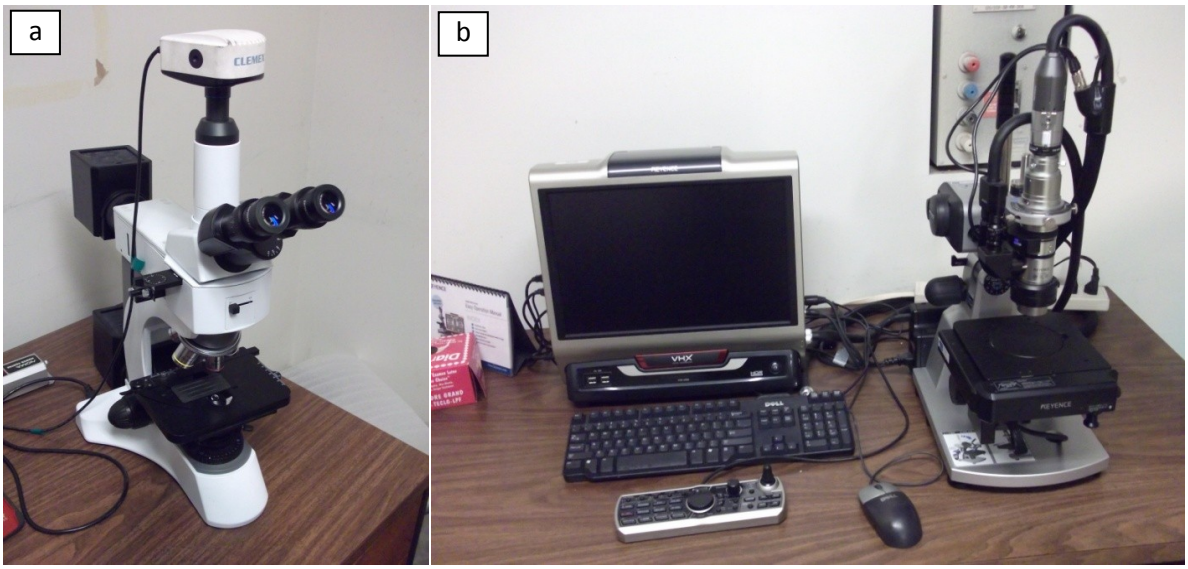

Figure 90: (a) Kingdak NMM-800TRF optical microscope and (b) Keyence VHX digital microscope.

4.7.3 Scanning Electron Microscope (SEM)

A variety of samples were analyzed using a scanning electron microscope (EVO MA10 from Zeiss) (see Figure 91). The SEM was equipped with secondary electron (SE), back-scattered electron (BSE), energy dispersive spectroscopy (EDS), electron back-scatter diffraction (EBSD), and X-ray computed tomography (CT) detectors. The SE detector was used to obtain high quality images whereas the BSE detector was used to differentiate metallic components from non-metallic ones with a high degree of certainty.

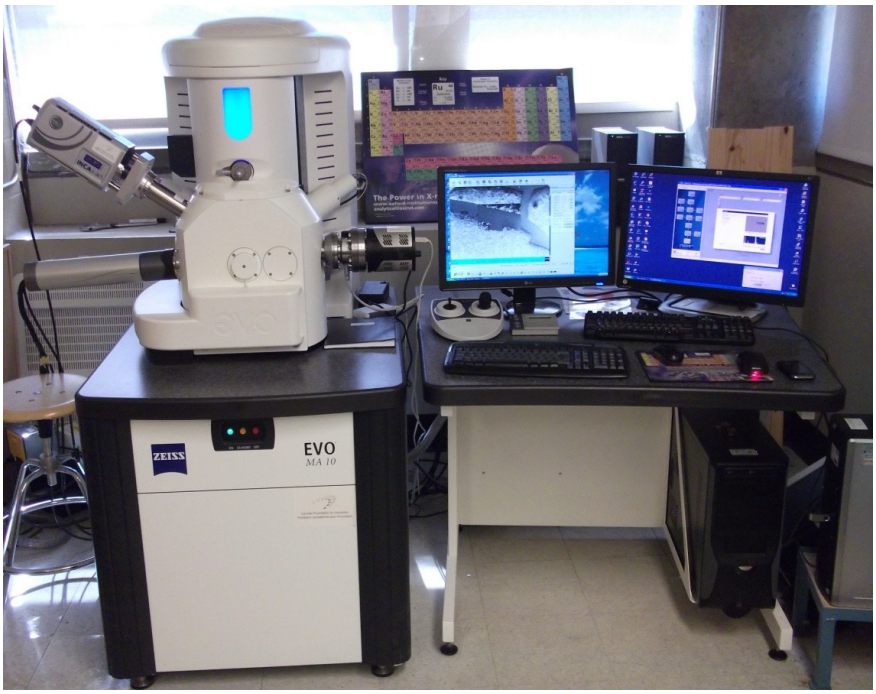

Figure 91: Zeiss EVO MA10 SEM.

4.8 Testing Equipment and Procedures

In order to further characterize the conductive coatings produced on the BMS 8-276, other equipment was required with accompanying procedures.

4.8.1 Indentation Hardness

Vickers micro-hardness measurements were taken for a specific tin coating produced on the BMS 8-276. This was done following the standard test method for Vickers hardness of metallic materials (ASTM E92-82R03) [84]. Using a Duramin-1 micro-hardness tester from Struers, a precise indentation was made with a 136° tapered diamond tip on the tin cross-section (see Figure 92). During this study, a load of 0.01kg was applied for 10 seconds on the indenter.

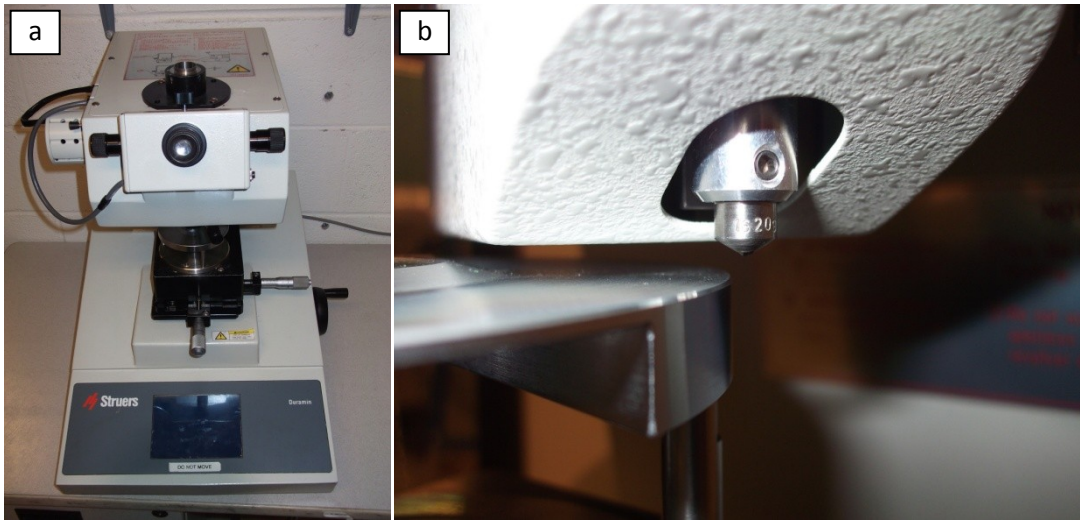

Figure 92: (a) Struers Duramin-1 micro-hardness tester with (b) close-up of indenter.

4.8.2 Surface Roughness

The surface roughness of the substrates was established prior to deposition using the digital microscope (VHX-2000 from Keyence) described earlier (see Figure 90b). Three dimensional images were produced using a magnification of 500X and vertical stage increments of 1µm. A software (Communication from Keyence) used the image produced to generate a height mapping array of the surface. The average roughness (R_a) was calculated by summing the absolute height deviation of the data points from the surface mean height [85]. From the 600 µm by 500 µm image, an array of 1200 by 1200 data points were utilized per measurement. The overall slopes in the X-Y planes (tilt) were accounted for and the height of each data point was corrected accordingly.

4.8.3 Electrical Resistivity

The electrical resistivity of the coatings produced was measured from the exposed coating surface using a four point probe resistivity sensor (provided by the Boeing Company) connected to a digital multimeter (Model 2010 from Keithley) (see Figure 93). The four point probe utilized a technique called "four terminal sensing" where the two furthest probes conveyed a current from which the resistance was captured by the two inner probes. When the sensor was pressed and held against the metalized composite surface, the sheet resistance of thin metal film was displayed at the multimeter interface. This resistance (in Ω) was multiplied with the coating thickness (in m) in order

to obtain the electrical resistivity (in Ωm) of the metalized coating. The measurement of the spring loaded probes is not affected by the surface finish of the coating as indicated by the test outlined in Appendix III.

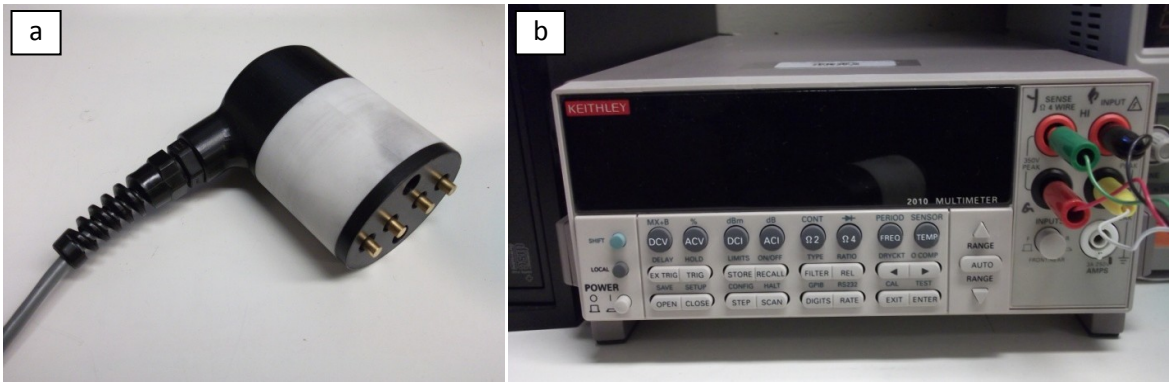

Figure 93: (a) Four point probe resistivity sensor and (b) Keithley Model 2010 digital multimeter.

4.8.4 Adhesion Strength

A portable adhesion tensile testing instrument (PATTI) was used to measure the adhesion strength of conductive coatings deposited on BMS 8-276 samples. The PATTI utilized for this study was the PosiTest AT-A from DeFelsko (see Figure 94). Tensile tests were conducted under ASTM D4541 [86].

Figure 94: DeFelsko PosiTest AT-A adhesion testing apparatus.

In order to perform a tensile test, a 20 mm diameter pull-stub was initially glued to the top surface of the coating using 907 Locktite epoxy (SKU 1813A244 from McMaster-Carr). After curing, all excess glue and coating surrounding the pull-stub was removed using the hole saw drill bit (see Figure 95). Not doing so would falsify the tensile adhesion strength value by including the shear stress component within the coating. If the coating area being tested remained attached to the rest of the coating, part of the stress would travel through the coating to the neighboring area (in a disk-like formation). The change in orientation of the stress (outwards) would cause a component of it to result in tensile adhesion to a greater area while the other component would create tensile force along the coating. As a result, a shear stress is created between the coating and the substrate as well as within the coating. The electronically controlled hydraulic pump automatically applied a continuous pull-off pressure rate specified by the user to the pull-stub. A rate of 50 psi/s (0.34 MPa/s) was selected for all adhesion tests of this study.

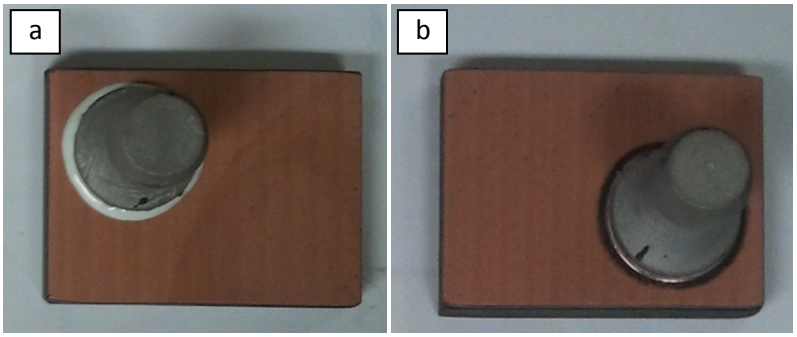

Figure 95: Example of pull-stub with excess cured glue (a) before and (b) after removal.

4.8.5 Salt Fog Corrosion Spray Test

A corrosion test was performed in agreement with the standard practice for operating salt spray apparatus (ASTM B117) [80]. The pH and salt concentration of the fog were measured every 24 hours. The chamber wet and dry bulb temperatures were also monitored on a daily basis. All parameters were kept within the outline values of the ASTM B117 standard. Samples of interest were placed in a salt fog environment for a total of 256 hours. Figure 96 presents the salt spray apparatus used for this study. All coated substrates' edges were taped prior to exposure. Some samples were removed prematurely to maintain a record of the corrosion's progression and to enable a side-by-side comparison of the samples.

Figure 96: Salt spray apparatus.

5 Coating Development and Adhesion Optimization

This chapter explains the experimental design and procedures developed to produce metalized BMS 8-276. Detailed test plans, results, and iterations are outlined in order to establish optimal CGDS parameters, substrate preparation, and material combinations. As mentioned in section 4.1, two types of metals (tin and copper) were used to create conductive coatings on BMS 8-276. Each section focuses on the conductive coating of a specific metal type.

5.1 Tin Coating Development

The deposition of tin on OMCs has seldom been attempted in the past let alone on BMS 8-276. It was mentioned in the literature review that CGDS behavior and material interaction greatly change when dealing with different materials (metal, polymer, and textiles). Due to the novelty of this project, few parameters were published regarding the deposition of tin on OMCs. Optimal conditions were established as an initial goal.

5.1.1 Pressure & Temperature

It was pointed out in section 2.3, that the pressure and temperature are amongst the most influential parameters in CGDS. As such, a range of pressures and temperatures were independently varied while holding all other parameters constant. The BMS 8-276 was prepared to expose a single LCFP. Unlike the WGFP, this substrate preparation exposes a smooth and consistent surface. The gas nature, standoff distance, nozzle type, orifice diameter, powder feeder wheel, powder feeder gas rate, powder feed rate, traverse velocity, and step size were held constant at values recommended by the CGDS supplier (Centerline (Windsor) Ltd). These values are provided in Table 13.

Table 13: CGDS Parameters Held Constant for the Tin Coating Development Test for Pressure and Temperature

CGDS Parameter	Value
Gas Nature	Nitrogen
Standoff Distance	10 mm
Nozzle Type	120 mm SS Nozzle
Orifice Diameter	2 mm
Powder Feeder Wheel	240 Medium Hole
Powder Feeder Gas Rate	30 scfh (0.85 m^3/h)
Powder Feed Rate	3 rpm (0.31 rad/s)
Traverse Velocity	10 mm/s
Step Size	1 mm

The pressure was initially set at 90 psi (0.62 MPa) for this is the lowest pressure achievable by the SST-P system and subsequently increased by increments of 20 psi (0.14 MPa) (in the range recommended by the supplier, Centerline (Windsor) Ltd). The temperature was initially set at 175°C (as recommended by the supplier, Centerline (Windsor) Ltd) and increased by increments of 25°C until a coating was successfully deposited. It is important to note here that the melting temperature of tin is 231.9°C. The pressure and temperature combinations are outlined in Figure 97.

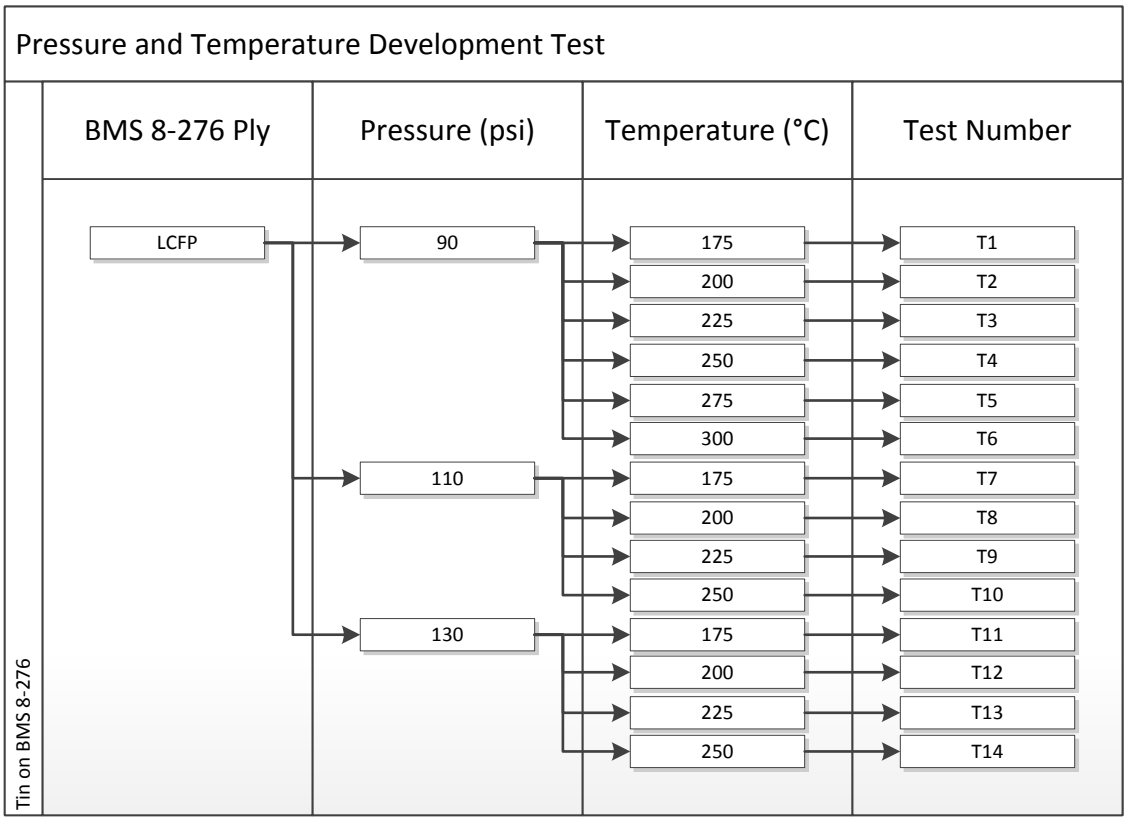

Figure 97: Pressure and temperature combinations for tin coating development test.

Cross-sectional analysis revealed that a high degree of erosion was present when spraying at high pressures and/or low temperatures. Figure 98 shows that the erosion went through an entire ply of CFRE near the center of the spray. Every test case experienced some sort of erosion; however, this was much less distinct in test cases when the stagnation pressure was 90 psi (0.62 MPa) (T1 to T6).

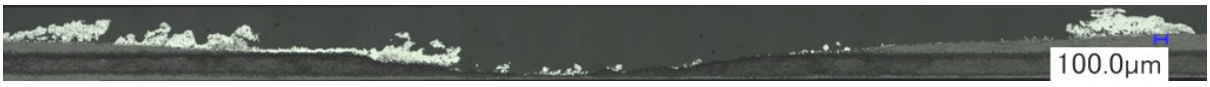

Figure 98: Cross-section of eroded BMS 8-276 after tin deposition (T14).

According to the equation developed in Section 2.3.4, increasing the stagnation pressure will increase the drag force and ultimately the velocity of the tin particles. Upon impact, the high kinetic energy is converted into plastic deformation and thermal energy. In this case, it is not the tough metallic particles that deformed but rather the organic substrate, hence the erosion. The energy required to deform the particle can be lowered by increasing the stagnation temperature of the gas. The metallic particles absorb the thermal energy of the gas through convection before the impact,

lowering the kinetic energy necessary to deform them. Increasing the temperature to 300°C resulted in a sudden increase in deposition for test T6 (see Figure 99). This major influence by the temperature on the deposition of metallic particles on organic substrates was also noted in the literature review [23]. The temperature was not further increased on account of the possibility of clogging the nozzle with molten material.

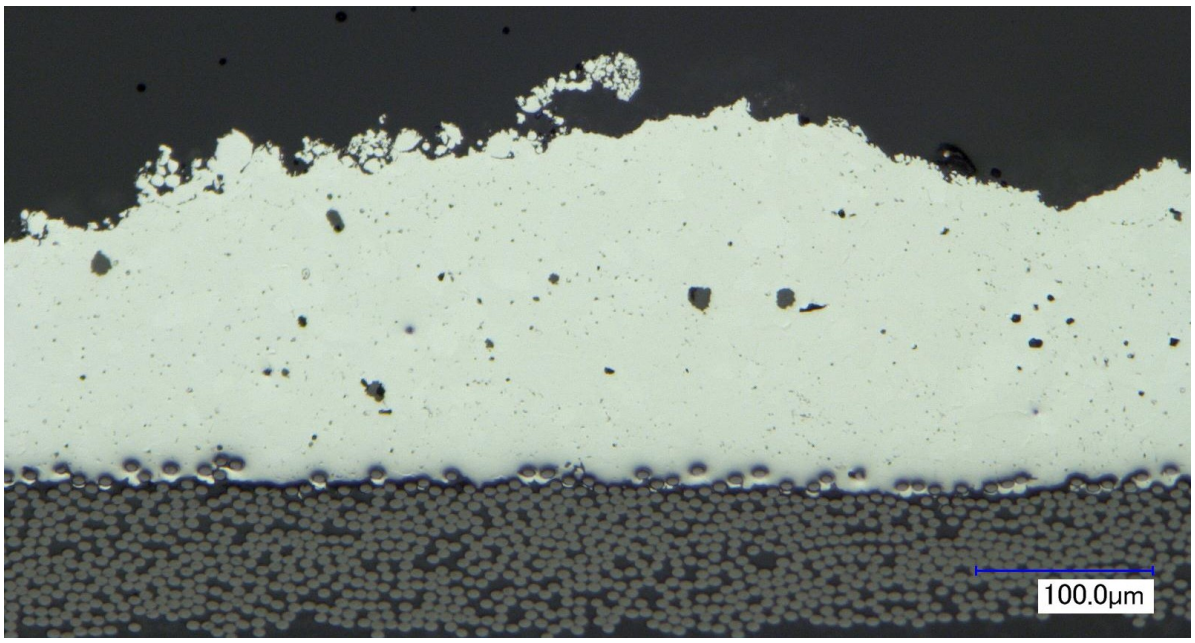

Figure 99: Cross-section of tin coated BMS 8-276.

5.1.1.1 Hardness

The hardness of sample T6 was measured using a Vickers microhardness tester. Five measurements were performed on the cross-section of the coating. The hardness value obtained was 10.39 ± 0.99$HV_{0.01}$ which is slightly higher than bulk tin (7-9 MPa). This indicates that very little cold working has taken place and that the tin coating is somewhat similar to bulk material. Upon visual inspection of the locations of indentation, cracking was observed. The cracks seem to outline the perimeter of the particles surrounding the indent location (see Figure 100). This information indicates that the cohesion between the particles within the coating may be low.

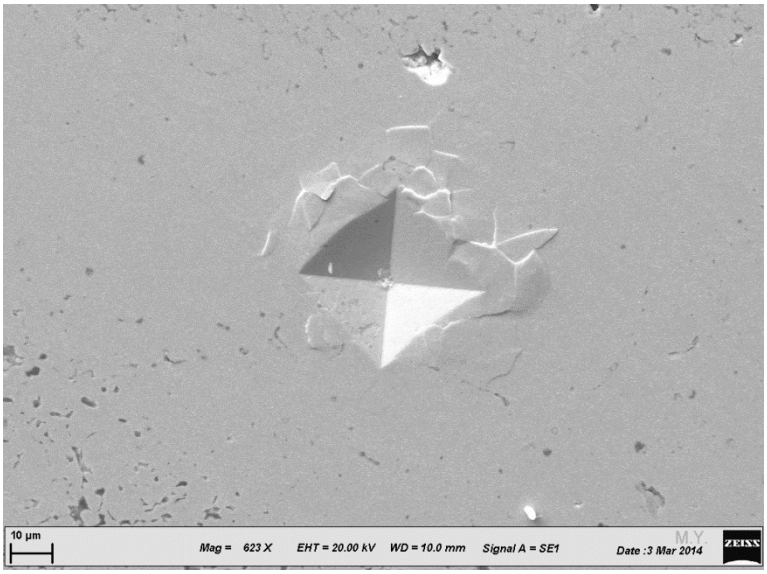

Figure 100: Micro-indentation of tin coating (T6) depicting crack propagation along particle perimeters.

5.1.2 Substrate Preparation

Many correlations have been made between the surface roughness of a substrate and the adhesion strength of its respective coating when mechanical interlocking is the primary adhesion mechanism (see literature review). This experiment was therefore conducted in order to produce such correlations for a tin coating on top of BMS 8-276 substrate. Both type of plies (LCFP and WGFP) contained within the BMS 8-276 (see section 4.3) were tested in order to determine which surface preparation will maximize adhesion. Figure 101 presents a variety of grits and blasting pressures that were combined to produce an array of roughness on both LCFPs and WGFPs. Four measurements were taken for each surface using the digital microscope in order to calculate the roughness (R_a).

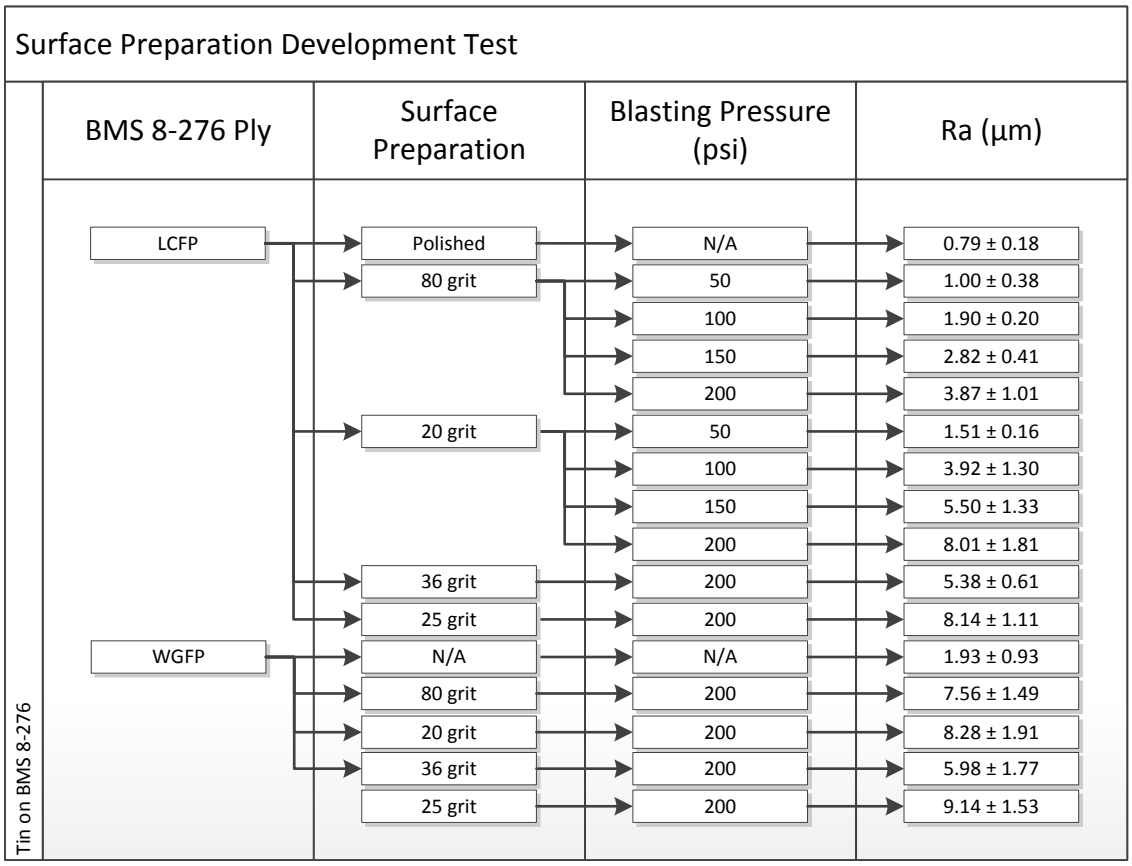

Figure 101: Roughness (R_a) measurements for an array of surface preparations including grit and blasting pressure combinations on laminar carbon-fibre ply (LCFP) and woven glass fibre ply (WGFP) of BMS 8-276.

Tin coatings were subsequently deposited on each sample using the same spray parameters outlined in Table 14. The pressure and temperature used come from the initial development test in section 5.1.1. The TV was increased from 10 mm/s to 30 mm/s in order to minimize the thickness. This was done in the hopes of maximizing adhesion (see section 2.3.6.1). However, the increased TV made the spray deposit in a discontinuous manner. The visually discernible pulsating spray was caused by the low frequency with which the powder feeder wheel holes were emptied (controlled by the PFR). This was amplified with the high TV which increased the distance travelled between each powder batch injection. As a result, the powder feeder wheel had to be changed from a 240 medium hole wheel to a 320 small hole wheel.

Table 14: CGDS Parameters Held Constant for the Surface Preparation Development Test

CGDS Parameter	Value
Gas Pressure	90 psi (0.62 MPa)
Gas Temperature	300°C
Gas Nature	Nitrogen
Standoff Distance	10 mm
Nozzle Type	120 mm SS Nozzle
Orifice Diameter	2 mm
Powder Feeder Wheel	320 Small Hole
Powder Feeder Gas Rate	30 scfh (0.85 m^3/h)
Powder Feed Rate	3 rpm (0.31 rad/s)
Traverse Velocity	30 mm/s
Step Size	1 mm

A PATTI test was used to evaluate the adhesion strength of the tin coating to each substrate. Four measurements were made for each surface preparation. In some cases, traces of glue were observed on the interface of the coating and the substrate (see Figure 102a). Cross-sectional analysis revealed that the coating was discontinuous which allowed the glue to seep through the coating and adhere to the substrate directly (see Figure 102b). This of course skewed the result of the adhesion strength, increasing the actual value.

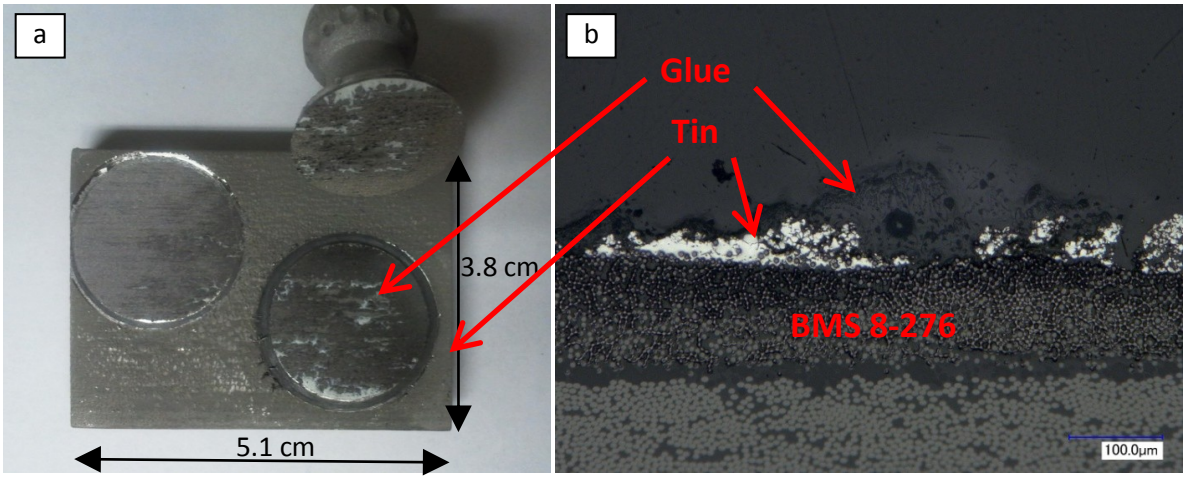

Figure 102: Seeped glue on tin coated BMS 8-276 (a) post PATTI pull and (b) cross-section.

36 results were deemed skewed (due to seeped glue) and were rejected from the data sample leaving only 28 admissible results. Figure 103 presents the adhesion strength results with respect to surface roughness. Points on the graph that do not have error bars for the adhesion strength represent only one value.

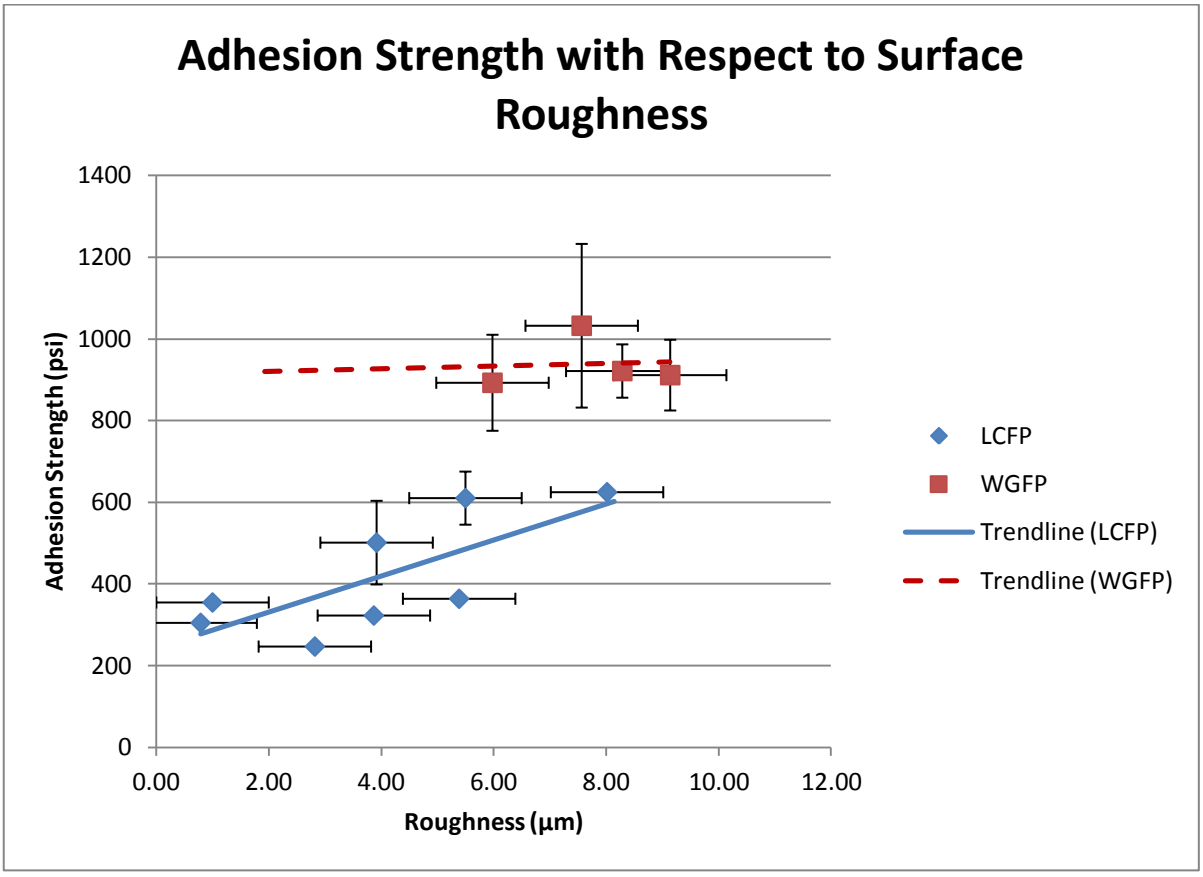

Figure 103: PATTI adhesion strength of tin coatings on LCFP and on WGFP BMS 8-276 for a variety of roughness. The relation between the roughness and the adhesion strength are emphasized using a linear trendline.

It is apparent that the tin coating behaves differently depending on the BMS 8-276 ply it was deposited on. The coating adhesion seems to have a positive correlation with the surface roughness of the LCFP BMS 8-276. Since we are dealing with a non-metallic substrate, metallurgical bonding is not possible. Thus this increase in adhesion strength must be the result of mechanical anchoring. Grit blasting is known to have a positive effect on mechanical bonding in CGDS. According to the trends in Figure 103, higher adhesion values could be achieved with higher roughness values for the LCFP BMS 8-276 whereas no trends are distinguishable for the WGFP BMS 8-276. The WGFP surface of the BMS 8-276 provides a more or less constant adhesion of 900 psi (6.2 MPa) which indicates

that the degree of mechanical interlocking is not affected by the grit blasting procedure. An important factor to take into consideration is the interwoven aspect of the WGFP. This fibre alternation might create favorable mechanical anchoring which may be more influential than the surface roughness.

5.1.3 Traverse Velocity (TV)

The coating discontinuities mentioned in the previous section (5.1.2) were thought to be caused by the change in TV since this was a CGDS parameter that was modified between section 5.1.1 and section 5.1.2. Cross-sectional inspection of the tin coatings produced in section 5.1.2, that were not pulled using the PATTI, revealed a porous wave-like pattern (see Figure 104). This pattern also appeared in samples T4, T5, T6, and T14 from section 5.1.1. All of these tests were sprayed at high stagnation temperature (greater than 250°C) which indicates that molten tin was likely the culprit. It is believed that the tin particles and recently deposited coating were locally heated near the spray area. It was therefore easier for particles to adhere to these highly heated areas for little kinetic energy was required. Particles within the gas flow, that would otherwise not adhere, managed to stick to these neighboring heated areas despite their low velocity. They remained mostly un-deformed creating extremely porous coatings. These porous coatings had a tendency to form on slightly elevated areas and always on one side of the prominence as seen in Figure 104. This fact further substantiated this theory since the spray pattern used allows for a dense coating to be initially deposited followed by a unidirectional warm flow of gas parallel to the spray surface.

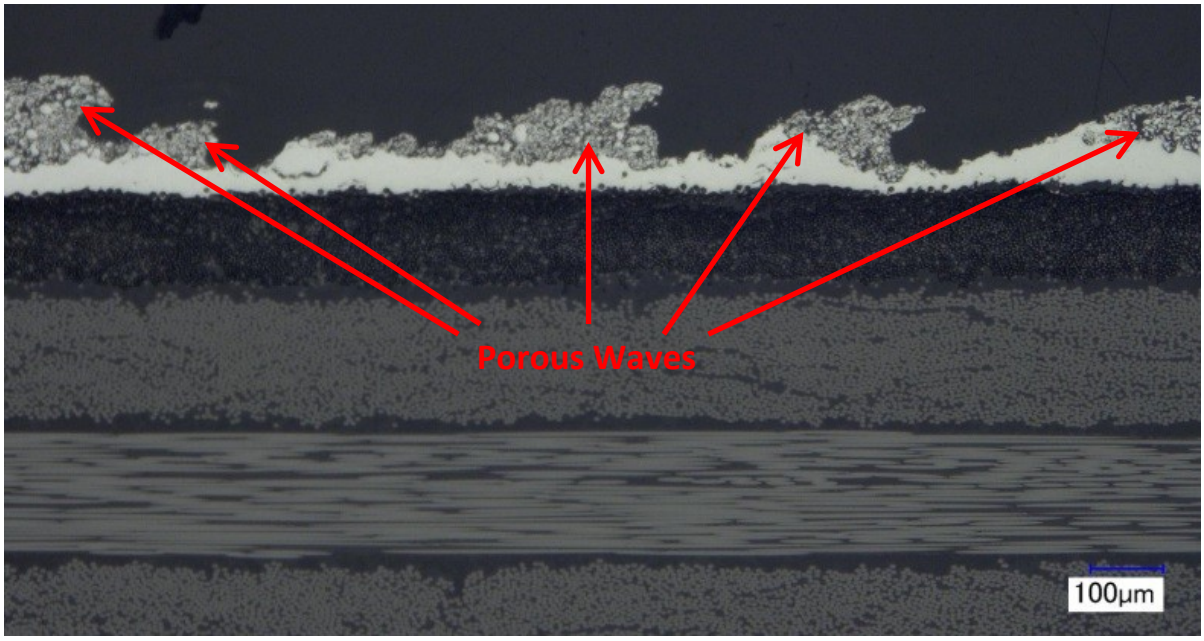

Figure 104: Tin coated BMS 8-276 with porous wave-like pattern.

In an attempt to eliminate the porous wave-like pattern from appearing, a test was designed to try minimizing the local heat when spraying. The CGDS parameters used for this test remain identical to the previous section with the exception of the powder feeder wheel and the TV (see Table 15).

Table 15: CGDS Parameters Held Constant for the Tin Coating Traverse Velocity Development Test.

CGDS Parameter	Value
Gas Pressure	90 psi (0.62 MPa)
Gas Temperature	300°C
Gas Nature	Nitrogen
Standoff Distance	10 mm
Nozzle Type	120 mm SS Nozzle
Orifice Diameter	2 mm
Powder Feeder Gas Rate	30 scfh (0.85 m^3/h)
Powder Feed Rate	3 rpm (0.31 rad/s)
Step Size	1 mm

The local heat during spray was minimized by increasing the TV. Figure 105 outlines how the powder feeder wheel and the TV were varied between sprays. With increasingly faster TVs, the

deposition of powder became pulsed if the powder feed rate remained unchanged (3rpm). However, this issue was mitigated by using the 320 small hole powder feeder wheel. This increased the frequency at which powder was injected without increasing the rate of powder flow. Each sample was analyzed and cross-sectional thickness measurements were taken (see Figure 105). In order to reach the desired thickness multiple passes could be repeated for future tests. Although the spray time and total thermal energy conveyed to the sample would remain theoretically the same, the instantaneous heat is more evenly distributed throughout the sample reducing the local heat peak.

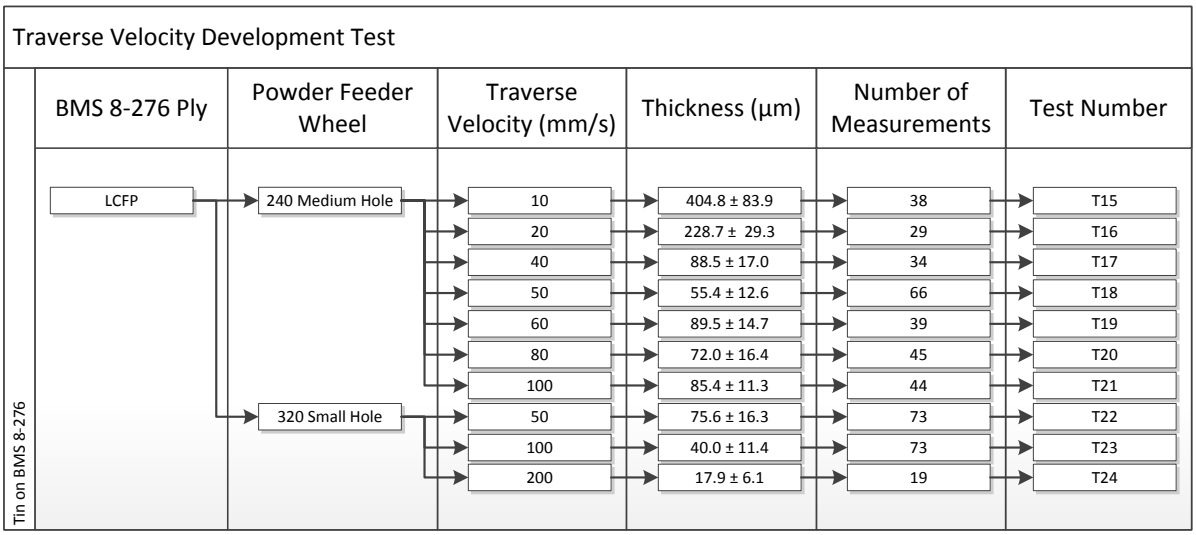

Figure 105: Traverse velocity development test with accompanying tin coating thickness on laminar carbon-fibre ply (LCFP) of BMS 8-276.

Figure 106 plots the thickness of each trial with respect to the traverse velocity for each powder feeder wheel. It can be concluded that the thickness is inversely proportional to the TV. These results also justify that both powder feeder wheels produce comparable powder flow rates when the feed rate is set to a specific value (e.g. 3 rpm). By using these results, we can define how many passes must be made in order to attain a desired thickness.

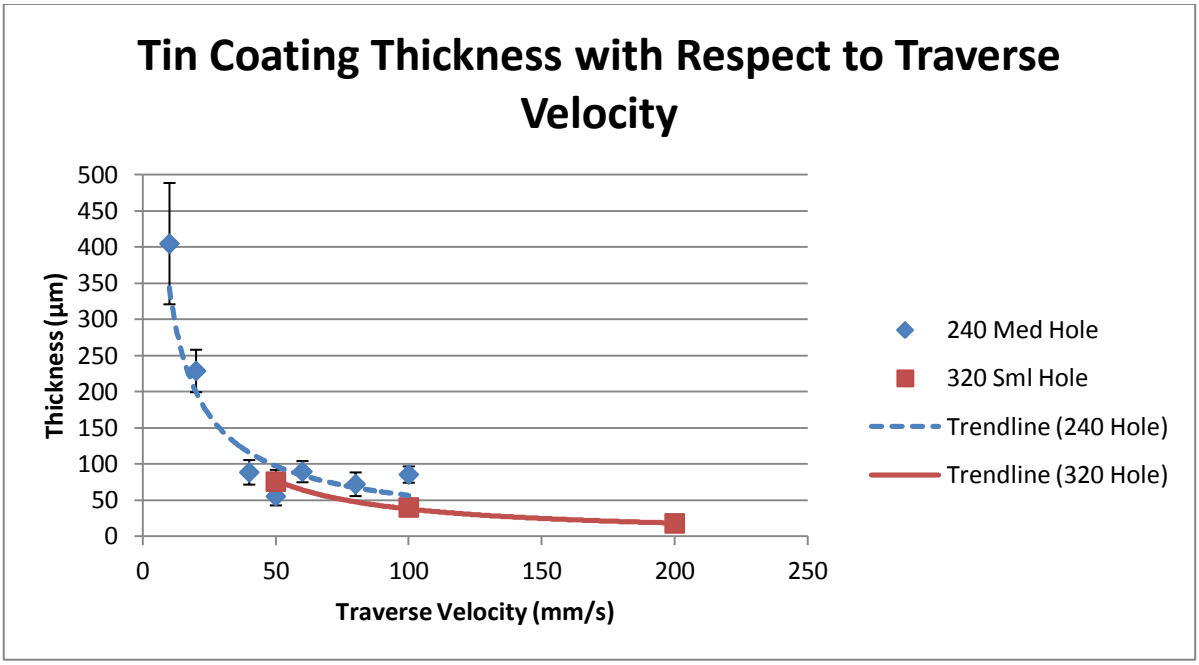

Figure 106: Tin coating thickness plotted with respect to the traverse velocity for two different powder feeder wheels: a 240 medium hole and a 320 small hole.

Cross-sectional analysis revealed that increasing the TV (≥ 50 mm/s) successfully eliminated the porous wave formation. Figure 107 presents an example of such dense tin coating in the case of sample T22. Thick, dense, and continuous tin coatings were produced by eliminating excess heat in the neighboring areas which prevents particles with low kinetic energy from sticking to them.

Figure 107: Cross-section of dense tin coating on LCFP BMS 8-276 (sample T22).

5.1.4 Deposition

A thin tin coating was deposited onto a WGFP BMS 8-276 using parameters outlined in Table 15 with a 320 small hole powder feeder wheel and a TV of 100 mm/s. The resulting coating seemed to have a hatched pattern driven texture (see Figure 108).

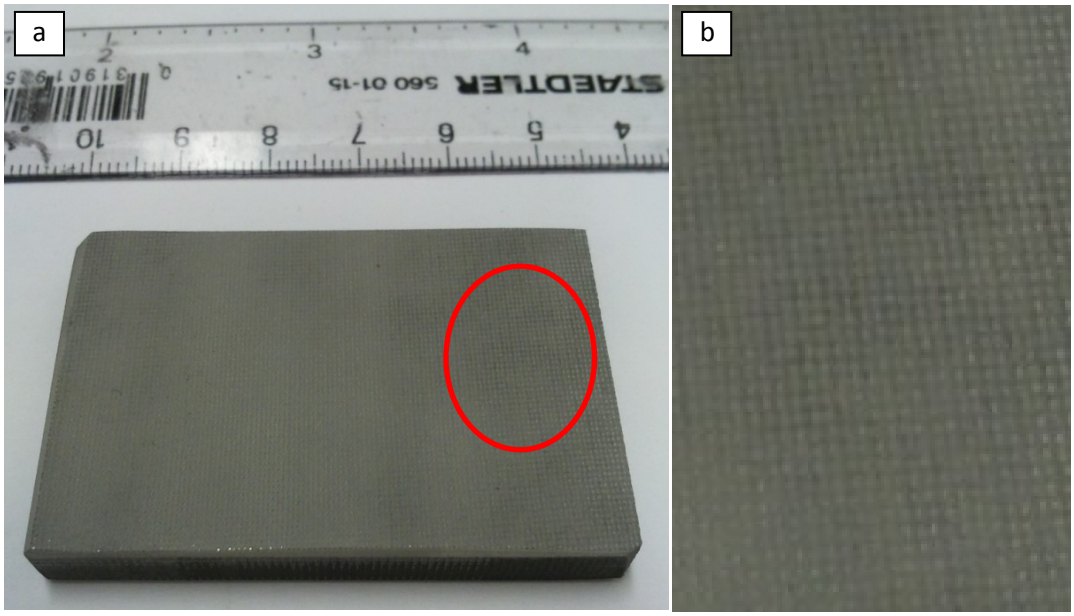

Figure 108: (a) textured surface of tin coating deposited at high traverse velocity (100 mm/s) on WGFP BMS 8-276 with (b) zoom of surface.

Cross-sectional analysis revealed that tin only deposited onto certain areas of the surface. Figure 109a depicts the alternating nature of the tin deposition on the WGFP BMS 8-276. Upon closer inspection, it was noted that the tin only deposited on the exposed glass fibres of the WGFP. Areas where the epoxy based-matrix was exposed did not result in successful deposition (see Figure 109b). A parallel can be drawn from the research conducted by Simon Baril-Gosselin where projected copper particles only adhered to copper particles of the co-cured bond coat and not the epoxy matrix (see section 2.2.7.2.2). Since the WGFP is composed of tows of glass fibres that intertwine, areas between tows are mainly composed of epoxy. This explains the alternating nature of the deposition of tin on the WGFP.

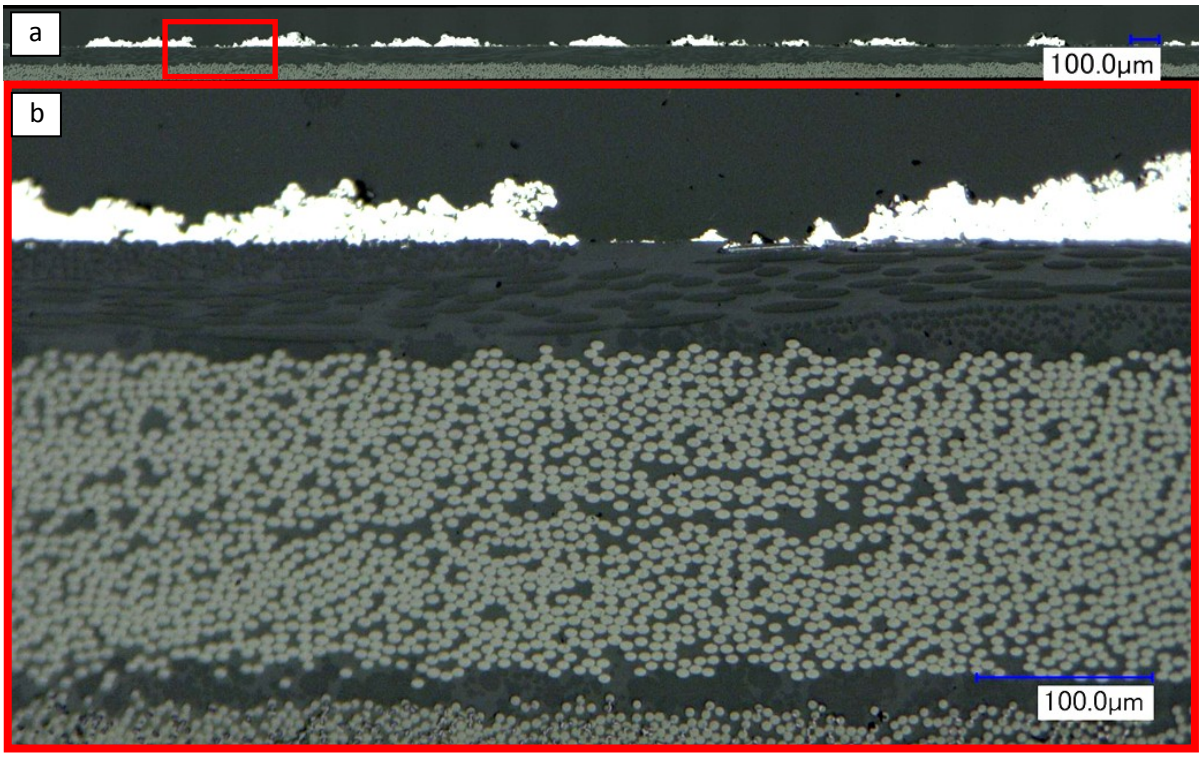

Figure 109: Cross-section of (a) tin coating deposited at high traverse velocity (100 mm/s) on WGFP BMS 8-276 with (b) close-up of deposition interruption.

A test was subsequently done to deposit tin on multiple LCFPs using identical parameters (see Table 15) and traverse velocities of 50 mm/s and 100 mm/s. The usual preparation method was used on the LCFP BMS 8-276 sample, however a slight incline was purposefully induced to expose multiple LCFPs (see Figure 110).

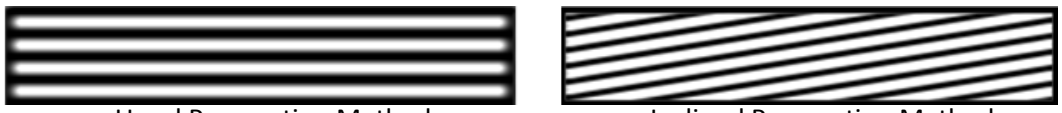

Figure 110: Representation of the usual preparation method exposing a single LCFP and the inclined preparation method exposing multiple LCFPs.

Subsequent tin sprays revealed that deposition does not occur between LCFPs (see Figure 111).

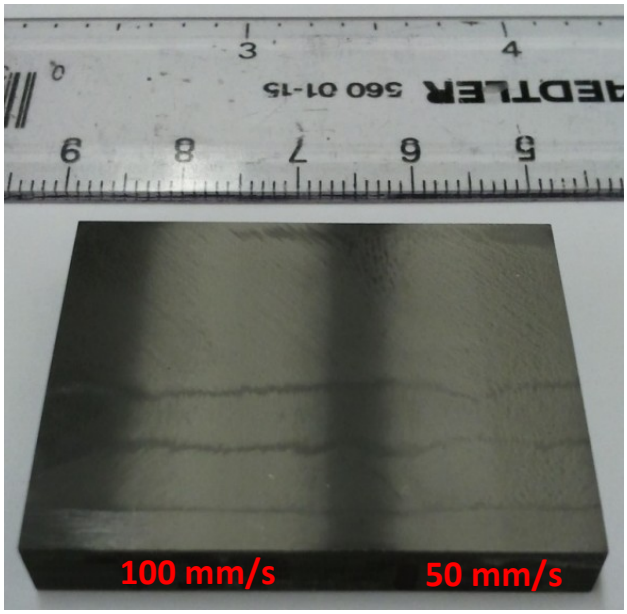

Figure 111: Tin coatings on multiple LCFPs of BMS 8-276 sprayed at 100 mm/s and 50 mm/s.

Cross-sectional analysis further substantiates the theory that the tin particles do not deposit on the toughening heterogeneous system. Figure 112a presents the entire tin coating deposited on the multiple LCFP BMS 8-276. From this image, it can be clearly seen that the coating discontinuities occur when the interface of each ply is exposed. Closer inspection of the discontinuity shows that the tin coating may drastically drop in thickness when reaching the toughened heterogeneous interface (see Figure 112b)

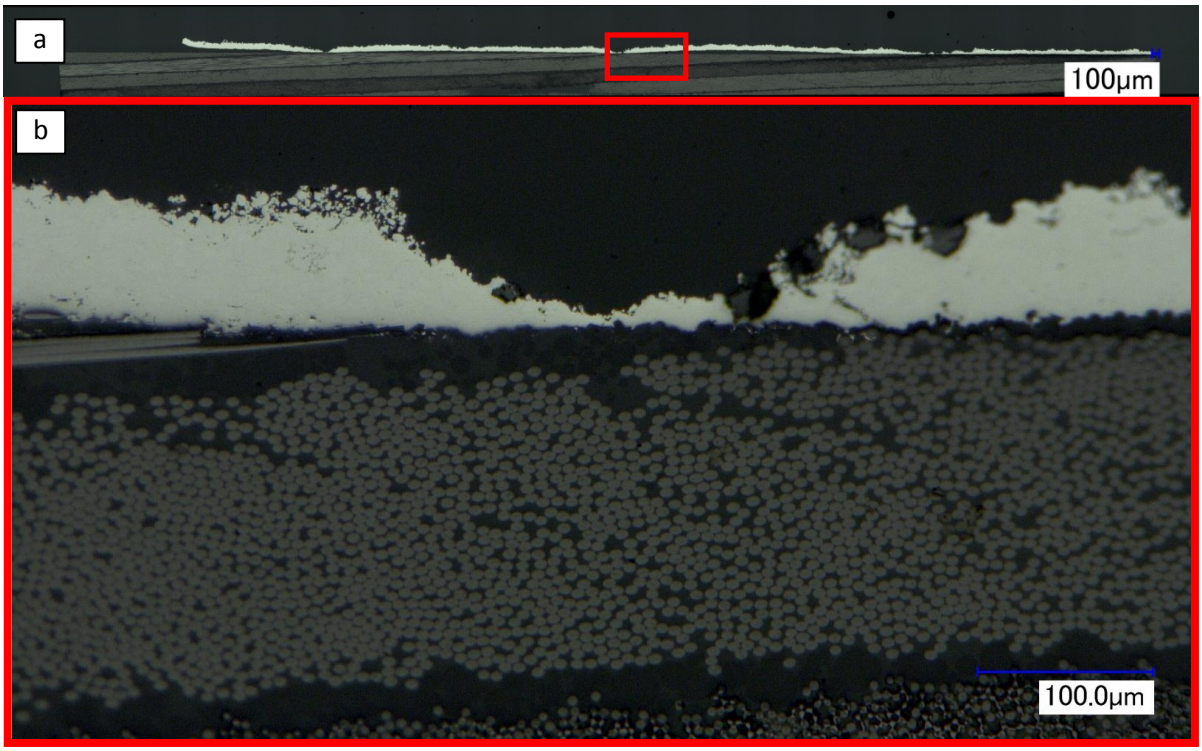

Figure 112: Discontinuous tin coating on BMS 8-276 with multiple LCFPs exposed the toughening heterogeneous system.

5.1.5 Build-up

Given that continuous tin coatings were successfully produced on WGFP BMS 8-276 in section 5.1.2, a test was performed to investigate how the tin coating builds-up on WGFP BMS 8-276. A tin coating was deposited onto a WGFP BMS 8-276 using parameters outlined in Table 15 with a 320 small hole powder feeder wheel and a TV of 200 mm/s. Multiple passes were made in a receding manner to vary the coating thickness. In other words, the first pass was done in order to deposit only on 8/9th of the sample. The second pass only covered 7/9th of the sample. The third pass covered 6/9th of the sample. This continues until the eighth pass covered only 1/9th of the sample. This method of proceeding produced a sample with a continuous tin coating where each pass can be analysed in a progressive way (see Figure 113).

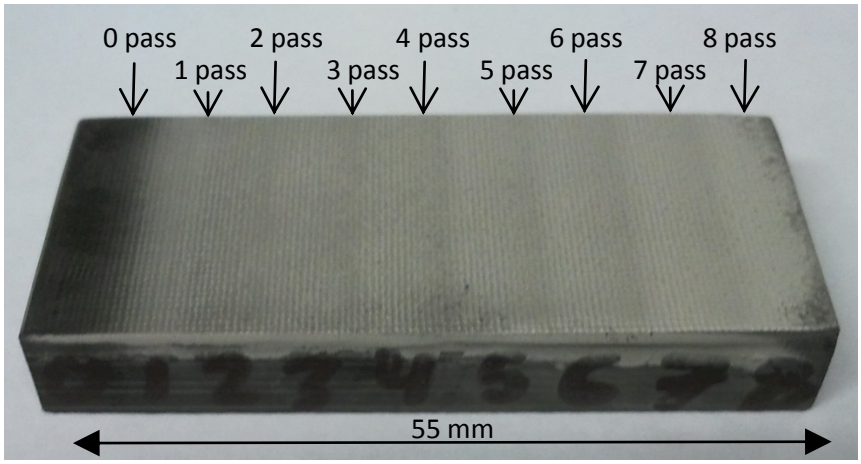

Figure 113: Tin coating thickness variation through receding multiple passes.

Cross-sectional analysis revealed that the first few passes deposit tin on the exposed fibres only, creating isolated mounts, whereas the next passes create bridging between the mounts, followed by a dramatic increase in the bridge thickness in order to become roughly equal to the mounts. All subsequent passes seem to increase the overall thickness of the tin coating in a uniform fashion (see Figure 114).

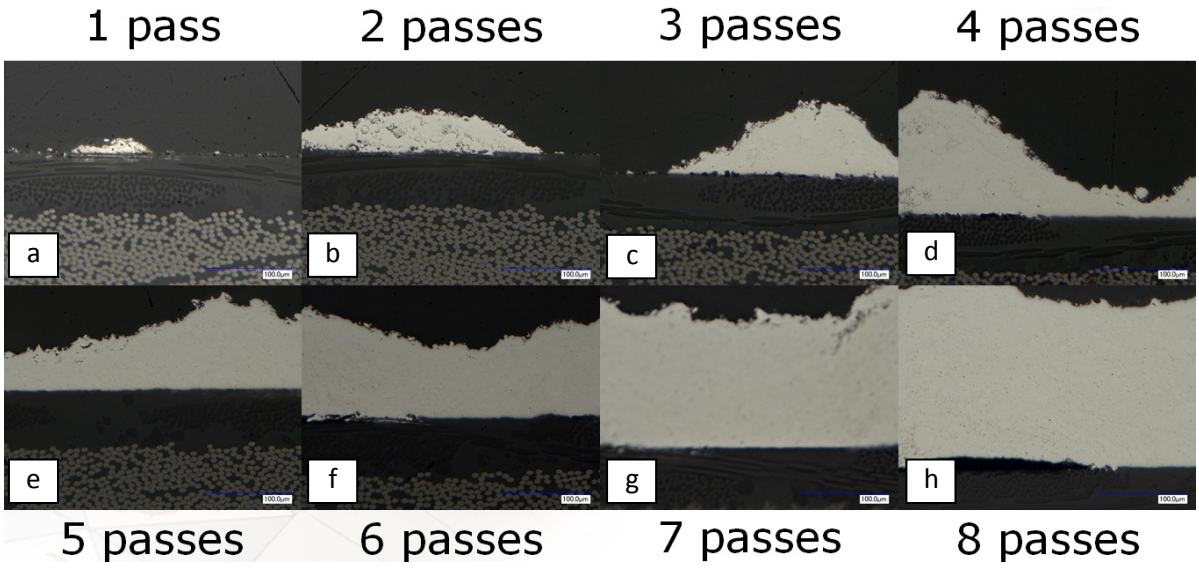

Figure 114: WGFP BMS 8-276 coated with tin deposited at high TV (200 mm/s) at (a) 1 pass, (b) 2 passes, (c) 3 passes, (d) 4 passes, (e) 5 passes, (f) 6 passes, (g) 7 passes, (h) 8 passes.

When comparing a tin coating produced at low TVs (see Figure 104) and a tin coating deposited at high TVs using multiple passes (see Figure 115), it is apparent that the coating quality is greatly

affected. A tin coating deposited at high traverse velocities using multiple passes has a much lower porosity and higher consistency. This drop in porosity is most likely due to an increase in impinging particles. The lower local heat prevents particles from easily adhering to the coating. Particles with low kinetic energy which otherwise would adhere without deformation, now simply impact previously deposited particles, further deforming them and filling out any possible pores.

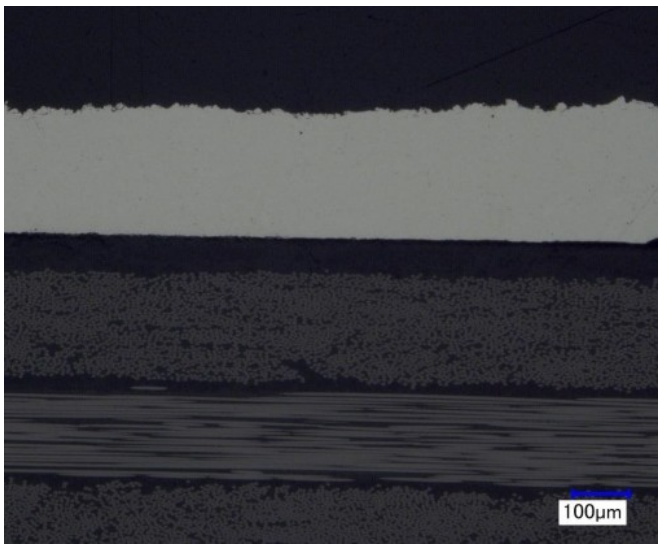

Figure 115: Thick tin coating deposited on WGFP BMS 8-276 at high TV using multiple passes.

5.1.6 Coating Thickness

This experiment was aimed at determining the effect of the coating thickness on the adhesion strength. As discussed in the literature review, thicker coatings are typically known to have lower adhesion strength (see Figure 21) [20]. This can be attributed to a low compressive residual stress at the interface of the coating and the substrate. It is thought that as a coating increases in thickness, the neutral axis moves towards the interface which lowers the adhesion strength. In order to quantify this effect, tin coatings of different thicknesses were deposited on WGFP BMS 8-276 with different surface finishes and tested using a PATTI. With the information provided in Figure 114, the minimal number of passes was established to be 4. Using the exact same parameters as in the previous section (5.1.5), tin coatings were deposited using a different number of passes (see Figure 116).

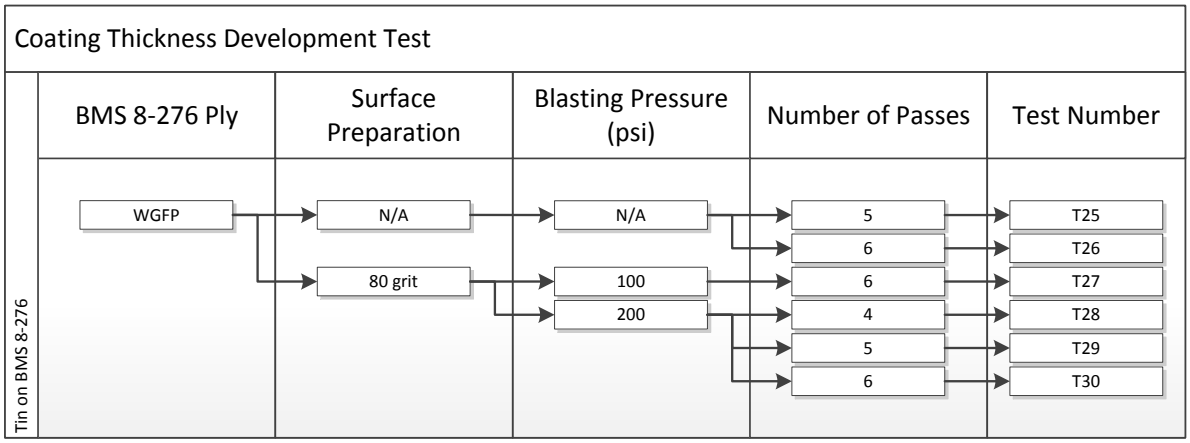

Figure 116: Surface preparation with blasting pressure for the coating thickness development test.

A total of 6 adhesion tests were performed using the PATTI test for each sample. The thickness of each test sample was measured by analyzing the cross-sections. At first glance, adhesion results seemed to indicate that the tin coatings thickness has a negative effect on the adhesion strength (see Figure 117). However, both test samples T25 and T26 had evidence of glue having seeped through the coatings and having remained on the BMS 8-276 surface post testing (much like in Figure 102). Cross-sectional analysis revealed that the tin coatings of samples T25 and T26 were discontinuous. The bridging effect had not taken place over the entirety of the surface leaving the WGFP exposed. All 12 data points were thus deemed unreliable, leaving no data points for the adhesion strength of either sample. This came as a surprise since the exact same spray and substrate conditions were used as in section 5.1.5. A possible explanation could be that the BMS 8-276 possesses manufacturing variations which affects the DR of the coating. It is thought that the minute variations of the epoxy covering the reinforcement fibres impacts the initial DR (creating the mounts). An increase in the quantity of epoxy will delay the bridging effect leaving the coating discontinuous. In other words, the thickness depends on the time it takes to deposit the initial bridged tin coating which is itself dependent on the initial surface conditions (BMS 8-276 manufacturing conditions). Minute variations in the preparations can cause inconsistent coating thickness.

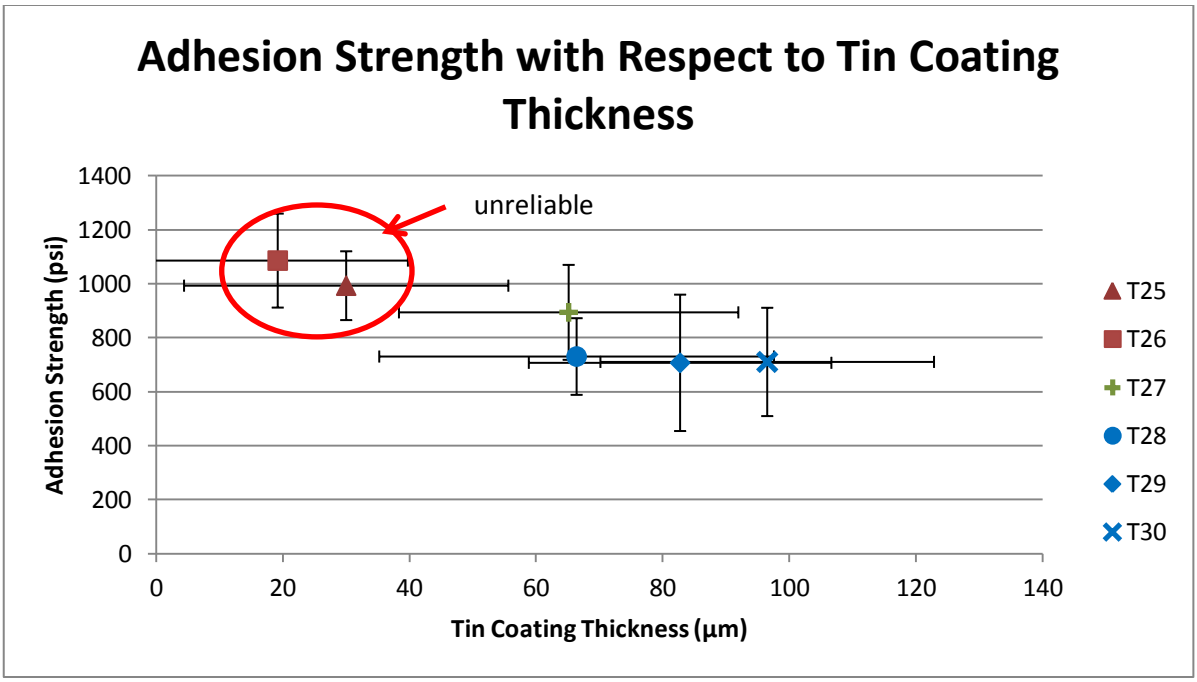

Figure 117: PATTI adhesion strength of tin coatings (sprayed with different passes) on "As Received" BMS 8-276, 80 grit blasted at 200 psi (1.38 MPa) and 80 grit blasted at 100 psi (0.69 MPa).

Besides samples T25 and T26, the results shown in Figure 117 do not indicate that the coating thickness has an important effect on the adhesion strength (for a thickness range of 60 µm to 100 µm). Even the slightly elevated adhesion strength of sample T27 still remains within the margin of error of the other samples. Furthermore, the overall adhesion strength observed during this test is nearly 200 psi (1.38 MPa) less than previously encountered in section 5.1.2 (above 900 psi or 6.2 MPa). The large error bars for the thickness can be attributed to the wavering thickness of the tin coating present in all 6 samples (thick mounts with thin bridges). However, these results do indicate that the overall thickness does increase with each pass for a given surface preparation. Appendix IV provides other tests performed on tin coatings to increase adhesion strength.

5.1.7 Mechanical Interlocking

As discussed in section 5.1.2, it is thought that the adhesion of tin originates from mechanical bonding between itself and the substrate. Previous tests have shown that the tin coating entraps reinforcement fibres as seen in Figure 99 and Figure 104. The degree of fibre embedment in the tin coating is believed to be an important factor in the adhesion strength. It can be noted in Figure 115 that the degree of entrapped reinforcement fibres is less prominent. This reduction of fibre

embedment could explain why the adhesion strength declined from section 5.1.2 to section 5.1.6. In order to evaluate the effect of the mechanical anchoring between the tin and embedded fibres, the following experiment was designed. It is suspected that the TV has an effect on the fibre embedment for this parameter was changed between section 5.1.2 and section 5.1.6. However, as discussed in section 5.1.3 and section 5.1.5, to create thick tin coatings free of porosity, multiple passes must be made at high TV. Hence, two different spray parameters were used for the experiment, each producing a different type of layer: the first layer and the build-up layer. The first layer essentially consisted of the first pass where the TV and the PFR was varied for each sample (see Figure 118). The PFR was set to 0.6 rpm (0.06 rad/s) as this was the slowest feed rate achievable by the Praxair powder feeder. By minimizing the PFR, lower traverse velocities can be used. The TV was lowered by the same factor as the PFR for sample T31 in order to maintain the quantity of powder injected into the flow identical to past tests in section 5.1.5 and section 5.1.6. The TV of samples T32 and T33 were further lowered to determine if the TV has an observable impact on the coating adhesion. For sample T34, the PFR was increased to produce a first layer of comparable thickness to samples T32 and T33. Using the trend from Figure 106 and the assumptions that the DE remained the same regardless of the spray parameters and that the DR is proportionally correlated to the PFR, a coating thickness was estimated for the first layer of each sample.

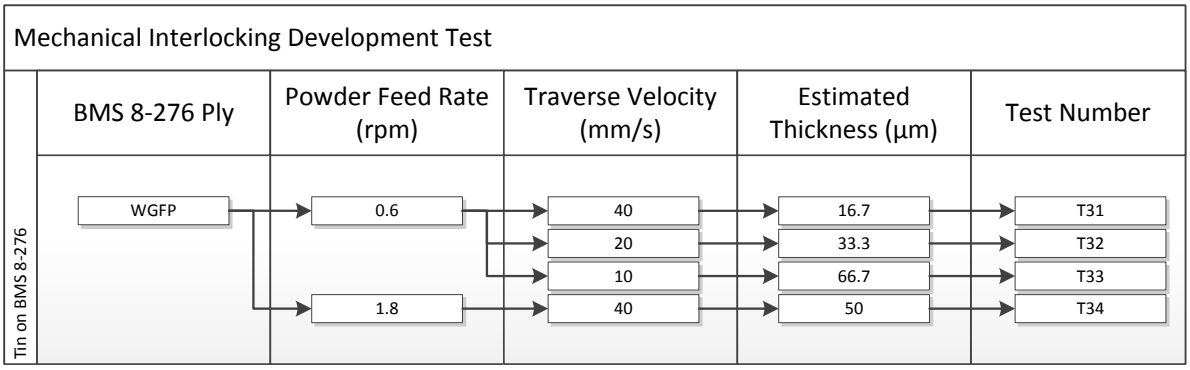

Figure 118: Tin Coating Traverse Velocity and Feed Rate Used for the First Pass Along With Estimated Thickness.

The TV and the PFR of the build-up layer were 200 mm/s and 3 rpm (0.31 rad/s) respectively for all test samples (identical to section 5.1.5). All other parameters for both types of layers are presented in Table 16.

Table 16: CGDS Parameters Held Constant for Both First Layer and Build-up Layer

CGDS Parameter	Value
Gas Pressure	90 psi (0.62 MPa)
Gas Temperature	300°C
Gas Nature	Nitrogen
Standoff Distance	10 mm
Nozzle Type	120 mm SS Nozzle
Orifice Diameter	2 mm
Powder Feeder Gas Rate	30 scfh (0.85 m^3/h)
Powder Feeder Wheel	320 Small Hole
Step Size	1 mm
Exposed Substrate Ply	WGFP

In order to produce coatings of equal thickness, the number of passes of the build-up layer varied according to Table 17. Again, it is important to keep in mind that these thicknesses are estimated from previous data and do not necessarily reflect the actual coating thickness produced.

Table 17: Tin Coating Build-Up Layer Number of Passes Along With Foreseen Thickness (Note: all other parameters can be viewed in Table 16)

Sample Number	Build-Up Layer Number of Passes	Build-Up Layer Thickness (µm)	Total Coating Thickness (µm)
T31	5	83.3	100
T32	4	66.7	100
T33	2	33.3	100
T34	3	50	100

Adhesion tests were performed on the samples using a PATTI test. Three adhesion tests were performed for each sample. However, traces of glue were found between the substrate and the pull-stub of all three tests performed on sample T31. In addition, one of the three tests performed on sample T34 also contained traces of glue remaining on the substrate leaving only two tests for analysis. Cross-sectional analysis performed on all samples indicated that certain discontinuities were prevalent in the coatings of samples T31 and T34 (see Figure 119). These discontinuities

allowed the glue from the adhesion test to reach the substrate and possibly skew the results. Because of the possible influence of the seeped glue, adhesion values acquired for sample T31 were completely unreliable and adhesion values for sample T34 were unreliable at times.

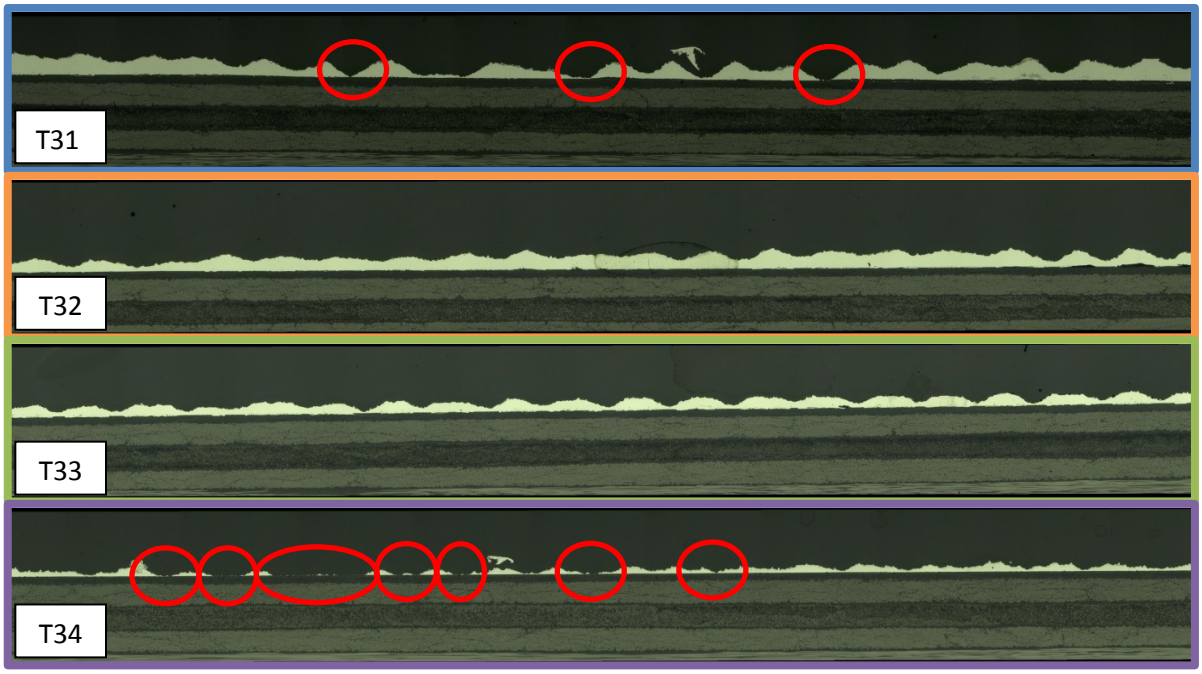

Figure 119: Cross-sections of samples T31, T32, T33, and T34. Discontinuities are present in samples T31 & T34.

When observing the results presented in Figure 120, the adhesion results of sample T31 are presented in red because they are deemed unreliable. It is also important to note that only two test points were kept for sample T34 (due to unreliability) whereas every other sample have three data points. From Figure 120, we see an increase in adhesion between samples T32 and T33.

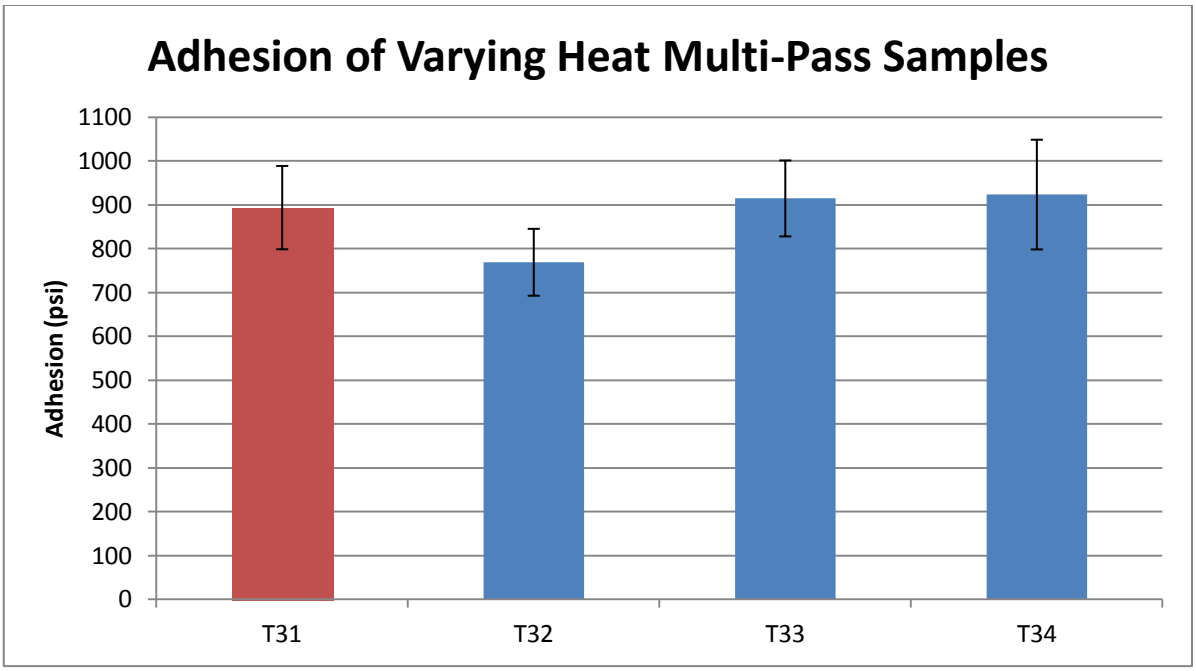

Figure 120: Adhesion values of varying heat multi-pass samples (T31, T32, T33, and T34). Three pulls were performed on each sample. The results of sample T31 is presented in red because tests were unreliable. Sample T34 only has two data points since one was deemed unreliable.

Optical inspection indicated that all samples, with the exception of sample T31 showed roughly equal signs of interlocking over the area between the tin coating and the BMS 8-276 (see Figure 121). However, upon closer analysis, we see that the degree of fibre embedment in the tin coating varies from one sample to the next. It is difficult to quantify the degree of fibre embedment; however samples can be subjectively compared.

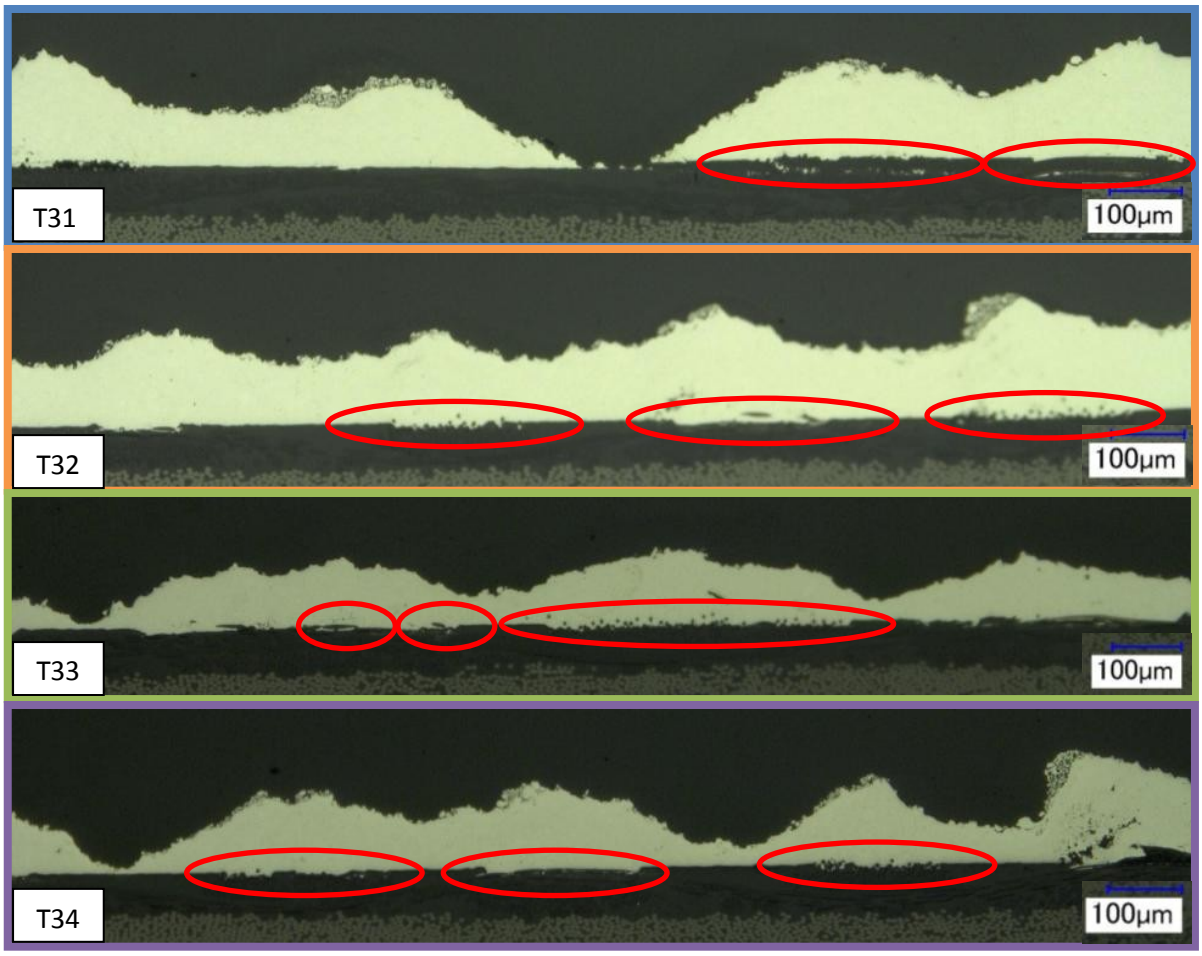

Figure 121: Cross-sections of samples T31, T32 T33, and T34 at 200X. The tin and glass fibre interlocking is highlighted by red ovals. Note that the tin coating of sample T31 is partially debonded from the BMS 8-276 substrate.

In Figure 122 we see that sample T33 has the deepest fibre embedment, closely followed by sample T32. Samples T31 & T34 have very shallow fibre embedment. As such, a link can be made between the degree of fibre embedment and the TV during deposition. Slower TVs result in increased fibre embedment. From Figure 120, we can correlate the degree of fibre embedment to the adhesion strength (sample T33 has more fibre embedment and a higher adhesion strength than sample T32).

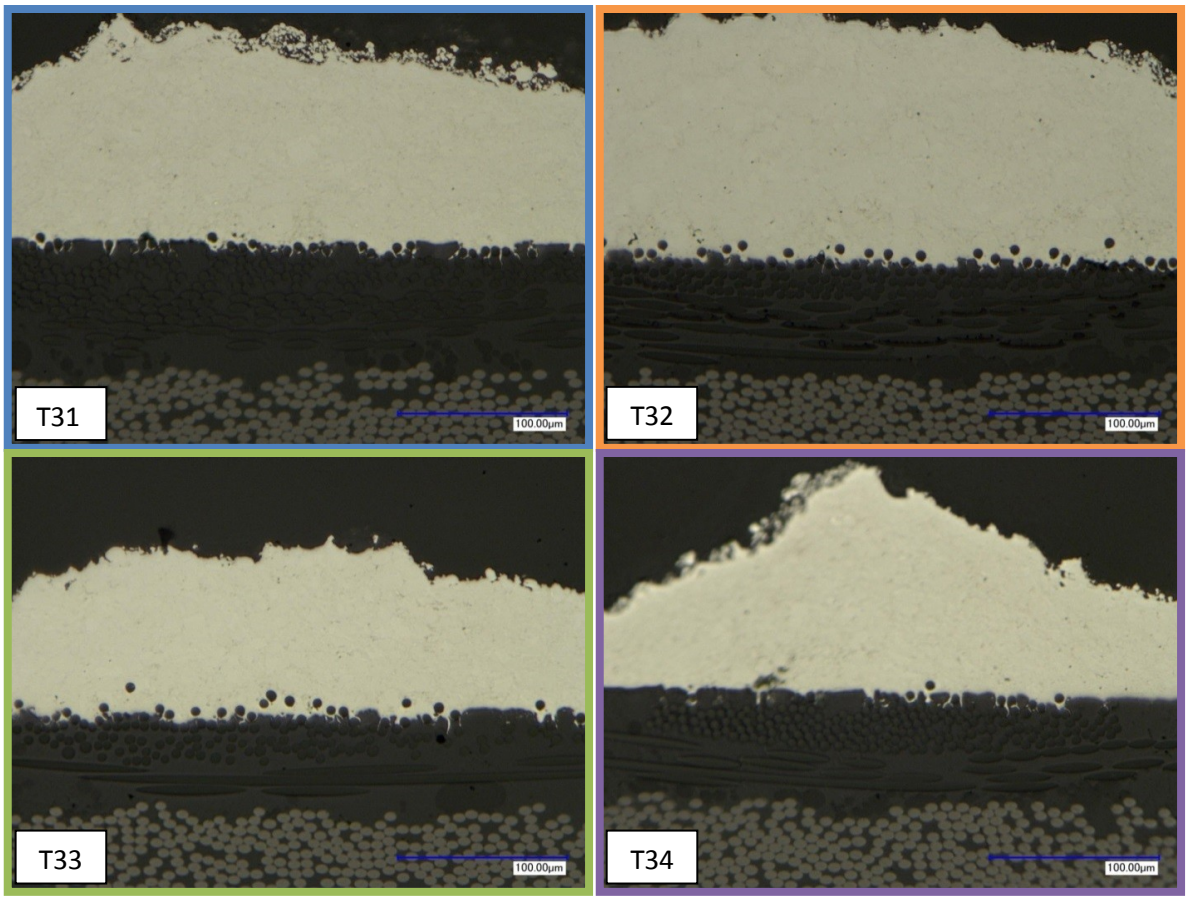

Figure 122: Cross-sections of samples T31, T32, T33, and T34 at 500X. Note that sample T32 has deeper fibre embedment in the tin coating than samples T31 & T34 and note that sample T33 has even deeper fibre embedment.

This indicates that lowering the TV slightly increases the adhesion strength. The elevated adhesion of sample T34 indicates that increasing the powder rate during the first pass can also be beneficial for the adhesion strength to a certain degree. It was established in section 5.1.3 that the tin coating will not deposit in a continuous and porous free fashion if the local heat is too elevated. On the other hand, it is this same heat that enables the impacting particles to adhere to the BMS 8-276 substrate. By limiting the particle rate during the first pass, only parts of the coating/substrate interface are optimally bonded lowering the overall adhesion of the coating. Thus in order to create the optimal adhering coating, the first pass must have a low TV combined with a sufficiently high PFR to produce the largest anchoring interface, yet not so high as to create a porous coating (see Figure 104).

To better understand the adhesion mechanisms at play, the surface of the BMS 8-276 post PATTI pull was analyzed using a SEM. From Figure 123, we see that the fibres from sample T33 are much

more exposed and protrude more from the surrounding epoxy than in any other sample. This increase in fibre exposure is thought to be due to the increase in localized heat during deposition. By increasing the heat during deposition, the epoxy is more likely to break than the reinforcing fibres. The reinforcing fibres of the BMS 8-276 can withstand high temperatures whereas the epoxy's properties can be severely impaired as the epoxy degrades with high heat. Therefore, increasing the heat will increase the degree of exposed reinforcement fibres. This further substantiates the increase in adhesion measured from sample T32 to sample T33. These SEM images also show that sample T33 has the highest degree of severed fibres, followed by samples T32, T34, and lastly T31. It is unclear at this point, if the PATTI pull caused the reinforcing fibres to sever or if they were severed during the deposition of the tin coating.

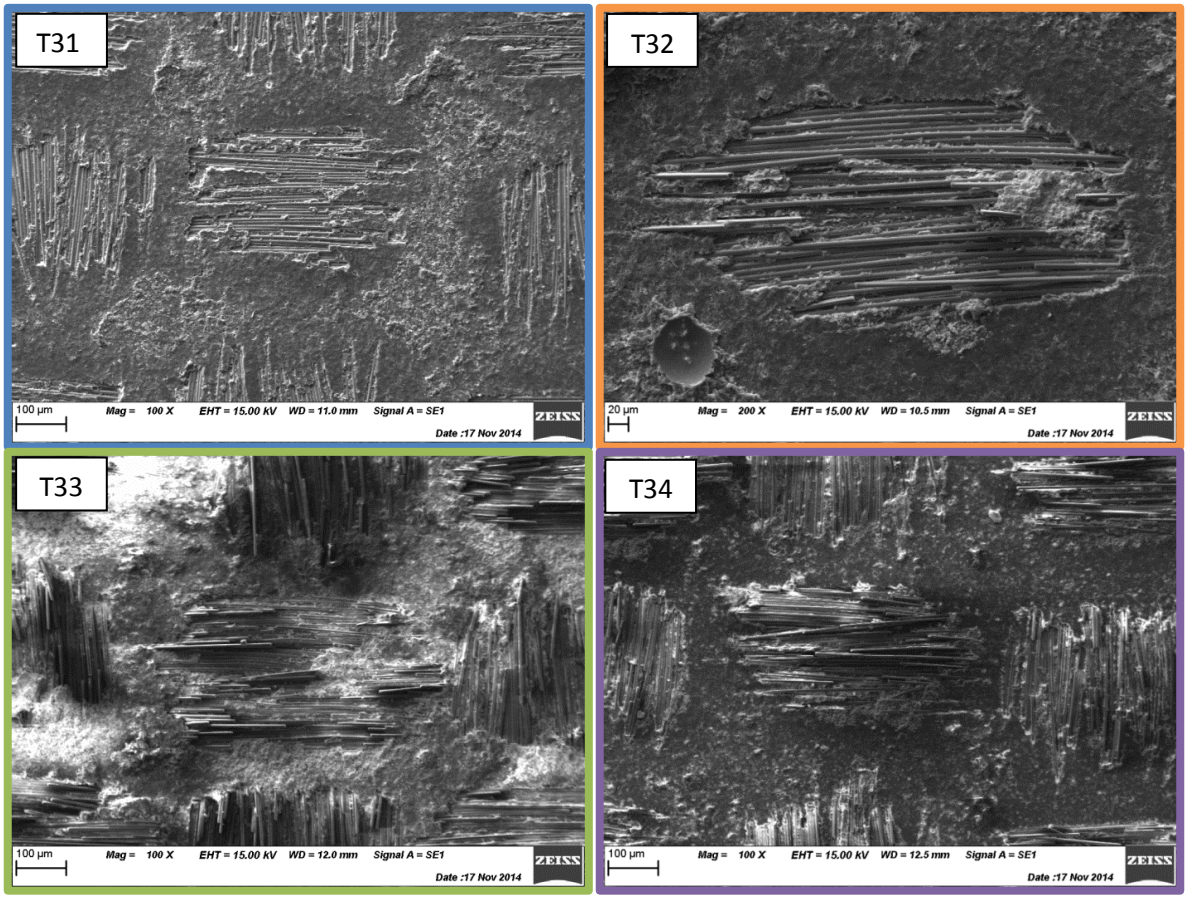

Figure 123: SEM images of the BMS 8-276 surface of samples T31, T32, T33, and T34 post PATTI pull depicting exposed glass fibres.

Backscatter analysis revealed that large quantities of tin remained on the surface of the BMS 8-276 after a PATTI pull test was performed on samples T31, T32, T33, and T34. From Figure 124, we can

see large quantities of tin present near the severed fibres of sample T33. Smaller build-ups of tin were evident near the exposed fibres of samples T32 and T34 whereas only traces were detected on sample T31. For samples T32, T33, and T34, the residual tin generally remained in an agglomerate form and is unevenly distributed across the surface. These agglomerates of tin denote the presence of good mechanical anchoring. It seems that increasing the PFR and lowering the TV for the first pass is beneficial for the adhesion. By increasing the local heat during deposition, improvements of bonding via mechanical interlocking can be visually verified.

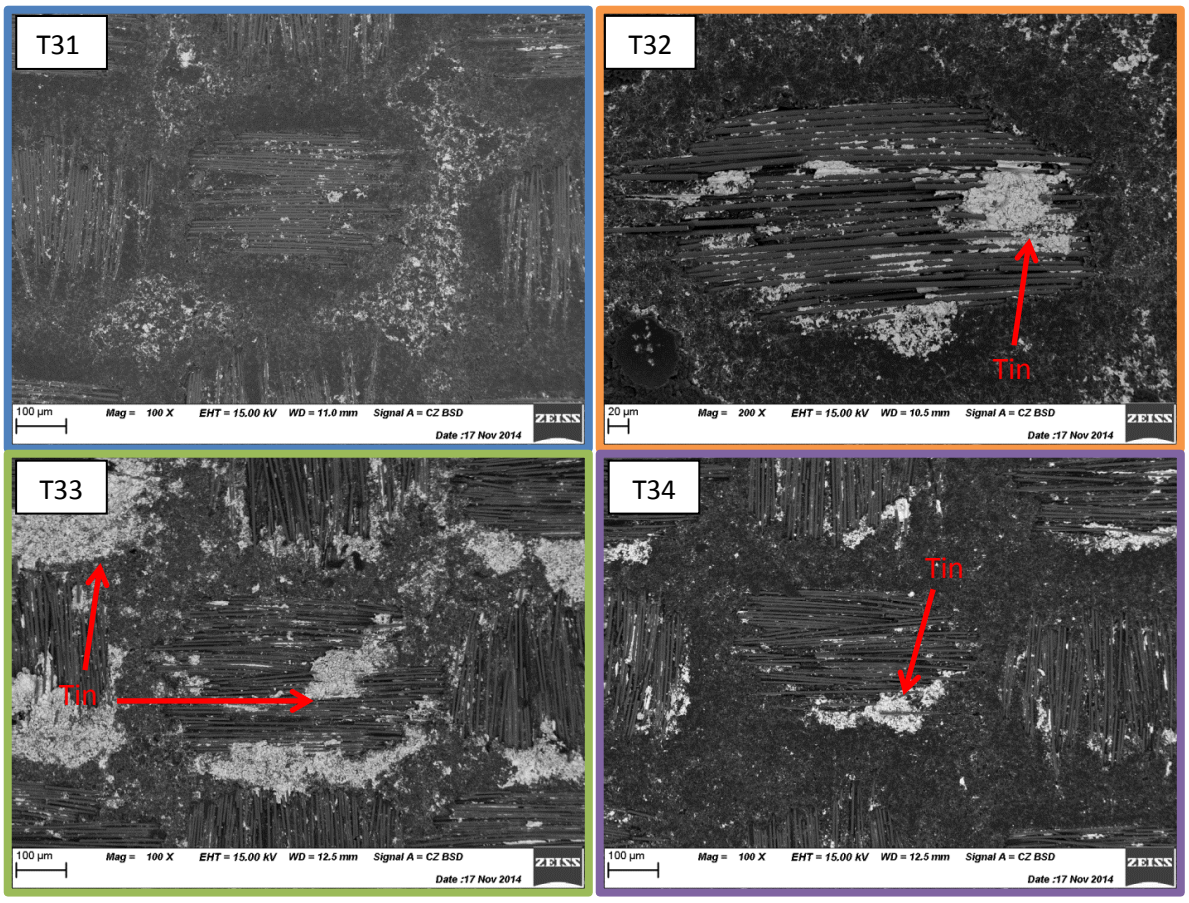

Figure 124: Backscattered images of the BMS 8-276 surface of samples T31, T32, T33, and T34 post PATTI pull depicting tin residue near glass fibres.

Figure 125 presents a SE image and a BSE image at a 1000 magnification of sample T33. From these images, severed fibres that are denuded of tin are observed along with a tin rich area neighboring these severed fibres and severed tin trapped between intact glass fibres. The denuded severed fibres are likely pull-outs from the tin coating which in this case acts as the matrix. This is a common failure mechanism in fibre reinforced composites. Most of the severed fibres have little to no tin

residue which is evidence that the adhesion between the glass fibres and the tin is low. In order to sever the fibres, the surrounding tin should have been thick enough to have a comparable toughness. It is important to note here that the fibres are pulled in a direction that is perpendicular to their general orientation causing them to bend and possibly rupture prematurely. In the case where the glass fibres are not severed, tin can be spotted between the fibres. The intact fibres indicate that the tin most likely severed from the remainder of the coating during the adhesion test. Given that these fibres are deeper in the BMS 8-276, the locally heated tin may not have separated the glass fibres enough while seeping between them during deposition. Once solidified, only a thin tin anchoring point remained leaving it vulnerable to stress concentration during tensile testing. The tin rich area neighboring the severed fibres is probably a location where the quantity and quality or the anchoring points are comparable to the cohesion of the tin coating.

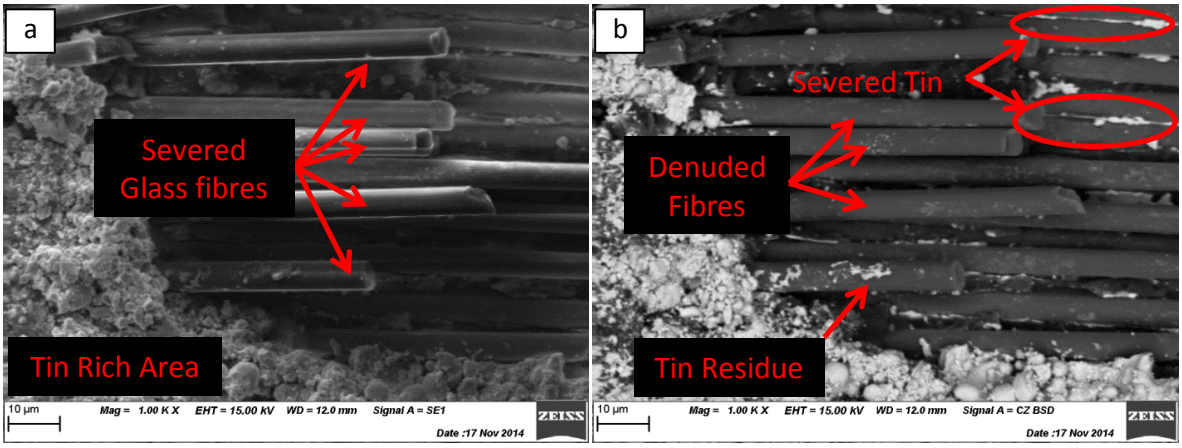

Figure 125: (a) Secondary electron (SE) image and (b) backscattered detection (BSD) image at a 1000 magnification of sample T33.

In short, there is evidence that the degree of fibre embedment is an important factor in the adhesion of the tin coating to the BMS 8-276 substrate. The degree of fibre embedment increases when the TV is lowered and the PFR is increased. The first pass should take these parameters into consideration in order to maximize adhesion of the tin coating.

5.1.7.1 Microstructure

A quick test was conducted on samples T31, T32, T33, and T34 to evaluate the microstructure of the deposited tin coatings. An etching solution, comprised of 2 mL of hydrochloric acid and 100 mL of

ethanol (95%), was produced following the "Standard Practice for Microetching Metals and Alloys" (ASTM E407-07) [87]. Upon exposure of 1 to 3 minutes, the solution attacks the grain boundaries of the pure tin exposing the microstructure of the coating. All four coatings demonstrated identical microstructure. No difference could be made between the first layer and the build-up layer. Figure 126 shows that the grain boundaries were not specifically targeted by the etching solution. However, a minimum of two different grain orientations can be distinguished by the smooth surfaces and the rough surfaces left behind (see Figure 126). The elevated deposition temperature allows for recrystallization to take place yet it remains unclear if this phenomenon occurred. Partial recrystallization would explain the lack of clear grain boundaries in certain areas of the coating.

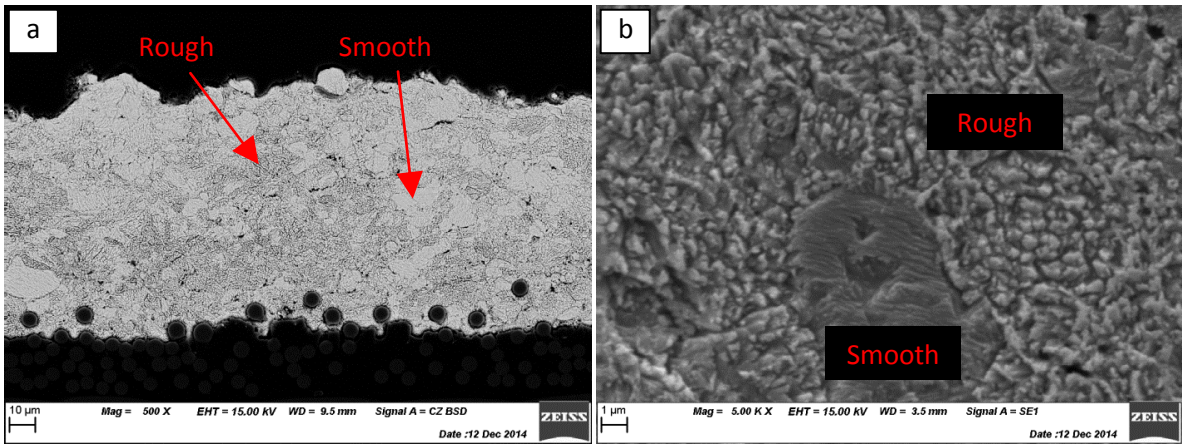

Figure 126: Etched cross-section of sample T32 at (a) low and (b) high magnification.

5.1.8 Wipe Tests

Wipe tests are a great way to investigate the deposition behavior of CGDS propelled particles. The wipe test conducted consisted of depositing a minute quantity of particles onto the substrate. By doing so, single particle impacts are observed and analyzed. With the exception of the PFR and the TV, all the CGDS parameters remained identical to the experiment of section 5.1.7 (see Table 16). Figure 127 presents the PFR and the TV used for each sample. In every wipe test, the PFR was shut off mid spray. This technique allows for only a few particles to remain in the flow ensuring that individual particles can be analyzed.

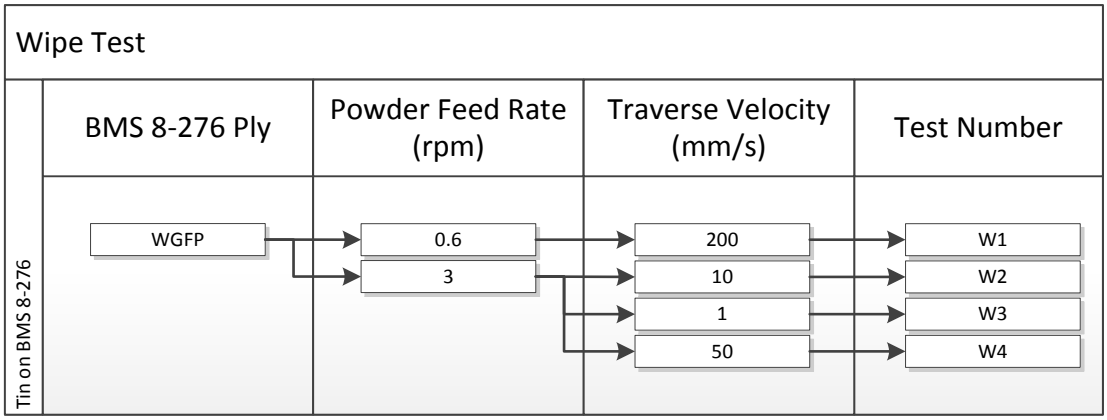

Figure 127: Coating traverse velocity and feed rate used for the wipe tests.

For sample W1, it was very difficult to time the PFR shutoff given the high TV. As such, the PFR was minimized to 0.6 rpm (0.06 rad/s) for that test (the lowest achievable feed rate on the Praxair powder feeder). For wipe test W2, the PFR was shutoff too early and required a temporary reopening to make a spot-like trace (see Figure 128). The TV of sample W3 was so low that large amounts of heat and powder began to accumulate splattering beyond the usual trace boundaries (see Figure 128).

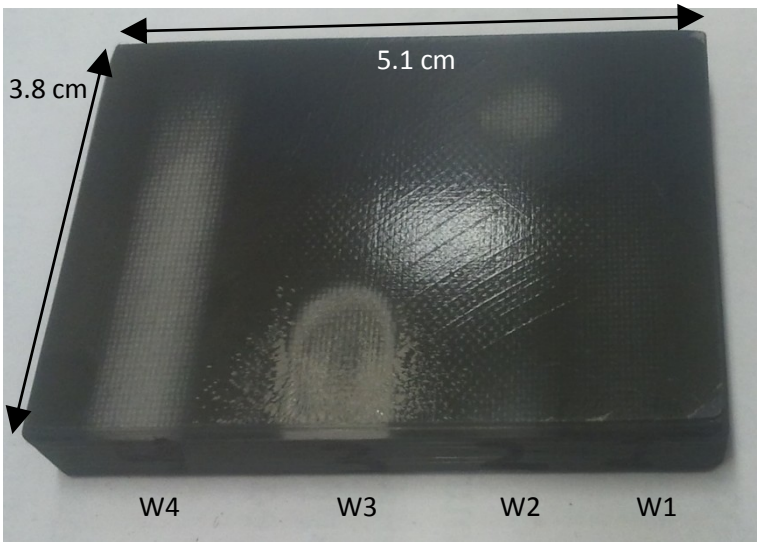

Figure 128: Wipe tests W1, W2, W3, and W4.

SEM images revealed that tin deposited in all 4 test cases (see Figure 129). From these images, we see that tin primarily deposits in a grid pattern. Only in test case W3, where a considerable quantity of powder had reached the substrate, do we see junction being made between tin deposits.

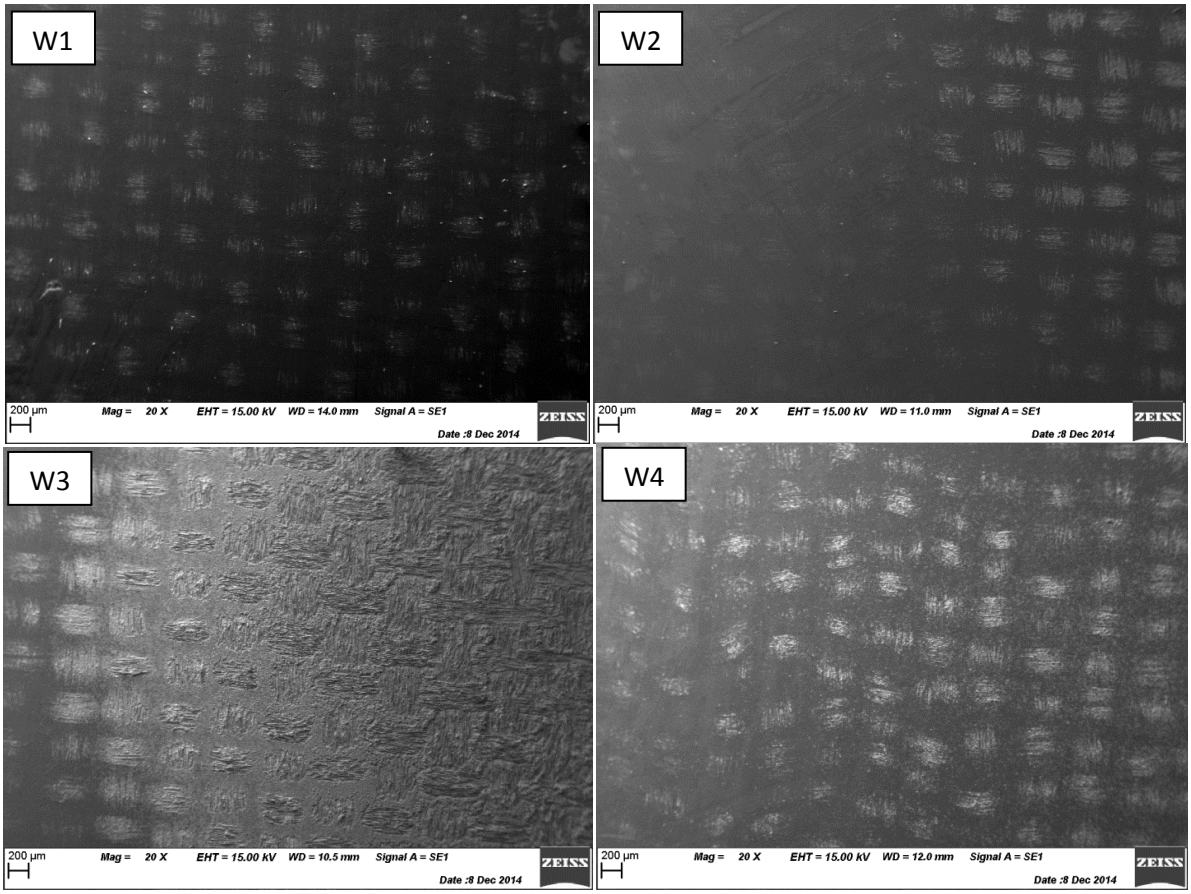

Figure 129: Low magnification SEM images of wipe test W1, W2, W3, and W4.

Higher magnification SEM images show that the tin particles deposit primarily in areas where glass fibres were in proximity to the surface (see Figure 130a). The weaving pattern of the glass fibres make it so that tows of fibres becomes in proximity to the surface in an alternating orientation. Even though the fibres are beneath epoxy, the SEM still manages to detect them as faint light strands. As the glass fibre strands get closer to the surface, they become brighter. Figure 130b reveals that the number of indentation marks on the epoxy from impacting particles is higher when glass fibres were in proximity to the surface. Figure 130c demonstrates that the tin particles adhere directly above reinforcement fibres close to the surface. Figure 130d exhibits a highly magnified SEM image of a single tin particle adhered to the WGFP BMS 8-276. It is thought that the reason behind these localized depositions can be explained by an increased likelihood of deformation. The elevated hardness of the glass fibres directly underneath the epoxy limits the epoxy's capability to absorb the particle impact in an elastic fashion. With less epoxy to strain, a plastic deformation

occurs leaving indentation marks where particles did not manage to adhere. Then again, tin particles also require high quantities of strain to deform and adhere to the substrate

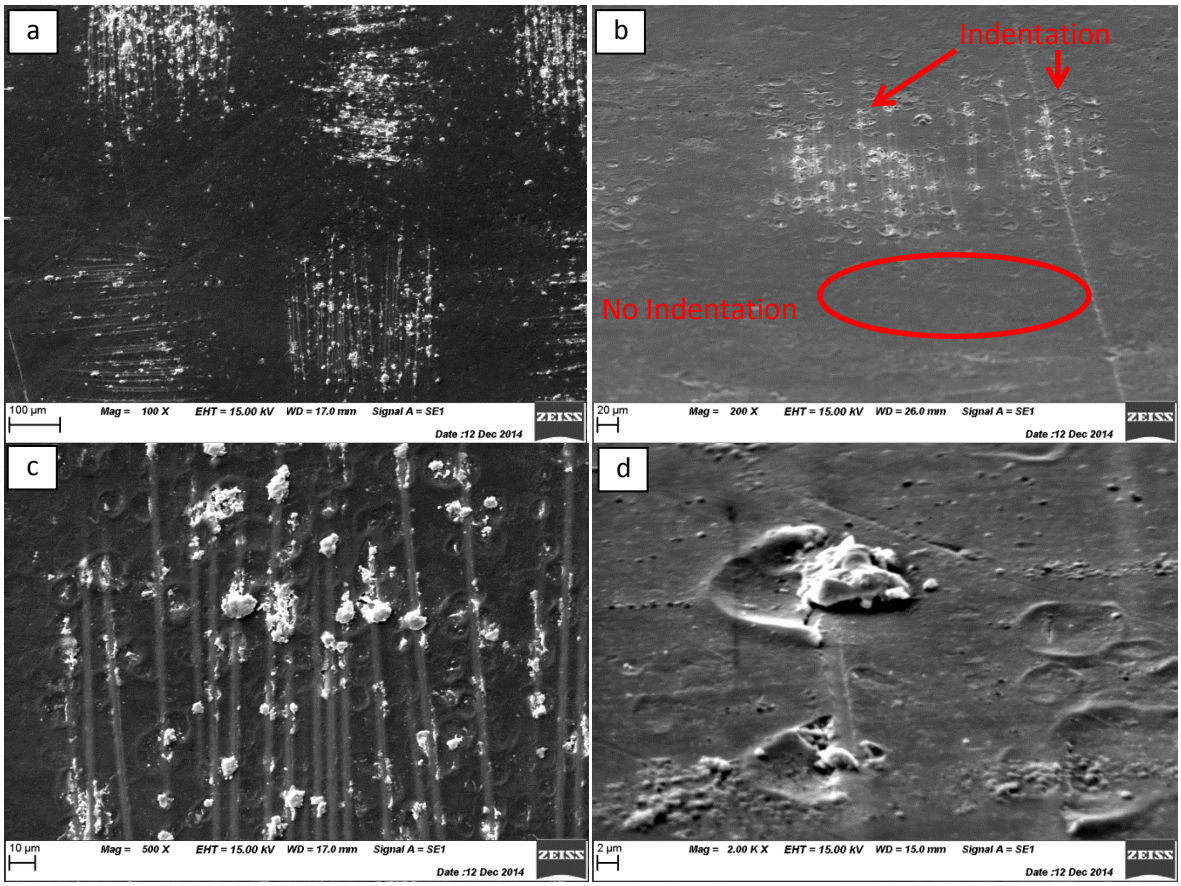

Figure 130: (a) SEM image of tin particles primarily deposited on areas where glass fibres are close to the surface, (b) showing an increase in the number of indentation marks near these areas and (c) tin particles directly adhering to locations above which reinforcement fibres are close to the surface (d) with high magnification of single tin particle deformed above epoxy covered glass fibre.

When looking at wipe tests of high TV (i.e. W1 and W4), instances of damaged epoxy was evident (see Figure 131). As explained before, high traverse velocities lower local heat during deposition. As a result, the substrate is cooler making it more brittle and likely to fracture. Fracturing the epoxy is not of great concern for these traverse velocities since earlier experiments have shown that a tin coating can indeed be deposited. However, Figure 131b presents a close-up of a specific substrate fracture where not only the epoxy but also the fibres were damaged. Damaging the fibres is not desired for they are believed to be involved in the adhesive strength of the deposited coating. The fractures observed varied from dozen of microns in size to cracks less than 1 micron wide (see Figure 131c & Figure 131d). The indentation marks analyzed sometimes included droplet-like

quantities of tin (see Figure 131d). This tin residue is thought to originate from a single impacting particle undergoing localized heating. As mentioned in section 2.3.6, the particle impact occurs in a very short period of time which causes localized heating. In this particular instance, the adhesion to the epoxy is thought to be low enough for the gas flow to blow the particle off leaving minute molten parts of the tin particle.

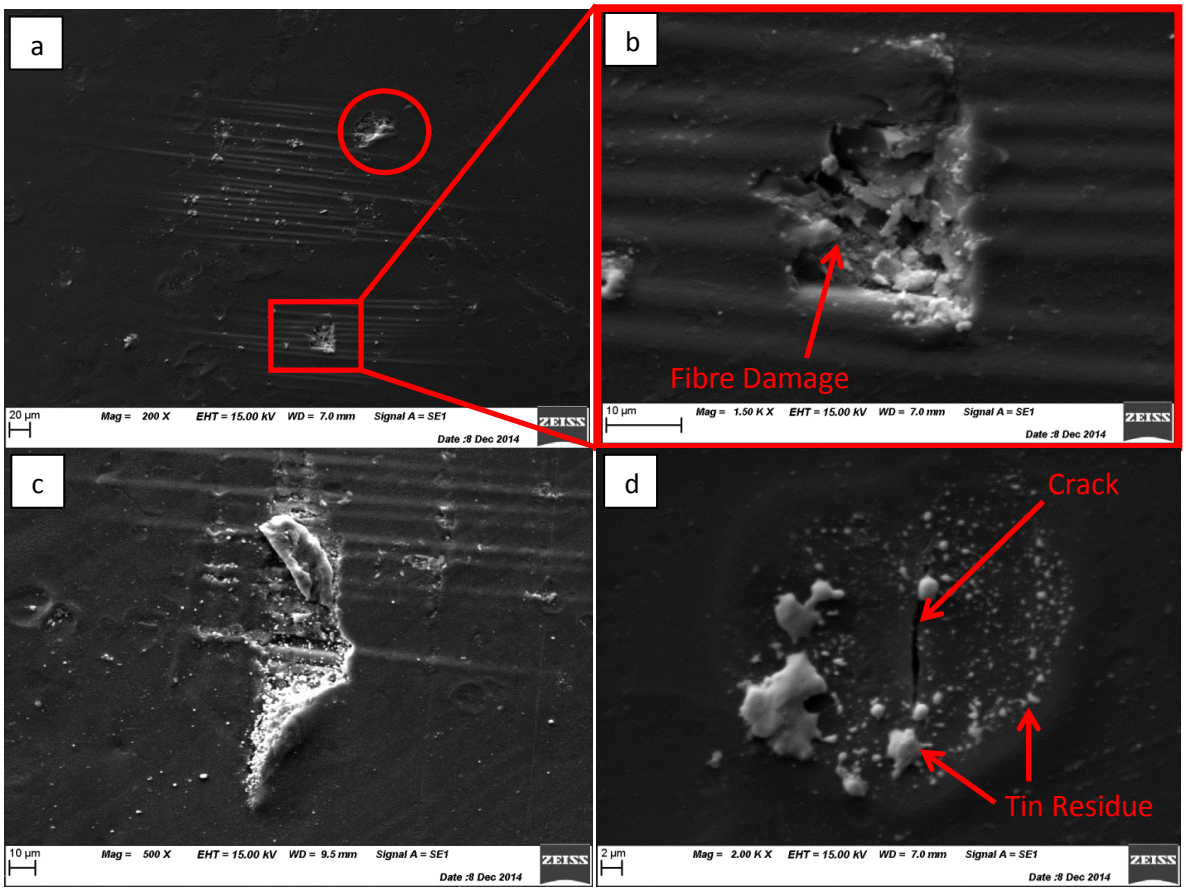

Figure 131: SEM images of fractured BMS 8-276 of (a) sample W4 with (b) close-up of fracture zone, (c) sample W1, and (d) micro-crack of sample W4.

When looking at the wipe test of extreme low TV (i.e. W3), the wave-like pattern seen in section 5.1.3 can be identified (see Figure 132a & Figure 132b). The large quantity of tin sprayed ends up semi-molten and splattered to nearby areas creating a porous coating. Figure 132c & Figure 132d, taken near the center of the spray, characterizes the large amount of erosion suffered by the BMS 8-276. It is suspected that the high local heat during deposition weakens the toughness of the epoxy making it vulnerable to erosion. Without the matrix's support, the woven glass fibres become

susceptible to fracture. In the absence of a coating build-up, the impacting particles continue to damage and erode the substrate.

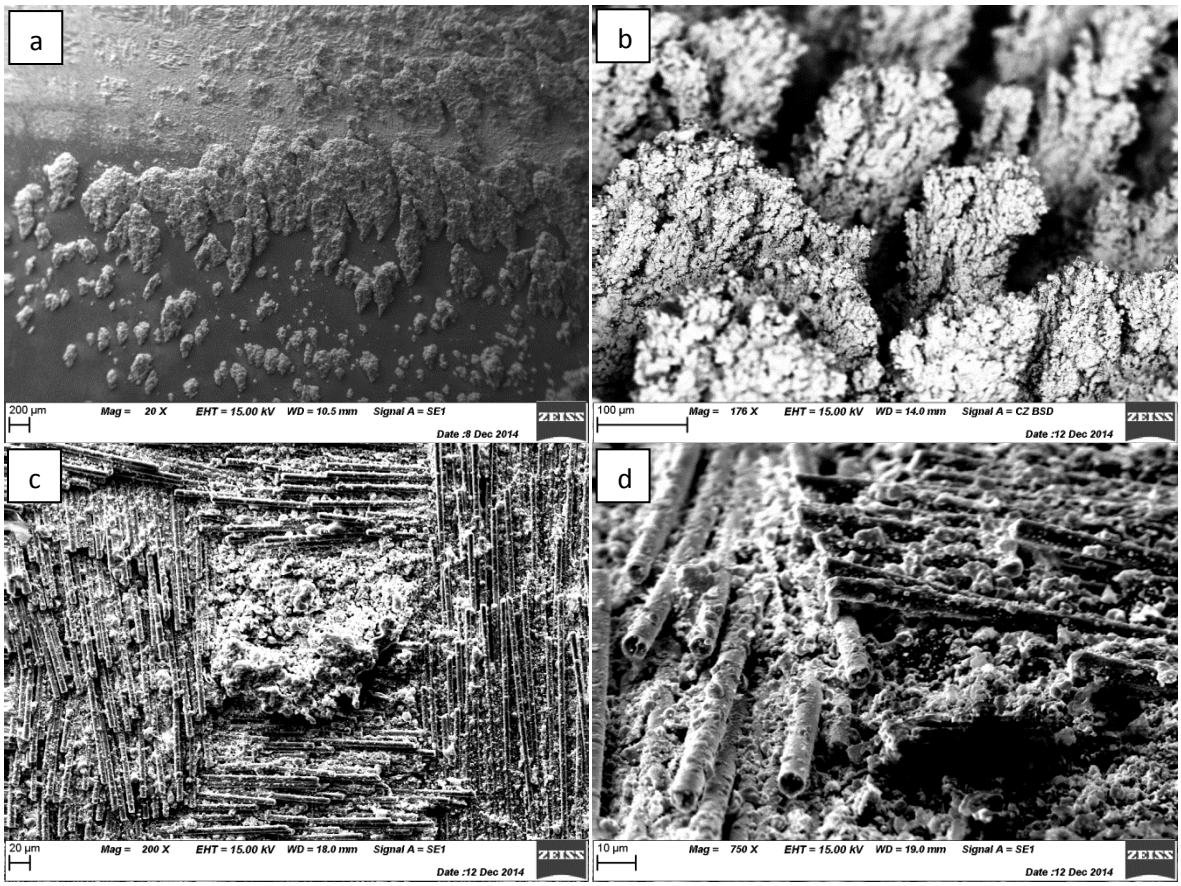

Figure 132: SEM images of wipe test W3 showing (a) tin platter with (b) magnified view of wave-like formation and (c) damaged substrate with (d) magnified view.

SEM images of wipe test W2 reveal that the epoxy is primarily attacked (see Figure 133). Little to no damage to the glass fibres was observed. These images prove that the relevance between the TV and the PFR for the first pass is of great importance. If the proper combination is not selected, anchoring points will not be formed and/or glass fibres will be damaged.

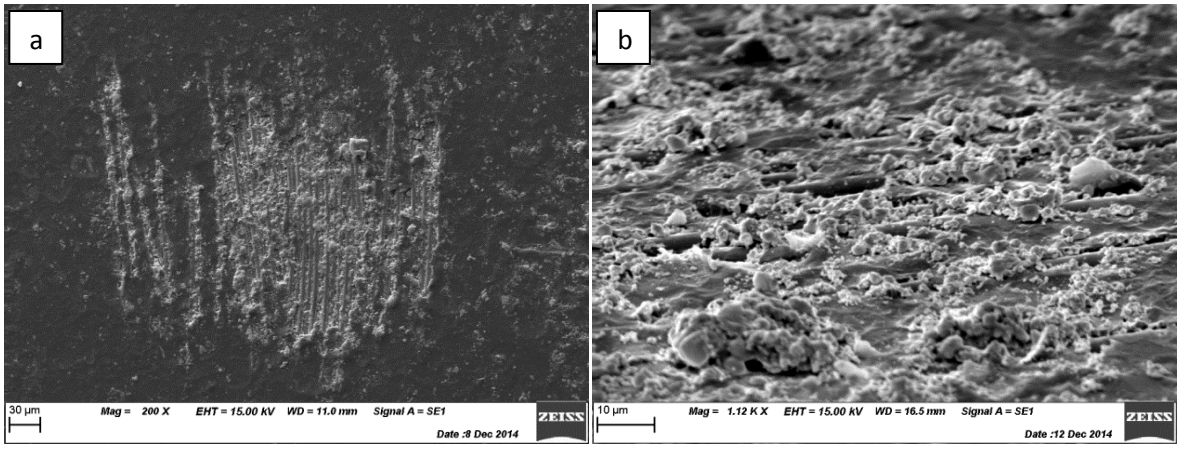

Figure 133: SEM images of (a) wipe test W2 with (b) angled magnification.

5.1.9 Summary

The experiments conducted in this section were able to characterize the effects of certain CGDS parameters while other experiments played a role in describing key components of the metallization of the BMS 8-276 using tin. To start, it was concluded that the stagnation temperature has a severe impact on the deposition of the tin. High temperatures are essential to soften the metallic particles in order to enable them to deform on impact without damaging the BMS 8-276. On the other hand, the stagnation pressure is not of great importance but should not be raised for this tends to cause erosion and damage to the substrate. It was also found that the WGFP provides superior adhesion for the tin coating as compared to the LCFP. The mechanical bonding between the tin coating and the WGFP of the BMS 8-276 appears to be constant regardless of the surface preparation (R_a). It was discovered that the tin particles do not deposit on the toughening heterogeneous system of the BMS 8-276 nor do they deposit on the epoxy matrix of the WGFP. However, it was found that discontinuities can be remedied by increasing the number of passes (creating a bridging effect). The thickness of the tin coating does not seem to have an important effect on the adhesion strength of the coating (for the thicknesses produced). The TV and PFR were shown to have pivotal roles in the degree of fibre embedment as well as in the microstructure of the tin coating. Low TV and high PFR proved beneficial for the adhesion of the tin coating to the WGFP of the BMS 8-276. Then again, high TV enabled the deposition of thick, dense, and continuous tin coatings (preventing a porous wave like formation from occurring).

5.2 Copper Coating Development

No scientific research has been published regarding the deposition of copper on BMS 8-276. The experiments conducted in section 5.1 can be used as a guide to explain possible BMS 8-276 behavior during spraying however, by changing the coating material, the CGDS parameters must once again be optimized. The novelty of this project implied that few parameters were published regarding the successful deposition and build-up of copper on OMCs. As such, much like in the case of tin, optimal parameters were established as an initial goal.

5.2.1 Pure Copper Deposition

As an initial test, pure copper powder was sprayed onto a WGFP BMS 8-276 at a variety of pressures and temperatures (see Figure 134).

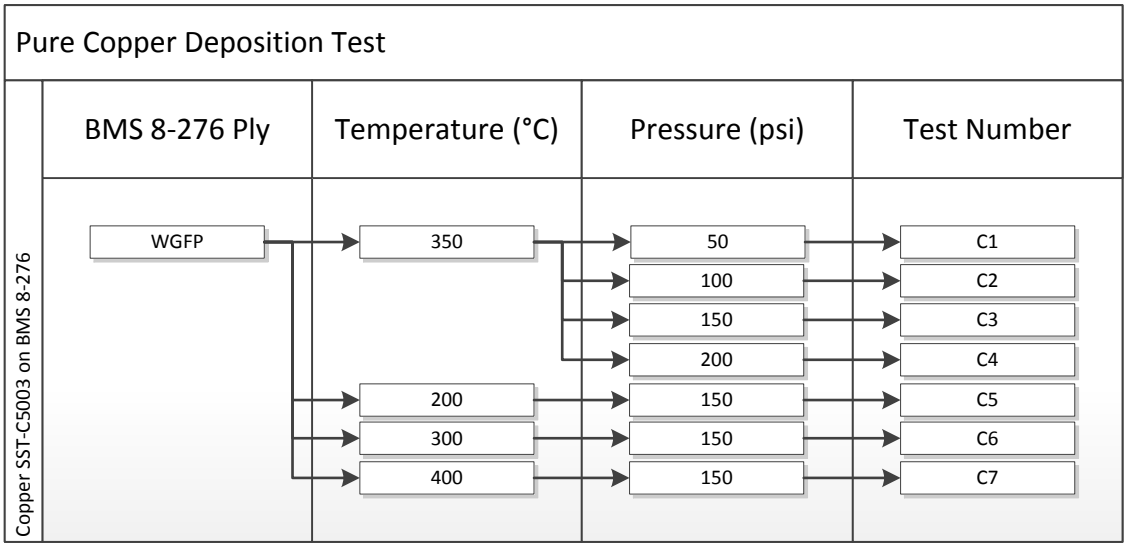

Figure 134: Pure copper deposition temperature and pressure.

All other CGDS parameters were held constant and are presented in Table 18. According to research covered in the literature review, the copper powder from Centerline (SST-C5003) has the highest chance to successfully deposit onto BMS 8-276 for it is irregularly shaped and the substrate matrix is composed of epoxy (see Figure 32a). As such, this powder was selected for this test.

Table 18: CGDS Parameters Held Constant for the Pure Copper Deposition Test.

CGDS Parameter	Value
Gas Nature	Nitrogen
Standoff Distance	10 mm
Nozzle Type	120 mm SS Nozzle
Orifice Diameter	2 mm
Powder Feeder Wheel	240 Medium Hole
Powder Feeder Gas Rate	30 scfh (0.85 m^3/h)
Powder Feed Rate	3 rpm (0.31 rad/s)
Traverse Velocity	15 mm/s
Step Size	2 mm

Unfortunately, no coating was deposited in all seven test cases (see Figure 135). In some instances, a copper tone can be detected visually indicating that isolated copper particles are likely resting on top of the BMS 8-276. It is suspected that the adhesion of the particles is extremely low. The elevated hardness of copper combined with the non-malleable substrate inhibits proper deformation and instead promotes erosion. In all cases, coating build-up did not occur. A bond coat must be incorporated to build a conductive copper coating onto a BMS 8-276 using CGDS.

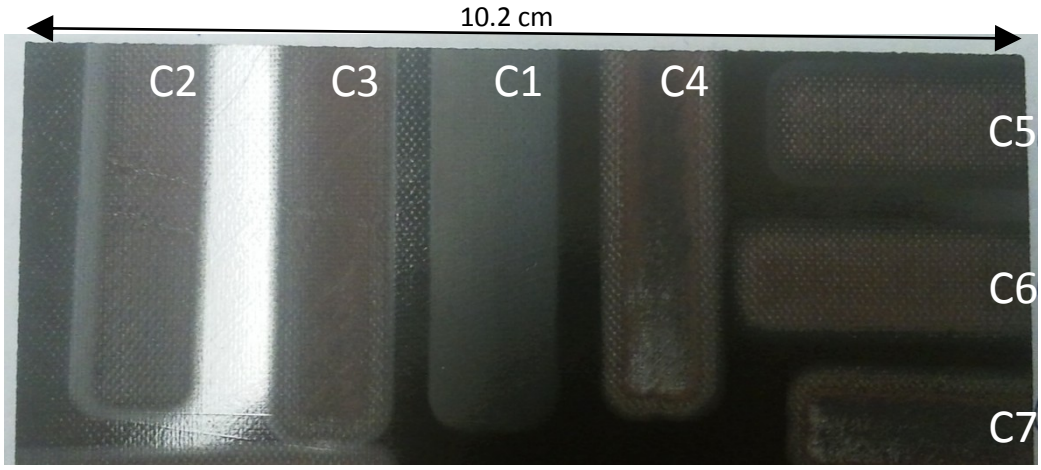

Figure 135: CGDS traces of pure copper deposition test.

5.2.2 Bond Coat Powder Selection

As expressed in the literature review, copper powder is available in a variety of shapes and sizes. As demonstrated by Simon's research, dendritical and spherical shaped copper particles can result in vastly different outcomes [29]. As such, two types of copper powders, produced by different manufacturers, were investigated in order to provide the best overall solution for this research. Trials were conducted using copper powder from Centerline (SST-C5003) and Praxair (Cu-159). Prior work regarding a copper/polymer bond coat has been done by a fellow colleague, Dr. Mohammed Yandouzi (see Appendix I: Dr. Mohammed Yandouzi's Work on Bond Coat Development). His work concluded that three of the four polymers tested (including PEEK 150PF from Victrex) could be successfully combined with aluminum or copper in a variety of feedstock compositions and deposited on BMS 8-276 using the LPCS process. Given the its excellent wear resistance and pre-established use in both thermal spray processes and aerospace application, PEEK was selected as the primary candidate [9], [82], [83]. Based on Dr. Mohammed Yandouzi's findings, the bond coat composition was set at 97.5wt% copper and 2.5wt% PEEK. The lowest quantity of PEEK was specifically selected to minimize stress created by thermal expansion (PEEK has the highest thermal expansion coefficient compared to BMS 8-276 and copper) and to maximize the conductivity of the bond coat. Three different powder combinations were tested (see Table 19). By mixing the two different copper powders in equal parts, a third data point was created emphasizing the influence of each powder which facilitates the decision making.

Table 19: Three Different Powder Combinations Used for the 97.5wt% Copper and 2.5wt% PEEK Bond Coat Trials

Powder Combination	SST-C5003	Cu-159	PEEK
1	97.5wt%	0wt%	2.5wt%
2	0wt%	97.5wt%	2.5wt%
3	48.75wt%	48.75wt%	2.5wt%

As a primary experiment, a range of pressures (60 psi to 150 psi) (0.41 MPa to 1.03 MPa) and temperatures (200°C to 350°C) were independently varied while holding all other parameters constant for each powder combination. The BMS 8-276 was prepared to expose a LCFP. The gas nature, standoff distance, nozzle type, orifice diameter, powder feeder wheel, powder feeder gas

rate, powder feed rate, traverse velocity, and step size were held constant at values recommended by the CGDS supplier (Centerline (Windsor) Ltd). These values are provided in Table 20.

Table 20: CGDS Parameters Held Constant for the 97.5wt% Copper and 2.5wt% PEEK Bond Coat Trials

CGDS Parameter	Value
Gas Nature	Nitrogen
Standoff Distance	10 mm
Nozzle Type	120 mm SS Nozzle
Orifice Diameter	2 mm
Powder Feeder Wheel	240 Medium Hole
Powder Feeder Gas Rate	30 scfh (0.85 m^3/h)
Powder Feed Rate	3 rpm (0.31 rad/s)
Traverse Velocity	10 mm/s
Step Size	2 mm

Based on these trials, a pressure of 110 psi (0.76 MPa) and a temperature of 350°C proved to be favorable conditions for all three types of bond coats. By increasing the pressure further, inconsistent deposition and erosion were noticed. When spraying with lower pressures the coating did not build-up as quickly and in some instances it did not build-up at all. For the temperature, the results indicated that a high temperature was imperative to the deposition of the composite bond coat. Even though the CGDS system can reach temperatures of 500°C, experiments conducted by fellow colleagues have indicated that the stainless steel nozzle is at risk of clogging when the temperature is brought beyond 350°C. As specified, these parameters provide optimal DE and uniformity for all three combinations of 97.5wt% copper and 2.5wt% PEEK bond coat.

With the parameters set above, 97.5wt% copper and 2.5wt% PEEK bond coats were deposited on large LCFP BMS 8-276 substrates to test their behavior when sprayed with a pure copper top coat. All parameters of the composite bond coat were set to identical values with the exception of the TV (see Table 21).

Table 21: CGDS Parameters Held Constant for the 97.5wt% Copper and 2.5wt% PEEK Bond Coat Selection

CGDS Parameter	Value
Gas Pressure	110 psi (0.76 MPa)
Gas Temperature	350°C
Gas Nature	Nitrogen
Standoff Distance	10 mm
Nozzle Type	120 mm SS Nozzle
Orifice Diameter	2 mm
Powder Feeder Wheel	240 Medium Hole
Powder Feeder Gas Rate	30 scfh (0.85 m^3/h)
Powder Feed Rate	3 rpm (0.31 rad/s)
Step Size	2 mm

The TV was specifically tailored to each powder combination to produce coatings of similar thickness (see Figure 136). It was observed that the composite bond coat composed with Cu-159 had a higher DE than the composite bond coat composed with SST-C5003. The composite bond coat composed with both SST-C5003 and Cu-159 lied somewhere in between.

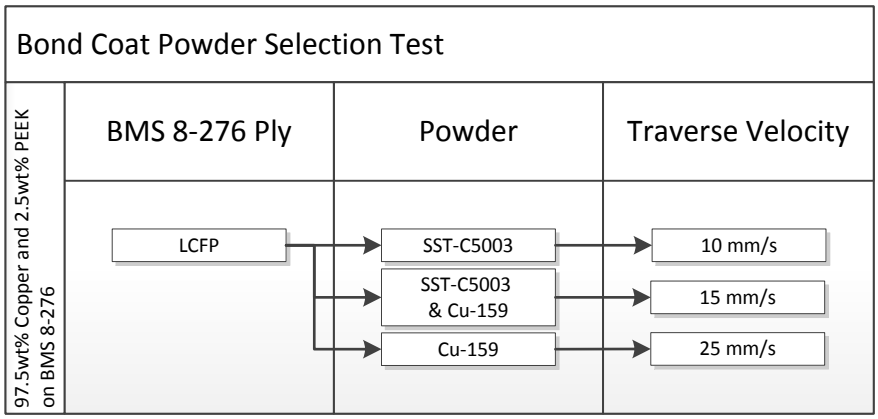

Figure 136: Traverse velocities for the bond coat powder selection test.

Figure 137 presents the three different bond coats successfully deposited on 4" X 6" (10.2 cm X 15.2 cm) LCFP BMS 8-276 substrates. All three types of bond coats demonstrated a smooth and uniform deposition. However, certain discontinuities are apparent throughout some coatings, especially the composite bond coat composed of 97.5wt% SST-C5003 and 2.5wt% PEEK. Difficulties were

encountered during the surface preparation of that particular sample making it uneven in particular locations. It is possible that the toughened heterogeneous interface was exposed in certain locations. Much like tin, it is thought that the composite bond coat may not deposit at an even rate on all the components of the BMS 8-276. This phenomenon will be further explored in section 5.2.3.

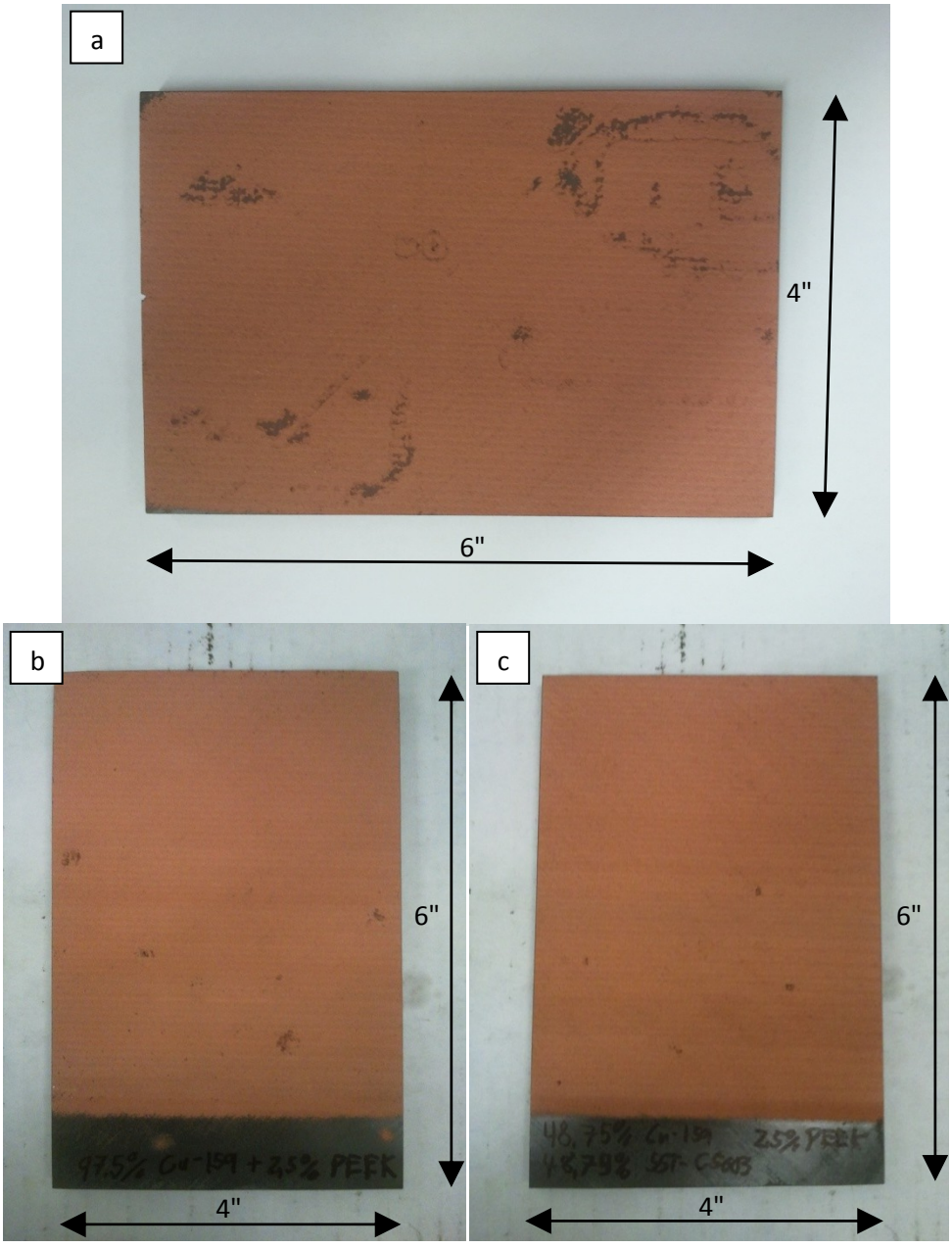

Figure 137: (a) 97.5wt% SST-C5003 and 2.5wt% PEEK bond coat on grit blasted BMS 8-276, (b) 97.5wt% Cu-159 and 2.5wt% PEEK bond coat on grit blasted BMS 8-276, and (c) 48.75wt% SST-C5003, 48.75wt% Cu-159 and 2.5wt% PEEK bond coat on grit blasted BMS 8-276.

An array of conductive top coats were subsequently deposited on all bond coat covered substrates. The majority of the spray parameters for each type of pure copper top coat remained unchanged from one spray to the next. The gas nature, standoff distance, traverse velocity, nozzle type, orifice diameter, powder feeder wheel, powder feeder gas rate, powder feed rate, and step size remained identical for all sprays (see Table 22)

Table 22: CGDS Parameters Held Constant for the Pure Copper Top Coats Trials

CGDS Parameter	Value
Gas Nature	Nitrogen
Standoff Distance	10 mm
Nozzle Type	120 mm SS Nozzle
Orifice Diameter	2 mm
Powder Feeder Wheel	240 Medium Hole
Powder Feeder Gas Rate	30 scfh (0.85 m^3/h)
Powder Feed Rate	3 rpm (0.31 rad/s)
Step Size	2 mm
Traverse Velocity	10 mm/s

Once again, the gas pressure and temperature were altered between sprays in order to establish effective parameters promoting deposition. Figure 138 presents the gas pressure and gas temperature combinations used for the top coat trials. Each top coat trial has been assigned a specific number (written beside the data point). The Praxair copper (Cu-159) top coats were delaminating from the 97.5wt% SST-C5003 and 2.5wt% PEEK bond coat and therefore were not deposited on other developed bond coats (97.5wt% Cu-159 and 2.5wt% PEEK as well as 48.75wt% SST-C5003, 48.75wt% Cu-159, and 2.5wt% PEEK).

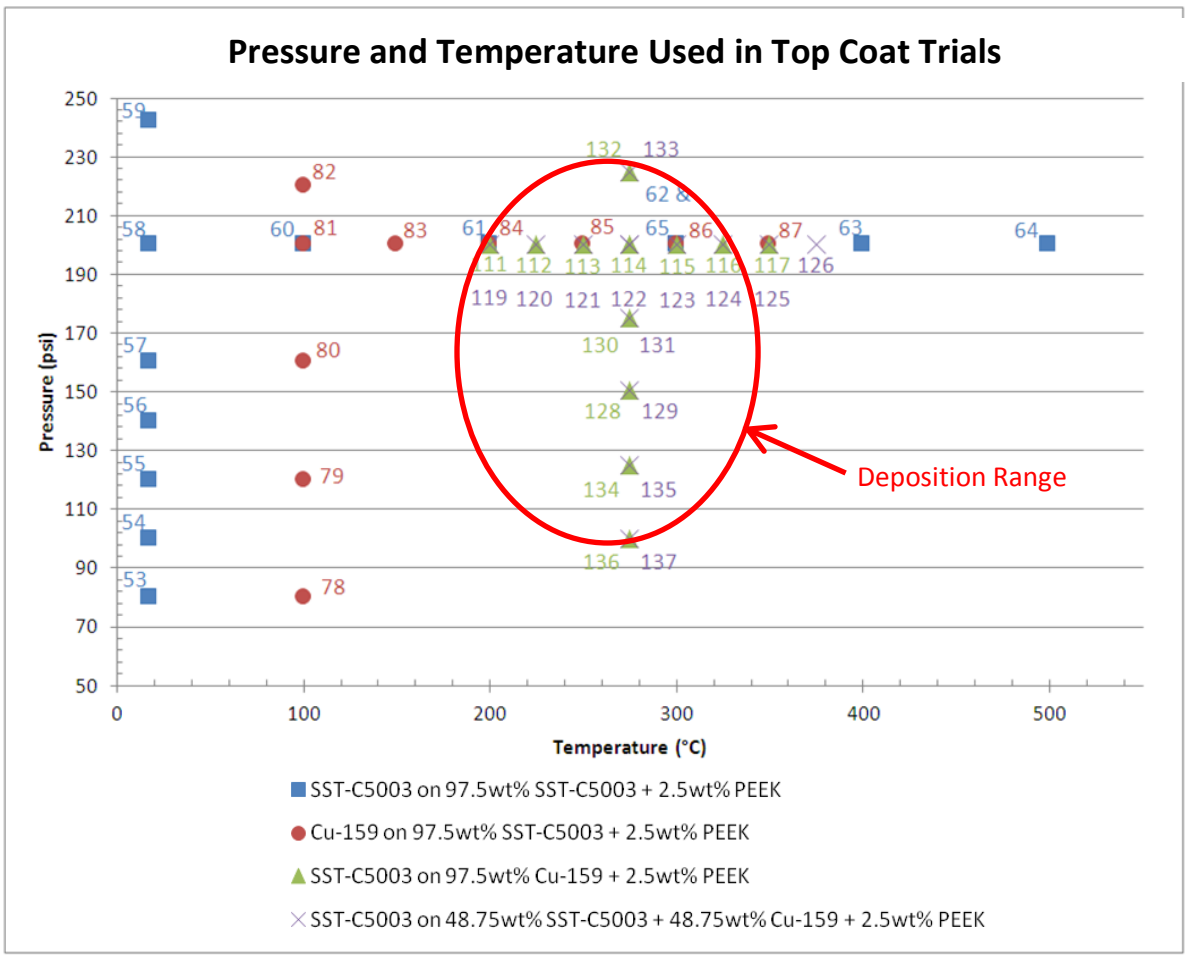

Figure 138: Pressure/temperature combinations used for the top coat trials (trial numbers are indicated beside each data point).

Figure 139 presents the pure copper top coats applied to the composite bond coats. It is important to note that despite their appearance, some top coats are in fact erosion marks of the composite bond coat from the sprays (the deposition range is outlined in Figure 138).

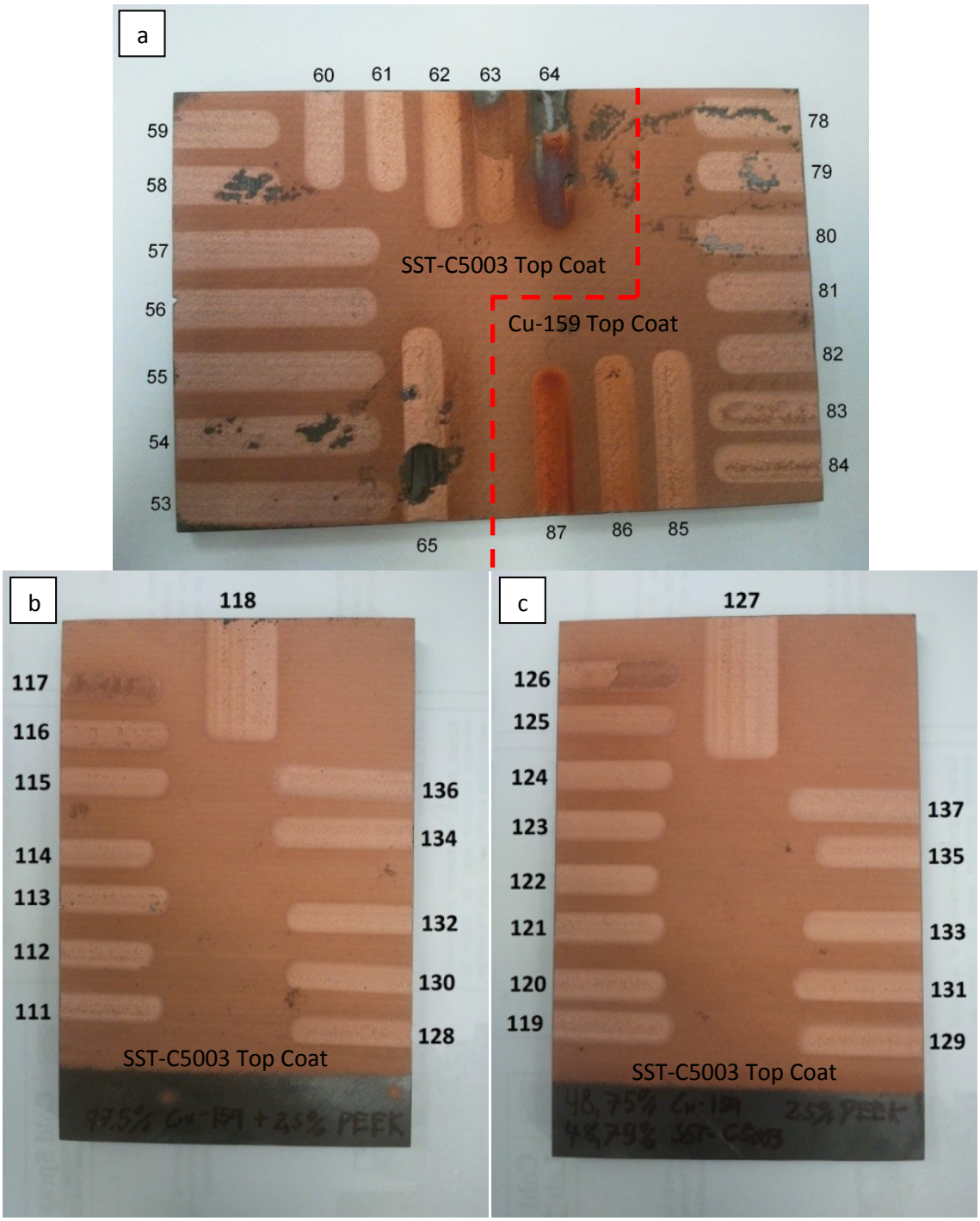

Figure 139: (a) Top coat trials on 97.5wt% SST-C5003 and 2.5wt% PEEK bond coat, (b) top coat trials on 97.5wt% Cu-159 and 2.5wt% PEEK bond coat, (c) top coat trials on 48.75wt% SST-C5003, 48.75wt% Cu-159 and 2.5wt% PEEK bond coat.

Table 23 presents a short comparative summary of the four different combinations tested. The top coat pure copper powder is specified in Table 23 along with the copper and PEEK mixture (in weight percent) used for the bond coat in each test case. Table 23 also indicates the specific trial number

for each top coat spray completed. The location of each top coat spray is noted along the edge of the substrate in the “Layout” section. Each top coat spray trial that resulted in copper deposition is indicated in the “Deposited Copper” section. It is to be noted that the trial numbers in parentheses represent trials that were not analyzed because of their fragile state. Optical images of the cross-sections are presented in the last sections of Table 23.

Table 23: Comparison of Different Copper Top Coats and Bond Coats

	Combination 1	Combination 2	Combination 3	Combination 4
Top Coat	SST-C5003	Cu-159	SST-C5003	SST-C5003
Bond Coat	97.5wt% SST-C5003 + 2.5wt% PEEK	97.5wt% SST-C5003 + 2.5wt% PEEK	97.5wt% Cu-159 + 2.5wt% PEEK	48.75wt% SST-C5003 + 48.75wt% Cu-159 + 2.5wt% PEEK
Spray Trial #	53-65	78-87	111-118 & 128, 130, 132, 134, 136	119-127 & 129, 131, 133, 135, 137
Deposited Copper	61, 62, (63, 64)	(83, 84), 85, 86, 87	All except 117	All except 137
Layout	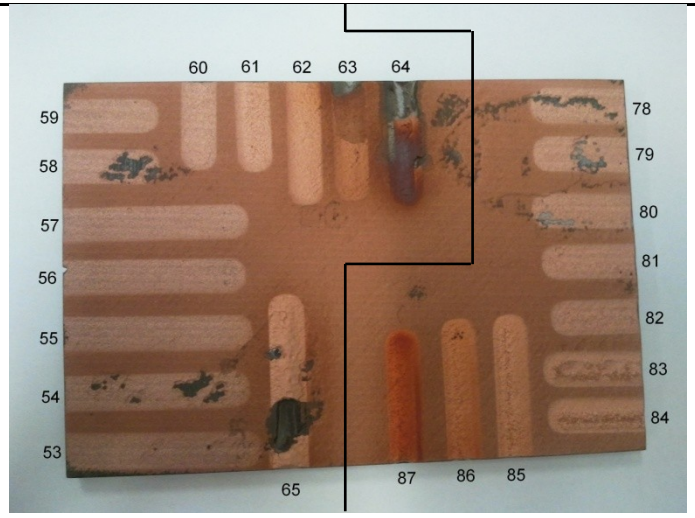		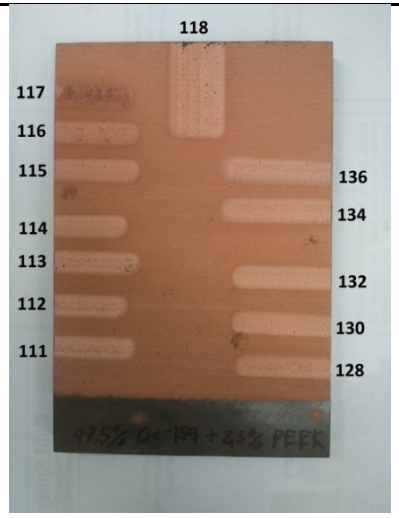	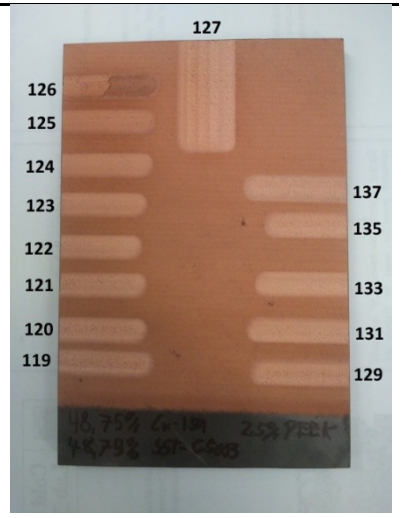

Example of an Optimal Cross-Section (100X)	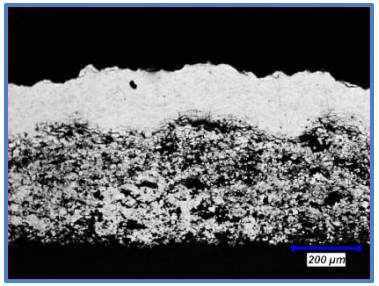	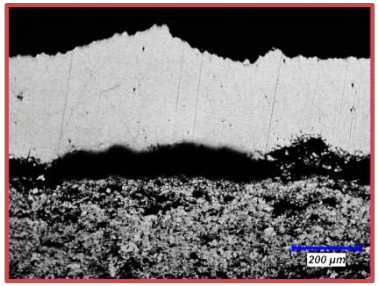	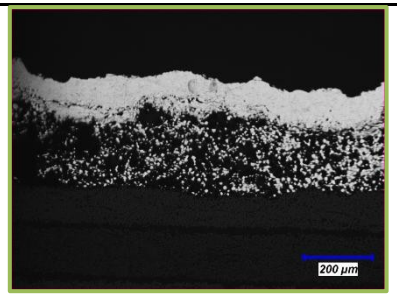	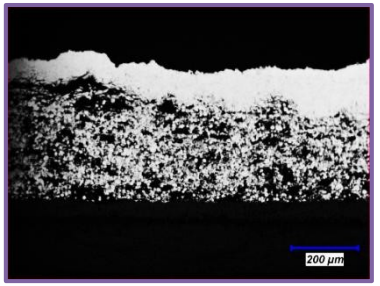
	Trial 62	Trial 86	Trial 130	Trial 124
Example of a Typical Top Coat (200X)	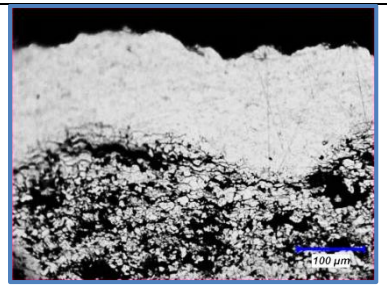	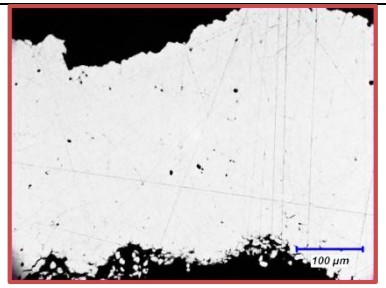	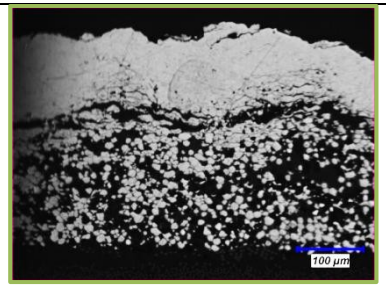	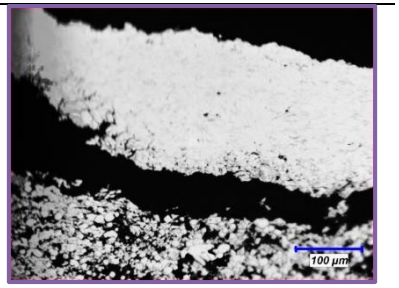
	Trial 62	Trial 87	Trial 132	Trial 125
Example of a Typical Bond Coat (200X)	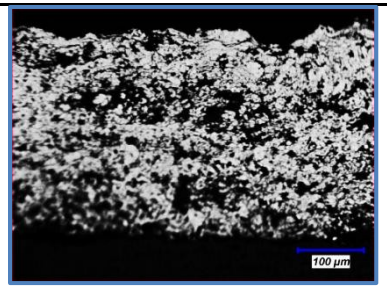	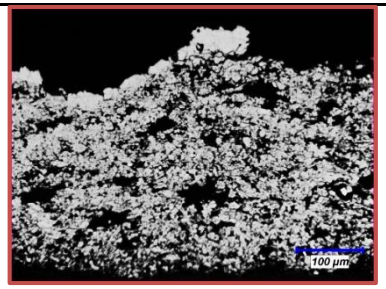	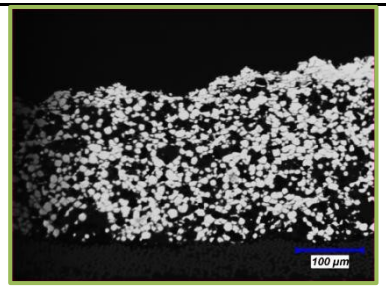	
	Trial 60	Trial 87	Trial 134	Trial 135
Notes	● Top coat has few cracks	● Top coat always delaminates from bond coat	● Cracks often found in top coat ● Delamination between top coat and bond coat is frequent	● Some cracks are apparent in the top coat ● Delamination between top coat and bond coat is frequent

Coatings from Combination 1 were characterized by a transition zone between the bond coat and the top coat (where the PEEK content slowly decreases). Concentrations of cracks were seen in the transition zone. The cracks could be created in the early deposition stage of the spray because of the soft bond coat. The initial copper particles that were deformed on the bond coat were not well constrained by the softened PEEK and thus were more susceptible to shift when hit by later copper particles, reducing the cohesion between the copper particles and facilitating the initiation of cracks.

All top coats from Combination 2, although fully dense and free of cracks, delaminated from the bond coat. The spherical shape of the copper powder (Cu-159) required more deformation which subsequently increased the compressive residual stresses at the surface of the top coat while increasing the corresponding tensile residual stresses at the interface with bond coat. This tensile stress is thought to be the primal cause of the top coat's delamination. This conclusion led to the early decision of removing Cu-159 powder as a possible candidate to produce a conductive top coat.

Coatings from Combination 3 were characterized by delamination between the top coat and bond coat as well as severe cracks in the top coat. The cracks could once again be initiated by the soft bond coat much like in Combination 1. The delamination between the top coat and the bond coat could be a result of poor cohesion between the spherical copper (Cu-159) in the bond coat and the dendritic copper (SST-C5003) in the top coat. The elongated particles of the SST-C5003 were more susceptible to deformation than the Cu-159 embedded in PEEK because the shape of the SST-C5003 promotes stress concentration which leads to yielding. As a result, the smooth spherical shape of the Cu-159 particles combined with the damping effect of the PEEK matrix prevents proper anchoring of the SST-C5003 powder thus resulting in delamination.

In Combination 4, with a mix of SST-C5003 and Cu-159 in the bond coat, traits of both Combination 1 and Combination 3 were apparent. Once again, instances of delamination between the top coat and bond coat as well as cracks in the top coat were noted in these trials.

Imaging software was used to analyze the composition of each bond coat. Figure 140 shows that the volume percent of copper in the coatings varied depending on the type of copper used in the

bond coat. Theoretical calculations estimated the volumetric percentage of copper to be 85% in a mixture of 97.5wt% copper and 2.5wt% PEEK without porosity (see Appendix V). As presented in Figure 140, the bond coat composed of 97.5wt% Cu-159 and 2.5wt% PEEK had the lowest volume percent of copper (≈51%).Both bond coats composed of 97.5wt% SST-C5003 and 2.5wt% PEEK had the highest volume percent of copper (≈81%). This variation can be a result of the dendritic shape of the SST-C5003 copper powder in comparison to the spherical shape of the Cu-159 copper powder. It is difficult to obtain a high volumetric percentage of a material that has spherical shaped particles because of the voids that occur between particles. In addition, it was noted that the 97.5wt% Cu-159 bond coat had regions of porosity of similar magnitude and shape as the Cu-159 powder. This is an indication that Cu-159 powder could have been removed from the bond coat surface during polishing leaving behind a pore. This explains the drastic increase in porosity in the bond coats containing Cu-159 particles.

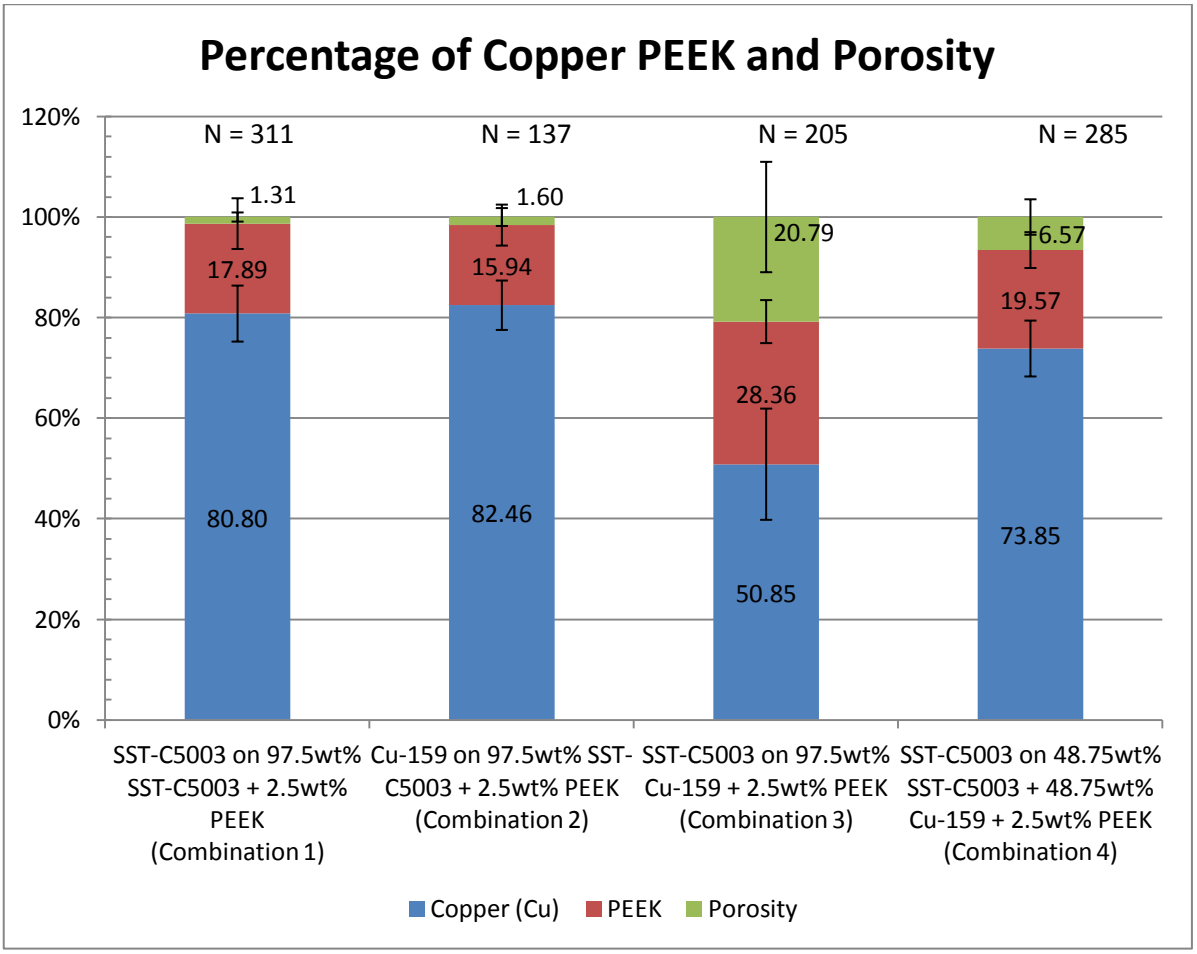

Figure 140: Bond coat composition percentages.

Taking all of the results into consideration, SST-C5003 top coat on a 97.5wt% SST-C5003 and 2.5wt% PEEK bond coat (Combination 1) seems to produce the overall best combination. The top coats contain very few cracks and show no signs of delamination with the bond coat. The use of spherical copper powder (Cu-159) in combinations 2, 3, and 4 was determined to be the culprit for the delamination of the top coat to the bond coat. In addition, the bond coat from Combination 1 presented low porosity. The introduction of spherical copper (Cu-159) into the bond coat increased the amount of voids due to pullout during polishing. This low adhesion between the PEEK and the Cu-159 further pressed the elimination of Cu-159 as a possible candidate for further optimization in this research. Combination 1 was therefore selected for further optimization. Optimal spray parameters for the SST-C5003 top coat seem to be in the neighborhood of 200 psi (1.39 MPa) and 250°C.

5.2.3 Deposition

Experiments conducted in the previous section indicated that the composite bond coat may not deposit evenly on all the components of the BMS 8-276. Much like tin (section 5.1.4), an experiment was devised to verify if the composite bond coat deposits on the toughening heterogeneous system of the BMS 8-276. Pieces of BMS 8-276 were prepared to purposefully expose multiple LCFPs. The LCFP interfaces on the substrate were not distinguishable by touch but only through visual inspection with proper lighting. Composite bond coats were subsequently sprayed using parameters established in the previous section. These sprays revealed a discontinuous deposition on the substrates (see Figure 141).

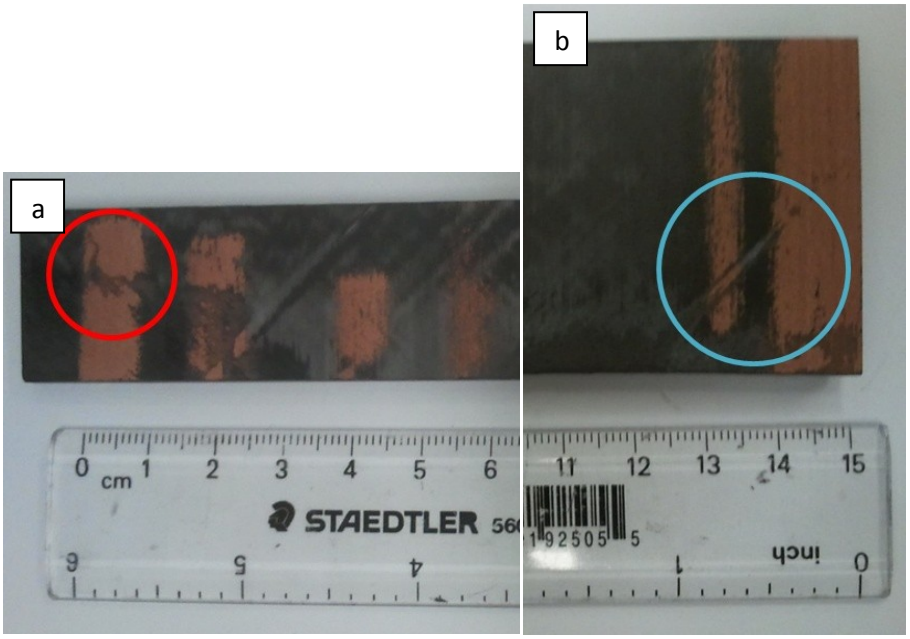

Figure 141: Discontinuities in 97.5wt% SST-C5003 and 2.5wt% PEEK bond coat on (a) a smooth BMS 8-276 substrate and (b) a BMS 8-276 substrate grit blasted with a 20 grit size at 150 psi (1.03 MPa). Both substrates have multiple LCFPs exposed.

A visual inspection of the coatings indicate that the discontinuities of the bond coat occur near the interface of the LCFPs. Figure 142 depicts the cuts that were made in order to analyze the discontinuities.

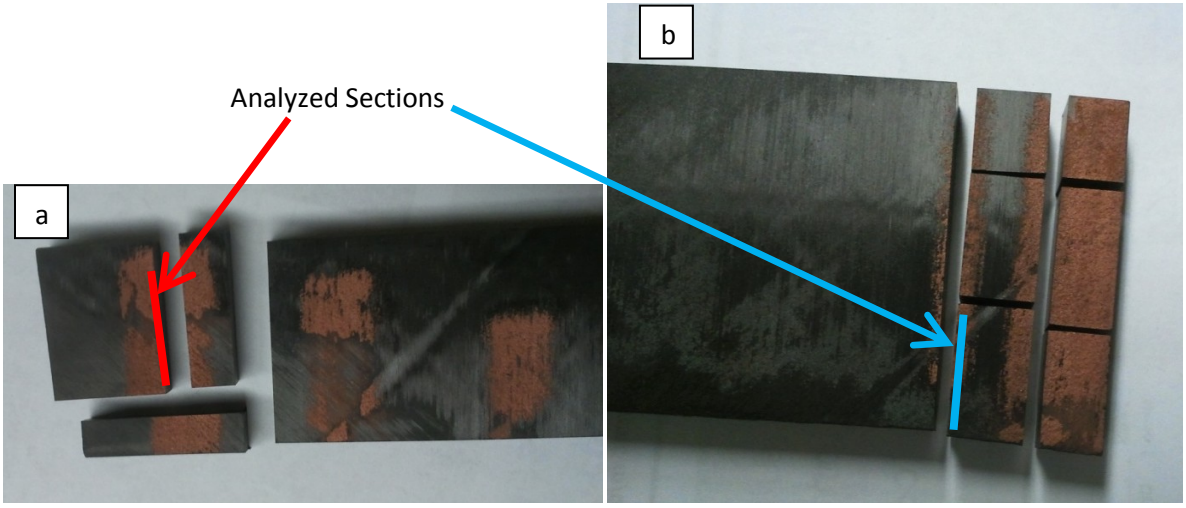

Figure 142: Analyzed sections of (a) 97.5wt% SST-C5003 and 2.5wt% PEEK Bond Coat on (a) a smooth BMS 8-276 substrate and (b) a BMS 8-276 substrate grit blasted with a 20 grit size at 150 psi (1.03 MPa) (see Figure 141). Both substrates have multiple LCFPs exposed.

The colored lines show the specific faces that were observed in Figure 143. Cross-sectional analysis of the highlighted faces shows two different instances where the toughening heterogeneous system of the BMS 8-276 is exposed without bond coat deposition. Figure 143a depicts a transition from one LCFP to another with the heterogeneous toughening material in between. Figure 143b and Figure 143c provide magnified images of the areas where the exposure of the toughening heterogeneous system begins and ends. Figure 143d shows an island of bond coat deposited on an island of carbon fibre reinforced epoxy surrounded by the toughening heterogeneous system.

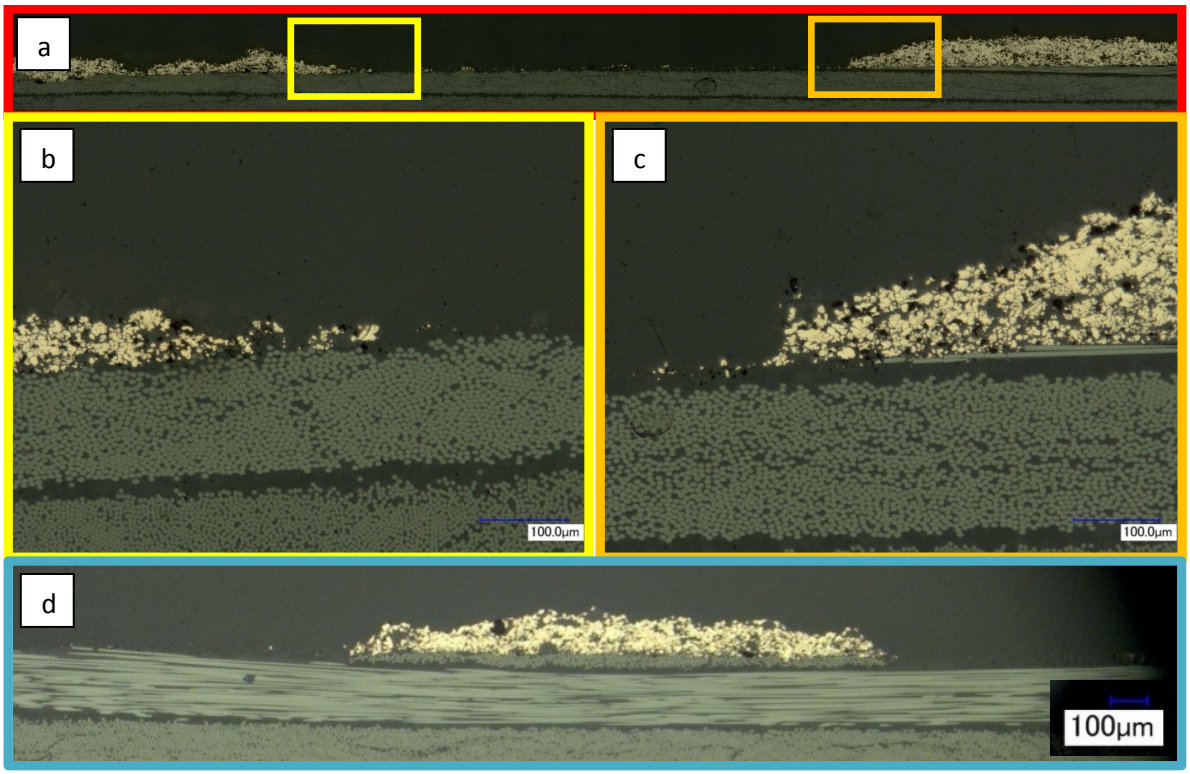

Figure 143: (a) Overall cut of a 97.5wt% SST-C5003 and 2.5wt% PEEK bond coat on a BMS 8-276 substrate (see Figure 142a), (b) Zoom of the location where the thermoplastic layer starts, (c) Zoom of the location where the carbon fibre reinforced epoxy layer starts, and (d) another 97.5wt% SST-C5003 and 2.5wt% PEEK bond coat on an island of CFRE surrounded by the toughening heterogeneous system (see Figure 142b).

In both cases, the bond coat stops adhering to the substrate when the toughening heterogeneous system is exposed. The toughening heterogeneous system was specifically added to the BMS 8-276 composite to protect it from damaging impacts (see section 2.2.6). The resin rich interlayer likely absorbs a majority of the energy of the impacting particles which prevents them from properly deforming. Without proper deformation, the particles cannot adhere to the surface and no coating is produced. This is a possible explanation why the composite bond coat does not deposit on the

toughening heterogeneous system of the BMS 8-276. By not exposing the toughening heterogeneous system, the bond coat should deposit in a continuous manner.

5.2.4 Composite Bond Coat on WGFP

The composite bond coat was not yet deposited on the WGFP of the BMS 8-276. The following test was aimed to determine the deposition behavior of the composite bond coat on the WGFP of the BMS 8-276. The parameters established in section 5.2.2 for the 97.5wt% SST-C5003 and 2.5wt% PEEK bond coat were used for all sprays conducted on the WGFP BMS 8-276 (see Table 24). As mentioned, these parameters provided optimal DE and uniformity for the LCFP of the BMS 8-276.

Table 24: CGDS Parameters Held Constant for the 97.5wt% SST-C5003 and 2.5wt% PEEK Bond Coat on WGFP BMS 8-276

CGDS Parameter	Value
Gas Pressure	110 psi (0.76 MPa)
Gas Temperature	350°C
Gas Nature	Nitrogen
Standoff Distance	10 mm
Nozzle Type	120 mm SS Nozzle
Orifice Diameter	2 mm
Powder Feeder Wheel	240 Medium Hole
Powder Feeder Gas Rate	30 scfh (0.85 m^3/h)
Powder Feed Rate	3 rpm (0.31 rad/s)

The traverse velocity, the step size, and the number of passes were revised between sprays in order to deposit an even and continuous bond coat on the WGFP BMS 8-276 (see Figure 144).

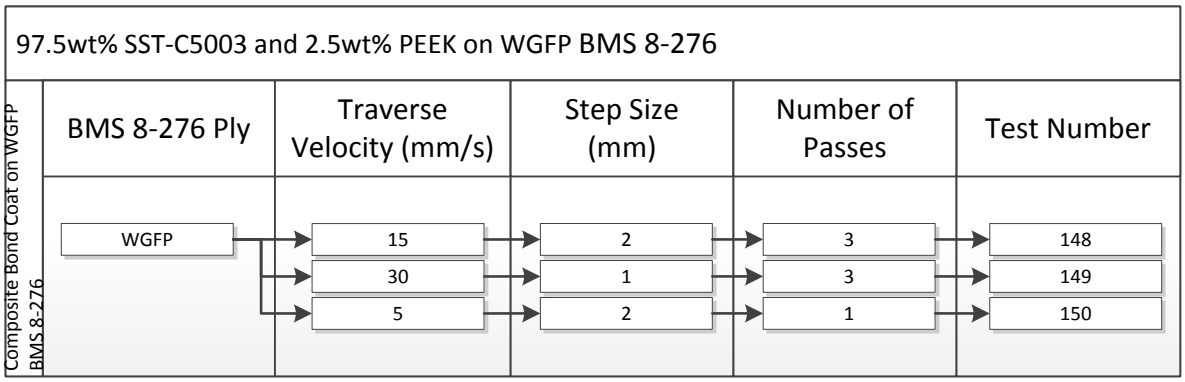

Figure 144: Traverse velocities, step sizes, and number of passes for the 97.5wt% SST-C5003 and 2.5wt% PEEK bond coats on WGFP BMS 8-276.

It was noticed that pits were developing during the deposition of trial number 148 (see Figure 145). For trial number 149, the TV was doubled and the step size was cut down to half while the number of passes remained identical. Theoretically, these changes should not alter the total amount of sprayed particles per area but distribute the powder and local heat more evenly. The result (depicted in Figure 145) was an increase in the quantity of pits throughout the coating. For the final trial (number 150), the step size was returned to 2mm, the TV was lowered dramatically, and the number of passes was also lowered in order to maintain an identical theoretical sprayed particles per area while increasing the local heat during deposition. These parameters provided a continuous bond coat (see Figure 145).

Figure 145: 97.5wt% SST-C5003 and 2.5wt% PEEK bond coat trial number 148, 149, and 150 on WGFP BMS 8-276.

Cross-sectional analysis revealed the variation between the thickest and thinnest points (excluding the discontinuities) of the composite coating were very large (>400 µm) (see Figure 146).

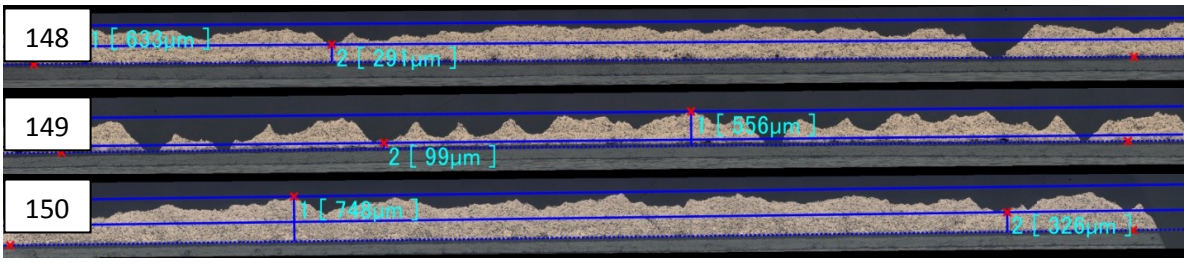

Figure 146: Variation between the thickest (1) and thinnest (2) (excluding the discontinuities) points of the composite coating on WGFP BMS 8-276.

Closer imaging of the pits revealed that deposition varied in a similar pattern as the fibre/epoxy concentration of the WGFP (see Figure 147). Deposition occurred in areas with high glass fibre concentration and exposure whereas pits occurred in areas where mostly epoxy was present.

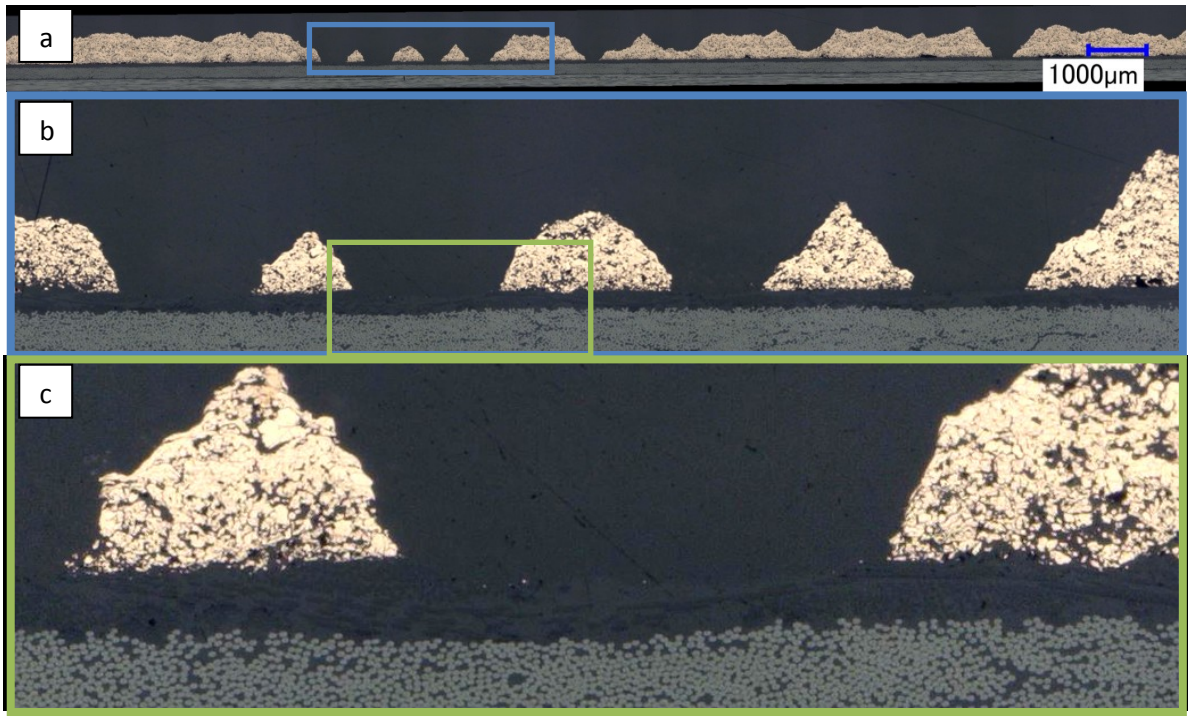

Figure 147: (a) 97.5wt% SST-C5003 and 2.5wt% PEEK bond coat trial number 149 on WGFP BMS 8-276 with (b & c) zoom on discontinuities.

As discussed in section 5.1.4, the WGFP is composed of tows of glass fibres that intertwine. Areas between tows are mainly composed of epoxy which promotes the formation of pits by preventing deposition. Much like the toughening heterogeneous system, epoxy has a great resistance to impact damage. The epoxy rich zones likely absorb most the energy of the impacting particles leaving them unable to deform and adhere to the surface. However, unlike tin, the composite bond coat does not seem to bridge as effectively creating deep pits or large variations in thickness.

5.2.5 Taguchi Optimization

Optimal pressure (110 psi) (0.76 MPa) and temperature (350°C) were established during preliminary testing (see section 5.2.2). Deviating from this temperature and pressure resulted in low deposition or erosion of the substrate. Similarly, other parameters should be optimized for the composite bond coat. A Taguchi method was used to optimize secondary parameters. Using this method, the individual influence of multiple parameters was evaluated. The objective was to analyze the bond coat with respect to thickness, resistivity, adhesion to the BMS 8-276 substrate, and porosity. The

following subsections introduce why the parameters, manipulated in this Taguchi experiment, were selected and details the experimental setup, execution, and analysis of the Taguchi method.

5.2.5.1 Taguchi Parameters

The parameters for this experiment were selected for a variety of reasons. Some were selected based on literature review or work completed by Dr. Yandouzi while others were selected because prior experiments conducted with tin indicated significant importance of the parameter. In certain instances, preliminary tests were conducted to delimit the acceptable variation of the parameters. In order for the analysis to render results, a successfully deposition of the composite bond coat (on the BMS 8-276) had to take place for all of the trials of the Taguchi experiment. The preliminary tests were used to establish the levels for each parameter (see section 4.6). Three levels were selected for each parameter in order to determine trends with a minimum the number of experiments.

5.2.5.1.1 Surface Finish

As cited in the literature review, the surface roughness is typically known to have an impact on the adhesion strength of coatings. Earlier experiments performed in section 5.1.2 indicated that the LCFP of the BMS 8-276 has a fluctuating adhesion that can be correlated with the substrate roughness when coated with tin. The WGFP of the BMS 8-276 was proven to be troublesome with the composite bond coat (see section 5.2.4). As a result, the LCFP was selected for this experiment. Some experiments were carried out in order to quantify the roughness of a LCFP BMS 8-276 with respect to certain surface preparations. Figure 148 presents the roughness (R_a) values for BMS 8-276 substrates that were grit blasted at pressure ranging from 50 psi to 200 psi (0.34 MPa to 1.38 MPa). Prior to grit blasting, all the substrates were polished to expose a single LCFP. Two measurements were taken for each pressure and grit combination using the digital microscope in order to calculate the roughness (R_a).

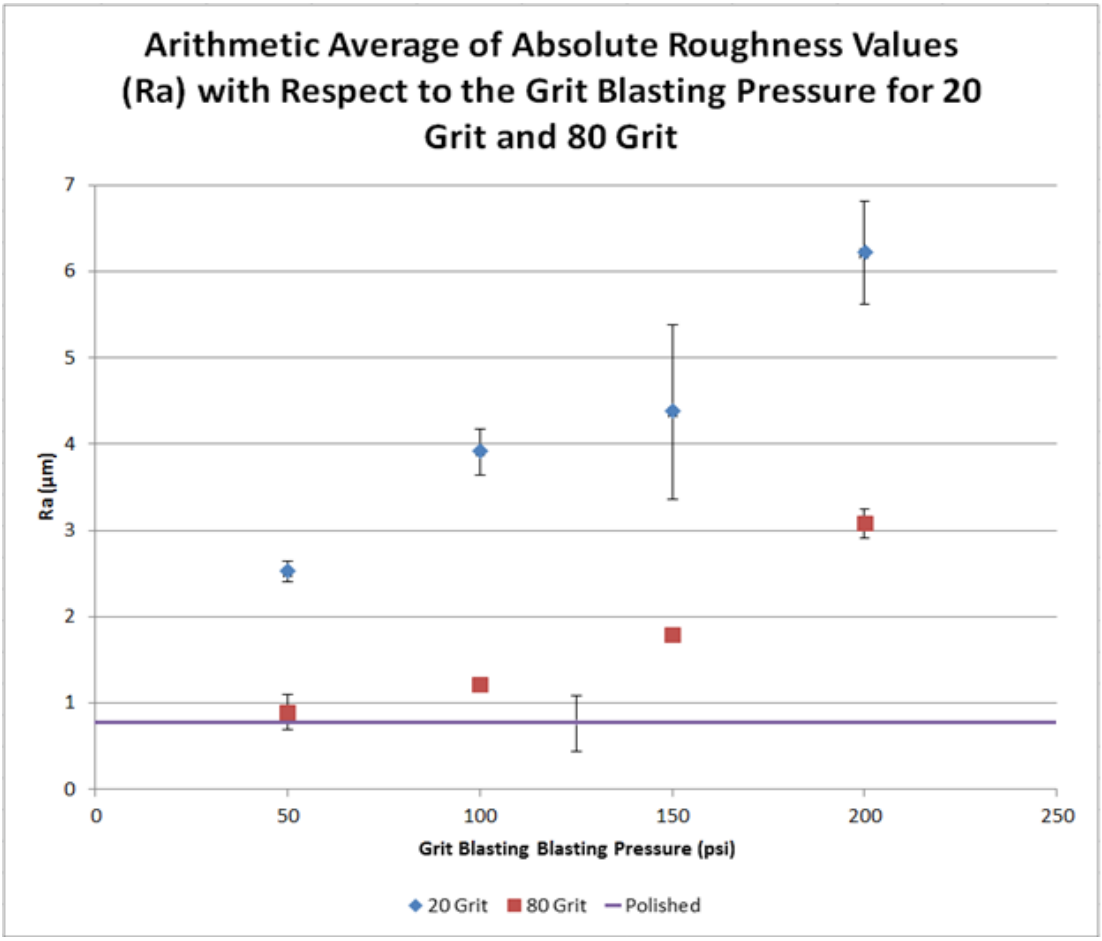

Figure 148: The arithmetic average of absolute roughness values (R_a) are shown with respect to the grit blasting pressure for both 20 and 80 grit. Note that some error bars are not visible due to their small size.

As depicted in Figure 148, the larger grit (20 grit) created a greater roughness on the substrate than the smaller grit (80 grit). As suspected, increasing the pressure increased the roughness of the substrate. This being said, high blasting pressures often resulted in multiple LCFPs being exposed. Earlier experiments demonstrated that the exposure of multiple LCFPs would result in a discontinuous coating (see section 5.2.3). As a result, the surface roughness was done at low pressure (50 psi) (0.34 MPa) for the Taguchi experiment. Even though the roughness values (R_a) are similar at low pressure (especially in the case of polished and 80 grit) they do not render a complete description of the topography of the surface and can therefore be considered different. The three levels used were a polished surface finish following the procedure outlined in section 4.4.1 (polished) and grit blasted surface finishes at 50 psi (0.34 MPa) using 20 grit and 80 grit following procedures outlined in section 4.4.2.

5.2.5.1.2 Bond Coat Composition

It was assumed at the beginning of this research that minimizing the quantity of PEEK in the bond coat would be beneficial in regards to stress created by thermal expansion as well as the overall conductivity of the bond coat (see section 5.2.2). However, it is unclear with what severity the bond coat composition impacts the bond coat's conductivity, adhesion to the BMS 8-276 substrate, thickness and porosity. Work done by Dr. Mohammed Yandouzi indicates that a composite bond coat can be successfully deposited onto a LCFP BMS 8-276 substrate with a feedstock composition of 97.5wt% SST-C5003 with 2.5wt% PEEK, 95wt% SST-C5003 with 5wt% PEEK, and 90wt% SST-C5003 with 10wt% PEEK (see Appendix I: Dr. Mohammed Yandouzi's Work on Bond Coat Development). As a result, these three compositions were selected as the levels for the Taguchi experiments.

5.2.5.1.3 Traverse Velocity (TV)

In section 5.1 it was determined that the TV had an important impact on the microstructure of the tin coating as well as influenced the adhesion strength through fibre embedment. It is unknown at this point if the TV has any effect on the composite bond coat. A test was conducted to determine what range of velocity can be used to deposit the composite bond coat. The TV of each trial was varied from 15mm/s to 30 mm/s in increments of 5 mm/s. All other parameters remained unchanged between trials and are specified in Table 25.

Table 25: Parameters Used for 97.5wt% SST-C5003 and 2.5wt% PEEK Bond Coats When Varying the Traverse Velocity

CGDS Parameter	Value
Gas Pressure	110 psi
Gas Temperature	350°C
Gas Nature	Nitrogen
Standoff Distance	10 mm
Nozzle Type	120 mm SS Nozzle
Orifice Diameter	2 mm
Powder Feeder Wheel	240 Medium Hole
Powder Feeder Gas Rate	30 scfh (0.85 m^3/h)
Powder Feed Rate	3 rpm (0.31 rad/s)
Step Size	2 mm
BMS 8-276 Surface Preparation	Polished

Figure 149 depicts the traces produced. The coatings deposited at 30 mm/s and 25 mm/s are discontinuous whereas the coatings deposited at 15 mm/s and 20 mm/s look continuous. Increasing the TV above 20 mm/s without PFR adjustments will induce discontinuities in the bond coat rendering it unsuitable to receive the pure copper top coat (see Figure 139).

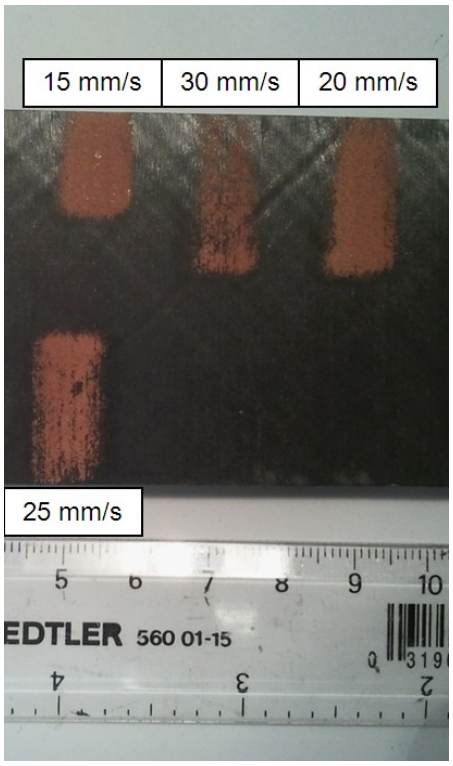

Figure 149: 97.5wt% SST-C5003 + 2.5wt% PEEK bond coat sprayed at different traverse velocities (15, 20, 25, and 30 mm/s) on a BMS 8-276 substrate.

The discontinuities are thought to be created by a lack of PEEK. From a statistical point of view, increasing the TV lowers the amount of PEEK reaching the substrate per surface area. As a result, there are areas where no PEEK will reach the substrate creating discontinuities in the bond coat. In addition, the PEEK particles have a large size distribution and can reach 150 µm in diameter (according to the distributor - Victrex). Large PEEK particles account for a large percentage of the PEEK content in the bond coat mixture (because of their large mass) but only contribute to a small area of coverage. As a result, this further increases the frequency of discontinuities in the bond coat. It was concluded that the TV should not be increased without proportionally adjusting the PFR for the Taguchi parameter. The traverse velocities of 10 mm/s, 15 mm/s, and 20 mm/s were paired with the PFRs of 2 rpm, 3 rpm, and 4rpm (0.21 rad/s, 0.31 rad/s, 0.42 rad/s) respectively for the Taguchi experiment.

5.2.5.1.4 Standoff Distance (SOD)

CS usually deals with metallic materials; its parameters are thus set to accommodate materials with such densities and sizes. The SOD is an important factor that is usually set between the ranges of 10 mm and 25 mm for metallic powders. Is it however unclear what SOD is appropriate for polymers. Also, it is important to note that the PEEK powder has a large size distribution which includes larger particles than conventional manufactured powders intended for CS. The combination of the large size and low density heightens its susceptibility to drag forces. An experiment was performed where the SODs of 5 mm, 10mm, 15 mm, and 20 mm were tried on a BMS 8-276 substrate. All other parameters are specified in Table 26.

Table 26: Parameters Used for 97.5wt% SST-C5003 and 2.5wt% PEEK Bond Coats When Varying the Standoff Distance

CGDS Parameter	Value
Gas Pressure	110 psi (0.76 MPa)
Gas Temperature	350°C
Gas Nature	Nitrogen
Nozzle Type	120 mm SS Nozzle
Orifice Diameter	2 mm
Powder Feeder Wheel	240 Medium Hole
Powder Feeder Gas Rate	30 scfh (0.85 m^3/h)
Powder Feed Rate	3 rpm (0.31 rad/s)
Step Size	2 mm
Traverse Velocity	15 mm/s
BMS 8-276 Surface Preparation	Grit Blasted at 90 psi (0.62 MPa)

When observing the results presented in Figure 150, the coatings deposited at a SOD of 5 mm seems to have the best overall deposition. In the case of the traces made at SODs of 10 mm and 15 mm, the coatings are continuous at the center but become discontinuous near the edges. The trace made at a SOD of 20 mm is discontinuous throughout.

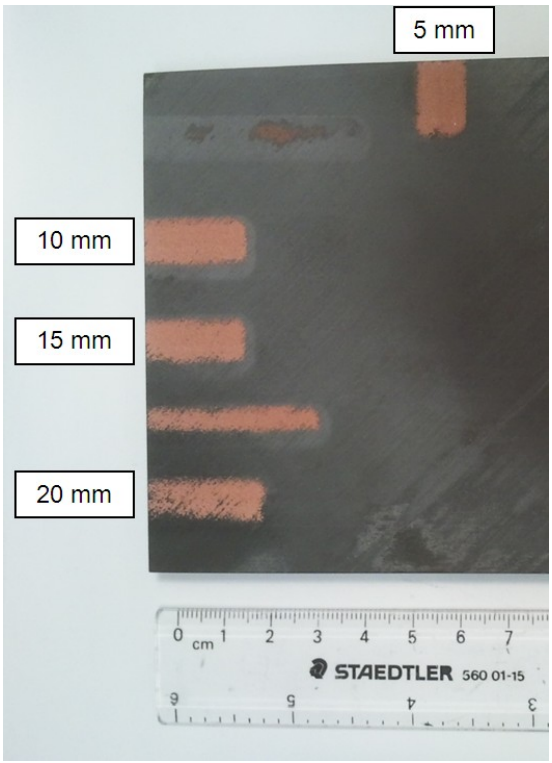

Figure 150: 97.5wt% SST-C5003 + 2.5wt% PEEK bond coat sprayed at different standoff distances (5, 10, 15, and 20mm).

It can be concluded that the shortest SOD seems beneficial for the DE. This could be attributed to the properties of the bonding agent (PEEK) discussed above. Bow shocks or even small changes in pressure can slow down the large yet light PEEK particles. Increasing the SOD prolongs the amount of time that the PEEK spends in an ever slowing fluid thus escalating the probability that the PEEK will reduce in speed. This theory also explains why the edges are affected before the center of the trace. The edges of the spray are more quickly affected by turbulence in the flow. The three levels of the SOD were set at 5mm, 10 mm, and 15 mm for the Taguchi experiment.

5.2.5.2 Taguchi Experiment

The Taguchi method was utilized to optimize the bond coat using minimal experiments. Four parameters were chosen to be varied at three different levels. By using three levels, more accurate trends can be withdrawn from the Taguchi method while maintaining the number of experiments to a minimum. The pressure and temperature were not selected for this experiment because previous tests demonstrated that deviating from the optimal pressure and temperature would result in no bond coat deposition on the BMS 8-276 substrate rendering the Taguchi experiment incomplete.

The four parameters selected were the surface finish, the bond coat composition (represented in PEEK percentage with the remainder composed of SST-C5003), the TV coupled with the PFR, and the SOD. Following the orthogonal array presented in Figure 52, a total of nine experiments (different sprays) were required in order to assess the effect of each parameter on the bond coat with respect to conductivity, adhesion to the BMS 8-276 substrate, thickness, and porosity (see Table 27).

Table 27: Taguchi Experiment Parameter in Orthogonal Array

Experiment	*Parameter*			
	Surface Finish	PEEK% (wt%)	Traverse Velocity (mm/s) – Powder Feed Rate (rpm)	Standoff Distance (mm)
1	Polished	2.5	10 – 2	5
2	Polished	5	15 – 3	10
3	Polished	10	20 – 4	15
4	80 grit	2.5	15 – 3	15
5	80 grit	5	20 – 4	5
6	80 grit	10	10 – 2	10
7	20 grit	2.5	20 – 4	10
8	20 grit	5	10 – 2	15
9	20 grit	10	15 – 3	5

All other spray parameters were unchanged from one experiment to the next. The gas pressure, gas temperature, gas nature, nozzle type, orifice diameter, powder feeder wheel, powder feeder gas rate, and step size remained identical for all sprays (see Table 28)

Table 28: Constant Parameters Used for the Bond Coat in the Taguchi Experiments

CGDS Parameter	Value
Gas Pressure	110 psi (0.76 MPa)
Gas Temperature	350°C
Gas Nature	Nitrogen
Nozzle Type	120 mm SS Nozzle
Orifice Diameter	2 mm
Powder Feeder Wheel	240 Medium Hole
Powder Feeder Gas Rate	30 scfh (0.85 m^3/h)
Step Size	2 mm

Using the surface preparation outlined in section 4.4, nine sets of substrates were prepared exposing a single LCFP (see Figure 151). It is important to note that some sets of experiments contain two test plates while others contain three.

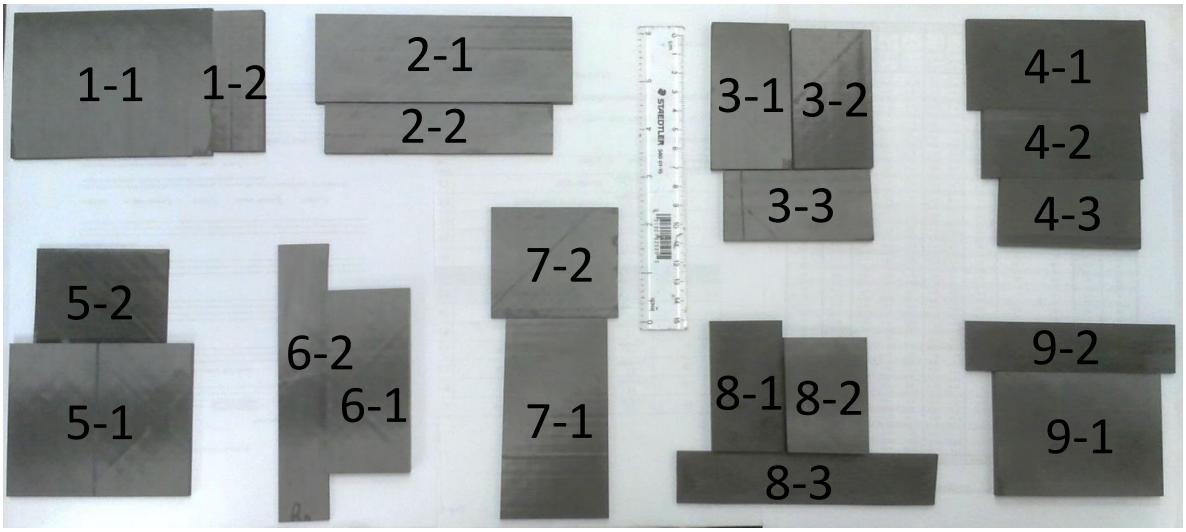

Figure 151: Single carbon fibre reinforced epoxy layer substrates used for the nine Taguchi experiment sets. The nine different sets of experiments are outlined in Table 27.

The proper surface finish was then applied to each experiment set and the bond coat was sprayed with the SST-P system (see Figure 152a). The bond coat of the experiment sets 3, 6, and 9 delaminated from the substrate (see Figure 152b).

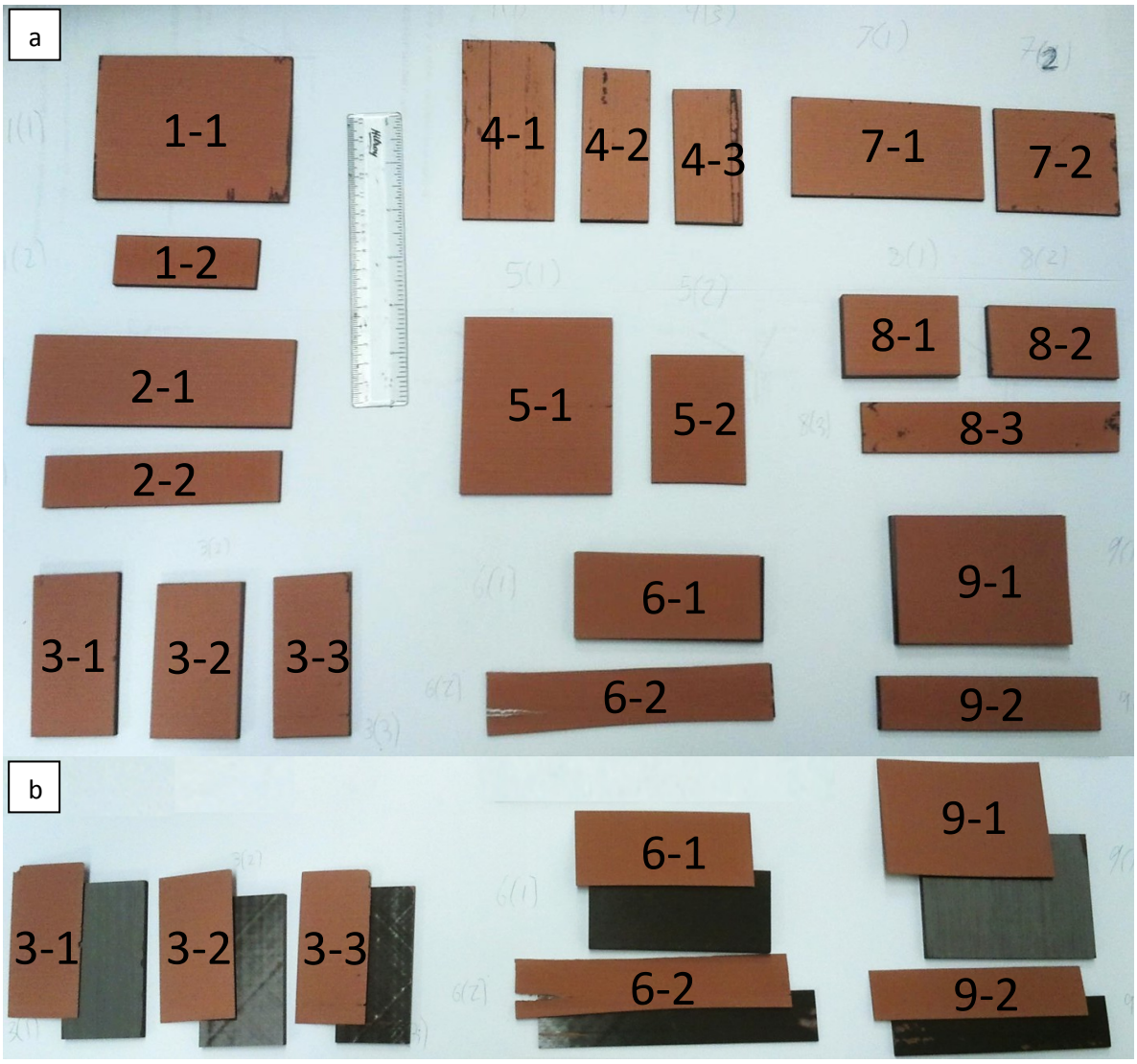

Figure 152: (a) All Taguchi bond coats deposited onto BMS 8-276 substrates and (b) delaminated bond coats.

It is to be noted that in all three sets of experiments (3, 6, and 9), the composition of the composite bond coat was 90wt% SST-C5003 and 10wt% PEEK. No other variable parameter was repeated between these experiments. By default, the high percentage of PEEK (10wt%) was deemed the culprit behind the delamination of these bond coats. Since PEEK has a larger coefficient of thermal expansion than copper and BMS 8-276, increasing the PEEK percentage will increase the average thermal expansion of the bond coat. This elevated mismatch in thermal expansion coefficients will increase the tensile residual stress in the coating which could have caused the delamination.

5.2.5.2.1 Thickness

The thickness of the composite bond coat of each test plate was measured through cross-sectional analysis using a digital microscope. A minimum of 40 measurements were taken for each set of experiments. Figure 153 plots the average thickness of each test plate for the nine sets of experiments. The sets containing 10wt% PEEK (sets 3, 6, and 9) in the feedstock powder produced bond coats with thicknesses reaching 500 µm to 600 µm. The sets containing 2.5wt% PEEK (sets 1, 4, and 7) in the feedstock powder produced 250 µm thick coatings on average. The sets containing 5wt% PEEK (sets 2, 5, and 8) in the feedstock powder produced coatings within thicknesses between the other sets.

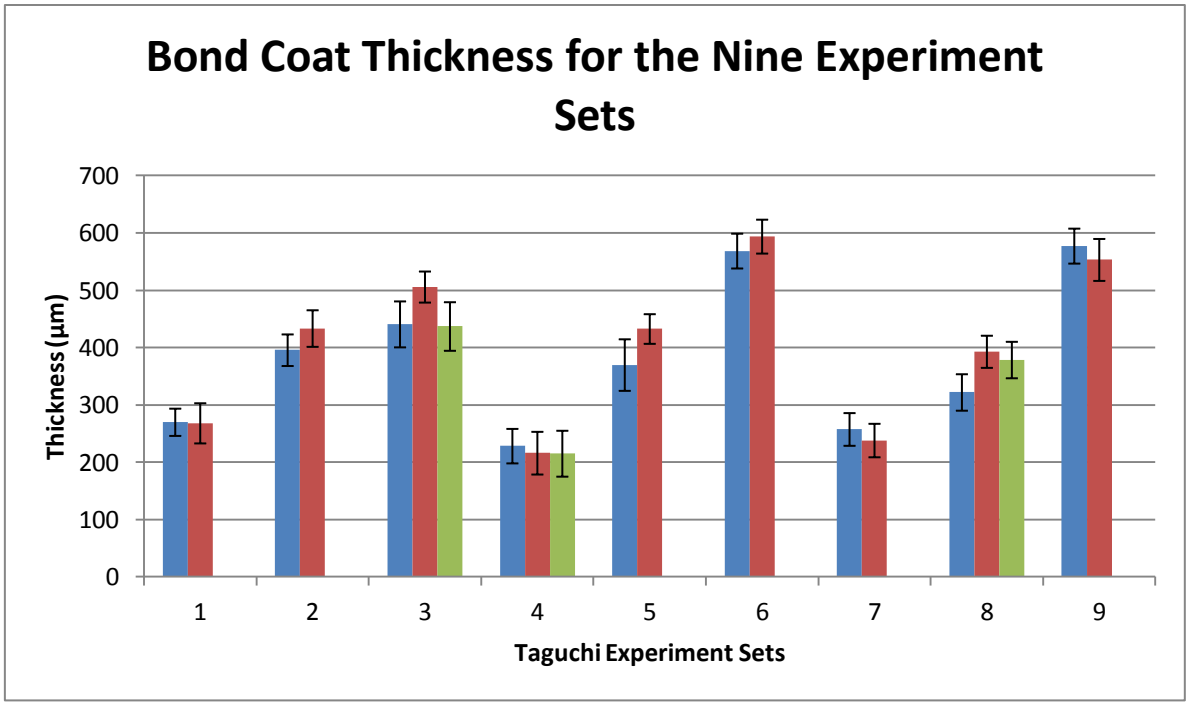

Figure 153: Thickness of the bond coats deposited on the nine sets of substrates with standard deviation. Please note that the blue, red and green bars represent the first, second and third test plates for each Taguchi experiment set respectively. Some sets contain two test plates whereas others have three.

The data was manipulated according to the Taguchi method in order to obtain an average SN ratio for each level of every parameter. When plotted, it is apparent that the PEEK percentage (bond coat composition) has the greatest influence on thickness for it has the largest range (R) followed by the SOD, the surface finish, and lastly the TV & PFR (see Figure 154).

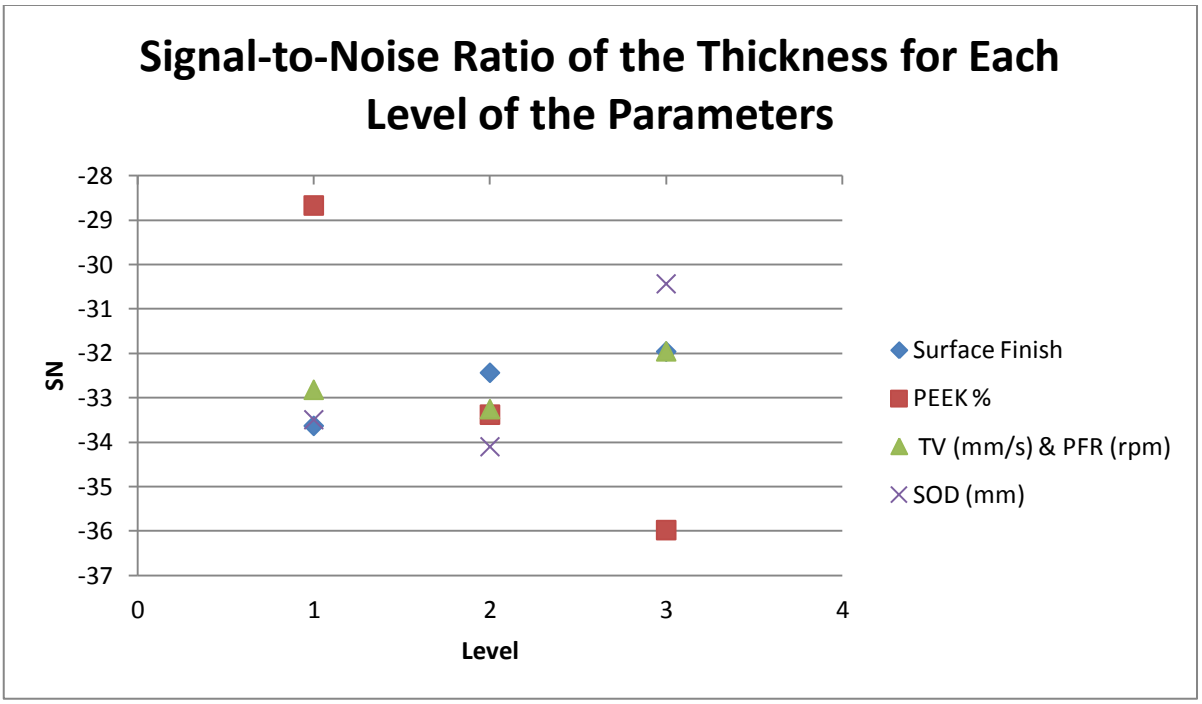

Figure 154: Signal-to-noise ratio of the thickness for each parameter according to the corresponding level.

Figure 154 also shows the PEEK percentage in the composition of the feedstock powder is positively correlated to the thickness (high SN indicates minimal thickness). It can be concluded that the feedstock composition (PEEK%) greatly affects the thickness of the bond coat. Increasing the PEEK weight percentage increases the thickness of the coating. During deposition, it is believed that the PEEK adheres to the BMS 8-276 substrate while the copper particles are simply trapped in between PEEK particles. It is also believed that the copper particles do not deposit as efficiently on themselves as they do on PEEK. Therefore, increasing the PEEK content increases the DE which increases the thickness.

5.2.5.2.2 Resistivity

The sheet resistances of all Taguchi bond coats were measured using a four point probe connected to a digital multimeter (see section 4.8.3). Given that the bond coats of sets 3, 6, and 9 had all delaminated from the substrate, the measurements were made only on the delaminated bond coats. A total of 10 measurements were taken per test plate (20 to 30 per set of experiment). The resistivity was then calculated using the average thickness of each bond coat calculated in the

previous subsection (see Figure 155). A wide range of resistivity was apparent. The largest resistivity was reached in set 3 (705 Ohm*m) and the lowest resistivity was reached in set 1 (1.03 Ohm*m).

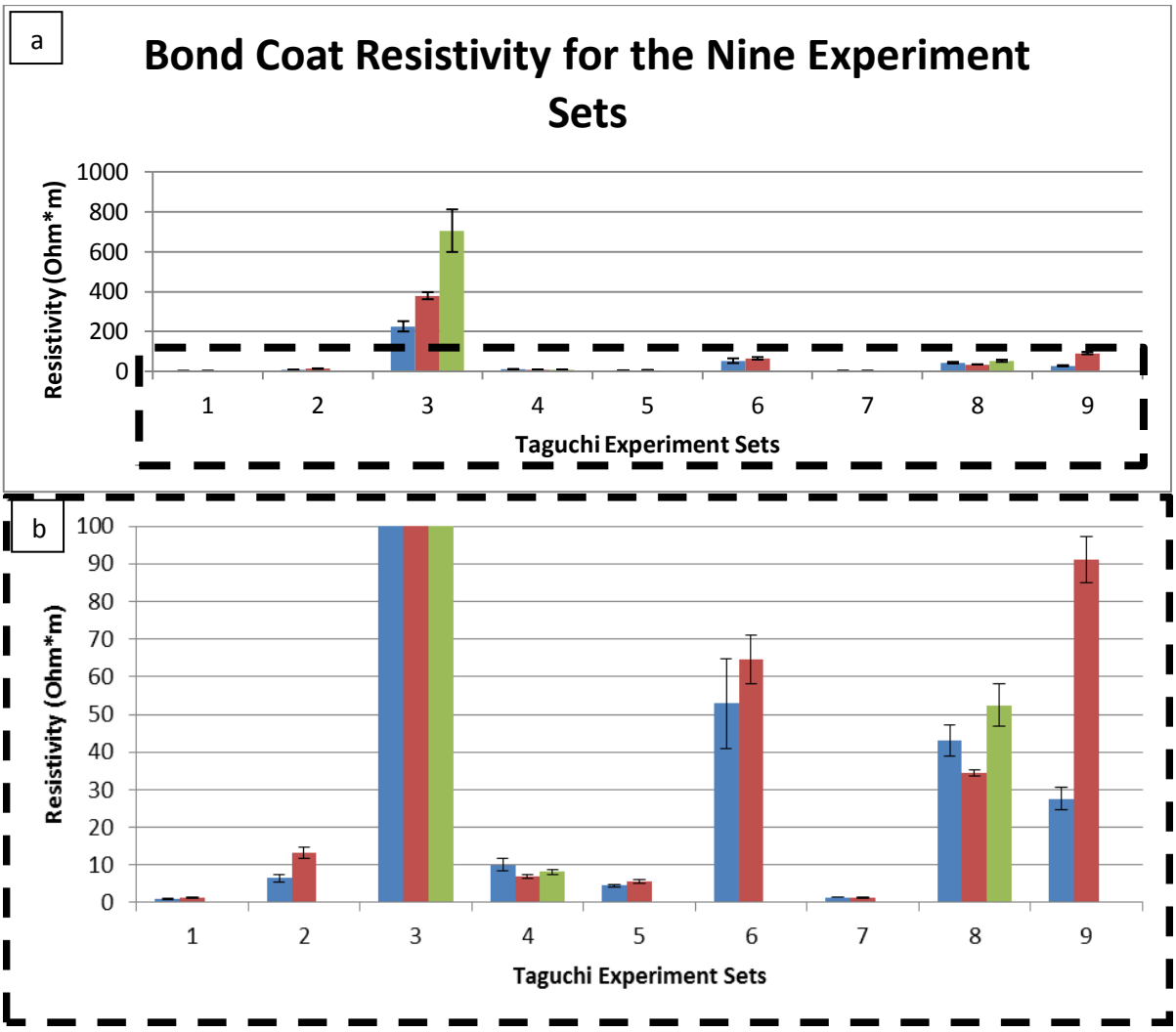

Figure 155: (a) Resistivity of the bond coats deposited on the nine sets of substrates with standard deviation. (b) Zoom of the smaller values. Please note that the blue, red and green bars represent the first, second and third test plates for each Taguchi experiment set respectively. Some sets contain two test plates whereas others have three.

Upon calculation of the SN numbers and R values, it was confirmed that the PEEK percentage (bond coat composition) was the most important parameter pertaining to resistivity (see Figure 156).

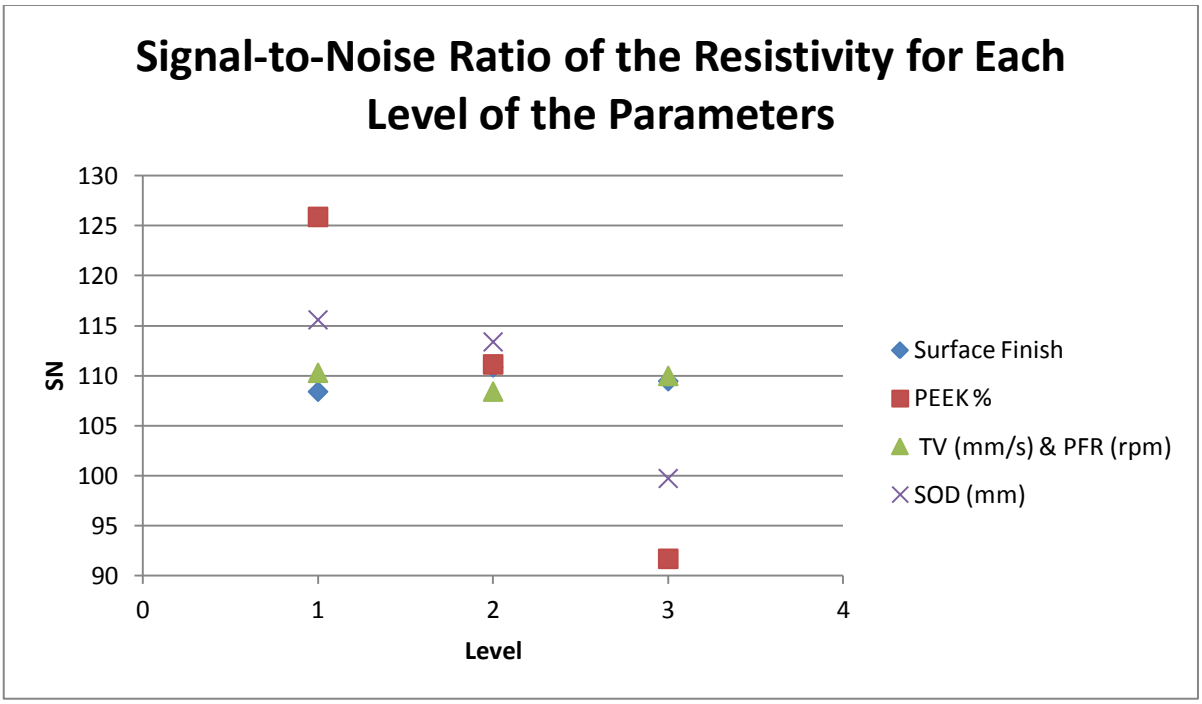

Figure 156: Signal-to-noise ratio of the resistivity for each parameter according to the corresponding level.

Figure 156 shows a clear positive correlation between the composition of the feedstock powder and the resistivity (high SN ratio indicate minimal resistivity). As suspected, increasing the PEEK content in the bond coat will increase the resistivity (lower the conductivity) since PEEK is a poor conductive material. The SOD is the second most influential parameter. Again, a positive correlation is apparent however, the effect seems to plateau once the SOD is set below 10 mm (level 2). If designed properly, the maximum gas velocity should be at the exit of the nozzle. After exiting the nozzle, the gas stream mixes with the atmosphere and begins to slow down. The large particle size of the PEEK combined with the low density heightens its susceptibility to drag forces. This means that these large PEEK particles, unlike conventional metallic particles, reach their terminal velocity much more quickly for they can be accelerated with less drag force. This also means that they can be decelerated quickly as well. By lowering the SOD, atmospheric influences are minimized which ensured high velocity and optimal deformation. It is suspected that this increase in deformation is what helps to lower the resistivity. The surface finish and the TV & PFR, were both closely classified (R values) and had little influence on the resistivity.

5.2.5.2.3 Adhesion

Adhesion tests were conducted on the bond coats that remained on the substrates using a PATTI test. The maximal number of adhesion tests was performed on each test plate (see Figure 157). In some cases 7 measurements were performed while others could only fit 1 measurement. The bond coats of the experiment sets 3, 6, and 9 were assigned zero values for adhesion (because they had already delaminated from the BMS 8-276 substrates).

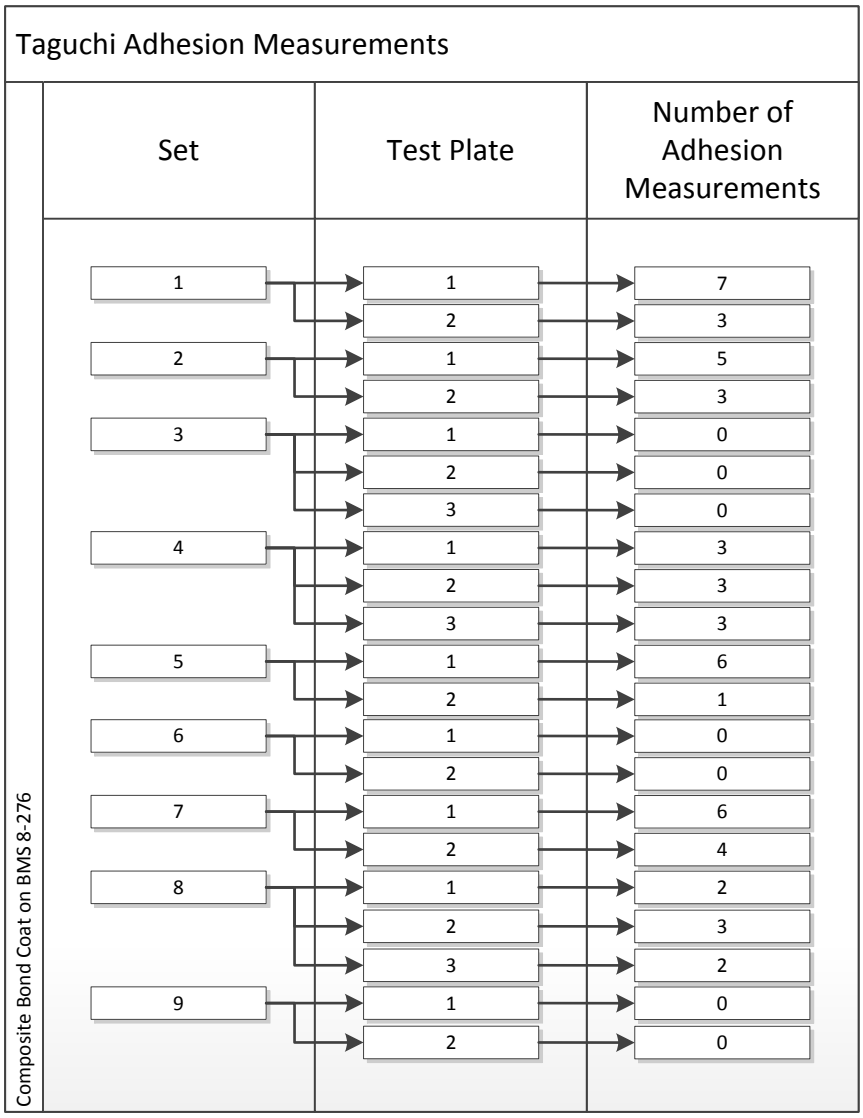

Figure 157: Number of adhesion measurements made with the PATTI for the Taguchi experiment.

The data was plotted for comparison in Figure 158. The largest adhesion value was reached in set 1 (177psi). High adhesion values were also seen in set 4 and 7 when compared to the other sets.

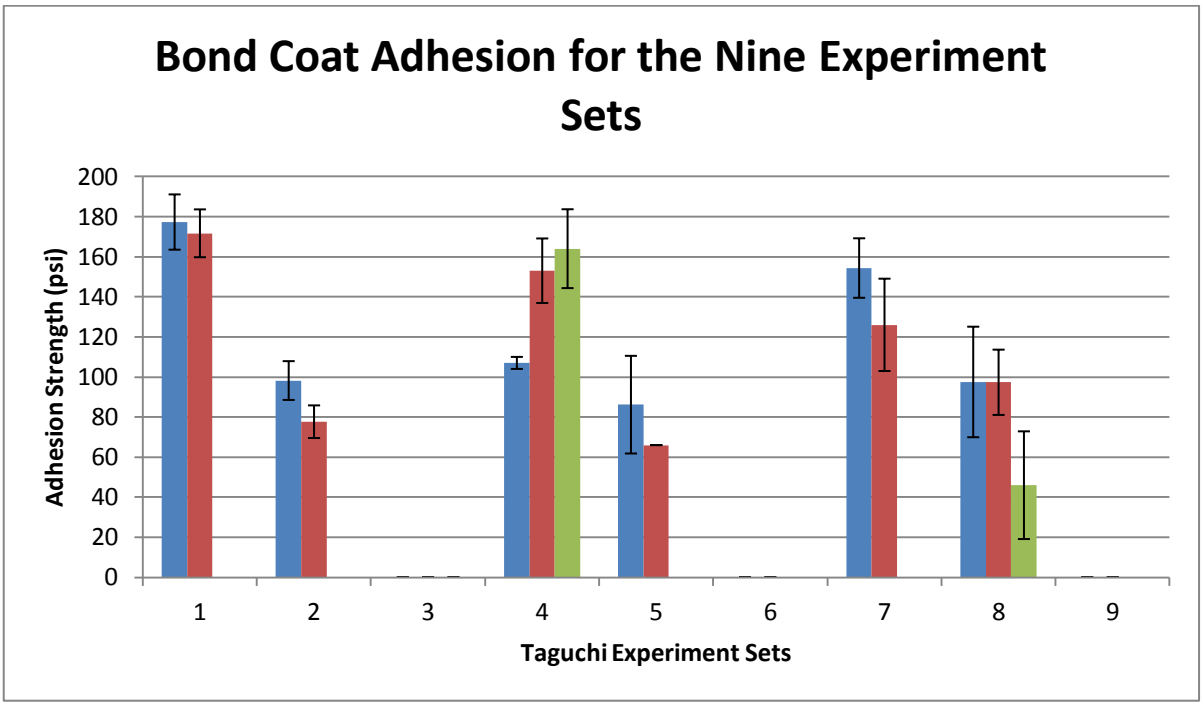

Figure 158: Adhesion of the bond coats deposited on the nine sets of substrates with standard deviation. Adhesion values of zero were assigned to the experiment sets 3, 6, and 9 because the bond coat delaminated. Please note that the blue, red and green bars represent the first, second and third test plates for each Taguchi experiment set respectively. Some sets contain two test plates whereas others have three.

Upon calculation of the SN ratios and R values, it was shown that the PEEK percentage (bond coat composition) had by far the largest influence on adhesion and it is negatively correlated (high SN ratio indicate maximal adhesion) (see Figure 159).

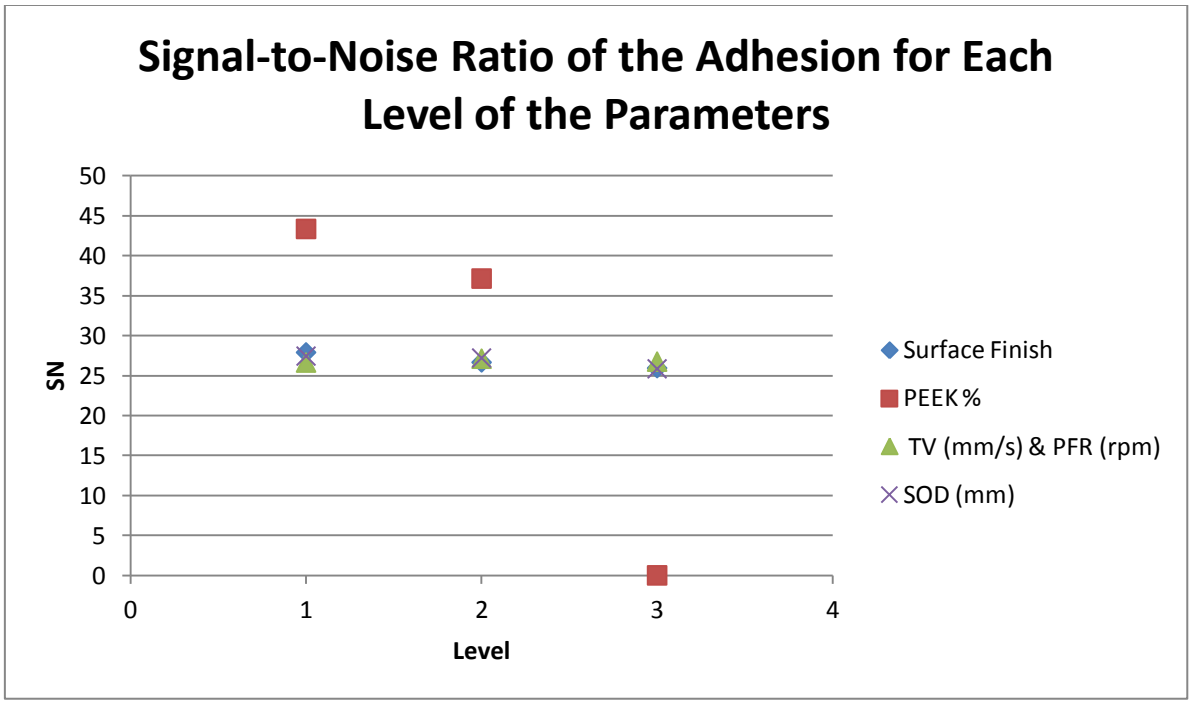

Figure 159: Signal-to-noise ratio of the adhesion for each parameter according to the corresponding level.

Figure 159 depicts that increasing the PEEK percentage in the feedstock powder lowered the adhesion. This could be caused by an increase in tensile residual stress in the bond coat. Since PEEK has a large thermal expansion coefficient and potentially reaches its glass temperature (343°C) during deposition, it undergoes a lot of strain. This strain results in large tensile stresses once the PEEK rich coating has cooled which enables delamination from the substrate. At first glance, the other parameters seem to have little influence on the adhesion strength of the bond coat to the substrate. However, this is largely emphasized by the large range of the bond coat composition. If closely analysed, it can be noted that both the surface finish and the SOD are negatively correlated to the adhesion strength.

5.2.5.2.4 Porosity

A sample section of each test plate was analyzed using imaging software for all Taguchi experiment sets. The software calculated the percentage of area representing porosity, copper and PEEK. These area percentages are assumed to be comparable to volumetric percentages. Over a dozen measurements were made for each test plate. It is fairly obvious that the measured copper and PEEK percentages were overwhelmingly influenced by the initial feedstock powder composition

(PEEK% parameter). The feedstock powders composed of 2.5wt% PEEK, 5wt% PEEK, and 10wt% PEEK produced bond coats with roughly 25% of PEEK, 30% of PEEK, and 42.5% of PEEK respectively. The porosity of the bond coat was measured and compiled in Figure 160. The lowest porosity achieved was roughly 2.75% whereas the highest reached 15.8%.

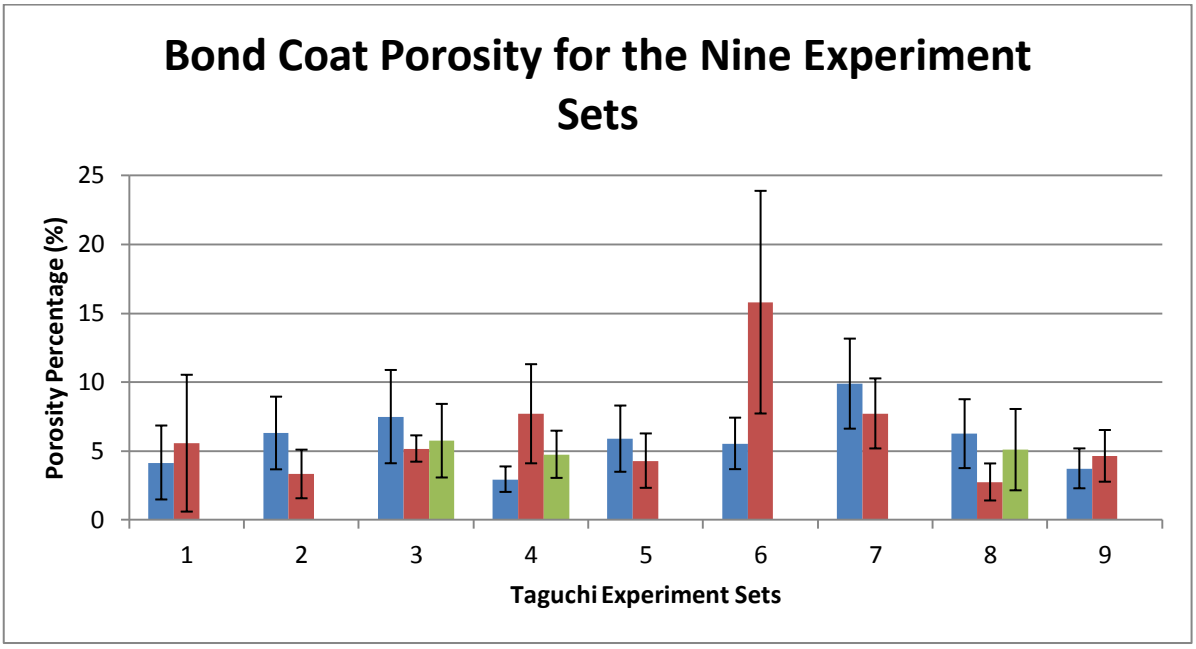

Figure 160: Porosity of the bond coats deposited on the nine sets of substrates with standard deviation. Please note that the blue, red and green bars represent the first, second and third test plates for each Taguchi experiment set respectively. Some sets contain two test plates whereas others have three.

Upon calculation of the SN numbers and R values, it was determined that the porosity is affected by the SOD followed by the PEEK percentage (bond coat composition), the TV & PFR, and the surface finish in a decreasing fashion. It is important to note that even the largest range calculated for the porosity remains lower than most other ranges calculated with respect to other objectives. This denotes the weak influence all of these parameters have on the porosity. In addition no clear trend can be withdrawn from Figure 161. For example, a polished or 20 grit surface finish seem to be beneficial for the porosity (high SN ratio indicate minimal porosity) while a surface finish of 80 grit is not. No general conclusions can be established from these results.

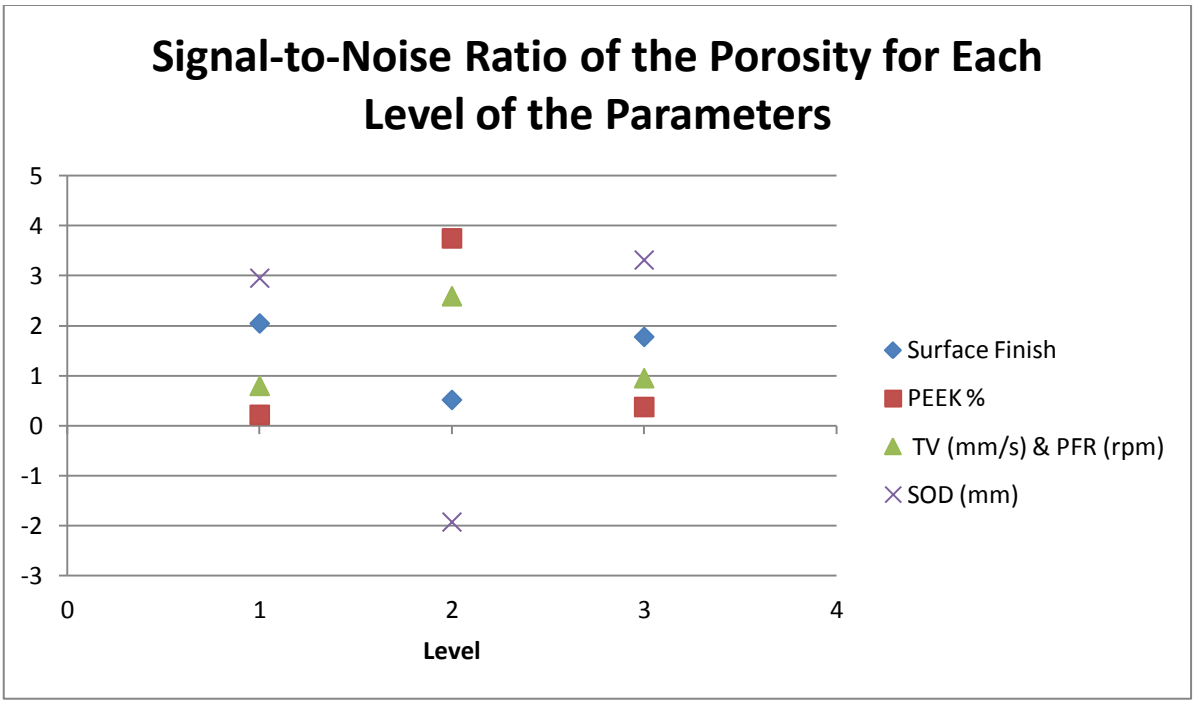

Figure 161: Signal-to-noise ratio of the porosity for each parameter according to the corresponding level.

5.2.5.2.5 Summary

By decoupling the parameters of the Taguchi method (see Figure 154, Figure 156, Figure 159, and Figure 161), each parameter (surface finish, PEEK%, FR & TV, and SOD) were individually analyzed with respect to its influence on the objective (thickness, resistivity, adhesion, or porosity). The small ranges (R) calculated for the surface finish indicated that it has little effect on all the objectives. A polished surface finish on the substrate was marginally beneficial for the adhesion and porosity yet somewhat disadvantageous for the resistivity and thickness. The polished surface finish was created upon exposing the LCFP using the technique described in section 4.4.1. As a result, it was decided that using a polished surface finish would be optimal since the addition of a grit blasting step (20 grit or 80 grit) has no discernible added value. The bond coat composition was by far the most influential parameter. Minimizing the PEEK content in the bond coat increased the adhesion and decreased both the thickness and the resistivity. The TV & PFR combination had very little effect on all the objectives. As such the decision was made to maximize the TV & PFR in order to minimize the spray time and future manufacturing costs. The SOD was mostly influential in regards to the resistivity. Maintaining the SOD below 10 mm minimized the resistivity. In addition, lowering the

SOD may increase the adhesion strength by a marginal difference. However, doing so may cause a slight increase in the coating thickness.

5.2.6 Bond Coat Composition

It was concluded in the Taguchi experiment from the previous section that the composition of the bond coat has a considerable influence on the adhesion, thickness, and resistivity of the deposited coating. By reducing the PEEK content in the bond coat, the adhesion increases while the thickness and resistivity decrease. The following test was done to further optimize the bond coat with respect to its composition. Based on the findings of section 5.2.5, the spray parameters were set (see Table 29).

Table 29: Parameters Used for Composite Bond Coat Optimization

CGDS Parameter	Value
Gas Pressure	110 psi (0.76 MPa)
Gas Temperature	350°C
Gas Nature	Nitrogen
Standoff Distance	5 mm
Nozzle Type	120 mm SS Nozzle
Orifice Diameter	2 mm
Powder Feeder Wheel	240 Medium Hole
Powder Feeder Gas Rate	30 scfh (0.85 m^3/h)
Powder Feed Rate	4 rpm (0.42 rad/s)
Traverse Velocity	20 mm/s
Step Size	2 mm
BMS 8-276 Surface Preparation	Polished

Five different composite bond coat powder mixes were prepared with PEEK weight percentages increments of 0.5wt%. starting from 0.5wt% up to 2.5wt% (see Figure 162).

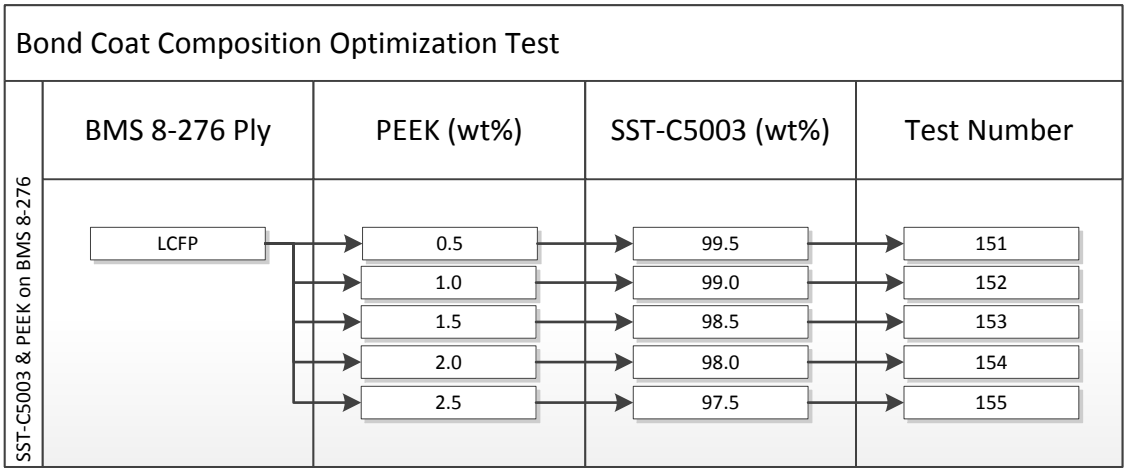

Figure 162: Composite Bond Coat Composition Optimization Test.

As seen in Figure 163, a few defects were present on the BMS 8-276 plates (causing lines where no deposition occurred). These defects occurred because the BMS 8-276 samples had a slight curve in the LCFPs (exposing the toughening heterogeneous system).

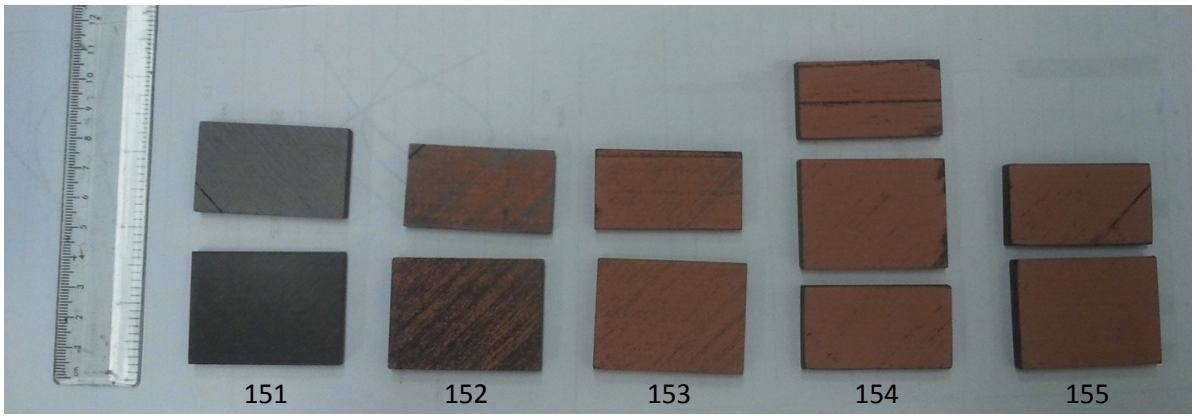

Figure 163: Deposited bond coats with varying feedstock composition.

Between three and four PATTI adhesion tests were performed on the coatings of samples 153, 154, and 155 (see Figure 164). The bond coats of samples 151 and 152 were deemed unfit for adhesion testing because of their severe discontinuous nature. The 20 mm pull-stub could not be glued to the coatings of samples 151 and 152 without also being glued to the substrate (which would have skewed the results).

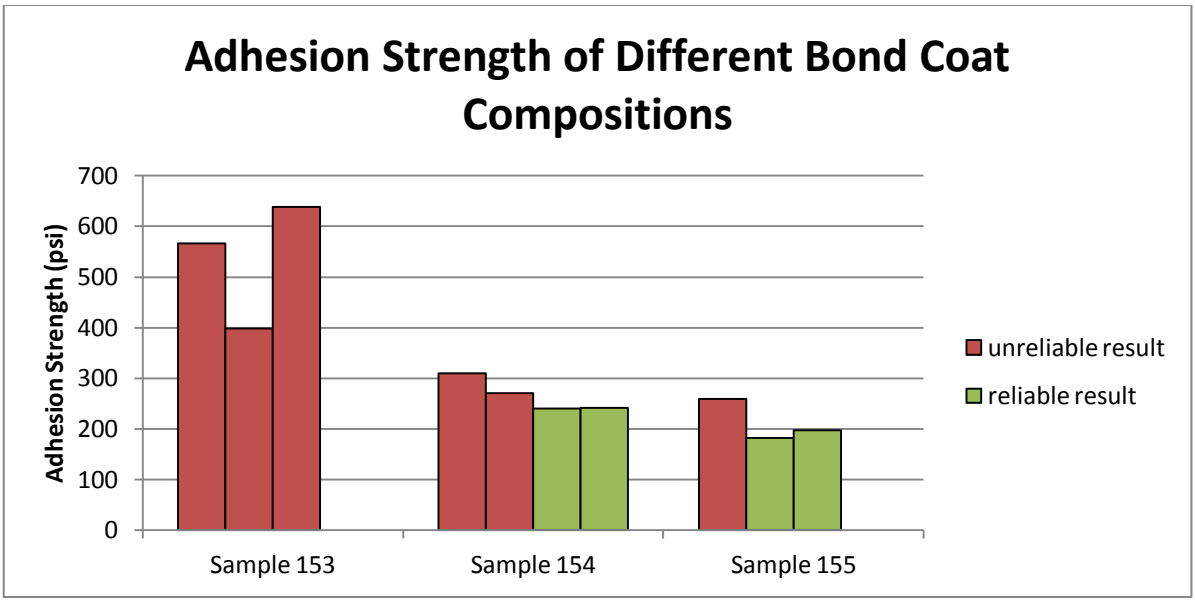

Figure 164: PATTI results of samples 153 (3 results), 154 (4 results) and 155 (3 results). The red coloured results indicate unreliable results caused by glue seeping between the coating and the substrate.

As encountered in previous experiments, the discontinuous nature of some coatings skewed the adhesion results, making them unreliable (and elevated). These skewed adhesion results are represented in red in Figure 164. It is apparent that decreasing the PEEK content in the feedstock composition lowers the DE. In this case, the low DE affected the continuity of the deposited coating which skewed most results. However, according to the reliable data of sample 154 and 155, lowering the PEEK content of the feedstock powder to 2.0wt% slightly increases the adhesion (conforms with conclusion from the Taguchi experiment). As described in the previous section, this behavior is explained by the high thermal expansion coefficient of PEEK. Given that the PEEK material is brought near its glass temperature during deposition, high strains can be expected. When coupled with its high thermal expansion coefficient, the PEEK material creates large amounts of stresses lowering the required force needed to remove the bond coat from the substrate. This slight increase in adhesion comes at the cost of a lower DE which may not be cost effective.

5.2.7 PEEK Particles Size Distribution

The PEEK powder acquired from Victrex was not specifically manufactured for use in CGDS while the SST-C5003 copper powder provided by Centreline was specifically tailored for the SST-P CGDS system used in this research. The particle size distribution of the PEEK powder is stated to be 0-150

µm whereas the SST-C5003 is 5-45 µm. An experiment was conducted to evaluate the influence of the PEEK particle size distribution on the adhesion strength of the composite coating. Using a RX-29 sieve for W. S. Tyler the PEEK powder was sieved into three different ranges before being combined with SST-C5003 in a 97.5wt% copper + 2.5wt% PEEK feedstock powder (see Figure 165).

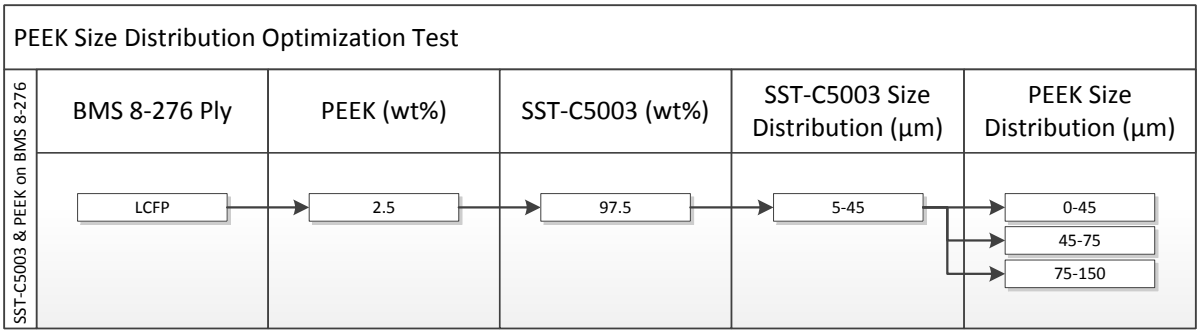

Figure 165: PEEK size distribution optimization test.

The three different feedstock powders were deposited onto polished BMS 8-276 substrates using the parameters specified in Table 29 (see Figure 166). It can be noted at this point that the samples produced with the PEEK particle size distribution range of 75-150 µm (see Figure 166) resemble the composite bond coat of sample 152 produced with 99.0wt% SST-C5003 and 1.0wt% PEEK (see Figure 163).

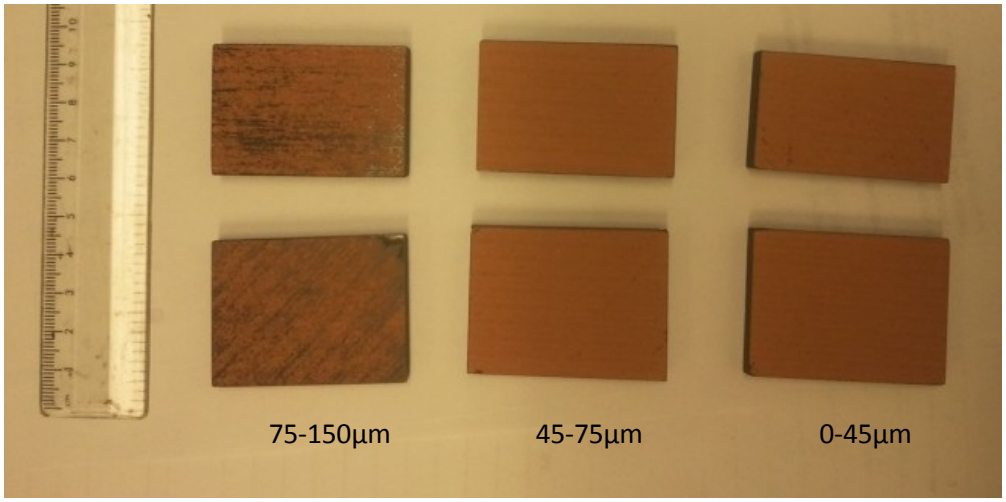

Figure 166: Deposited bond coats with 97.5wt% SST-C5003 + 2.5wt% PEEK with PEEK particle size distribution ranges of 75-150µm, 45-75 µm, and 0-45 µm.

The composite bond coats produced with PEEK particles between 75 µm and 150 µm were discontinuous making it impossible to perform adhesion tests. As for the other two PEEK particles distribution ranges, three adhesion measurements were taken for each range. Figure 167 presents the average adhesion strength and distribution of the results.

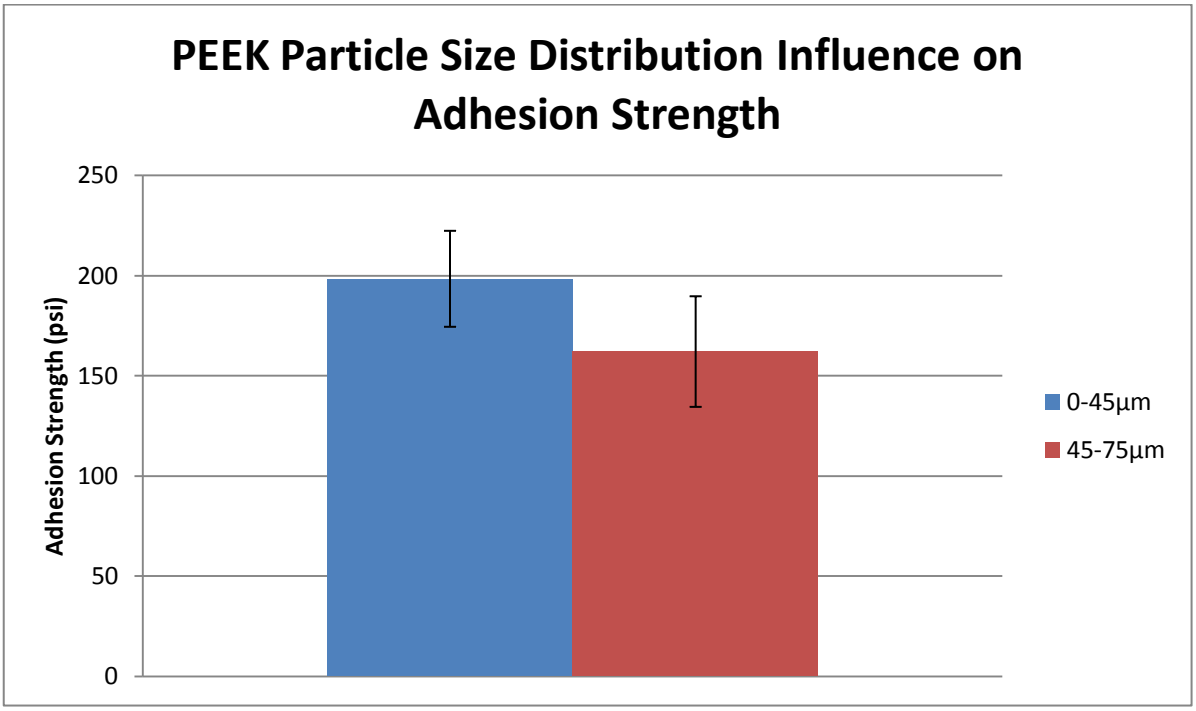

Figure 167: Adhesion strength of Composite bond coat made from 97.5wt% SST-C5003 + 2.5wt% PEEK feedstock powder with 0-45 µm and 45-75 µm PEEK particle size distribution ranges.

From the results presented in Figure 167, it can be concluded that the smaller (0-45 µm) PEEK particle distribution is beneficial for the composite bond coat's adhesion. Cross-sectional analysis presented in Figure 168 provides a visual confirmation that smaller PEEK particles provide a more homogeneous feedstock blend.

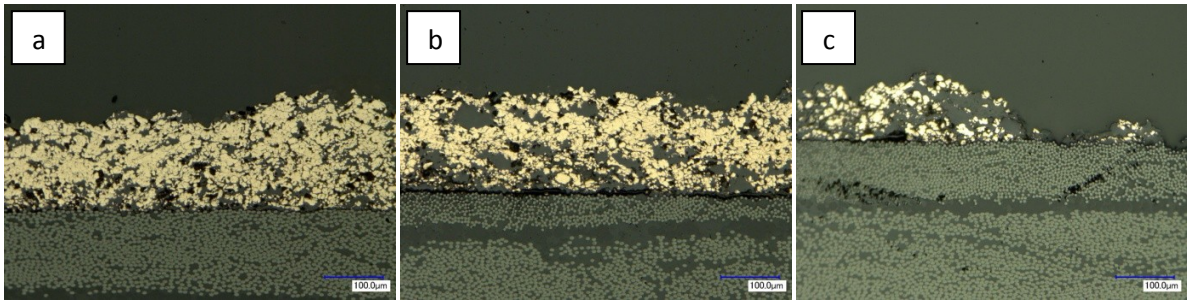

Figure 168: Cross-section of composite bond coat produced with 97.5wt% SST-C5003 and 2.5wt% PEEK with (a) 0-45 µm, (b) 45-75 µm, and (c) 75-150 µm PEEK particle distribution.

Further analysis with microscopic imaging revealed that decreasing the size of the PEEK particles increases the proportion of copper in the bond coat (see Table 30). Much like in section 5.2.2, the weight percentages (wt%) were calculated from volume compositions (see Appendix V: Bond Coat Theoretical Volume Composition Calculation).

Table 30: Bond Coat Composition Different PEEK Particle Size Distribution Ranges

PEEK Size Distribution Range	Bond Coat Copper % (wt%)	Bond Coat PEEK % (wt%)	Bond Coat Porosity (vol%)
0-45 µm	94.13	4.85	1.02
45-75 µm	92.75	5.93	1.32
75-150 µm	79.36	18.87	1.77

Results from Table 30 indicate that there is an increase in the deposition efficiency of the copper particles in the bond coat when the PEEK particle size is reduced (0-45 µm). Very large PEEK particles can account for a substantial mass percentage of the PEEK composition in the composite feedstock powder making their quantity smaller. When deposited, these large particles do not cover a large surface for they remain thicker than their smaller counterparts leaving surrounding areas devoid of PEEK. Without the presence of PEEK, projected copper particles simply erode the substrate without deposition (see section 5.2.1). This can cause pits and discontinuities to occur in the bond coat causing severe variations in thickness. This also explains why there is an increase in the percentage of copper in the bond coat produced with 0-45 µm PEEK. In addition to preventing pits and other discontinuities from occurring, decreasing the size of the PEEK particles increases their likelihood to be deformed by subsequent particle impacts (notably the copper particles). PEEK deformation is thought to be of great importance to the overall adhesion of the bond coat. Highly

deformed PEEK will fill gaps between the BMS 8-276 substrate and the copper particles sealing them and creating a suction-like force between the two. Reducing the PEEK size also distributes the thermal expansion stresses created during cooling in a more uniform way. Furthermore, the increase in the percentage of copper also helps explain the reason for the increase in adhesion. Since PEEK has a very large thermal expansion, lowering its relative content in the bond coat will reduce the tensile residual stress in the bond coat. This has the effect of increasing the adhesion between the bond coat and the substrate. Table 30 also presents evidence that the porosity tends to be lower for the bond coats composed of small PEEK particles (0-45µm). This explanation can address the increase in adhesion seen in Figure 167. Appendix VI presents other experiments that were conducted in an attempt to increase the adhesion of the composite bond coat to the BMS 8-276.

5.2.7.1 Pure PEEK Coating

In order to assess the adhesive properties of the PEEK to the BMS 8-276, a test consisting of spraying only PEEK onto the BMS 8-276 substrate was made. A few trials were made varying the TV in order to successfully deposit 0-45 µm PEEK onto LCFP BMS 8-276 (see Figure 169).

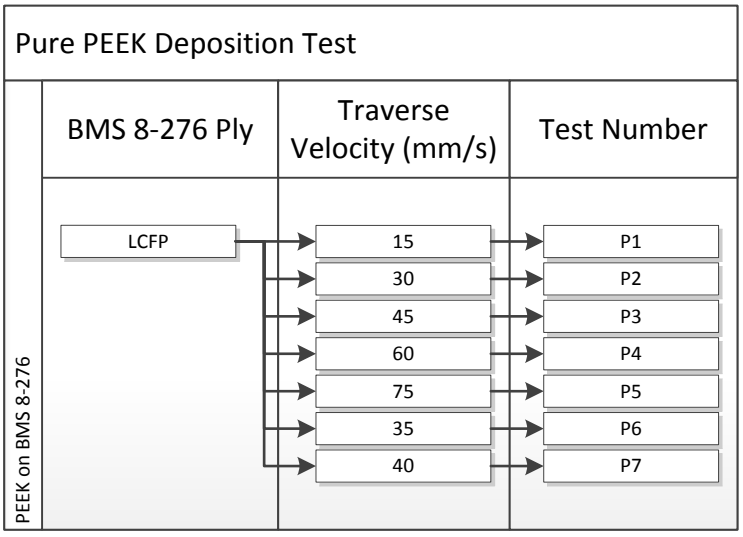

Figure 169:Pure PEEK deposition test.

All other parameters remained constant and are presented in Table 31.

Table 31: Parameters Used for Pure PEEK Deposition on LCFP of BMS 8-276

CGDS Parameter	Value
Gas Pressure	110 psi (0.76 MPa)
Gas Temperature	350°C
Gas Nature	Nitrogen
Standoff Distance	5 mm
Nozzle Type	120 mm SS Nozzle
Orifice Diameter	2 mm
Powder Feeder Wheel	240 Medium Hole
Powder Feeder Gas Rate	30 scfh (0.85 m^3/h)
Powder Feed Rate	3 rpm (0.31 rad/s)
Traverse Velocity	20 mm/s
Step Size	2 mm
BMS 8-276 Surface Preparation	Polished

During deposition, only trial P3 did not flake off from the substrate (see Figure 170). As such, a PEEK coating deposited on an entire 2" X 1.5" (5.1cm X 3.8 cm) BMS 8-276 plate (see Figure 170).

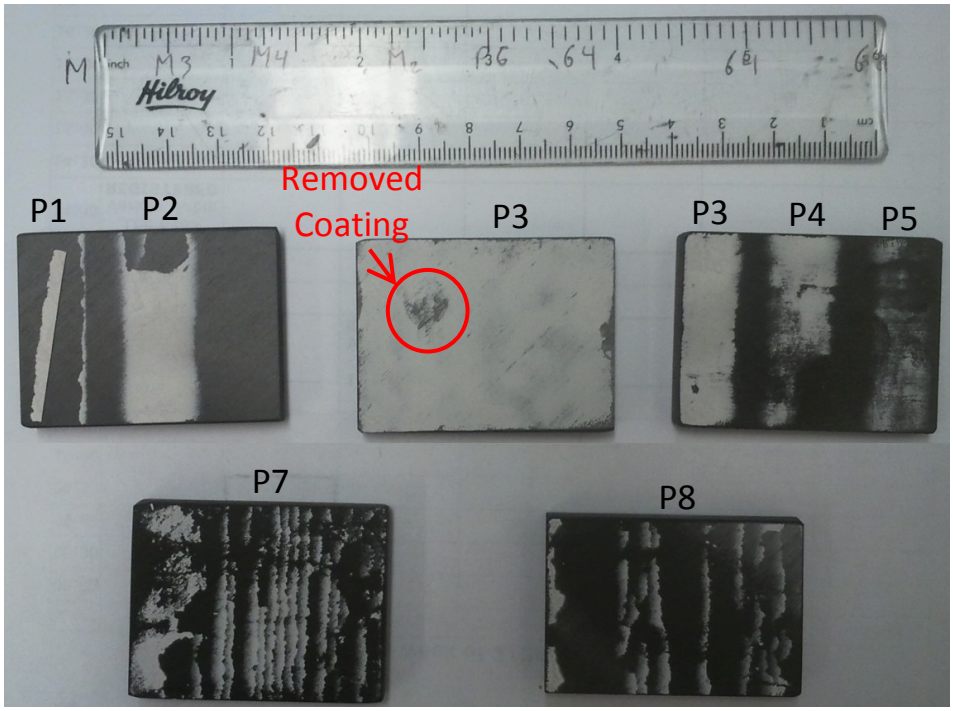

Figure 170: Pure PEEK coating on BMS 8-276 substrate.

This coating was unfortunately characterized by very poor adhesion. The fragile coating could easily be removed by simply scratching the coating. A cross-section of the coating shows that the PEEK particles remain largely spherical which indicates that little deformation has taken place (see Figure 171).

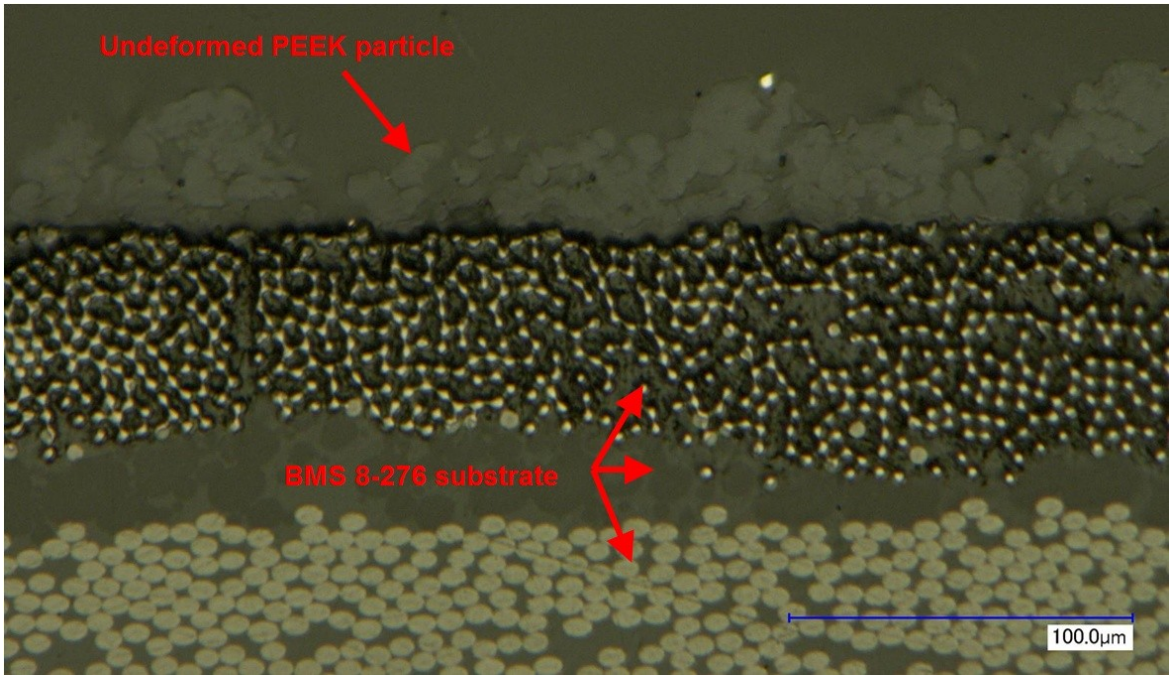

Figure 171: Cross-section of pure PEEK coating on BMS 8-276 substrate.

Because PEEK is not dense, it can easily be accelerated in the nozzle and decelerated as it approaches the substrate. In other words, PEEK particles have low momentum (compared to metals) which translates to little energy available to deform the particle upon impact. Without proper deformation, the adhesive properties of the PEEK drop drastically. When mixed with copper, the PEEK particles are deformed by subsequent impacting copper particles which is suspected to help increase adhesion. It is therefore imperative to keep both PEEK and copper particles together when spraying.

5.2.8 Copper on Tin Bond Coat

The copper and PEEK composite bond coat turned out to have a very low adhesion strength to the substrate. A pure copper (SST-C5003) top coat was thus attempted to be deposited onto a tin coated WGFP BMS 8-276 composite. The WGFP was chosen because the tin coating proved to have a higher adhesion when deposited on the WGFP rather than the LCFP of the BMS 8-276 (see section 5.1.2). Trials were conducted where the gas pressure, the gas temperature, and the traverse velocity were modified according to Figure 172. The pressure was initially set at 200 psi (1.38 MPa) according to the top coat trials conducted in section 5.2.2.

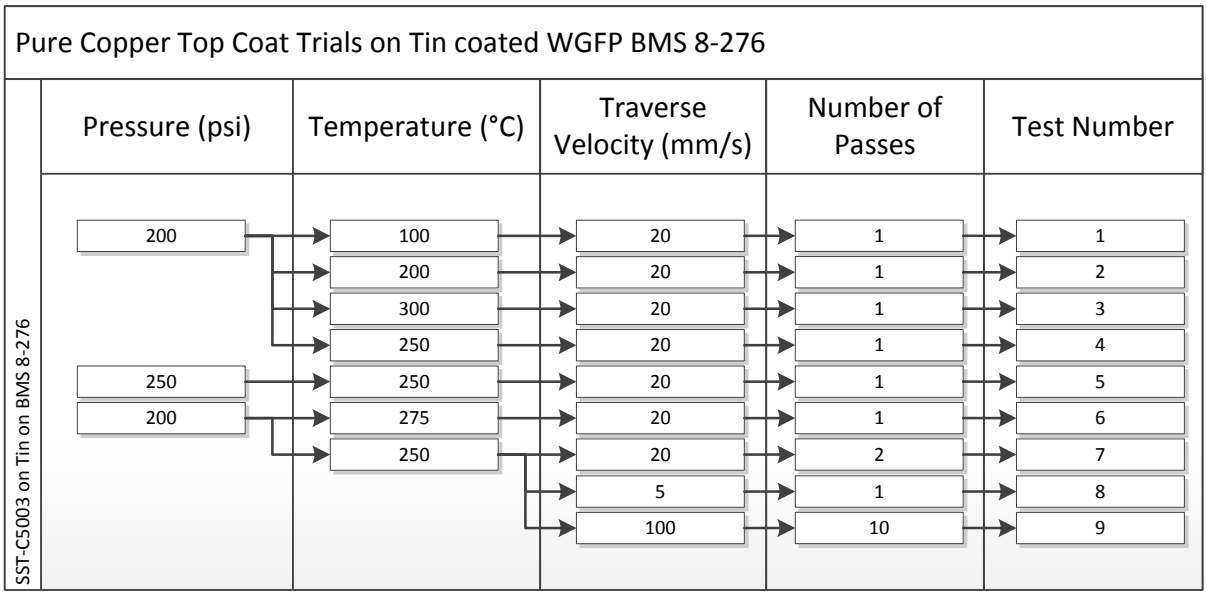

Figure 172: Pure copper top coat trials on tin coated WGFP BMS 8-276.

All other spray parameters remained unchanged between trials (see Table 32).

Table 32: Constant Parameters Used for the Top Coat Trials on Tin Coated WGFP BMS 8-276

CGDS Parameter	Value
Gas Nature	Nitrogen
Standoff Distance	10 mm
Nozzle Type	120 mm SS Nozzle
Orifice Diameter	2 mm
Powder Feeder Wheel	240 Medium Hole
Powder Feeder Gas Rate	30 scfh (0.85 m^3/h)
Powder Feed Rate	3 rpm (0.31 rad/s)
Step Size	2 mm

Figure 173 presents the pure copper (SST-C5003) top coat trials on the tin (SST-S6001) coated WGFP BMS 8-276 composite.

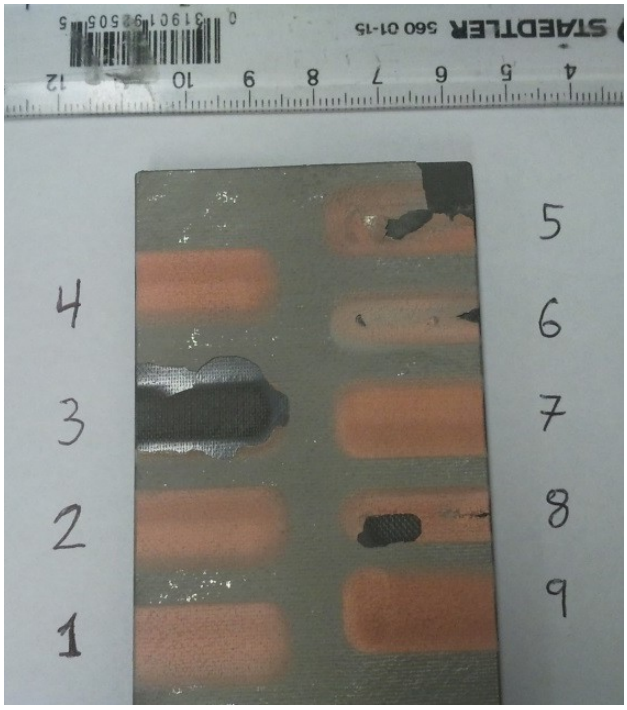

Figure 173: Pure copper (SST-C5003) top coat trials on tin (SST-S6001) coated WGFP BMS 8-276 composite.

When observing the top coat trials, it was determined that increasing the temperature above 250°C induces local melting and loss of mechanical properties of the tin bond coat. Doing so results in

cracking, delamination, and ultimately flaking of the tin bond coat (see Figure 173 – Trials 3 and 6). Similarly, lowering the TV also increases the local heat which ultimately damages the tin bond coat in a comparable manner (see Figure 173 – Trial 8). Conversely, further increasing the TV (such as in the case of trial 9) should minimize any effect on the tin bond coat. Increasing the pressure beyond 200 psi (1.38MPa) will also damage the tin bond coat. High pressures increase the velocity of the projected particles which beyond a certain threshold can result in erosion instead of deposition. This is especially true in the case where the sprayed particles have a higher hardness than the substrate or bond coat. When looking at the cross-section of trial 9, it can be stated that the pure copper top coat has a high density and appears to have little to no voids between itself and respective bond coat (see Figure 174). It is important to note that the lines going across the copper top coat are polishing marks.

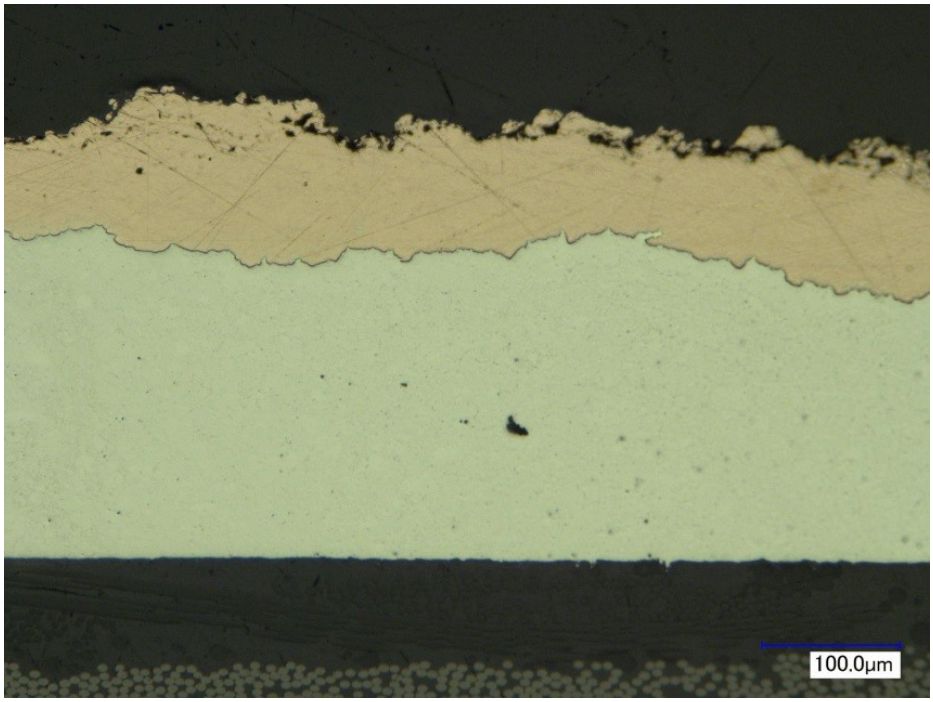

Figure 174: Cross-section of trial number 9.

6 Coating Evaluation (Characterization)

This chapter provides a detailed description of the characterization experiments used to evaluate the coatings produced in the previous chapter. The metalized BMS 8-276 were tested with respect to their electrical resistivity, chemical inertness, and adhesion strength using industry based standards. The tests are presented in the chronological order they were performed. Additional test were also specifically performed on the tin coated BMS 8-276 to evaluate the possibility of an allotropic transformation of the deposited tin material and to demonstrate the versatility of the CGDS procedure.

6.1 Surface Electrical Resistivity

One of the most important parameter to consider is the conductivity of the metalized BMS 8-276 since its main purpose is to protect the substrate in the event of a lightning strike. In this experiment, the electrical resistivity of each type of coating produced were measured with a four point probe resistivity sensor (identical to industry) connected to a digital multimeter. The electrical resistivity of the samples produced was evaluated according to BAC5056 (a Boeing Company process specification best suited for this application). If the measured resistivity did not reside within the classifications type 1, 2, or 3 or surpass them, the conductivity of the sample was deemed unfit for lightning protection.

A variety of coatings deposited on 1.5" X 2" (5.1 cm X 3.8 cm) samples of BMS 8-276 were produced for analysis. Sheeting made of bulk copper was also cut into 1.5" X 2" (5.1 cm X 3.8 cm) samples for comparative purposes. A list of the samples that were analyzed is presented in Table 33. Please note that some samples have two coatings (top coat and bond coat) while others only have one (top coat). In addition, the bulk copper sheeting does not have a substrate.

Table 33: Combinations of Top Coats and Bond Coats on BMS 8-276 with Comparative Copper Sheeting Used for Resistivity Measurements

Number of Samples	Top Coat	Bond Coat	BMS 8-276 Ply
12	Tin	NA	WGFP
12	Copper	Tin	WGFP
7	Copper	Copper & PEEK	LCFP
3	Copper & PEEK	NA	LCFP
5	Bulk Copper	NA	NA

All tin (SST-S6001) coatings were deposited on WGFP BMS 8-276 using the parameters provided in Table 34.

Table 34: Tin Coating Parameters Used (Top Coat and Bond Coat)

CGDS Parameter	Value
Gas Pressure	90 psi (0.62 MPa)
Gas Temperature	300°C
Gas Nature	Nitrogen
Standoff Distance	10 mm
Nozzle Type	120 mm SS Nozzle
Orifice Diameter	2 mm
Powder Feeder Wheel	320 Small Hole
Powder Feeder Gas Rate	30 scfh (0.85 m^3/h)
Powder Feed Rate	3 rpm (0.31 rad/s)
Step Size	1 mm
Traverse Velocity	200 mm/s

Initially, 6 passes were done to deposit the tin coatings. However, these coatings proved to be unfit to receive a pure copper top coat due to their discontinuity. When measuring the sheet resistance, all discontinuous coatings had drastically higher electrical resistances than the continuous coatings. The sheet resistance was thus monitored between each subsequent pass to determine when the coating became continuous. A drop in electrical resistance was noticeable when discontinuities were eliminated. This method can be used to produce a thin yet continuous tin coating regardless

of manufacturing inconsistencies of the BMS 8-276 (solving possible issues outlined in section 5.1.6). All the coatings produced had sheet resistances below 1mΩ immediately following deposition. Once the coatings cooled off, the sheet resistances dropped to about half (≈0.5mΩ) of the initial sheet resistance. This can be explained in parts by the positive correlation that exists between the resistance and the temperature of tin. Given that the temperature of the coating could have been near its melting point immediately after deposition, it is also possible that the tin underwent a phase change. As mentioned in section 2.2.7.2.4, tin can transform into a rhombic crystal structure (γ-tin) above 161°C. It is possible that the newly deposited tin had a γ phase and transformed into β-tin after cooling down causing the drop in resistance.

98wt% SST-C5003 and 2.0wt% sieved (0-45 μm) PEEK coatings were deposited using a single pass at the parameters specified in Table 35 on LCFP BMS 8-276.

Table 35: 98wt% SST-C5003 and 2.0wt% Sieved (0-45μm) PEEK Coating Parameters Used (Top Coat and Bond Coat)

CGDS Parameter	Value
Gas Pressure	110 psi (0.76 MPa)
Gas Temperature	350°C
Gas Nature	Nitrogen
Standoff Distance	10 mm
Nozzle Type	120 mm SS Nozzle
Orifice Diameter	2 mm
Powder Feeder Wheel	240 Medium Hole
Powder Feeder Gas Rate	40 scfh (1.13 m^3/h)
Powder Feed Rate	3 rpm (0.31 rad/s)
Step Size	2 mm
Traverse Velocity	15 mm/s

Copper (SST-C5003) top coats were deposited on some tin coated BMS 8-276 as well as on some copper & PEEK coated BMS 8-276. Seven passes were made to deposit the pure copper top coats using the parameters specified in Table 36.

Table 36: Pure Copper Top Coat Parameters Used

CGDS Parameter	Value
Gas Pressure	200 psi (1.38 MPa)
Gas Temperature	250°C
Gas Nature	Nitrogen
Standoff Distance	10 mm
Nozzle Type	120 mm SS Nozzle
Orifice Diameter	2 mm
Powder Feeder Wheel	320 Small Hole
Powder Feeder Gas Rate	30 scfh (0.85 m^3/h)
Powder Feed Rate	2 rpm (0.21 rad/s)
Step Size	1 mm
Traverse Velocity	100 mm/s

The electrical sheet resistance of each 1.5" X 2" (5.1 cm X 3.8 cm) sample was measured with a four point probe resistivity sensor (identical to industry) connected to a digital multimeter. One measurement was taken per sample. Cross-sectional analysis was used to determine the thickness of each sample by calculating the average between the thickest and thinnest points of the coating (see Figure 175).

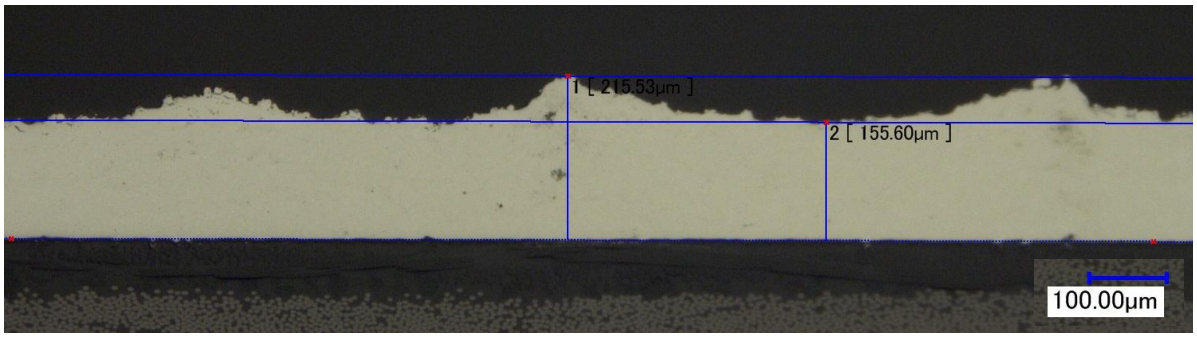

Figure 175: Example of thickest and thinnest points of the coating used to calculate the average thickness for each sample.

In order to compare the resistivity of each sample to the classifications type 1, 2, and 3 of the specification BAC5056, the sheet resistance of each type of sample was plotted with respect to its thickness (see Figure 176). It is important to note that each classification of BAC5056 possesses a

range of acceptable thicknesses and a maximal resistance value for each type. Any sample residing beneath these resistance values and thicknesses were considered fit to protect the BMS 8-276 against a lightning strike (highlighted in green in Figure 176b).

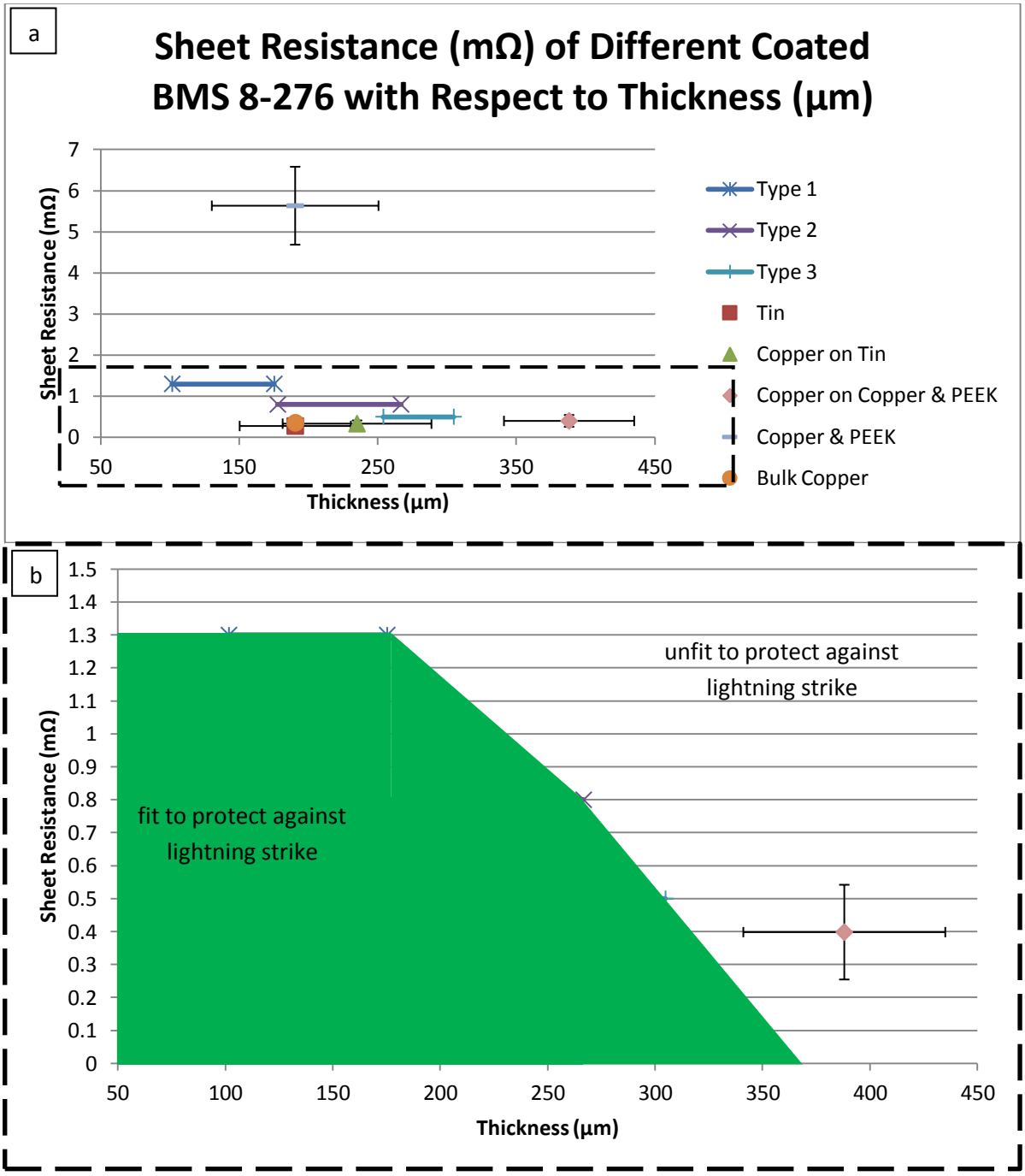

Figure 176: (a) Sheet resistance with respect to thickness of a variety of samples (see Table 33) plotted against BAC5056 classifications. (b) Zoom of samples fit to protect the BMS 8-276 against a lightning strike (highlighted in green).

It can be noted that the bulk copper sheeting had very little variance making its error bars minuscule in Figure 176 and thus not able to be seen. The copper and PEEK coating was not conductive enough according to BAC 5056. When a pure copper top coat was added to it, the conductivity was sufficiently increased however, the thickness was too large to pass the BAC 5056 requirements. Perhaps if a thinning process was added between depositing the composite bond coat and the copper top coat (uniformly thinning the bond coat), the coating would pass the specifications. It is also interesting to note that, on average, the simple tin coated BMS 8-276 samples exceed the tin coated BMS 8-276 samples with an additional copper top coat. The overall sheet resistance slightly increased when adding a pure copper top coat which defeats the initial intent of adding the top coat. In addition, the thickness was increased making the metallization process heavier and thus less efficient. This result leads to the conclusion that the tin must have better metallurgical bonding within its coating than the pure copper one in order to overcome its lower natural conductivity. An SEM image of a tin coating depicts agglomerated particles proving the high degree of metallurgical bonding that exists within this coating (see Figure 177).

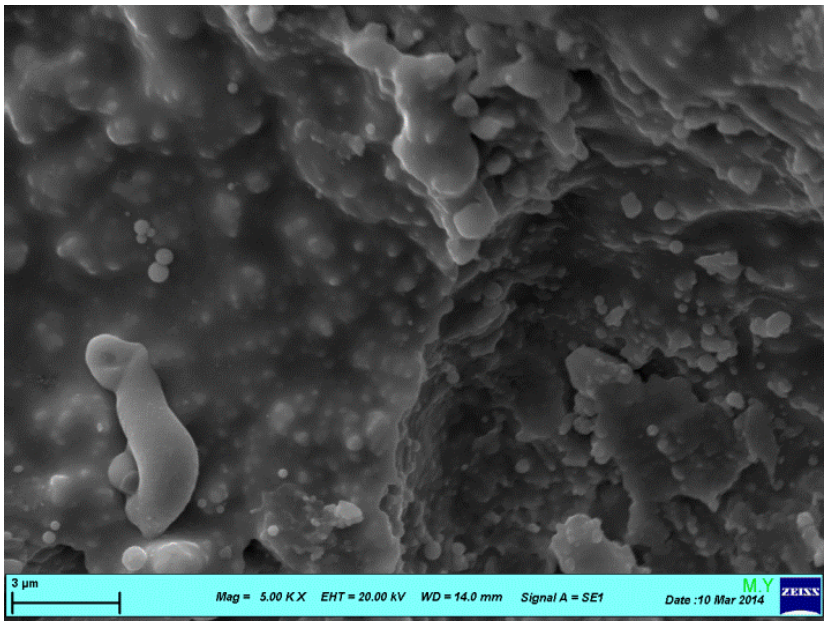

Figure 177: Agglomerated tin particles on a coated BMS 8-276.

It seems as though the simple tin coating would be the optimal choice for metalizing the BMS 8-276 strictly judging from a resistivity point of view.

6.2 Salt Fog Corrosion Behavior

A protective finishing layer such as a primer, paint, and/or epoxy is likely to be applied over the conductive coating. However, wear and accidental scuffs may expose the conductive coating and/or underlying BMS 8-276. The metalized BMS 8-276 samples should be able to tolerate environmental conditions typically seen by aircraft to a certain extent. Neutral salt fog tests are a common industry standard to determine the corrosive properties of components. A salt spray test in accordance with ASTM B117 standard was performed on the 1.5" X 2" (5.1 cm X 3.8 cm) samples produced in section 6.1 [80]. In this test, the samples were placed in a corrosive spray chamber for a certain period of time. Again, pieces of bulk copper sheeting were placed along with the metalized BMS 8-276 samples as a comparative reference for visual inspection. The metalized BMS 8-276 samples were considered acceptable if they perform in a similar manner than the bulk copper. A list of the coatings that were analyzed is presented in Table 37.

Table 37: List of Coatings Placed in Salt Spray Corrosion Chamber

Test Case	*Number of Samples*	*Top Coat*	*Bond Coat*	*BMS 8-276 Ply*	*Scribed*
1	6	Tin	NA	WGFP	no
2	6	Tin	NA	WGFP	yes
3	6	Copper	Tin	WGFP	no
4	6	Copper	Tin	WGFP	yes
5	6	Copper	Copper & PEEK	LCFP	no
6	1	Copper	Copper & PEEK	LCFP	yes
7	2	Copper & PEEK	NA	LCFP	no
8	1	Copper & PEEK	NA	LCFP	yes
9	5	Bulk Copper	NA	NA	NA

Some samples were scribed in order to expose the underlying BMS 8-276 substrate. This is a common practice to simulate a defect in manufacturing and observe possible interactions between the different components of the metalized composites. All samples were taped at the edges using masking tape as shown in Figure 178 with the exception of the bulk copper sheeting. Taping the edges prevents corrosion products from infiltrating between the coating and the substrate at the perimeter.

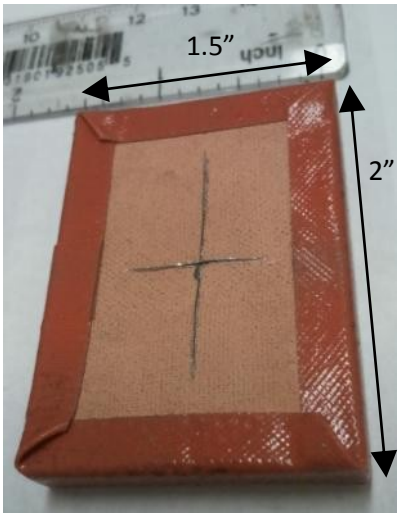

Figure 178: Example of a taped 1.5" X 2" (5.1 cm X 3.8 cm) sample before salt spray corrosion test.

After 256 hours of operation, no discernible increase in corrosion was noted and the test was stopped. Unfortunately, some of the taping came undone after a period of time. This was especially true for the corners of the samples. Once exposed, the edges of the samples were susceptible to the corrosive environment. However, no accelerated corrosion seemed to have occurred.

In the test cases 1 and 2, discoloration of the tin was observable (see Figure 179). A wide range of colors can be distinguished including, blue, purple, yellow, brown, and white. Tin oxide (SnO) is often blue or black whereas tin dioxide (SnO2) is white. However, the thickness of the tin oxide is known to interfere with light in a destructive and constructive way which can result in a variety of colors much like the present situation. The scribing of the coating did not seem to have had any impact on the progression of the corrosion from an observable standpoint. The tin, in this case, may act as a sacrificial anode.

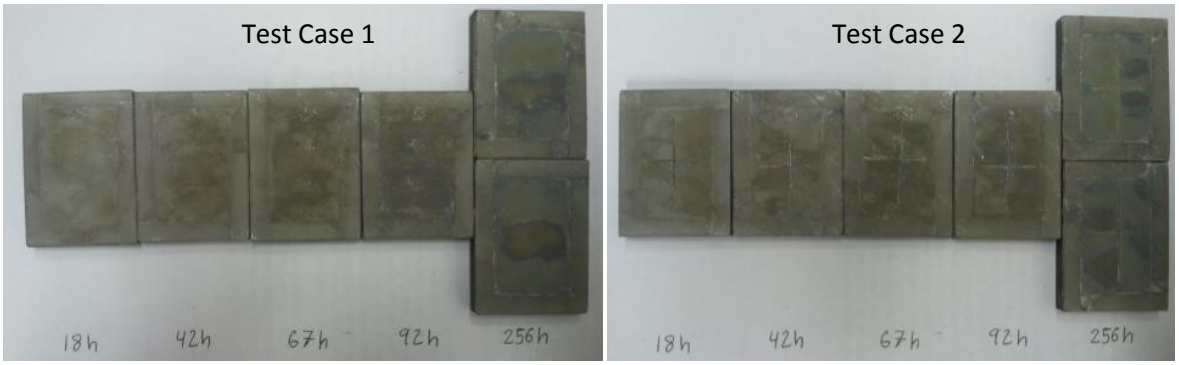

Figure 179: Salt spray corrosion test cases 1 and 2. The time spent in the salt spray chamber is indicated under each sample.

In the test cases 3 and 4, severe corrosion occurred (see Figure 180). The combination of tin and copper most likely created a galvanic cell. Pitting and discoloration can be observed on these samples. The brownish-red color is cuprous oxide (Cu_2O) while the black color near the edges indicates the presence of cupric oxide (CuO). Taping the edges did not always prevent corrosion from occurring. A dark corrosion product can be observed at the edges of some samples. This corrosion product occurred under the intact tape. The blue-green corrosion products are a combination of green brochantite ($Cu_4SO_4(OH)_6$), green malachite ($Cu_2CO_3(OH)_2$), and blue azurite ($Cu_4(CO_3)_2(OH)_6$). The pale corrosion products could be caused by an interaction between the copper top coat and tin bond coat. These corrosion products are more prevalent in the test case 4 where the coating was scribed indicating corrosive instability between the materials.

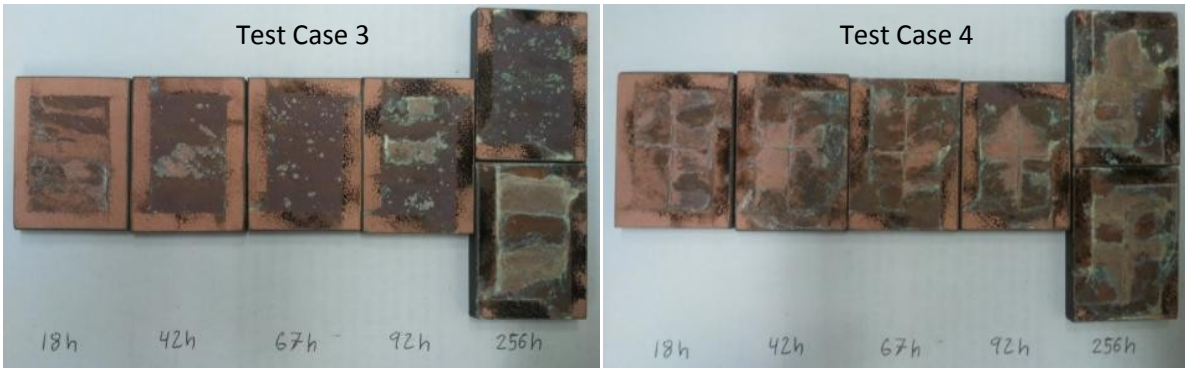

Figure 180: Salt spray corrosion test cases 3 and 4. The time spent in the salt spray chamber is indicated under each sample.

In the test cases 5, 6, 7, and 8, similar corrosion products were present (see Figure 181). Once again brownish-red colored cuprous oxide (Cu_2O) and black colored cupric oxide (CuO) formed at the

center and edges respectively. In all four test cases, teal colored corrosion products formed at the junction of the cuprous oxide and the cupric oxide much like in test cases 3 and 4. However, in the test cases 7 and 8, the brownish-red colored cuprous oxide turned purple after a prolonged exposure to the salt spray. Complexes of copper(III) are known to have a purple color. Given that these two test cases had a mix of copper and PEEK exposed at the surface, the formation of complex copper(III) compounds is possible. In test cases 6 and 8, the combination of copper and carbon (the exposed fibres of the BMS 8-276 when scribing) could also result in the formation of complex copper compounds.

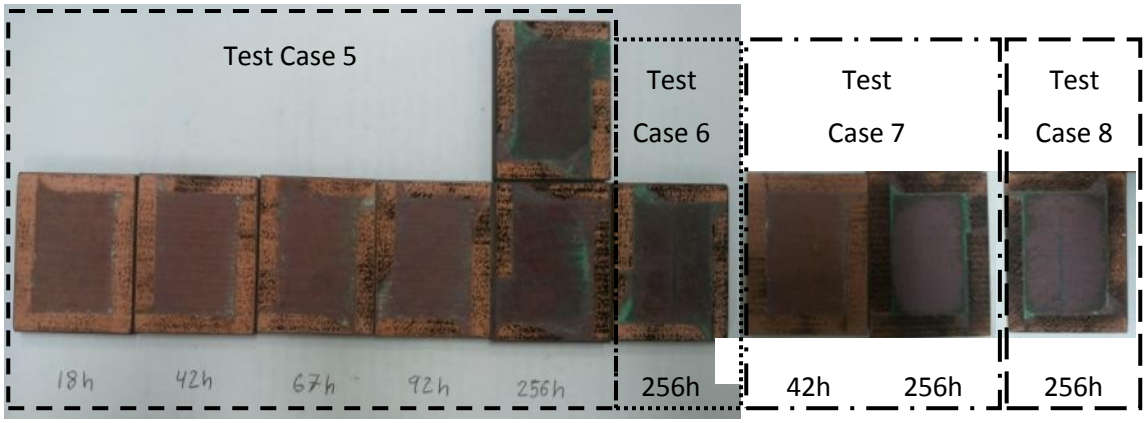

Figure 181: Salt spray corrosion test cases 5, 6, 7, and 8. The time spent in the salt spray chamber is indicated under each sample.

The test case 9 was used as a control for the copper coated samples. Minor reddish discoloration occurred evenly across the samples along with some localized green oxidation (see Figure 182). An extra smaller piece of copper sheeting was added to the picture to show the full color transition. As previously mentioned, these are typical copper oxides. It is important to note that the edges of these samples were not taped during the corrosion test. When compared to test cases 5, 6, 7, and 8, the corrosion of the bulk copper sheeting is less severe.

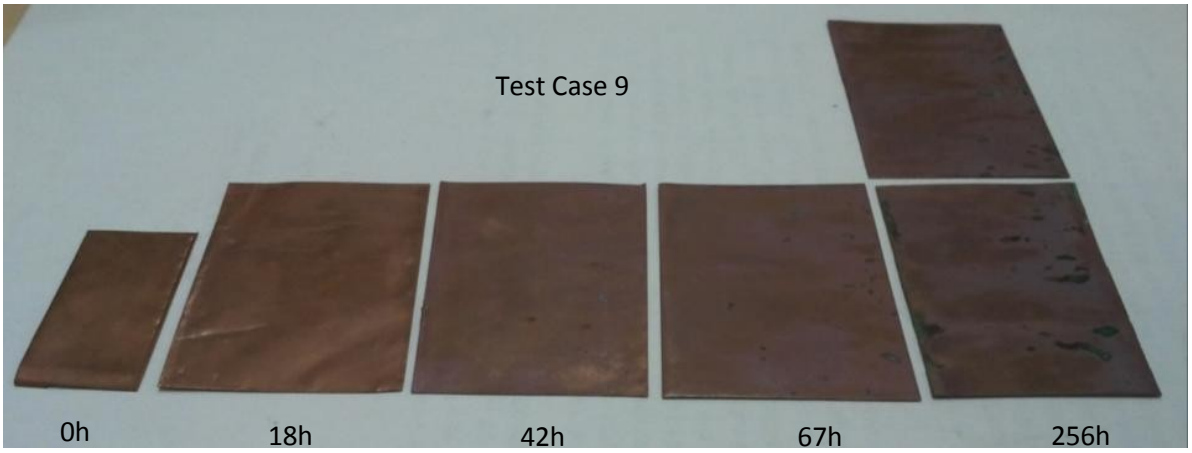

Figure 182: Salt spray corrosion test case 9. The time spent in the salt spray chamber is indicated under each sample.

It is important to note at this point that the sheet resistance of each coating was measured once removed from the corrosive environment. A single value was generated for each sample using the four point probe resistivity sensor connected to a digital multimeter. The values of Test Case 7 were removed from this analysis for their recorded sheet resistance was disproportionally high when compared to the other samples (much like in Figure 176a). In addition, the low sample number discredited any trends that could arise from the two values. When plotting the sheet resistance with respect to the time spent in the corrosion chamber, no trends could be identified with absolute certainty (see Figure 183).

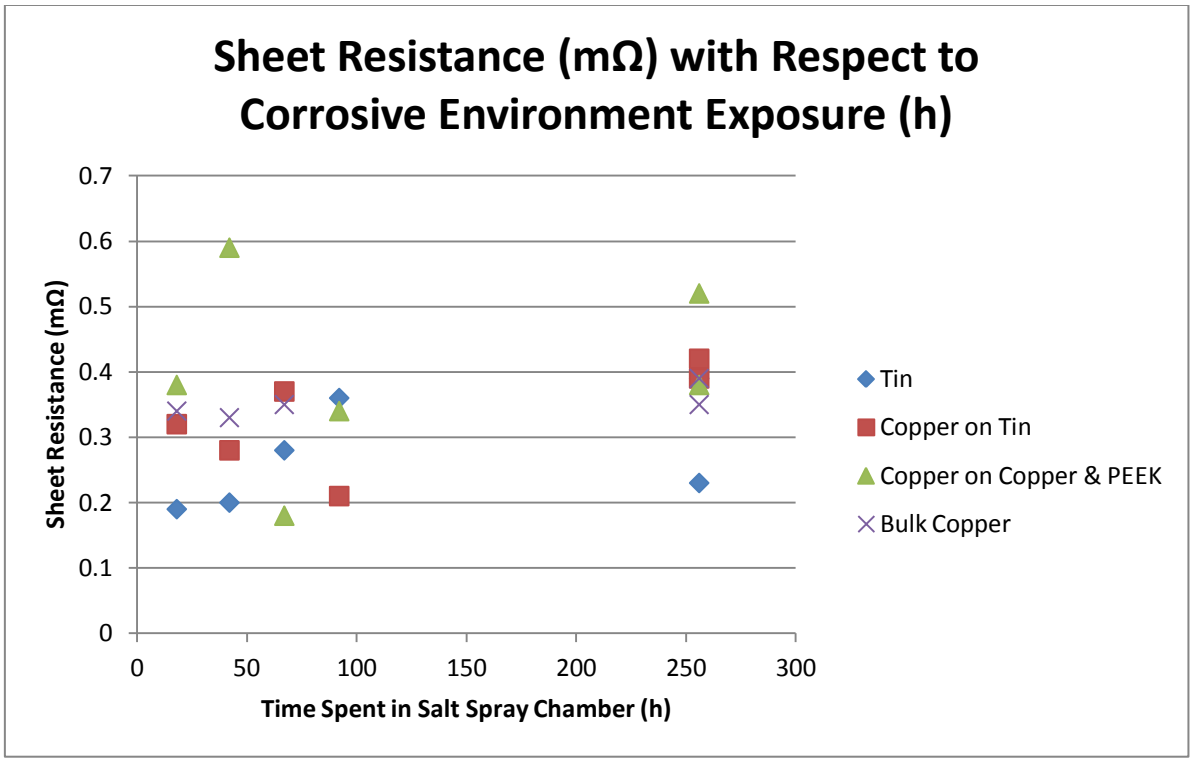

Figure 183: The sheet resistance with respect to the time spent in the corrosion chamber.

It can be stated that the sheet resistance is marginally higher after 256h of exposure than after 18h. However, the variability of the sheet resistance measurement seemed to outweigh the influence of corrosive environment exposure. The corrosion products accumulated over the surface of the coatings do not seem to inhibit the conductive nature of the coatings.

Cross-sectional analysis revealed that little internal corrosion had taken place on the samples (see Figure 184). With the exception of Test Case 7, the superficial corrosion visually observed on the samples manifested as a dark coating only a few microns thick. An example of a small pit can be seen in Test Case 1 (see Figure 184a). Any superficial cracks that were present in the pure copper top coat of Test Case 3 and Test Case 5 became sites where corrosion can easily take place (see Figure 184b & c). It is thought that the irregular topography combined with the exposed chemically inert PEEK caused the increased corrosion penetration in Test Case 7 (see Figure 184d). When comparing the corrosion of the bulk copper sheeting (Test Case 9), it can be stated that the degree of corrosion is similar to all other test cases with the exception of Test Case 7 (see Figure 184e).

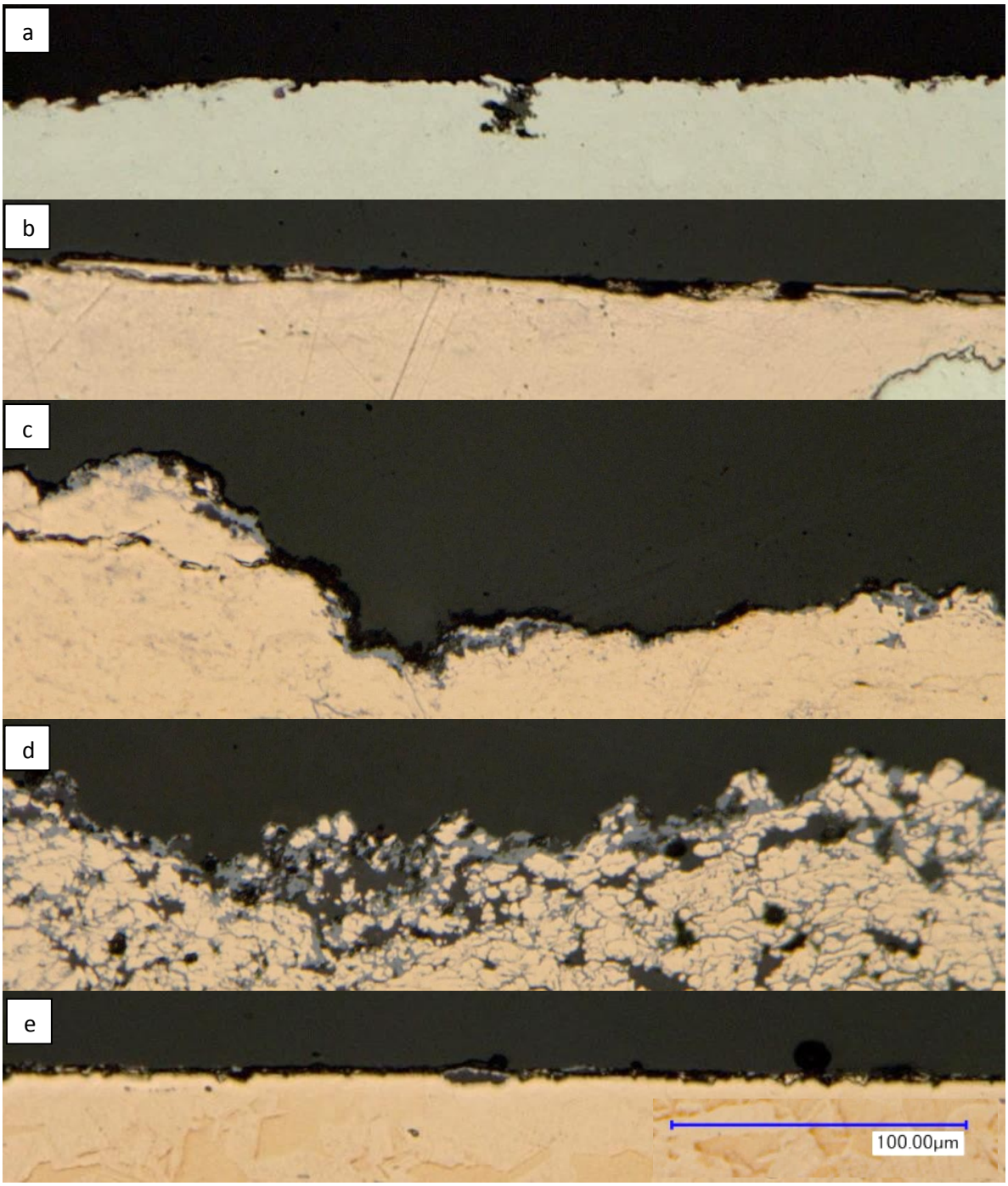

Figure 184: Cross-sectional image of non-scribed area of (a) Test Case 1, (b) Test Case 3, (c) Test Case 5, (d) Test Case 7, and (e) Test Case 9.

Analysis at the scribe location revealed that the tin often peeled when scribed creating a seam between itself and the BMS 8-276 (see Figure 185a & b). Crevices like these tend to experience accelerated corrosion. As concluded during visual inspection, mixing copper and tin created a

galvanic cell which further accelerates corrosion (see Figure 185b). Corrosion also occurred in both cases using copper & PEEK (see Figure 185c & d). Once the chemically inert PEEK and epoxy are exposed, the more reactive copper corroded.

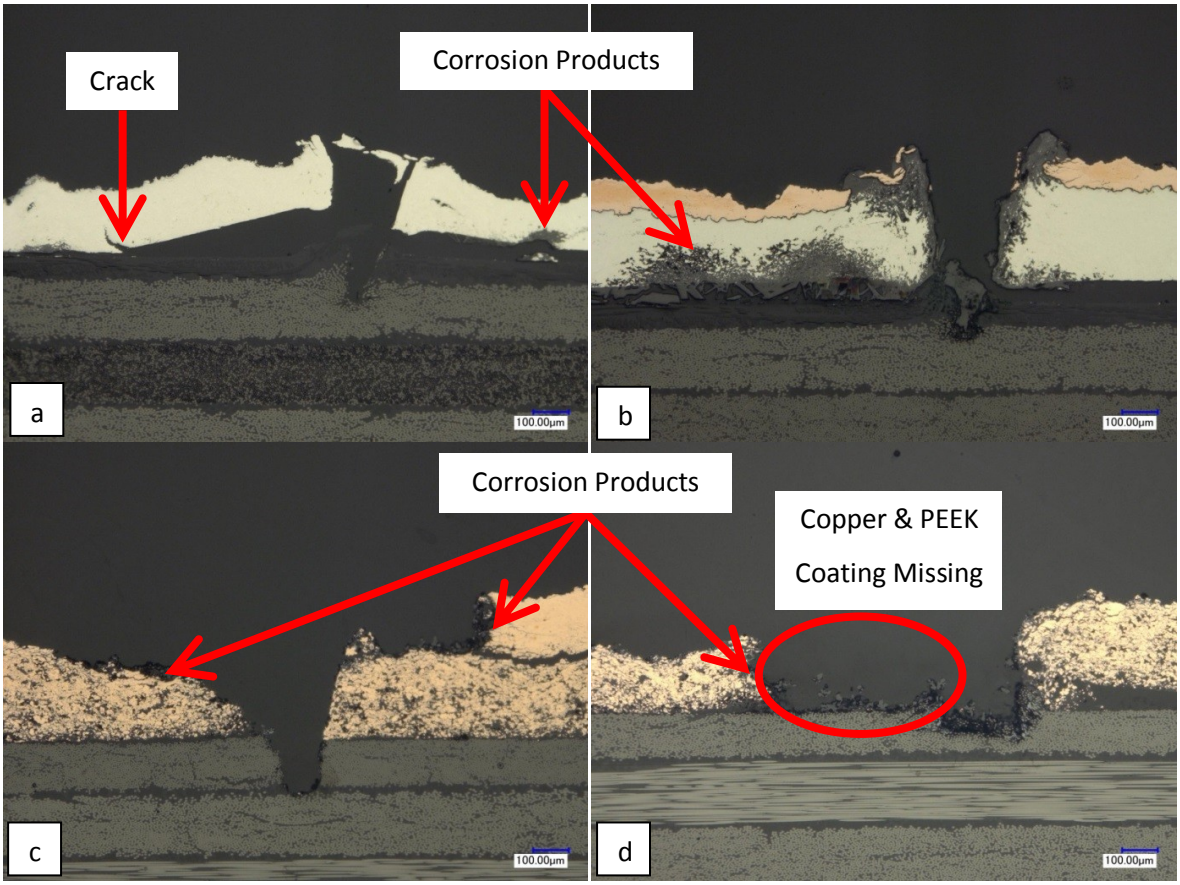

Figure 185: Cross-sectional image of scribe of (a) Test Case 2, (b) Test Case 4, (c) Test Case 6, and (d) Test Case 8.

Although the copper & PEEK coatings did not create crevices, there is evidence that a piece of copper & PEEK coating did peel from the BMS 8-276 substrate near the scribed location in a particular instance (see Figure 185d). Unlike with tin, the copper & PEEK coating broke-off from the remainder of the coating. This indicates that the copper & PEEK coating may have a lower cohesion that the tin coating. This also shows that the tin coating is much more ductile whereas the copper & PEEK coating is brittle in nature. The ductility of the tin coating is further demonstrated by the crack propagation prevention. A crack can be seen in Figure 185a on the tensile face of the bend of the tin coating. No other cracks were observed on other samples. This crack most likely occurred while scribing the sample. The amplitude of the bend likely created large tensile stresses which resulted in

a crack formation and propagation. However, the ductility of the tin coating prevents further propagation. Considering that aircraft undergo large strains when in flight, the ductile nature of the tin coating is of great importance. For example, whenever an airplane wing bends and twists when flying through turbulence, it is imperative that the metal coating remains intact to ensure proper conductivity.

From a corrosive standpoint, it would be optimal to utilize a combination of copper & PEEK coated with a pure copper top coat as far as metalizing the BMS 8-276 goes. A simple tin coating would have been the coating of choice had it not peeled from the BMS 8-276 when scribed.

6.3 Adhesion Strength

The adhesion strength is another vital factor in this research. Without proper adhesion, the conductive coating may delaminate and disrupt the conductive pathway. The Boeing Company standard D6-51343, intended for other thermal spray processes, was the best suited reference adhesion value given the originality of this research. According to this industry standard, a minimal adhesion of 2000 psi is required to pass. As such, any adhesion strength of a coating that resided below 2000 psi (13.79 MPa) was considered a fail. All adhesion testing were done using a Pneumatic Adhesion Tensile Testing Instrument (PATTI).

Adhesion testing was performed on the same samples used in the salt spray chamber from the previous section (6.2). Unfortunately, the glue used between the pull-stubs and certain tin coated substrates broke leaving the coating completely intact. These instances only occurred for high adhesion results (>1200 psi) (>8.27 MPa) indicating the adhesive limit of the glue. Only a single PATTI measurement could be taken from each sample. The compiled results presented in Figure 186 do not show evidence that exposure to a corrosive environment affects the adhesion strength of the coatings.

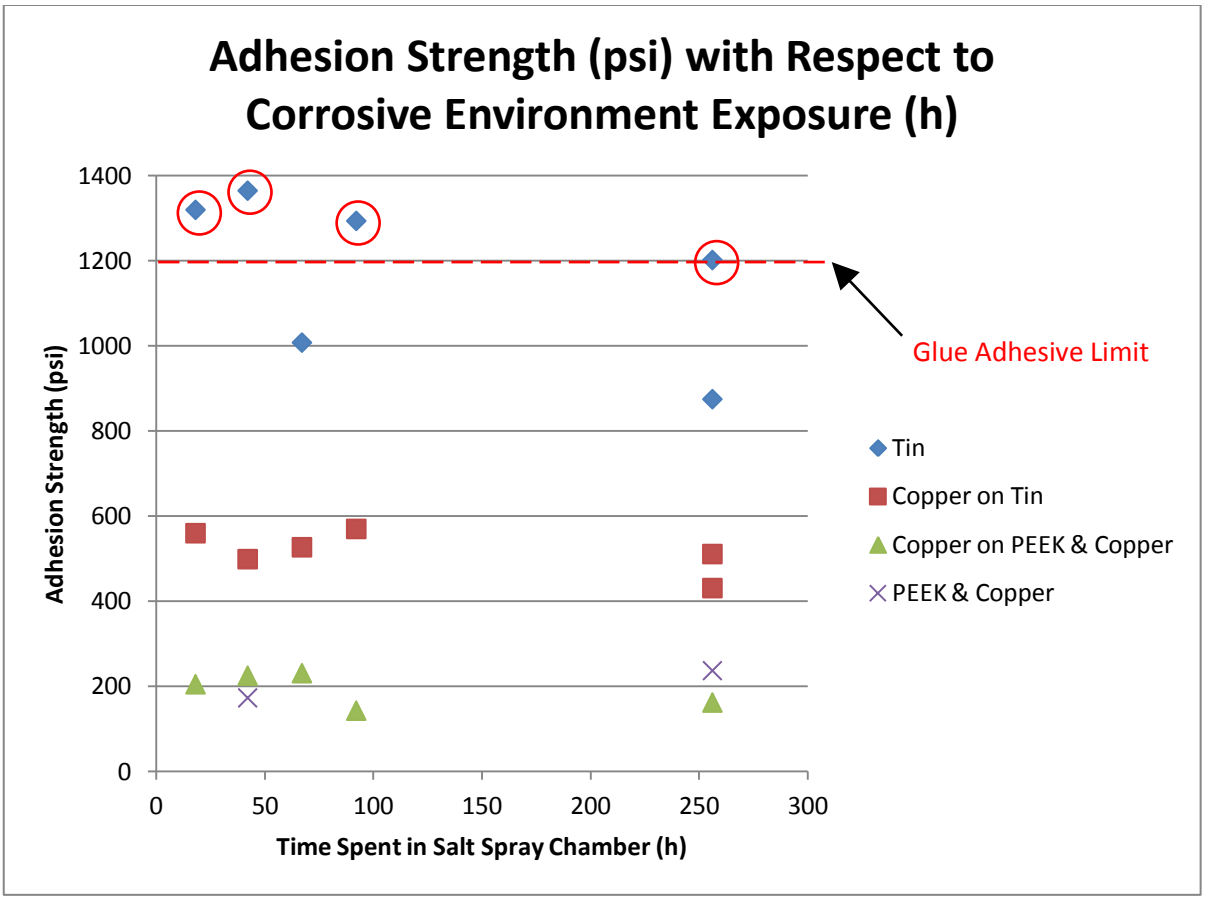

Figure 186: The adhesion strength with respect to the time spent in the corrosion chamber.

Figure 186 also presents the disparity between the different types of coatings. The simple tin coating offers the highest adhesion, followed by the combined copper on tin coating, and lastly the PEEK & copper coatings (with and without a pure copper top coat). The addition of a pure copper top coat does not affect the overall adhesion of the PEEK & copper bond coat to the BMS 8-276 substrate. A large disparity can observed between the adhesion of the tin coatings without a pure copper top coat (≈1200psi or 8.27 MPa) and the tin coatings with a pure copper top coat (≈500 psi or 3.45 MPa). It can be concluded that adding a copper top coat to the tin bond coat lowers the adhesion of the tin to the BMS 8-276. Because of the poor glue properties, it is unclear where the specific adhesion value of the simple tin coating lies. However, it is fairly certain that had the glue not failed, the values registered would have been slightly higher yet in the vicinity of the values obtained. This can be expected given the two data points where the glue did not fail. The variability between the adhesion values are much larger for the tin coatings (±200 psi or ±1.38 MPa) than for any other coating deposited on the BMS 8-276 (±50 psi or ±0.34 MPa). This increase in variability

could be a result of the high adhesion strength of these coatings. Another cause could be the method by which the PATTI is performed on the coating. When the coating surrounding the pull-stub is removed using a hole saw drill bit, the neighboring tin may peel from the substrate much like when scribed (see Figure 185 of section 6.2). This can greatly affect the adhesion of the coating depending on the severity of the peeled area. It is believed that the tin peels from the BMS 8-276 under high stress because of its high cohesion. It becomes easier for the tin coating to break off from the substrate than it is to break from itself. This also indicates that the tin coating is highly malleable whereas the composite bond coat is more brittle.

From an adhesive standpoint, all of the coatings deposited on the BMS 8-276 fall short of The Boeing Company standard D6-51343. This being said, the optimal choice would be the tin coating without a pure copper top coat for its adhesion remains at least twice as high as any other type of coating produced.

6.4 Allotropic Transformation Test

As stated in subsection 2.2.7.2.4, one of the main concerns with using tin as a conductive material for airplane components composed of BMS 8-276 is the allotropic transformation that can take place. Tin undergoes an allotropic transformation from its β phase to an α phase below 13.2°C which results in visually observable cracking and wart growth. An experiment was conducted to determine if this transformation would occur on tin (SST-S6001) coated BMS 8-276 using the SST-P system. A total of six samples were taken from previous experiments conducted in section 5.1.6 and section 5.1.7 and placed in a conventional refrigerator (held at 6°C), a conventional freezer (held at -18°C), and a specialized freezer (held at -80°C) for a period of 3000 hours (see Figure 187).

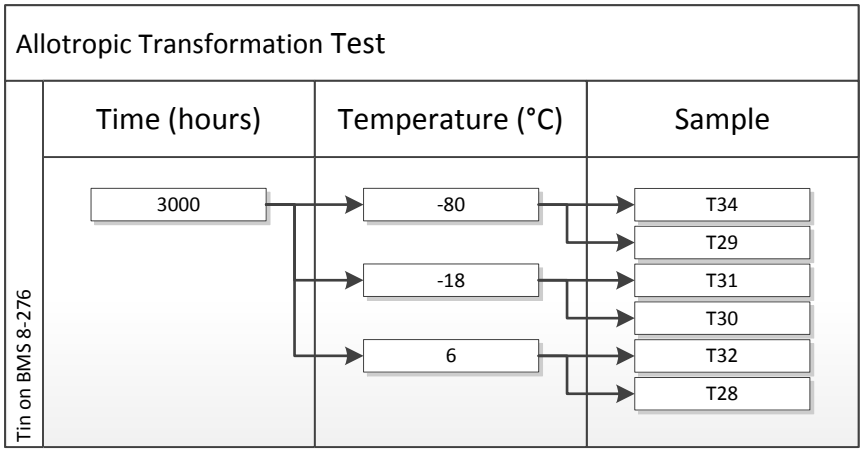

Figure 187: Allotropic transformation test where samples from section 5.1.6 and section 5.1.7 were placed in three different refrigerators held at -18°C, -80°C, and 6°C respectively for a period of 3000 hours.

The tin coatings of the samples were visually undistinguishable from each other for they all looked similar. An example of these samples is given in Figure 188. Please note that all tin coatings were initially deposited on 2" X 1.5" (5.1cm X 3.8 cm) WGFP BMS 8-276 samples. However, some samples were cut post-deposition in order to observe their cross-section. In addition, adhesion tests were conducted on the samples, leaving behind a circularly shaped BMS 8-276 surface without a tin coating.

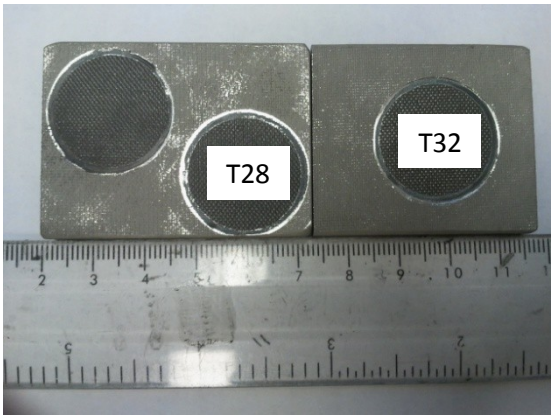

Figure 188: An example of the tin coated WGFP BMS 8-276 samples prior to the 3000h allotropic transformation test.

After 3000 hours of cold temperature exposure, the samples were removed from their respective refrigerators. As depicted in Figure 189, no allotropic transformation can be distinguished. No cracking or warts can be observed at the surface. There is no discernible discolouration.

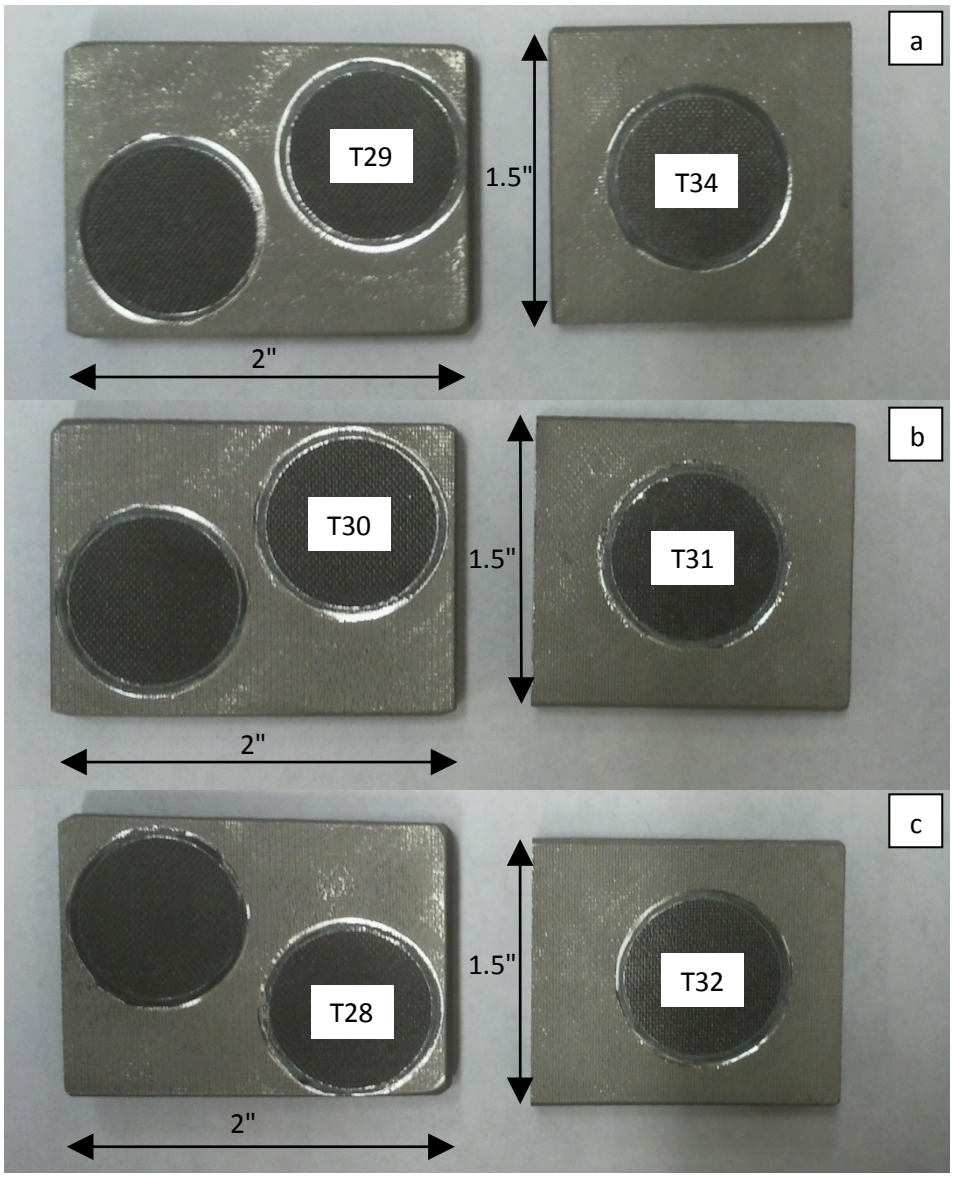

Figure 189: Allotropic transformation test samples after 3000 hours in a (a)- 80°C, (b) -18°C, and (c) 6°C temperature environment.

Researchers agree that the surface of a tin sample is the favourable region for the nucleation of the α-phase tin which further strengthens the notion that no allotropic transformation has taken place here. In fact, the samples look identical as they did prior to the 3000 hour test. Perhaps the sluggish nature of the transformation of β-Sn to α-Sn requires more time to take visual effect. The lack of an α nucleate could have also prolonged the transformation by adding an incubation period. In theory, the reaction of the samples exposed to a temperature of -80°C should have been under a larger driving force than the samples placed at -18°C or 6°C; yet, no allotropic transformation occurred on

the samples regardless of the exposure temperature. Looking at the chemical composition of the tin material (SST-S6001), elements such as lead (0.042wt%), bismuth (0.03wt%), and antimony (0.009wt% to 0.015wt%) can be noted (see Table 8). As mentioned in section 2.2.7.2.4, such elements are known to suppress the β-to-α transition. In certain cases, even minor impurities (parts per million range) of these elements have completely inhibited the allotropic transformation. However, elements such as zinc, aluminum, magnesium, and manganese, which are known to accelerate tin pest formation, do not appear in the chemical composition analysis of SST-S6001 (see Table 8). The composition of tin remains one of the most influential factors in the allotropic transformation. In this case, it is clear that the chemical composition of the SST-S6001 powder opposes such transformation. Other factors such as the manufacturing conditions (during deposition in this case) could also influence the transformation of tin.

6.5 Curved Surface

Given the superior performance of the tin coating, an additional experiment was performed. In order to demonstrate the application potential of this process, a tin coating was deposited on curved composites. The composites were produced at the University of Ottawa using prepreg carbon fibre reinforced epoxy (see section 4.3.2). The spray parameters used are presented in Table 38.

Table 38: Tin Coating Parameters Used for Convexe and Concave CFRP

CGDS Parameter	Value
Gas Pressure	90 psi (0.62 MPa)
Gas Temperature	300°C
Gas Nature	Nitrogen
Standoff Distance	10 mm
Nozzle Type	120 mm SS Nozzle
Orifice Diameter	2 mm
Powder Feeder Wheel	320 Small Hole
Powder Feeder Gas Rate	30 scfh (0.85 m^3/h)
Powder Feed Rate	3 rpm (0.31 rad/s)
Step Size	1 mm

Traverse Velocity	200 mm/s

A thick tin coating was deposited on both, convex and concave composite surfaces (Figure 190). A large number of passes had to be made in order to produce a uniform coating. It is important to note however that the composites produced are not identical to the BMS 8-276 but serve as a comparable material. A drop in DE is likely caused by the change of material rather than the curvature. Both samples had to be repositioned to minimise the variation of the SOD while spraying.

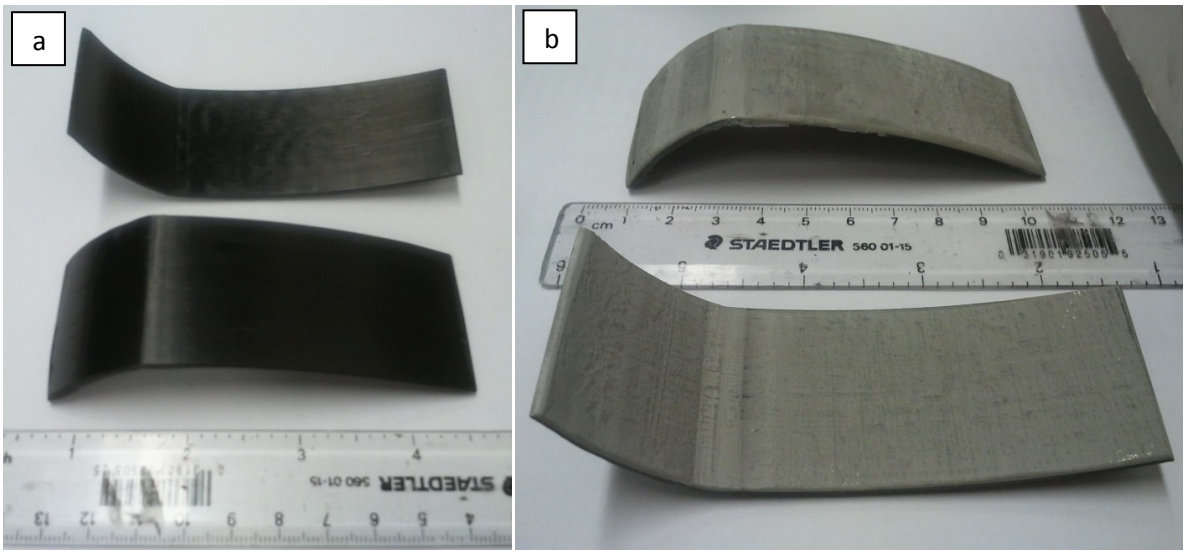

Figure 190: (a) Convex and concave pre-impregnated carbon fibre reinforced epoxy composites (b) coated with tin.

7 Conclusion and Future Work

This research resulted in the successful metallization of a BMS 8-276 sample using a commercially available CGDS system. It was found that both copper and tin powders could be deposited on the aerospace grade composite; however, the copper required a bond coat to be initially deposited on the BMS 8-276. Without a bond coat, the hard copper particles simply eroded the BMS 8-276. Two bond coats were tested with varying degrees of success. The first consisted of a mixture of copper and PEEK while the other was the simultaneously developed tin coating. When depositing tin on the BMS 8-276, whether used as a bond coat or not, it was found that the WGFP provided the best adhesion. Surface treatments did not affect the adhesion of the tin coating to the WGFP of the BMS 8-276 and so the elimination of the surface treatment step was done altogether (The tin coating was deposited on the "As Received" WGFP). For the copper and PEEK bond coat, the LCFP proved superior than the WGFP of the BMS 8-276 as a surface for deposition. The primary reason behind the elimination of the WGFP was the exposure of epoxy in the absence of fibres. Much like the toughening heterogeneous system, zones rich in epoxy prevented the deposition of the composite bond coat. However, unlike tin, the composite bond coat does not effectively bridge over these zones resulting in the creation of deep pits. As such, the copper and PEEK bond coat had to be deposited on a single LCFP of the BMS 8-276. It was decided that using a polished surface finish was optimal since the addition of a grit blasting step provided no discernible value. Theories to explain the adhesion mechanisms of the two different types of coatings were elaborated using various results obtained during experiments. Heat was the predominant factor used to soften the tin particles during deposition in order to deform them. Impacting tin particles eroded the epoxy matrix and exposed the glass fibres of the WGFP. The tin adhered to the substrate by seeping between these fibres and enveloping them within the coating creating mechanical anchoring between the two. In the case of the composite bond coat, deformation is caused by a combination of kinetic energy and heat. Adhesion is made possible by the deformation of the PEEK particles which is primarily caused by subsequent impacting copper particles. Well deformed PEEK is believed to bond the copper particles to the BMS 8-276 by fill gaps between the two which seals them and creates a suction-like force. In addition to the various experiments, elaborated to define and optimize the parameters that affect the successful deposition of a conductive coating on a BMS 8-276 substrate, a total of three major tests were made to characterize and compare these developed coatings with respect to electrical resistivity, corrosion, and adhesion.

From a resistivity point of view, it was concluded that tin coating outperformed any other coating developed during this research. Nevertheless, all the other coatings also passed the conductive restrictions imposed by the Boeing Company's standard with the exception of the copper and PEEK bond coat. Without a pure copper top coat, the coating is not conductive enough according to BAC 5056. When a pure copper top coat is added to it, the conductivity is sufficiently increased however, the thickness is too large to pass the BAC 5056 requirements. These conclusions remain true even after 256 hours of exposure in a salt fog spray chamber. The corrosion products accumulated over the surface of the coatings do not seem to inhibit the conductive nature of the coatings.

When compared from a corrosive standpoint, a copper & PEEK bond coat combined with a pure copper top coat would be the optimal choice. Admittedly, the corrosion products in all the coatings produced were quite low and comparable to the degree of corrosion on a bulk copper sheeting with the exception of the copper and PEEK bond coat without a top. The superficial corrosion visually observed on the samples was only a few microns in thickness. Scribing the coatings and exposing the BMS 8-276 substrate revealed that the tin coating had a tendency to peel from the substrate and create a narrow crevice that leads to accelerated corrosion. This further enhances when the tin coating is covered by a copper top coat which creates a galvanic cell. Analysis of the copper & PEEK coating revealed that part of the coating broke-off near the scribe location. The tin's tendency to bend demonstrates its ductility whereas the copper & PEEK coating can be characterized as brittle. The ductility of the tin coating may be of some value if applied to an aircraft undergoing strain. The simple tin coating would have been the coating of choice had there not been a crevice formed when scribed.

On the adhesive front, no coating produced on the BMS 8-276 passed the objective of reaching 2000 psi (13.79 MPa) outlined in the Boeing Company standard D6-51343. Although this standard is intended for other thermal spray processes, it is the best suited reference adhesion value given the originality of this research. Out of the selection of failures, the simple tin coating (without a pure copper top coat) is the best option. Its adhesion strength to the WGFP of the BMS 8-276 was recorded somewhere around 1200psi. However, it is to note that the poor adhesive property of the glue used caused premature tensile failure to occur in 67% of the adhesion tests performed on the tin coatings. Had the glue not failed, slightly higher adhesion values could be anticipated. Adding a pure copper top coat to this tin coating lowered the adhesion strength of the coating to the BMS 8-

276 to roughly 500 psi (3.45 MPa). Given this was the only difference between the two sets of results, it can be concluded that adding a copper top coat to the tin bond coat lowers the adhesion of the tin to the BMS 8-276. Adhesion results of copper and PEEK coatings both with and without a pure copper top coat were measured to be near the 200 psi (1.38 MPa) mark. For this bond coat, no effect with regards to the adhesion strength was noticed when adding a pure copper top coat. The adhesion strength of all types of coatings produced was not affected when exposed to salt fog for 156 hours.

With the tin coating being the overall superior option, additional experiments were conducted to verify the non-occurrence of an allotropic transformation in the deposited tin material and to demonstrate the promising industrial applications of the CGDS process for onsite repair work.

In closing, this research covers only the initial steps required to take this technology to the industrialization stage. In order to better qualify the conductive coatings produced, an electrical charge comparative to that of a lightning bolt should be induced on a coated BMS 8-276. Its capability to be used as a temporary conduit (like an airplane) should be evaluated. Furthermore, the extent of damage should be monitored and proper repair methods (including the CGDS process) should be established. Additional research must be done to further analyze the adhesion mechanisms at play and ultimately optimize the adhesion strength of the conductive coatings. For example, Bray et al. have further improved a process by adding thermal energy to the deposition zone with the use of a laser source, in such a way to reduce particle yield stresses, facilitate greater bond strengths and promote higher coating densities [21]. Another option to optimize adhesion strength could be to reduce the metallic particle distribution (much like with PEEK in section 5.2.7). Experiment utilizing atmospheric plasma could be done much like Coulon et al. to increase the adhesion strength of metallic coated CFRP composites [16]. Techniques to further expose the reinforcing fibres are of particular interest given the correlation between degree of fibre embedment and the adhesion strength of the tin coating (outlined in section 5.1.7). Future work should also focus on evaluating the metalized coatings with respect to stress and strain requirements. The conductive coating's ability to remain functional is of great importance.

References

[1] "787 Dreamliner Design Highlights | Boeing Commercial Airplanes," *Boeing's New Airplane*. [Online]. Available: http://www.newairplane.com/787/design-highlights/#/visionary-design/composites/advanced-composite-use. [Accessed: 04-Sep-2014].

[2] Greg Sweers, Bruce Birch, and John Gokcen, "Lightning Strikes: Protection, Inspection, and Repair," *AERO*, no. 4, 2012.

[3] Clarence E. Rash, "When Lightning Strikes | Flight Safety Foundation," *AeroSafety World*, vol. 9, no. 6, Jul-2014.

[4] G. Gardiner, "Lightning Strike Protection For Composite Structures," *CompositesWorld*, 01-Jul-2006. [Online]. Available: http://www.compositesworld.com/articles/lightning-strike-protection-for-composite-structures. [Accessed: 09-Sep-2014].

[5] H. Kawakami and P. Feraboli, "Lightning strike damage resistance and tolerance of scarf-repaired mesh-protected carbon fiber composites," *Compos. Part Appl. Sci. Manuf.*, vol. 42, no. 9, pp. 1247–1262, Sep. 2011.

[6] Walter Polt, "A little friction at Boeing," *Boeing Frontiers Online*, vol. 3, no. 5, Sep-2004.

[7] J. R. Davis, *Handbook of Thermal Spray Technology*, Illustrated edition. Materials Park, OH: ASM International, 2004.

[8] E. Njuhovic, A. Witt, M. Kempf, F. Wolff-Fabris, S. Glöde, and V. Altstädt, "Influence of the composite surface structure on the peel strength of metallized carbon fibre-reinforced epoxy," *Surf. Coat. Technol.*, vol. 232, pp. 319–325, Oct. 2013.

[9] X. L. Zhou, A. F. Chen, J. C. Liu, X. K. Wu, and J. S. Zhang, "Preparation of metallic coatings on polymer matrix composites by cold spray," *Surf. Coat. Technol.*, vol. 206, no. 1, pp. 132–136, Oct. 2011.

[10] H. Lee, H. Shin, S. Lee, and K. Ko, "Effect of gas pressure on Al coatings by cold gas dynamic spray," *Mater. Lett.*, vol. 62, no. 10–11, pp. 1579–1581, Apr. 2008.

[11] H. Assadi, F. Gärtner, T. Stoltenhoff, and H. Kreye, "Bonding mechanism in cold gas spraying," *Acta Mater.*, vol. 51, no. 15, pp. 4379–4394, Sep. 2003.

[12] S. Black, "Lightning strike protection strategies for composite aircraft," *CompositesWorld*, 01-May-2013. [Online]. Available: http://www.compositesworld.com/articles/lightning-strike-protection-strategies-for-composite-aircraft. [Accessed: 09-Sep-2014].

[13] L. Gunter, "Dustbusters!," *Frontiers*, vol. 6, no. 3, pp. 44–45, Jul-2007.

[14] A. G. Miller, D. T. Lovell, and J. C. Seferis, "The evolution of an aerospace material: Influence of design, manufacturing and in-service performance," *Compos. Struct.*, vol. 27, no. 1–2, pp. 193–206, 1994.

[15] S. L. Donaldson and D. B. Miracle, *ASM Handbook Composites Volume 21*, 10 edition., vol. 21, 21 vols. Materials Park, Ohio: ASM International, 2001.

[16] J. F. Coulon, N. Tournerie, and H. Maillard, "Adhesion enhancement of Al coatings on carbon/epoxy composite surfaces by atmospheric plasma," *Appl. Surf. Sci.*, vol. 283, pp. 843–850, Oct. 2013.

[17] A. Liu, M. Guo, J. Gao, and M. Zhao, "Influence of bond coat on shear adhesion strength of erosion and thermal resistant coating for carbon fiber reinforced thermosetting polyimide," *Surf. Coat. Technol.*, vol. 201, no. 6, pp. 2696–2700, Dec. 2006.

[18] "Expanded Metal - Expanded Metal Foil - Expanded Metal Mesh - Expanded Plastic - Dexmet Corporation." [Online]. Available: http://www.dexmet.com/Aircraft-Lightning-Strike-Protection.html. [Accessed: 05-Sep-2014].

[19] P. C. King, A. J. Poole, S. Horne, R. de Nys, S. Gulizia, and M. Z. Jahedi, “Embedment of copper particles into polymers by cold spray,” *Surf. Coat. Technol.*, vol. 216, pp. 60–67, Feb. 2013.
[20] A. Ganesan, M. Yamada, and M. Fukumoto, “The Effect of CFRP Surface Treatment on the Splat Morphology and Coating Adhesion Strength,” *J. Therm. Spray Technol.*, vol. 23, no. 1–2, pp. 236–244, Jan. 2014.
[21] R. Lupoi and W. O’Neill, “Deposition of metallic coatings on polymer surfaces using cold spray,” *Surf. Coat. Technol.*, vol. 205, no. 7, pp. 2167–2173, Dec. 2010.
[22] N. An, G. P. Tandon, and K. V. Pochiraju, “Thermo-oxidative performance of metal-coated polymers and composites,” *Surf. Coat. Technol.*, vol. 232, pp. 166–172, Oct. 2013.
[23] A. Ganesan, J. Affi, M. Yamada, and M. Fukumoto, “Bonding behavior studies of cold sprayed copper coating on the PVC polymer substrate,” *Surf. Coat. Technol.*, vol. 207, pp. 262–269, Aug. 2012.
[24] A. Ganesan, M. Yamada, and M. Fukumoto, “Cold Spray Coating Deposition Mechanism on the Thermoplastic and Thermosetting Polymer Substrates,” *J. Therm. Spray Technol.*, vol. 22, no. 8, pp. 1275–1282, Dec. 2013.
[25] X. R. J. Kirmann, “Effects of the alkaline permanganate etching of epoxy on the peel adhesion of electrolessly plated copper on a fibre-reinforced epoxy composite,” *J. Adhes. Sci. Technol. - J ADHES SCI TECHNOL*, vol. 12, no. 4, pp. 383–397, 1998.
[26] P. Lammel, B. Torun, C. Kleber, and G. Grundmeier, “In-situ AFM study of the electrodeposition of copper on plasma modified carbon fibre-reinforced polymer surfaces,” *Surf. Coat. Technol.*, vol. 221, pp. 22–28, Apr. 2013.
[27] M. Menningen, H. Weiss, and U. Fischer, “Metallic wear resistant coatings for carbon fibre epoxy composite rolls,” *Surf. Coat. Technol.*, vol. 71, no. 2, pp. 208–214, Mar. 1995.
[28] H. Ye and J. Wang, “Preparation of aluminum coating on Lexan by cold spray,” *Mater. Lett.*, vol. 137, pp. 21–24, Dec. 2014.
[29] Simon Baril-Gosselin, “Improving Integrally Heated Composite Tooling Through Cold Sprayed Copper Coatings and Heat Transfer Simulations,” Masters, University of Ottawa, Ottawa, 2013.
[30] U. S. Tewari, A. P. Harsha, A. M. Häger, and K. Friedrich, “Solid particle erosion of carbon fibre– and glass fibre–epoxy composites,” *Compos. Sci. Technol.*, vol. 63, no. 3–4, pp. 549–557, Feb. 2003.
[31] X. Roizard, M. Wery, and J. Kirmann, “Effects of alkaline etching on the surface roughness of a fibre-reinforced epoxy composite,” *Compos. Struct.*, vol. 56, no. 3, pp. 223–228, May 2002.
[32] Y. Xu and I. M. Hutchings, “Cold spray deposition of thermoplastic powder,” *Surf. Coat. Technol.*, vol. 201, no. 6, pp. 3044–3050, Dec. 2006.
[33] E. Avallone, T. Baumeister, and A. Sadegh, *Marks’ Standard Handbook for Mechanical Engineers*, 11 edition. McGraw-Hill Professional, 2006.
[34] D. Seo, K. Ogawa, K. Sakaguchi, N. Miyamoto, and Y. Tsuzuki, “Parameter study influencing thermal conductivity of annealed pure copper coatings deposited by selective cold spray processes,” *Surf. Coat. Technol.*, vol. 206, no. 8–9, pp. 2316–2324, Jan. 2012.
[35] T. Stoltenhoff, C. Borchers, F. Gärtner, and H. Kreye, “Microstructures and key properties of cold-sprayed and thermally sprayed copper coatings,” *Surf. Coat. Technol.*, vol. 200, no. 16–17, pp. 4947–4960, Apr. 2006.
[36] R. C. McCune, W. T. Donlon, O. O. Popoola, and E. L. Cartwright, “Characterization of copper layers produced by cold gas-dynamic spraying,” *J. Therm. Spray Technol.*, vol. 9, no. 1, pp. 73–82, Mar. 2000.
[37] T. Stoltenhoff, H. Kreye, and H. J. Richter, “An analysis of the cold spray process and its coatings,” *J. Therm. Spray Technol.*, vol. 11, no. 4, pp. 542–550, Dec. 2002.

[38] W. B. Choi, L. Li, V. Luzin, R. Neiser, T. Gnäupel-Herold, H. J. Prask, S. Sampath, and A. Gouldstone, "Integrated characterization of cold sprayed aluminum coatings," *Acta Mater.*, vol. 55, no. 3, pp. 857–866, Feb. 2007.
[39] "CenterLine Supersonic Spray Technology (SST)-Practical Cold Spray Solutions - Powders." [Online]. Available: http://www.supersonicspray.com/en/products_full?pg=SE45000&rp=14. [Accessed: 12-Nov-2014].
[40] W. Peng, "An investigation of Sn pest in pure Sn and Sn-based solders," *Microelectron. Reliab.*, vol. 49, no. 1, pp. 86–91, Jan. 2009.
[41] W. D. Callister and D. G. Rethwisch, *Materials Science and Engineering: An Introduction*, 8 edition. Wiley, 2009.
[42] Y. J. Joo and T. Takemoto, "Transformation of Sn–Cu alloy from white tin to gray tin," *Mater. Lett.*, vol. 56, no. 5, pp. 793–796, Nov. 2002.
[43] W. J. Plumbridge, "Tin pest issues in lead-free electronic solders," in *Lead-Free Electronic Solders*, Springer US, 2007, pp. 307–318.
[44] M. Leodolter-Dworak, I. Steffan, W. J. Plumbridge, and H. Ipser, "Tin Pest in Sn-0.5Cu Lead-Free Solder Alloys: A Chemical Analysis of Trace Elements," *J. Electron. Mater.*, vol. 39, no. 1, pp. 105–108, Jan. 2010.
[45] A. A. Matvienko, A. A. Sidelnikov, and V. V. Boldyrev, "The influence of relaxation of stresses occurring during the β → α transformation of tin on the kinetics of the transformation," *Solid State Ion.*, vol. 101–103, Part 1, pp. 641–645, Nov. 1997.
[46] S. Gialanella, F. Deflorian, F. Girardi, I. Lonardelli, and S. Rossi, "Kinetics and microstructural aspects of the allotropic transition in tin," *J. Alloys Compd.*, vol. 474, no. 1–2, pp. 134–139, Apr. 2009.
[47] D. Di Maio and C. Hunt, "On the absence of the β to α Sn allotropic transformation in solder joints made from paste and metal powder," *Microelectron. Eng.*, vol. 88, no. 1, pp. 117–120, Jan. 2011.
[48] Y. Kariya, N. Williams, C. Gagg, and W. Plumbridge, "Tin pest in Sn-0.5 wt.% Cu lead-free solder," *JOM*, vol. 53, no. 6, pp. 39–41, Jun. 2001.
[49] J.B. Calvert, "Tin," 12-Nov-2002. [Online]. Available: http://mysite.du.edu/~jcalvert/phys/tin.htm. [Accessed: 25-May-2015].
[50] O. Semenova, H. Flandorfer, and H. Ipser, "On the non-occurrence of tin pest in tin–silver–indium solders," *Scr. Mater.*, vol. 52, no. 2, pp. 89–92, Jan. 2005.
[51] S. Sampath, X. Y. Jiang, J. Matejicek, L. Prchlik, A. Kulkarni, and A. Vaidya, "Role of thermal spray processing method on the microstructure, residual stress and properties of coatings: an integrated study for Ni–5 wt.%Al bond coats," *Mater. Sci. Eng. A*, vol. 364, no. 1–2, pp. 216–231, Jan. 2004.
[52] A. Papyrin, V. Kosarev, S. Klinkov, A. Alkhimov, and V. M. Fomin, *Cold Spray Technology*, 1 edition. Amsterdam; London: Elsevier Science, 2006.
[53] T. Schmidt, F. Gaertner, and H. Kreye, "New developments in cold spray based on higher gas and particle temperatures," *J. Therm. Spray Technol.*, vol. 15, no. 4, pp. 488–494, Dec. 2006.
[54] R. W. Fox, P. J. Pritchard, and A. T. McDonald, *Introduction to Fluid Mechanics*, 7 edition. Hoboken, N.J: Wiley, 2008.
[55] Daniel A. MacDonald, "Restoration of Aluminum Aerospace Parts and Coatings using Cold Gas Dynamic Spraying," University of Ottawa, Ottawa, 2014.
[56] J. G. Legoux, E. Irissou, and C. Moreau, "Effect of Substrate Temperature on the Formation Mechanism of Cold-Sprayed Aluminum, Zinc and Tin Coatings," *J. Therm. Spray Technol.*, vol. 16, no. 5–6, pp. 619–626, Dec. 2007.

[57] K. Taylor, B. Jodoin, and J. Karov, “Particle loading effect in cold spray,” *J. Therm. Spray Technol.*, vol. 15, no. 2, pp. 273–279, Jun. 2006.
[58] R. Morgan, P. Fox, J. Pattison, C. Sutcliffe, and W. O’Neill, “Analysis of cold gas dynamically sprayed aluminium deposits,” *Mater. Lett.*, vol. 58, no. 7–8, pp. 1317–1320, Mar. 2004.
[59] T. Hussain, D. G. McCartney, P. H. Shipway, and D. Zhang, “Bonding Mechanisms in Cold Spraying: The Contributions of Metallurgical and Mechanical Components,” *J. Therm. Spray Technol.*, vol. 18, no. 3, pp. 364–379, Sep. 2009.
[60] M. Grujicic, C. L. Zhao, W. S. DeRosset, and D. Helfritch, “Adiabatic shear instability based mechanism for particles/substrate bonding in the cold-gas dynamic-spray process,” *Mater. Des.*, vol. 25, no. 8, pp. 681–688, Dec. 2004.
[61] T. Schmidt, H. Assadi, F. Gärtner, H. Richter, T. Stoltenhoff, H. Kreye, and T. Klassen, “From Particle Acceleration to Impact and Bonding in Cold Spraying,” *J. Therm. Spray Technol.*, vol. 18, no. 5–6, pp. 794–808, Dec. 2009.
[62] D. Giraud, *Étude des composantes mécanique et métallurgique dans la liaison revêtement-substrat obtenue par projection dynamique par gaz froid pour les systèmes «Aluminium/Polyamide6,6» et «Titane/TA6V»*. Paris, ENMP, 2014.
[63] P. C. King, C. Busch, T. Kittel-Sherri, M. Jahedi, and S. Gulizia, “Interface melding in cold spray titanium particle impact,” *Surf. Coat. Technol.*, vol. 239, pp. 191–199, Jan. 2014.
[64] S. V. Klinkov, V. F. Kosarev, and M. Rein, “Cold spray deposition: Significance of particle impact phenomena,” *Aerosp. Sci. Technol.*, vol. 9, no. 7, pp. 582–591, Oct. 2005.
[65] J. R. S. M. Grujicic, “Computational analysis of the interfacial bonding between feed-powder particles and the substrate in the cold-gas dynamic-spray process,” *Appl. Surf. Sci.*, pp. 211–227, 2003.
[66] P. Richer, B. Jodoin, and L. Ajdelsztajn, “Substrate roughness and thickness effects on cold spray nanocrystalline Al−Mg coatings,” *J. Therm. Spray Technol.*, vol. 15, no. 2, pp. 246–254, Jun. 2006.
[67] Tyler Samson, Daniel MacDonald, Ruben Fernández, and Bertrand Jodoin, “Effect of Pulsed Waterjet Surface Preparation on the Adhesion Strength of Cold Gas Dynamic Sprayed Aluminium Coatings,” *J. Therm. Spray Technol.*, In Press.
[68] A. Moridi, S. M. H. Gangaraj, S. Vezzu, and M. Guagliano, “Number of Passes and Thickness Effect on Mechanical Characteristics of Cold Spray Coating,” *Procedia Eng.*, vol. 74, pp. 449–459, 2014.
[69] T. W. Clyne and S. C. Gill, “Residual Stresses in Thermal Spray Coatings and Their Effect on Interfacial Adhesion: A Review of Recent Work,” *J. Therm. Spray Technol.*, vol. 5, no. 4, pp. 401–418, Dec. 1996.
[70] T. H. Van Steenkiste, J. R. Smith, and R. E. Teets, “Aluminum coatings via kinetic spray with relatively large powder particles,” *Surf. Coat. Technol.*, vol. 154, no. 2–3, pp. 237–252, May 2002.
[71] T. Schmidt, F. Gärtner, H. Assadi, and H. Kreye, “Development of a generalized parameter window for cold spray deposition,” *Acta Mater.*, vol. 54, no. 3, pp. 729–742, Feb. 2006.
[72] J. Wu, H. Fang, S. Yoon, C. Lee, and H. Kim, “Critical Velocities for High Speed Particle Deposition in Kinetic Spraying,” *Mater. Trans.*, vol. 47, no. 7, pp. 1723–1727, 2006.
[73] C.-J. Li, W.-Y. Li, and H. Liao, “Examination of the critical velocity for deposition of particles in cold spraying,” *J. Therm. Spray Technol.*, vol. 15, no. 2, pp. 212–222, Jun. 2006.
[74] F. Raletz, M. Vardelle, and G. Ezo’o, “Critical particle velocity under cold spray conditions,” *Surf. Coat. Technol.*, vol. 201, no. 5, pp. 1942–1947, Oct. 2006.

[75] C.-J. Li, W.-Y. Li, Y.-Y. Wang, G.-J. Yang, and H. Fukanuma, “A theoretical model for prediction of deposition efficiency in cold spraying,” *Thin Solid Films*, vol. 489, no. 1–2, pp. 79–85, Oct. 2005.
[76] S. V. Klinkov and V. F. Kosarev, “Measurements of cold spray deposition efficiency,” *J. Therm. Spray Technol.*, vol. 15, no. 3, pp. 364–371, Sep. 2006.
[77] D. L. Gilmore, R. C. Dykhuizen, R. A. Neiser, M. F. Smith, and T. J. Roemer, “Particle velocity and deposition efficiency in the cold spray process,” *J. Therm. Spray Technol.*, vol. 8, no. 4, pp. 576–582, Dec. 1999.
[78] Stephanie Fraley, Mike Oom, Ben Terrien, and John Zalewski, “Design of experiments via taguchi methods: orthogonal arrays,” 27-Nov-2007. [Online]. Available: https://controls.engin.umich.edu/wiki/index.php/Design_of_experiments_via_taguchi_methods:_orthogonal_arrays. [Accessed: 07-Apr-2015].
[79] J. L. Rosa, A. Robin, M. B. Silva, C. A. Baldan, and M. P. Peres, “Electrodeposition of copper on titanium wires: Taguchi experimental design approach,” *J. Mater. Process. Technol.*, vol. 209, no. 3, pp. 1181–1188, Feb. 2009.
[80] G01 Committee, “Practice for Operating Salt Spray (Fog) Apparatus,” ASTM International, 2011.
[81] K. H. Ko, J. O. Choi, H. Lee, and B. J. Lee, “Influence of oxide chemistry of feedstock on cold sprayed Cu coatings,” *Powder Technol.*, vol. 218, pp. 119–123, Mar. 2012.
[82] L. H. Strait and R. D. Jamison, “Application of PEEK Coatings to C/PEEK Substrates by Plasma-Spray Process,” *J. Compos. Mater.*, vol. 28, no. 3, pp. 211–233, Feb. 1994.
[83] M. Lauzon, “Diversified Plastics Inc., PEEK playing role in space probe,” *Plastics News*, 04-May-2012. [Online]. Available: http://www.plasticsnews.com/article/20120504/NEWS/305049956/diversified-plastics-inc-peek-playing-role-in-space-probe. [Accessed: 03-Mar-2015].
[84] E28 Committee, “Test Method for Vickers Hardness of Metallic Materials,” ASTM International, 2003.
[85] E. P. DeGarmo, J. T. Black, and R. A. Kohser, *Materials and Processes in Manufacturing*, 9th Edition Update edition. Hoboken, N.J: Wiley, 2003.
[86] D01 Committee, “Test Method for Pull-Off Strength of Coatings Using Portable Adhesion Testers,” ASTM International, 2009.
[87] E04 Committee, “Practice for Microetching Metals and Alloys,” ASTM International, 2007.

Appendix I: Dr. Mohammed Yandouzi's Work on Bond Coat Development

Earlier work regarding a copper/polymer bond coat has been done by a fellow colleague, Dr. Mohammed Yandouzi. Although never published, Dr. Yandouzi's work was used as a guide to set initial parameters of this research. The following is a short summary of his results.

Experiments were conducted with different classes and compositions of composite (copper/polymer) powders. These tests focused on spraying different metal and polymer composites on the BMS 8-276 composite plates using the LPCS process (SST-P system). Four types of polymer materials (two thermosets and two thermoplastics) were selected. The polymer powders were mixed with different composition to Copper (SST-C5003 from Centerline) and Aluminum (SST-A5001 from Centerline) powders. A summary of the composite powders is presented in Table 39.

Table 39 Feedstock Powder Composition (metalwt% - polymerwt%) (Green indicates successful deposition and red indicates no deposition)

		Thermoset		Thermoplastic	
		Polyfast (Struers)	Techno.3000 (Anamet)	Condufast (Struers)	PEEK (Victrex)
Metal	Copper (SST-C5003) (Centerline)	50 - 50 80 - 20 90 - 10 95 - 05	50 - 50 80 - 20 90 - 10 95 - 05 97.5 - 2.5	50 - 50 80 - 20	90 - 10 95 - 05 97.5 - 2.5
	Aluminum (SST-A5001) (Centerline)	50 - 50 80 - 20 90 - 10	50 - 50 80 - 20 80 - 20 90 - 10 95 - 05	50 - 50 80 - 20	90 - 10 95 - 05 97.5 - 2.5

For each starting powder, a series of spray trials were conducted and the best conditions were determined for each powder composition. Three of the four polymer powders were successfully utilized to coat the substrate (Polyfast, Techno 3000, and PEEK). The Condufast polymer resulted in no coating build-up and severe substrate erosion was observed.

Appendix II: Attempts to Expose a Single LCFP

A series of experiments were elaborated with the specific goal to eliminate the toughening heterogeneous system, located between the LCFPs of the BMS 8-276, from appearing at the surface of the substrate. The exposure of the toughening heterogeneous system of the BMS 8-276 results in discontinuities in the deposited coatings. The experiments can be separated into two types: chemical and mechanical.

Chemical Surface Preparation

Heat

In order to see the effect of heat on the toughening heterogeneous system, the BMS 8-276 substrate was sprayed with air at 500°C (see Table 40 for full spray details).

Table 40: Parameters Used for the Heat Test on the BMS8-276 Substrate

CGDS Parameter	Value
Gas Pressure	70 psi (0.48 MPa)
Gas Temperature	500°C
Gas Nature	Air
Traverse Velocity	1 mm/s
Standoff Distance	10 mm
Nozzle Type	120 mm SS Nozzle
Orifice Diameter	2 mm
Step Size	1 mm

When spraying at high temperatures, it was apparent that the toughening heterogeneous system turned brown. Cross-sectional revealed that the toughening heterogeneous system does react to the heat. As depicted in Figure 191, voids are formed in the toughening heterogeneous system.

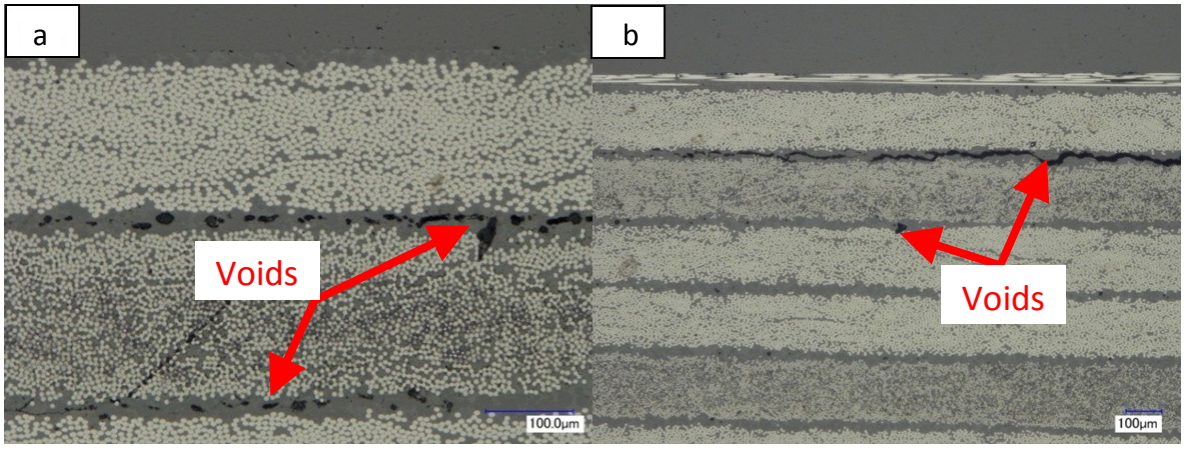

Figure 191: (a) 500X and (b) 200X cross-sections of the heat tested BMS8-276 depicting voids formed by the high temperatures.

Interestingly, these voids do not appear in the toughening heterogeneous system if the latter is exposed on the surface of the BMS8-276. The voids are thought to be caused by off gassing of the toughening heterogeneous system during heating. This change in the substrate cannot be present in the final coating. Therefore, these high temperatures must be avoided.

Acids

Another chemical experiment, elaborated with the specific goal to attack the toughening heterogeneous system located between the LCFPs of the BMS 8-276 was etching. Since the toughening heterogeneous system is composed of an unknown material, a random set of acids were selected. Small BMS 8-276 substrate samples were prepared exposing multiple LCFPs. These samples were left face down in small pools of acid for 24 hours (see Figure 192).

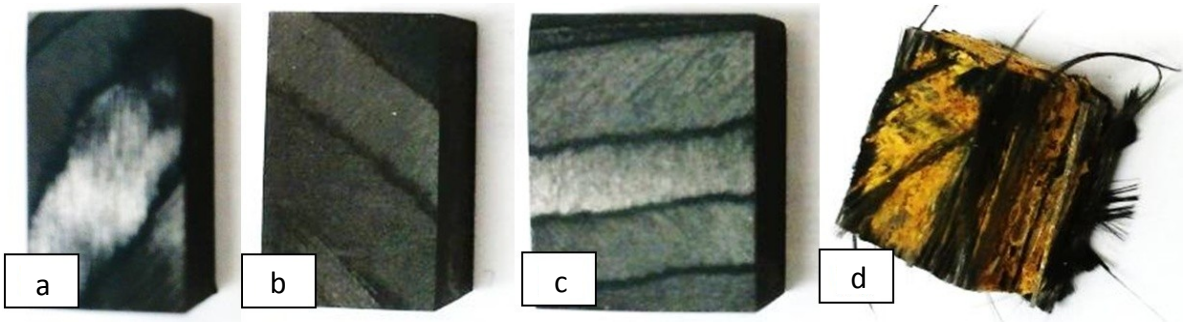

Figure 192: Twenty-four hour acid test using (a) hydrochloric acid (HCl), (b) methylene chloride (CH_2Cl_2), (c) hydrofluoric acid (HF), and (d) nitric acid (HNO_3).

Further analysis revealed that only the nitric acid had an effect on the composite. As seen in Figure 193, the nitric acid dissolved not only the toughening heterogeneous system but the epoxy as well. This left the carbon fibres of the BMS 8-276 free to move about. Because the integrity of the epoxy is compromised, this method cannot be used to remove the toughening heterogeneous system of the substrate.

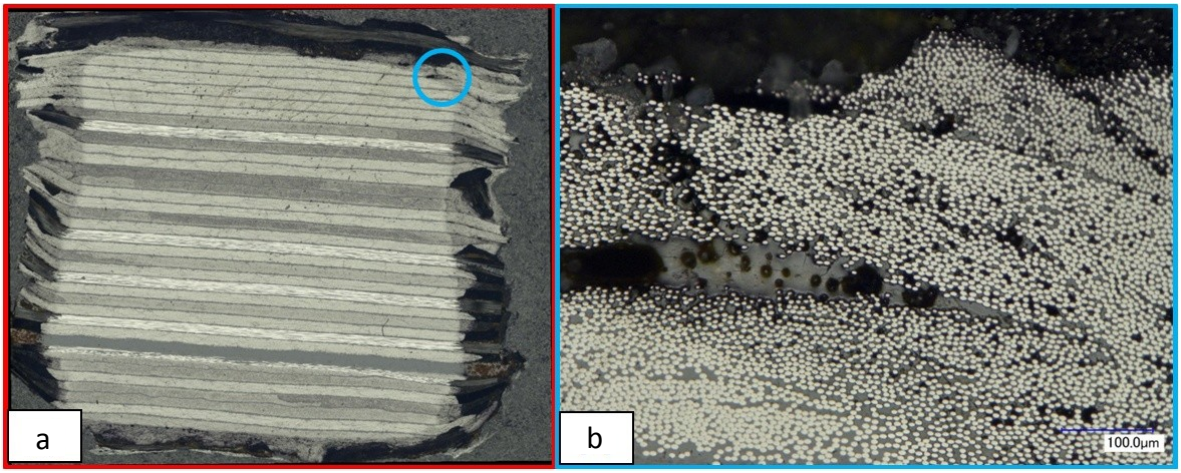

Figure 193: (a) A section view of the nitric acid tested BMS8-276 substrate and (b) a 500X zoom of the upper right corner.

Solvents

A variety of solvents were also used in an attempt to remove the toughening heterogeneous system from the substrate. Again, small BMS 8-276 samples were prepared and placed in a small pools of solvent for twenty-four hours (see **Error! Reference source not found.**). All three were unsuccessful in achieving the goal.

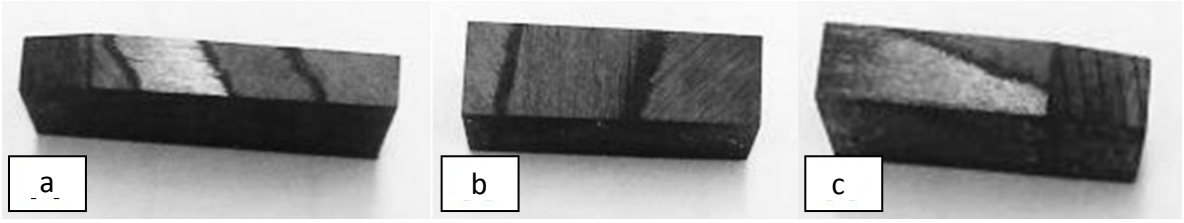

Figure 194:Twenty-four hour solvent test using (a) isopropyl alcohol (C_3H_7OH), (b) ethyl acetate ($CH_3COOCH_2CH_3$), and (c) ethanol (CH_3CH_2OH).

Mechnical Surface Preparation

Grit Blasting

An attempt to target the toughening heterogeneous system of the BMS 8-276 was made by modifying the pressure of the grit blasting procedure. Pressures of 10, 20, 40, and 60 psi (0.07, 0.14, 0.28, 0.41 MPa) were used to grit blast the surface of a BMS 8-276 substrate that exhibited a transition between two LCFPs. The distance from the nozzle to the substrate was kept at approximately 2.5 cm at an angle of 45°. A mixture of 80 and 20 grit was used. Table 41 provides magnified images of the surface of the various samples before and after the grit blasting step.

Table 41: Before and After Images of BMS8-276 Substrate Surface Grit Blasting Process at Different Pressures

Pressure	*Before Grit Blasting*	*After Grit Blasting*
10 psi (0.07 MPa)	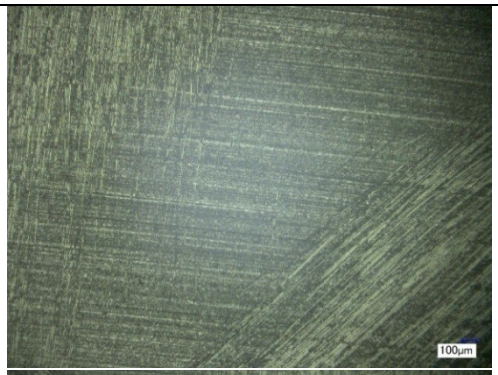	
20 psi (0.14 MPa)		
40 psi (0.28 MPa)	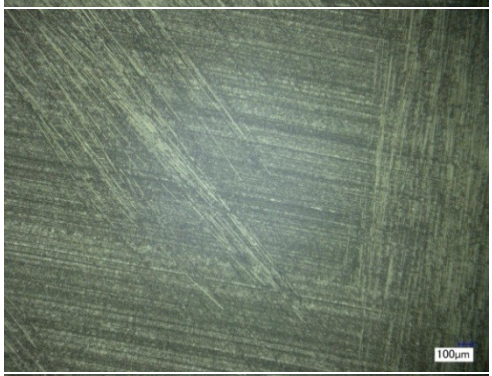	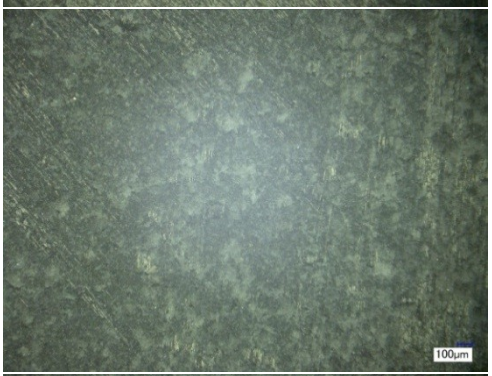
60 psi (0.41 MPa)		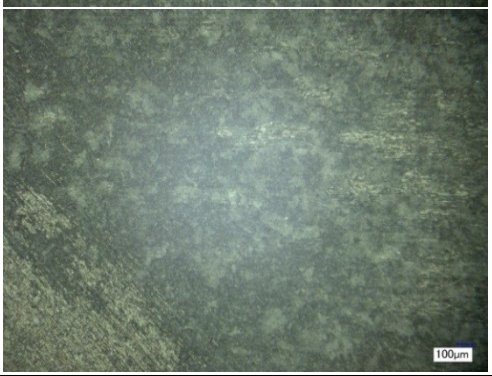

It is to be noted that in Table 41, the toughening heterogeneous system is striated before the grit blasting process because the BMS 8-276 substrate preparation method (grinding). Grit blasting at

low pressures (10 psi and 20 psi) (0.07 MPa and 0.14 MPa) does not seem to change anything other than the appearance of the toughening heterogeneous system. Increasing the pressure up to 40 psi (0.26 MPa) and 60 psi (0.41 MPa) seems to attack the carbon fibres of the LCFPs more so than the toughening heterogeneous system. The brittle nature of the carbon fibres makes them poor candidates to withstand the impact loading of the high speed grit whereas the toughening heterogeneous system is conceived to withstand impacts.

Hot Grit Blasting

In order to weaken the toughening heterogeneous system, heat was introduced to the grit blasting process. The BMS8-276 substrate was grit blasted using the SST-P system with 80 grit sized aluminium oxide. The temperature was varied from 100°C to 500°C at 100°C intervals. All other parameters were kept constant and are specified in Table 42.

Table 42: Constant Parameters Used for the Hot Grit Blasting Process on the BMS8-276 Substrate

CGDS Parameter	Value
Gas Pressure	60 psi (0.41 MPa)
Gas Nature	Air
Traverse Velocity	10 mm/s
Standoff Distance	15 mm
Nozzle Type	120 mm SS Nozzle
Orifice Diameter	2 mm
Powder Feeder Wheel	120 Large Hole
Powder Feeder Gas Rate	30 scfh (0.85 m^3/h)
Powder Feed Rate	1 rpm (0.1 rad/s)
Step Size	1 mm

Two sets of tests were made. The first set consisted of passing over the substrate only once (see Figure 195) whereas for the second set the gun passed over the same area for a total of 5 times (see Figure 196).

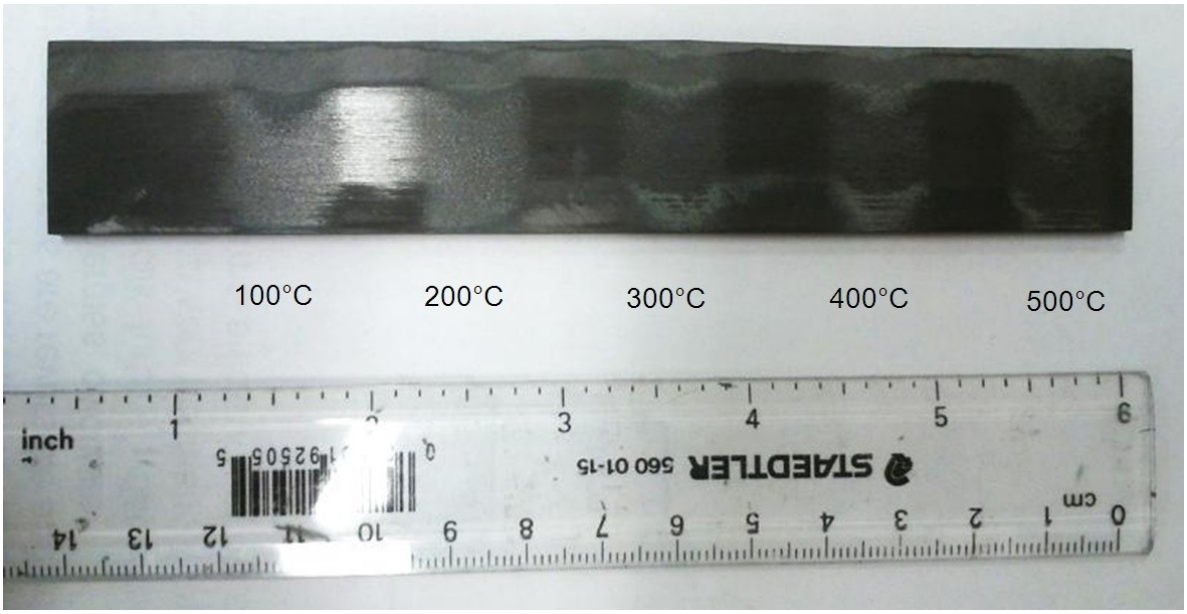

Figure 195: Hot grit blasting test at 100°C, 200°C, 300°C, 400°C and 500°C, passing only once above the same area at the parameters specified in Table 42. There is an increase in the exposure of the toughening heterogeneous system (in white) regardless of the temperature.

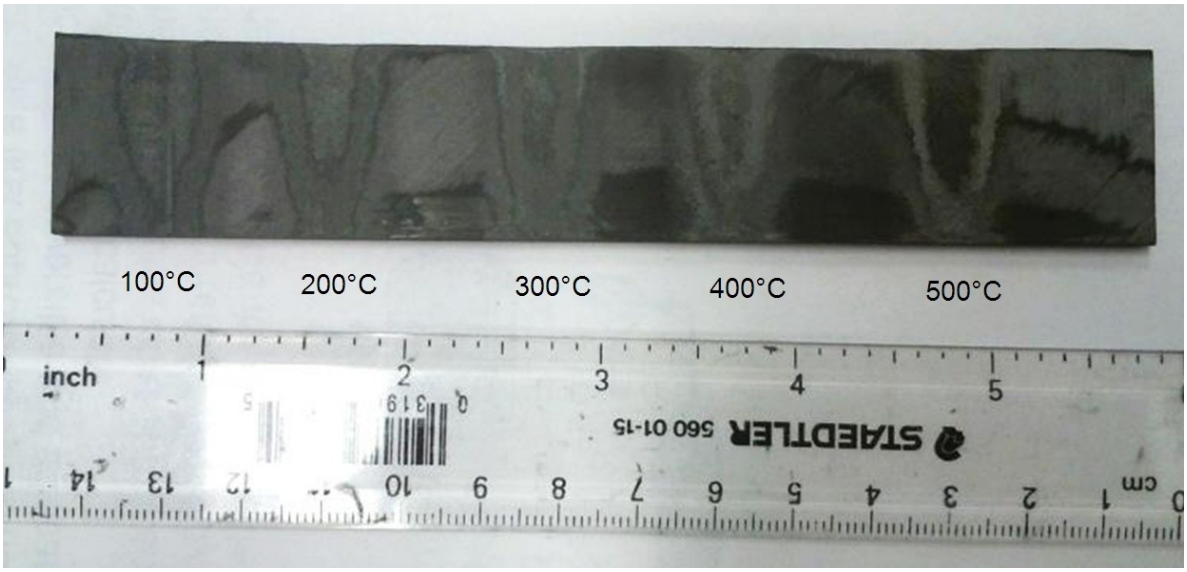

Figure 196: Hot grit blasting test at 100°C, 200°C, 300°C, 400°C and 500°C, passing 5 times above the same area at the parameters specified in Table 42. Severe wear is apparent and the blasting process seems to target and erode the LCFP more efficiently than the toughening heterogeneous system.

Upon observation of the area that was hot grit blasted in Figure 195, it is visible that the toughening heterogeneous system increases in the ratio of superficial area exposed in comparison to the LCFP regardless of the temperature. From this, we can conclude that that the hot grit blasting process

erodes the LCFP more efficiently than the toughening heterogeneous system. Further treatment will simply increase the erosion and reach deeper plies as manifested in Figure 196.

Milling

Knowing that the BMS 8-276 substrate has relatively planar layers, milling it to a single LCFP was attempted. For the most part, this method was ineffective. Properly aligning the layers with the mill was a difficult challenge. When tightened in the vise, the BMS 8-276 substrates bent considerably causing its layers to lose planarity. Furthermore, the substrate substantially heated up during prolonged milling causing its layers to peel. In the optimal circumstance, the substrate was milled to expose two LCFP (see Figure 197). Ultimately, the outcome of this technique is very specific to the substrate at hand and yields a very low percentage of useful substrates with a small area of interest.

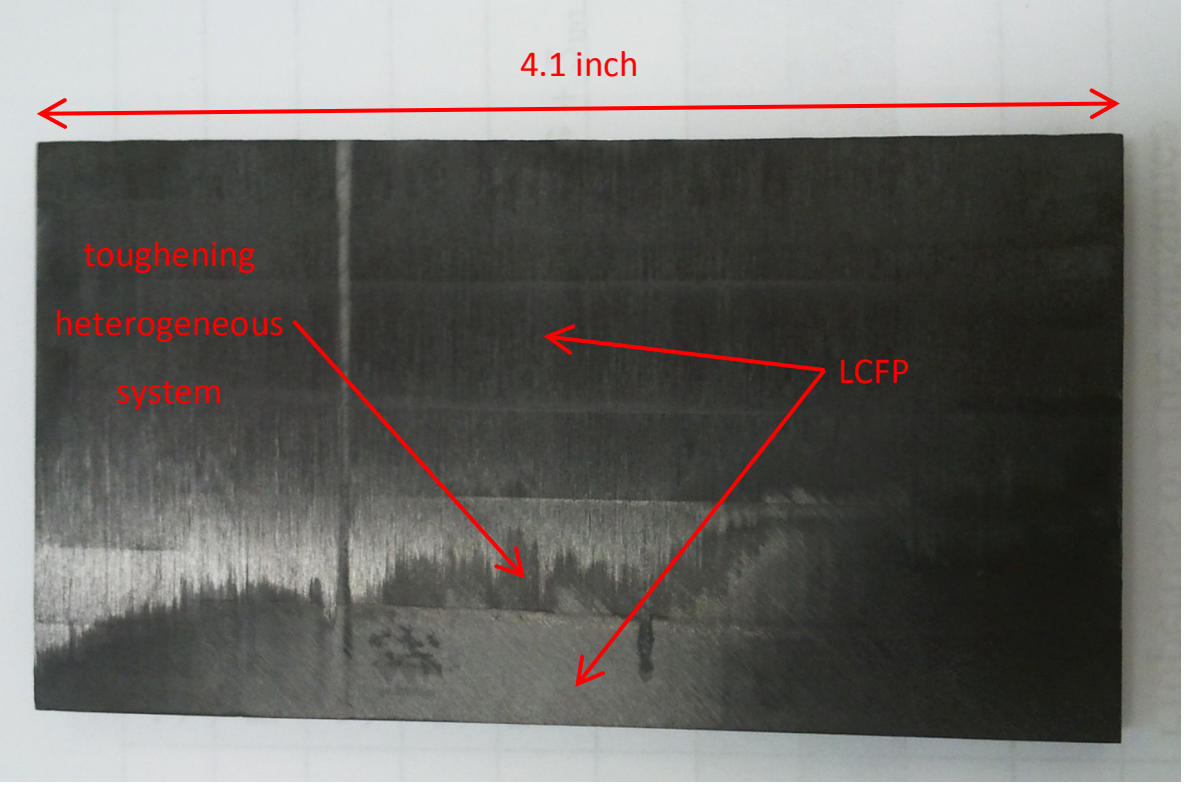

Figure 197: Milled BMS 8-276 substrate with two LCFP exposed.

Grinding

Much like milling, grinding the BMS 8-276 substrate to single LCFP is a possibility given that the substrate itself has planar layers. Unlike milling, grinding does not require the use of a vise, eliminating the issue of the substrate bending. In addition grinding has little heat production due to the use of a cooling fluid and thus peeling of the layers is also reduced. Using this method, a single LCFP can be exposed on the surface of the majority of the BMS 8-276 substrates at hand (see Figure 198). As such, this substrate preparation method has been determined to be the preferred one (see section 4.4.1).

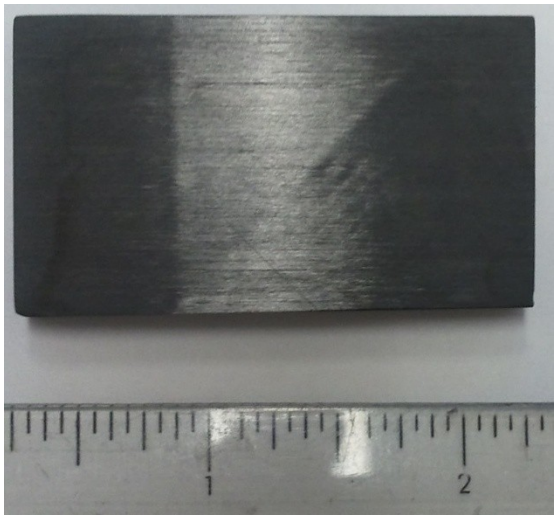

Figure 198: Grinded BMS 8-276 substrate with a single LCFP exposed.

Appendix III: Effect of Surface Finish on Resistivity Measurements

A quick experiment was conducted to test the sensitivity of the four point probe resistivity sensor to the surface finish of the coating. A tin coated BMS 8-276 sample roughly measuring 1" by 2", was used for this experiment. Resistivity measurements were done on the as-sprayed surface finish and where then re-measured after the coating underwent a polishing process (see Figure 199).

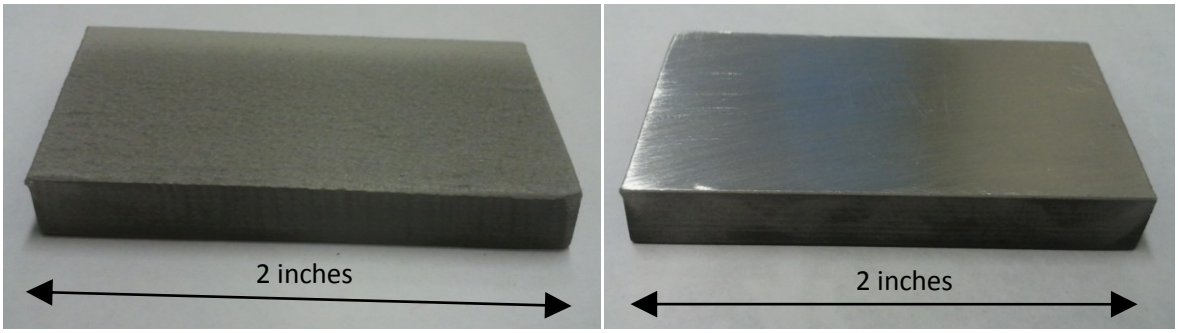

Figure 199: Tin coated BMS 8-276 as-sprayed (left) and polished (right).

Five measurements were taken using the four point probe resistivity sensor for each surface finish (see Table 43).

Table 43: Sheet Resistance of As-Sprayed and Polished Surface Finish

Surface Finish	Sheet Resistance (Ohm)
As-Sprayed	0.00008 ± 0.00003
Polished	0.00015 ± 0.00010

It was anticipated that the smooth finish would have improved the contact and lowered the resistance. However, the results presented in Table 43 indicate that the surface finish has no major effect on the sheet resistance measurements of the four point probe resistivity sensor. One could argue that the change in thickness induced by the polishing process has a larger effect than the surface finish given the slightly higher resistance measurements. Regardless, these results indicate that the surface finish remains insignificant when measurements are made using the four point probe resistivity sensor.

Appendix IV: Attempts to Increase Adhesion of Tin Coating to BMS 8-276

An attempt to increase the adhesion of the tin coating was done using glass beading. Glass beading is often used to introduce compressive stresses on coatings. This technique can delay crack propagation and increase the adhesion of coatings that are subjected to tensile residual stresses. Although CGDS coatings are mainly known to have compressive residual stresses, this test was done to assure the compressive nature of the tin coatings and to eliminate possible tensile stresses.

Tin coatings were produced at two different thicknesses on LCFP BMS 8-276 substrates of roughly 1.5" X 2" (5.1 cm X 3.8 cm). The TV was changed from one sample to the next in order to produce the two thicknesses (see Table 44).

Table 44: Traverse Velocity of Samples T40 and T42

Sample	*Traverse Velocity (mm/s)*
T40	50
T42	100

All other spray parameters remained constant for these coatings and are specified in Table 45.

Table 45: Constant Spray Parameters Used to Produce Tin Coatings on LCFP BMS 8-276 Substrates

CGDS Parameter	Value
Gas Pressure	90 psi (0.62 MPa)
Gas Temperature	300°C
Gas Nature	Nitrogen
Standoff Distance	10 mm
Nozzle Type	120 mm SS Nozzle
Orifice Diameter	2 mm
Powder Feeder Wheel	320 Small Hole
Powder Feeder Gas Rate	30 scfh (0.85 m^3/h)
Powder Feed Rate	3 rpm (0.31 rad/s)
Step Size	1 mm

Some of the coatings produced were left "As Sprayed" whereas others were glass beaded at pressures of 30 psi (0.21 MPa) and 60 psi (0.41 MPa) (see Figure 200). The glass beading was done using compressed air at an angle of 45°. The No. 10 type spherically shaped glass beads were 100-170 mesh in size.

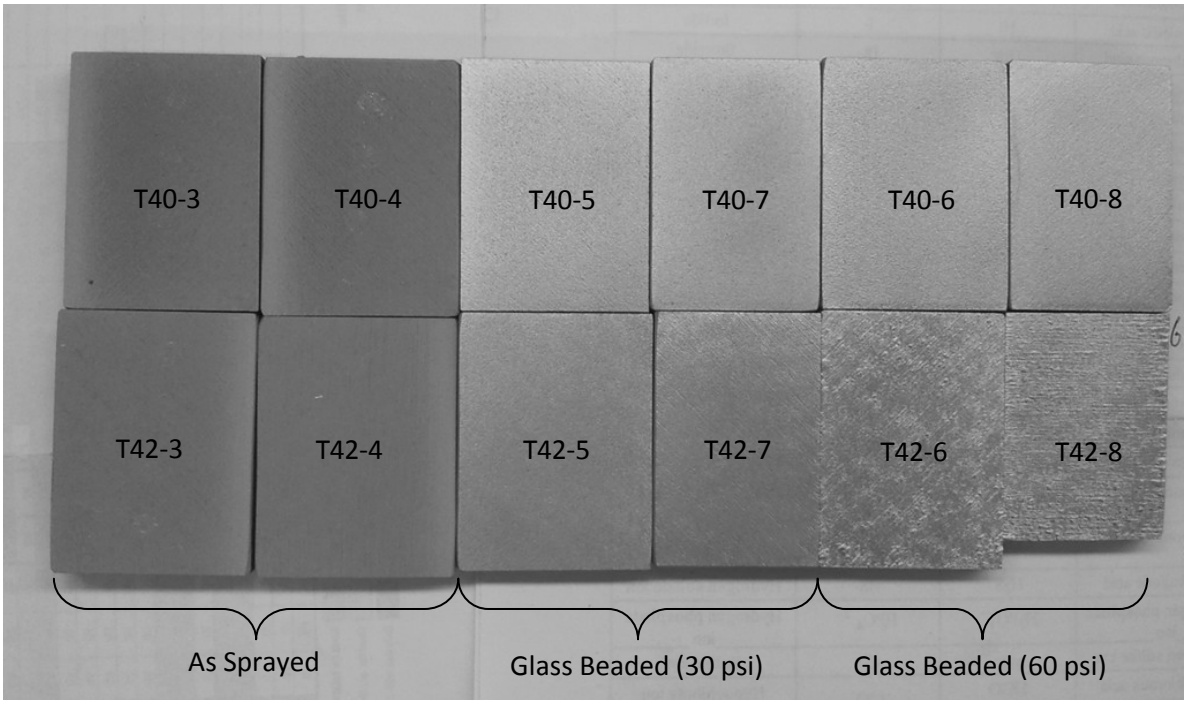

Figure 200: Glass beaded tin coatings (T40 & T42) on BMS 8-276 substrates.

PATTI Adhesion tests were performed and are presented in Figure 201.

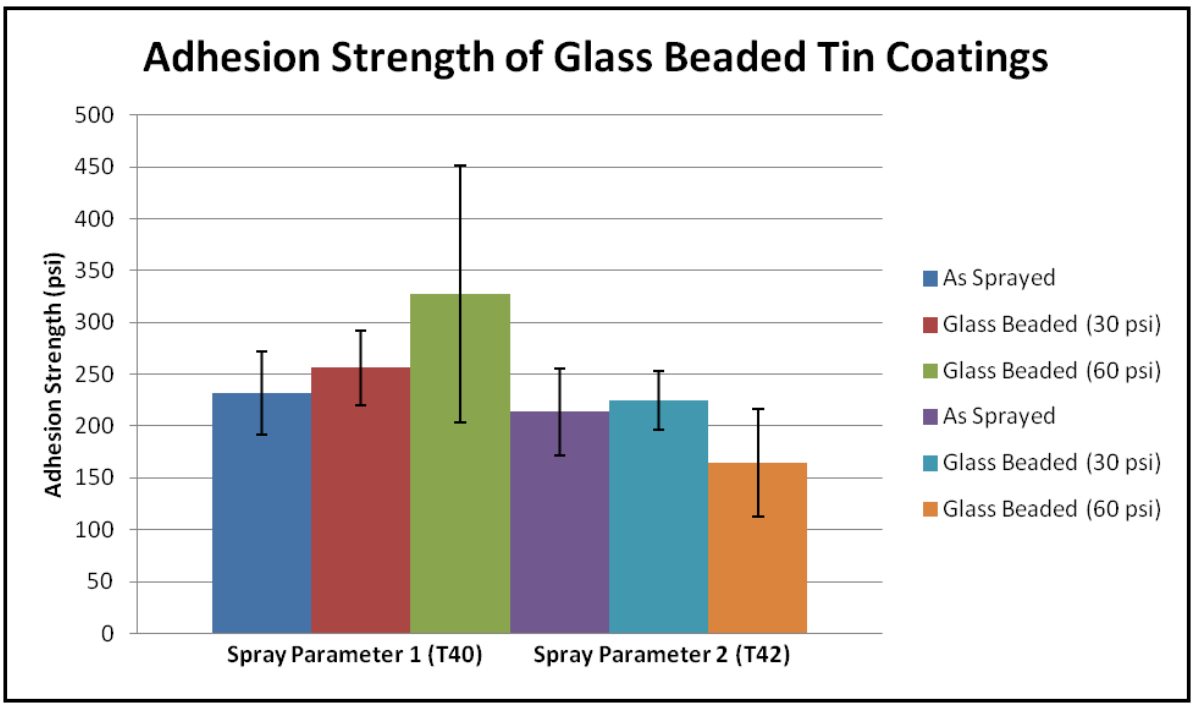

Figure 201: Adhesion of glass beaded tin coatings deposited at two different spray parameters. Note that the high adhesion of the T40 spray parameters that were glass beaded at 60 psi (green) emanates from a single high adhesion value of 513 psi while the rest of the adhesion were recorded near 265 psi.

Figure 201, shows that glass beading has inconsistent effects on the adhesion of the tin coatings to the BMS 8-276 substrates. For T40, glass beading seems to slightly increase the adhesion strength whereas a slight rise and subsequent drop can be seen of sample T42. It is important to note that one adhesion measurement of the tin coating T40-6 reached 513 psi after being glass beaded at 60 psi. This single high value greatly influenced the results. The drop in adhesion of the 60 psi (0.41 MPa) glass beaded T42 samples can be attributed to the severe deformation of the thin coating. The higher velocity glass beads had enough energy to create deformations which penetrated the coating in its entire thickness (see Figure 202). Because the T42 coatings were thin, large strains left the coating stripped of its mechanical properties causing delamination from the substrate.

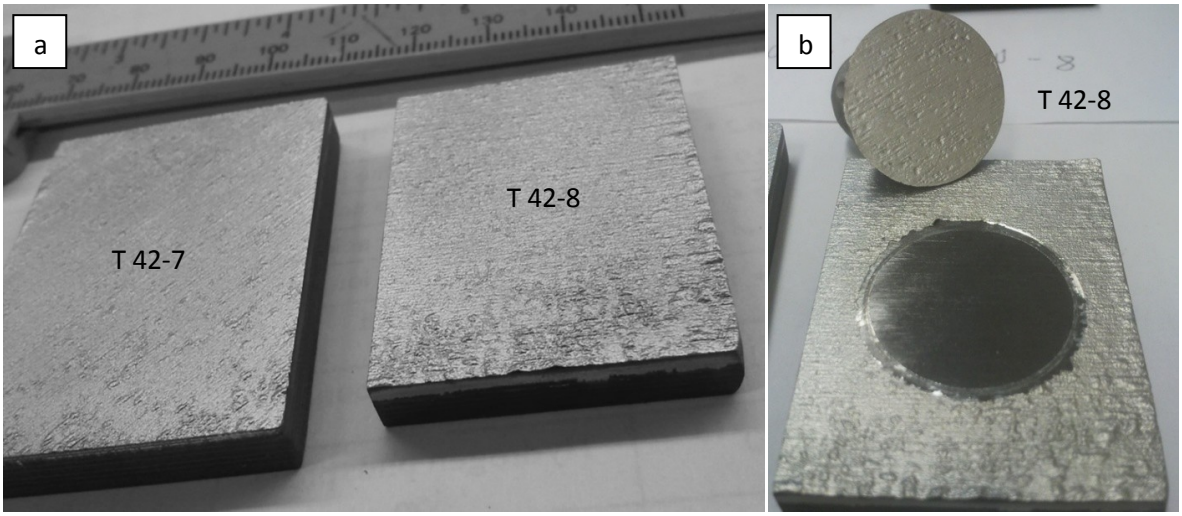

Figure 202: Tin coating deformation on top (a) and at the interface (b) of the BMS 8-276 substrate.

It can be concluded that the glass beading process could be helpful to increase the adhesion of thick tin coatings. It is believed that increasing the thickness of the coating moves the neutral axis towards the interface which lowers the adhesion strength. By increasing the compressive residual stresses through glass beading, may be increased. However coatings produced by CGDS are typically not under tensile residual stresses. Glass beading thin coatings seems to reduce the adhesion strength by damaging the coating.

Appendix V: Bond Coat Theoretical Volume Composition Calculation

The theoretical volume composition of the composite bond coat is estimated as follows. To begin, it is assumed that the copper and PEEK, once deposited, are fully dense regardless of the manufactured conditions. Hence the density of the bulk materials is used in these calculations. The following equations were developed and used to calculate the volume percentage of the copper and the PEEK constituents of the bond coat.

$$Vol\%_{Copper} = \frac{\frac{wt\%_{Copper}}{\rho_{Copper}}}{\frac{wt\%_{Copper}}{\rho_{Copper}} + \frac{wt\%_{PEEK}}{\rho_{PEEK}}}$$

$$Vol\%_{PEEK} = \frac{\frac{wt\%_{PEEK}}{\rho_{PEEK}}}{\frac{wt\%_{Copper}}{\rho_{Copper}} + \frac{wt\%_{PEEK}}{\rho_{PEEK}}}$$

Using the densities provided in section 4.1 and the weight percentages set in section 5.2.2, the corresponding volume percentage of the composite powder can be calculated.

$$Vol\%_{Copper} = \frac{\frac{97{,}5\%}{8.94\ g/cm^3}}{\frac{97.5\%}{8.94\ g/cm^3} + \frac{2.5\%}{1.3\ g/cm^3}} = 85.01\%$$

$$Vol\%_{PEEK} = \frac{\frac{2.5\%}{1.3\ g/cm^3}}{\frac{97.5\%}{8.94\ g/cm^3} + \frac{2.5\%}{1.3\ g/cm^3}} = 14.99\%$$

The calculations estimate the volumetric percentage of copper to be 85% in a mixture of 97.5wt% copper and 2.5wt% PEEK without porosity. The remaining 15% of the volume should be composed of PEEK.

Appendix VI: Attempts to Increase Adhesion of Composite Bond Coat to BMS 8-276

A variety of tests were conducted in an attempt to increase the adhesion strength of the composite bond coat to the BMS 8-276. The following section enumerates these experiments and provides procedural details along with overall conclusions.

Thickness

Efforts were made to increase the adhesion strength by minimizing the thickness of the bond coat. Literature indicates that increasing the thickness of a coating tends to decrease its adhesion strength. The thickness was modified by changing the TV. Three sets of samples were sprayed at TVs of 15 mm/s, 20 mm/s, 25 mm/s, and 30 mm/s. Each set contained a slightly different 0-45 µm PEEK content in the feedstock powder mixture (1.5wt%, 2.0wt%, and 2.5wt%). All other spray parameters were kept constant (see Table 46)

Table 46: Constant Spray Parameters Used to Produce Tin Coatings of Different Thicknesses on LCFP BMS 8-276 Substrates

CGDS Parameter	Value
Gas Pressure	110 psi (0.76 MPa)
Gas Temperature	350°C
Gas Nature	Nitrogen
Standoff Distance	10 mm
Nozzle Type	120 mm SS Nozzle
Orifice Diameter	2 mm
Powder Feeder Wheel	240 Medium Hole
Powder Feeder Gas Rate	30 scfh (0.85 m^3/h)
Powder Feed Rate	3 rpm (0.31 rad/s)
Step Size	2 mm

Figure 203 presents the thicknesses recorded for each bond coat. It can be concluded that increasing the TV will lower the thickness of the bond coat to a certain limit. All of the coatings sprayed with 1.5wt% PEEK + 98.5wt% SST-C5003 feedstock powder were either discontinuous or

did not deposit at all. Other coatings showed a rise of discontinuity when sprayed at increasingly higher TV.

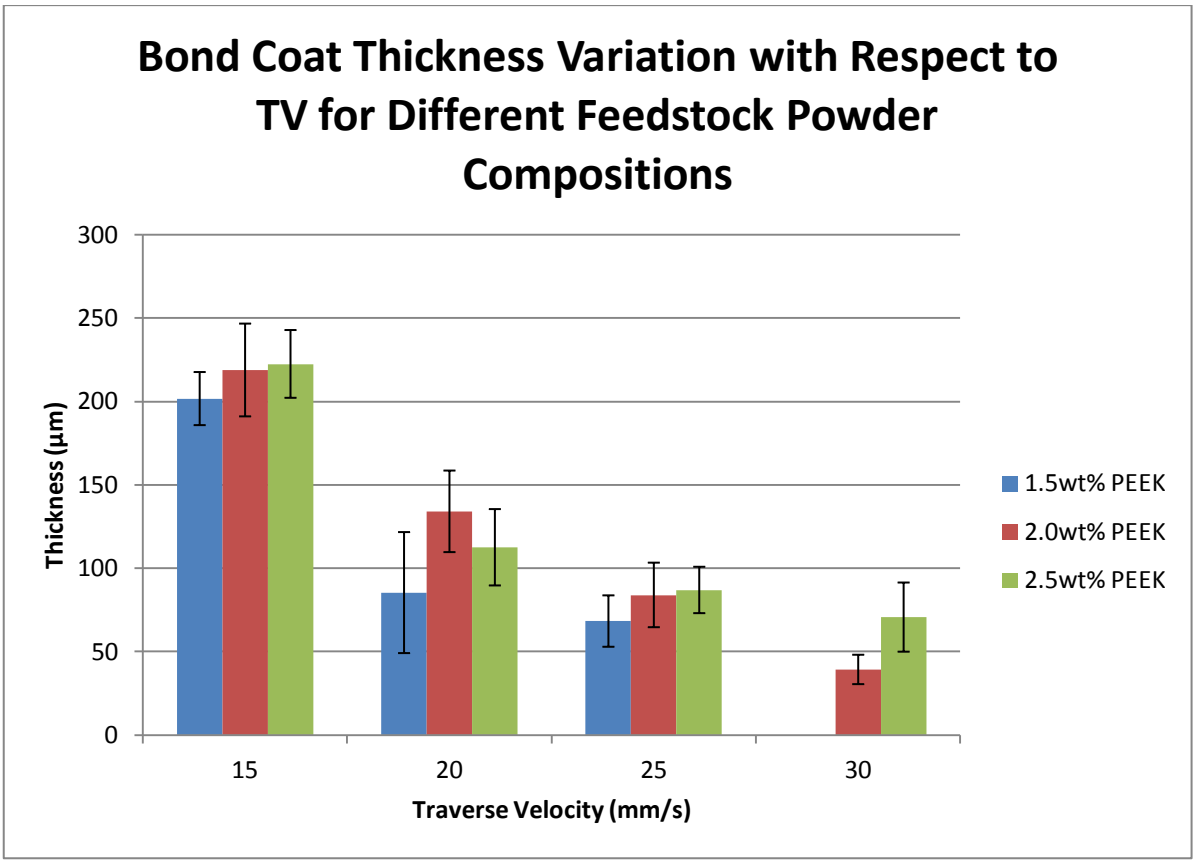

Figure 203: Bond coat thickness variation with respect to traverse velocity for different feedstock powder compositions (three sets). There is no column for the 1.5wt% PEEK + 98.5wt% SST-C5003 bond coat sprayed at 30 mm/s because no coating was deposited at this parameter. It is important to note that some of the thinner coatings were discontinuous in nature.

PATTI adhesion tests were performed on all the coatings. Again, the discontinuous nature of some of the coatings skewed certain results. This being said, only adhesion values of the bond coat composed from a 2.5wt% PEEK + 97.5wt% SST-C5003 were considered. From Figure 204, an argument could be made that increasing the TV increases the adhesion strength of the bond coat to the substrate to some extent.

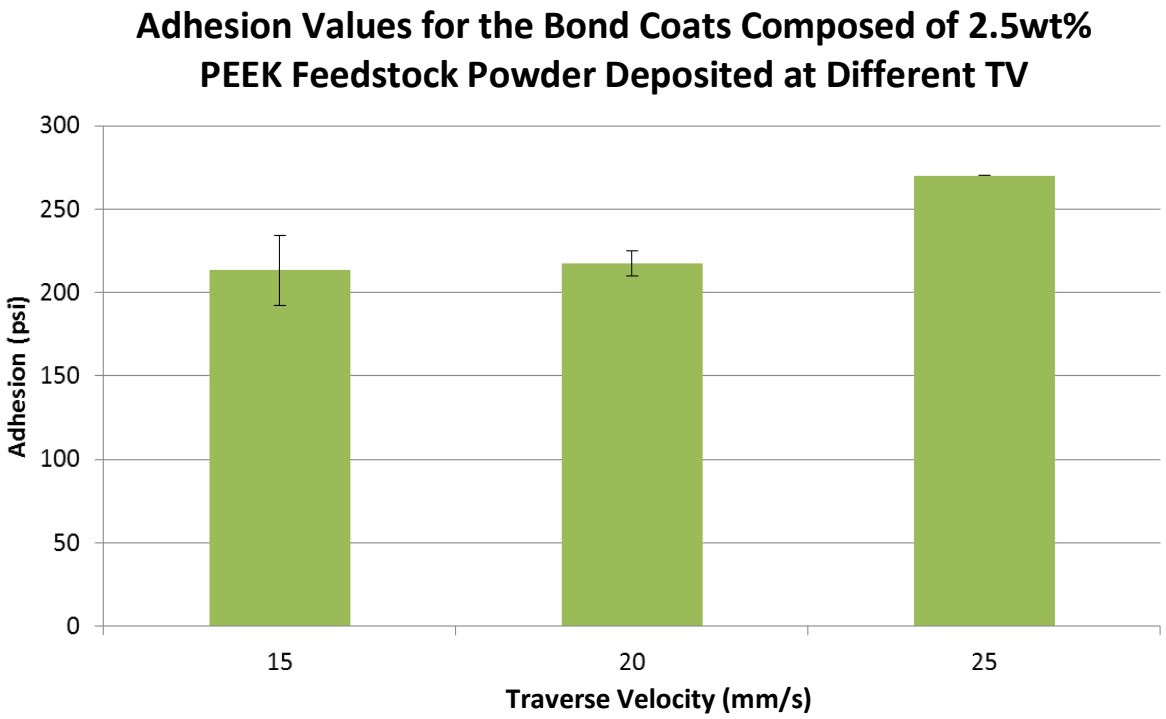

Figure 204: Adhesion values for the bond coats composed of 2.5wt% PEEK feedstock powder deposited at traverse velocities of 15 mm/s, 20 mm/s, and 25 mm/s. Note that there is no standard deviation for the bond coat deposited at 25 mm/s because only one value was successfully recorded.

Upon further analysis of the bond coats, a general trend was noticed in the composition. As depicted in Figure 205, increasing the TV tends towards an increase in the PEEK content of the deposited bond coat.

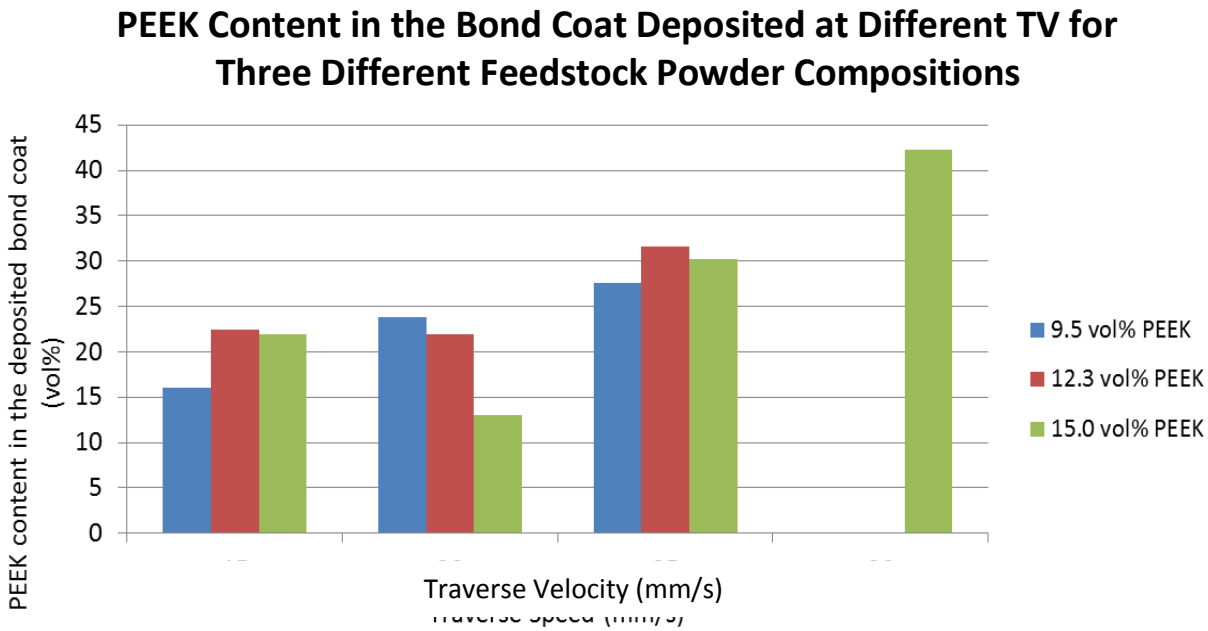

Figure 205: PEEK content in the bond coat deposited at traverse velocities of 15 mm/s, 20 mm/s, 25 mm/s, and 30 mm/s for feedstock powder compositions of 9.5vol% (1.5wt%), 12.3vol% (2.0wt%), and 15.0vol% (2.5wt%).

The theory that the bond coat starts with the initial deposition of a pure PEEK underlayer that adheres to the substrate and is built up with subsequent copper and peek deposition helps explain why such a trend is observed. Regardless of the velocity, a pure PEEK underlayer must be deposited before subsequent copper and PEEK can deposit. This indicates that a thin bond coat will have a greater proportion of PEEK than a thick bond coat. Thus, the TV (affecting the bond coat thickness) also has an effect on the composition of the bond coat. High increase in PEEK could also affect the adhesion of bond coat in a negative way. As mentioned earlier, although the thickness is lowered at high TV, the adhesion does not necessarily increase and an increase in PEEK content could be the reason why.

Heat Treatment

Further attempts to increase the adhesion strength of the bond coat to the substrate were made. A heat treatment process was developed and applied to sets of samples. Two different types of bond coats were deposited on BMS 8-276. The first consisted of 2.5wt% PEEK + 97.5wt% SST-C5003 sprayed at a TV of 20 mm/s and the second consisted of 2.0wt% PEEK + 98.0wt% SST-C5003 sprayed at a TV of 15 mm/s. All other spray parameters remained identical and are presented in Table 46. For each set, three samples were given a 2 hour heat treatment at 150°F (66°C) and three samples

were kept aside for comparison. The results presented in Figure 206 show that this heat treatment had no effect on the adhesion of the composite bond coat to the BMS 8-276 substrate.

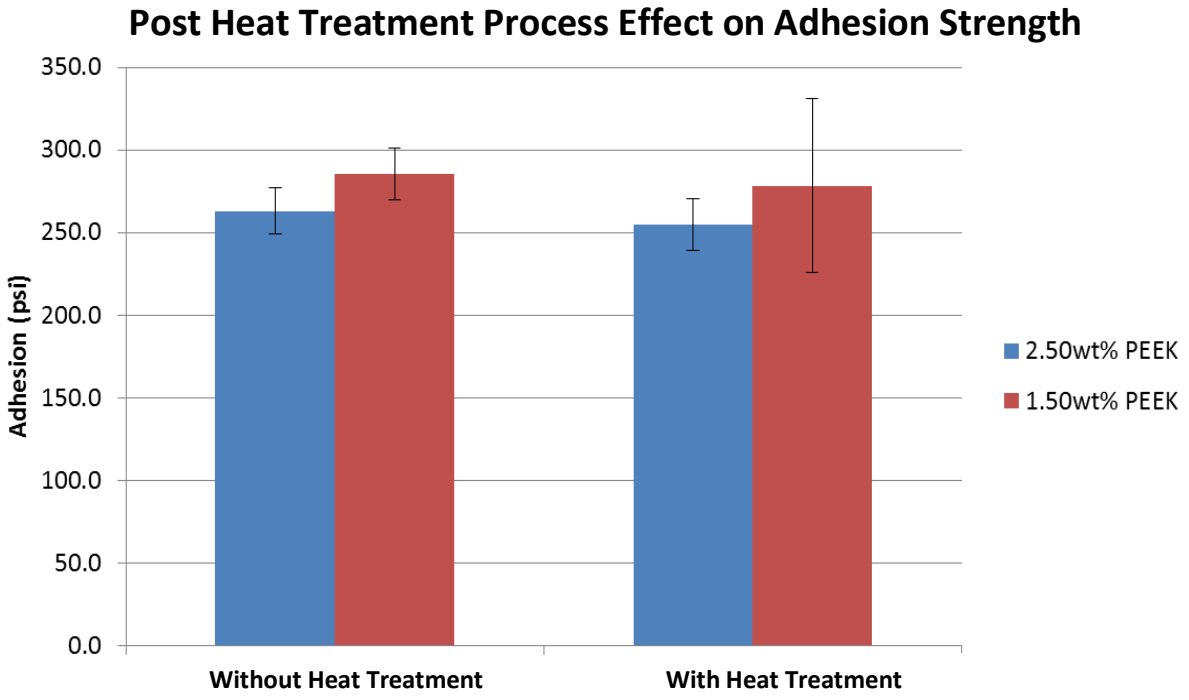

Figure 206: Effect of heat treatment process on the adhesion strength of the composite bond coat to the BMS 8-276.

Milled Composite Feedstock Powder

A mix of 97.5wt% SST-C5003 + 2.5wt% PEEK (0-45 µm) was milled using a planetary mill (see section 4.2.2). Figure 207 depicts the flatted shape of the copper powder and compares it to the non-milled powder mix.

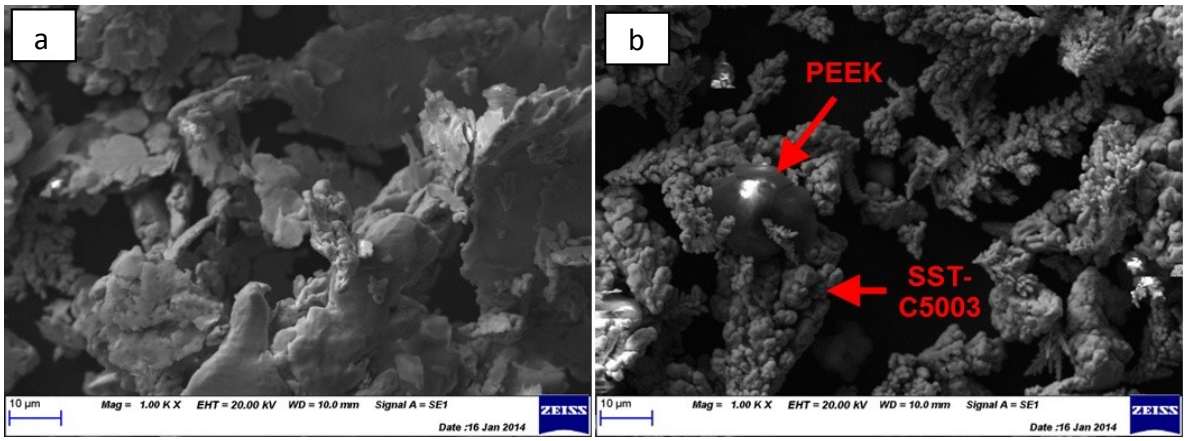

Figure 207: (a) SEM image of 97.5 wt% SST-C5003 + 2.5 wt% PEEK (0-45µm) powder milled for 16 minutes in a planetary mill and (b) not milled.

No PEEK particle could be identified with certainty in the milled powder (partially due to PEEK's low conductivity). A small quantity of this powder was produced and sprayed onto a LCFP BMS 8-276 sample using the parameters specified in Table 47.

Table 47: Spray Parameters Used for Milled Composite Powder on LCFP BMS 8-276 Substrate

CGDS Parameter	Value
Gas Pressure	110 psi (0.76 MPa)
Gas Temperature	350°C
Gas Nature	Nitrogen
Traverse Velocity	15 mm/s
Standoff Distance	10 mm
Nozzle Type	120 mm SS Nozzle
Orifice Diameter	2 mm
Powder Feeder Wheel	240 Medium Hole
Powder Feeder Gas Rate	30 scfh (0.85 m^3/h)
Powder Feed Rate	3 rpm (0.31 rad/s)
Step Size	2 mm
Surface Finish	Polished

As depicted in Figure 208a, the powder initially deposited and then progressively stopped. It is possible that an insufficient quantity of powder was produced causing feeding issues. This would

have decreased the DR which explains the progressive decline in deposition. However, it is believed that the milling process minimized the probability of the PEEK reaching the substrate causing a decrease in DE. By physically combining the two powders together, the statistical chance of the PEEK powder reaching the BMS 8-276 substrate before the copper relies on the orientation of the composite particle and is not a guarantee. Cross-sectional analysis showed that the deposited powder is substantially deformed (see Figure 208b).

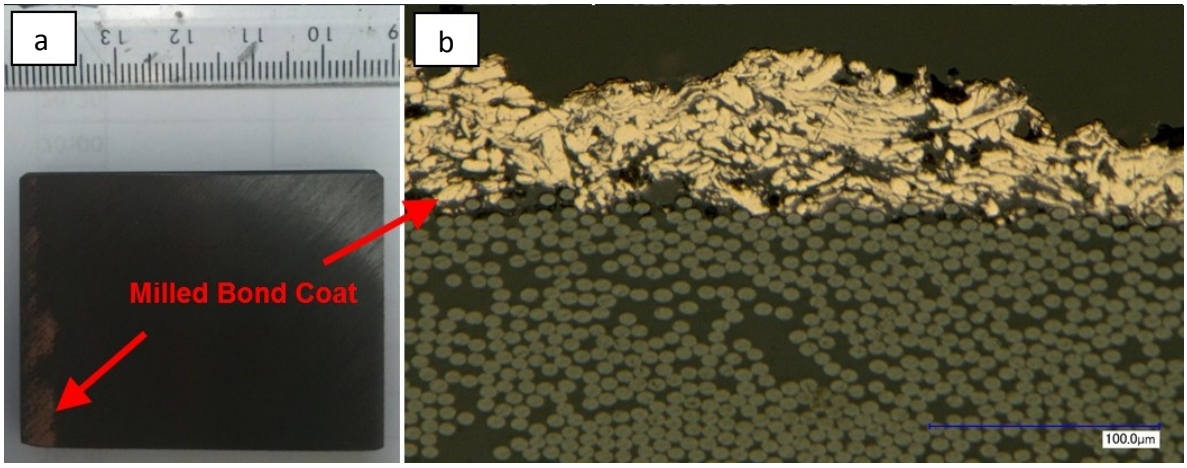

Figure 208: (a) Deposited milled powder on BMS 8-276 substrate with (b) cross-sectional.

Unfortunately, adhesion tests could not be performed on the discontinuous coating produced. It is unclear if this approach could increase adhesion; however, because of the long milling times, low quantity output, and decrease in DE, this approach was terminated.